Karlsruher Institut für Technologie

Institut für Mikro- und Nanoelektronische Systeme

Development of a novel SQUID-based microcalorimeter and software for microwave SQUID multiplexer optimisation

Zur Erlangung des akademischen Grades eines
DOKTORS DER NATURWISSENSCHAFTEN
von der KIT-Fakultät für Physik des
Karlsruher Instituts für Technologie (KIT)

angenommene

DISSERTATION

von

Constantin Schuster
aus Worms

Tag der mündlichen Prüfung:	12.07.2024
Referent:	Prof. Dr. Marc Weber
Korreferent:	Prof. Dr. Sebastian Kempf

Erklärung

Ich versichere wahrheitsgemäß, die Arbeit selbstständig verfasst, alle benutzten Hilfsmittel vollständig und genau angegeben und alles kenntlich gemacht zu haben, was aus Arbeiten anderer unverändert oder mit Abänderungen entnommen wurde sowie die Satzung des KIT zur Sicherung guter wissenschaftlicher Praxis in der jeweils gültigen Fassung beachtet zu haben.

Karlsruhe, den 18.07.2024 Constantin Schuster

I dedicate this thesis to

Dr. Steffen Blomeier

for successfully dissuading me from studying chemistry

Microcalorimeters are energy-dispersive single-particle detectors offering a unique combination of an outstanding energy resolution and a near-unity quantum efficiency. They measure the temperature rise caused by the absorption of energetic particles using a highly sensitive temperature sensor. Despite their excellent performance, the most mature detector technologies have yet to reach the fundamental resolution limit set by thermodynamic energy fluctuations. Moreover, the optimisation of readout techniques for large-scale arrays is still ongoing. In this context, we present a novel SQUID-based microcalorimeter with an in-situ tunable gain. Its temperature sensor is based on the strong temperature dependence of the magnetic penetration depth of a superconducting material operated just below its critical temperature. We describe in detail the underlying physics and report on the performance of prototype devices. We found that, in contrast to other microcalorimeters, our devices show no hysteresis, and that they can potentially achieve an energy resolution of $\mathcal{O}(400\,\mathrm{meV})$ for soft X-ray photons. For optimising the readout of large-scale arrays, we have developed a software package to simulate the complex dynamics, resulting from non-linear effects, and performance of a microwave SQUID multiplexer. The latter is presently most promising for reading out cryogenic detector arrays. We apply this software to find design parameters strongly reducing the readout noise. We find that, for example, a SQUID screening parameter of $\beta_\mathrm{L} = 0.4$ or a radio frequency flux amplitude $\Phi_\mathrm{rf} = 0.3\,\Phi_0$ are optimal.

Entwicklung eines neuartigen SQUID-basierten Mikrokalorimeters, und Software zur Optimierung von Mikrowellen-SQUID-Multiplexern

Mikrokalorimeter sind energiedispersive Einzelteilchendetektoren, die eine herausragende Energieauflösung mit einer Quanteneffizienz nahe 1 verbinden. Über einen hochempfindlichen Temperatursensor messen sie den Temperaturanstieg, der auf die Absorption eines energetischen Teilchens folgt. Trotz ihrer exzellenten Leistungsmerkmale haben auch die fortschrittlichsten Detektortechnologien das Auflösungslimit bedingt durch durch thermodynamische Energiefluktutationen noch nicht erreicht. Zudem wird weiterhin aktiv an der Optimierung der Auslese großer Detektorarrays gearbeitet. Vor diesem Hintergrund präsentieren wir ein neuartiges, SQUID-basiertes Mikrokalorimeter mit in-situ regelbarer Sensitivität. Sein Temperatursensor basiert auf der starken Temperaturabhängigkeit der magnetischen Eindringtiefe eines Supraleiters knapp unterhalb seiner Sprungtemperatur. Wir beschreiben detailliert seine Funktion und präsentieren Messungen an ersten Prototypen. Im Gegensatz zu anderen Mikrokalorimetern zeigen unsere Prototypen keine Hysterese, und können theoretisch eine Energieauflösung $\mathcal{O}(400\,\mathrm{meV})$ für weiche Röntgenstrahlung erreichen. Zur Optimierung der Auslese großer Detektorarrays haben wir ein Softwarepacket entwickelt, um das nicht-lineare Verhalten von Mikrowellen-SQUID-Multiplexern zu simulieren. Diese sind, aus aktueller Sicht, besonders gut zur Auslese von Detektorarrays geeignet. Mithilfe dieser Software identifizieren wir geeignete Entwurfsparameter, die das Rauschen reduzieren. Unter anderem sind ein Abschirmparameter von $\beta_\mathrm{L} = 0.4$ oder eine Amplitude von $\Phi_\mathrm{rf} = 0.3\,\Phi_0$ des hochfrequenten Flussbeitrags optimal.

Contents

1 Introduction **1**

2 Cryogenic Microcalorimeters: Current state of development **5**

2.1 Overview of existing microcalorimeter technologies 5

2.1.1 Operation principle of cryogenic microcalorimeters 5

2.1.2 Magnetic Microcalorimeters 8

2.1.3 Transition Edge Sensors 10

2.1.4 Magnetic Penetration-depth Thermometers 12

2.2 dc-SQUID-based readout of cryogenic microcalorimeters 12

2.2.1 Fundamentals of dc-SQUIDs 13

2.2.2 dc-SQUID detector readout 16

2.3 SQUID multiplexing techniques 18

2.3.1 Time-division multiplexing 18

2.3.2 Code-division multiplexing 20

2.3.3 Frequency-domain multiplexing 21

2.3.4 Microwave SQUID multiplexing 22

3 Theory of the λ-SQUID **23**

3.1 The λ-SQUID: A superconducting microcalorimeter with in-situ tunable gain 23

3.2 Mutual inductance between parallel superconducting lines 26

3.2.1 Method of Sheen *et al.* 30

3.2.2 Method of Chang *et al.* 31

3.2.3 Comparison and testing of Chang's and Sheen's methods 32

3.2.4 Importance of the reference patch 33

3.2.5 Temperature dependent mutual inductance of superconducting striplines 35
3.3 Noise analysis of the λ-SQUID 38

4 Prototype λ-SQUID-like devices 39
4.1 Fabrication technology 39
4.2 Experimental methods 42
4.2.1 Static mutual inductance measurements 44
4.2.2 Mutual inductance measurements using flux ramp modulation 46
4.3 λ-SQUIDs with aluminium λ-coils 47
4.3.1 Temperature-dependent mutual inductance M_{in} 47
4.3.2 Comparison to simulated data 54
4.3.3 Noise performance estimate 58
4.4 λ-SQUIDs with Mo/AuPd bilayer λ-coils 61
4.4.1 Integration of Mo/AuPd bilayers into the fabrication process 62
4.4.2 Temperature-dependent mutual inductance M_{in} 64
4.5 Unexplained excess sensitivity in a singular λ-SQUID prototype 66

5 Design considerations to optimise λ-SQUIDs 69
5.1 Generalised description of the λ-coil 69
5.2 λ-coils with a stripline geometry 73
5.2.1 Variation of the sensor coil width 75
5.2.2 Variation of sensor- and input coil width 78
5.2.3 Variation of the sensor coil thickness 79
5.2.4 Variation of the number of sensor coil windings 80
5.3 Future developments 82
5.3.1 Microwave λ-SQUID Multiplexing 82
5.3.2 Direct absorption λ-SQUID bolometer 84
5.3.3 Superconducting Screening Thermometer 84

5.3.4 Micro-susceptometer SQUID 86

6 Microwave SQUID Multiplexing 89

6.1 Inductively coupled non-hysteretic, unshunted rf-SQUIDs 89

6.1.1 Vanishing probe tone power $P_{\mathrm{exc}} \to 0$ 91

6.1.2 Vanishing screening currents $\beta_{\mathrm{L}} \to 0$ 91

6.1.3 General case 91

6.2 Single μMUX channel 92

6.2.1 Dynamical lumped element resonator model 94

6.3 Readout and linearisation 99

6.4 Hybrid microwave SQUID multiplexing 103

6.4.1 First HμMUX device and multiplexed readout 104

6.4.2 Bandwidth and noise performance of HμMUX compared to μMUX . . 107

6.5 Overview of the software framework for μMUX simulation 109

6.5.1 Generation of noise traces 110

6.5.2 Calculation of the quasi-static magnetic flux threading the the SQUID loop 111

6.5.3 Derivation of the effective inductance shift 111

6.5.4 Calculation of the actual resonance frequency 112

6.5.5 Derivation of the transmission coefficient 112

6.6 Detailed description of the simulation framework 112

6.6.1 Vanishing probe tone power $\Phi_{\mathrm{rf}} \to 0$ 114

6.6.2 Vanishing screening currents $\beta_{\mathrm{L}} \to 0$ 115

6.6.3 General case 116

7 Applications of numerical μMUX simulations 119

7.1 Default simulation parameters 119

7.2 Software verification 121

7.2.1 Dependence of the flux noise on the probe tone power 121
7.2.2 Bandwidth- and noise penalty of hybrid microwave SQUID multiplexing 123
7.3 Towards a full device optimisation of microwave SQUID multiplexers . . . 125
7.3.1 Optimal screening parameter β_{L} and probe tone frequency f_{exc} 125
7.3.2 Ideal probe tone power P_{exc} 128
7.3.3 Optimal ratio between maximum frequency shift and resonator bandwidth 129
7.4 Potential other applications of the simulation framework 132
7.4.1 Linearity of FRM readout 132
7.4.2 Noise shaping 133
7.4.3 Probe tone modulation 134

8 Conclusion and Outlook **139**

Bibliography **145**

1. Introduction

In recent years, cryogenic microcalorimeters such as superconducting transition-edge sensors (TESs) [Irw05, Ull15] or magnetic microcalorimeters (MMCs) [Fle05, Kem18] have become integral to several fields of physics due to their remarkable combination of near-unity quantum efficiency and outstanding energy resolution. They generally consist of a particle absorber in strong thermal contact to a highly sensitive temperature sensor, and are weakly thermally coupled to a heat bath. Upon absorption of an energetic particle in the absorber, the temperature of the detector rises proportionally to the deposited energy. The task of measuring the energy of an incoming particle therefore reduces to measuring a small temperature change with utmost precision, so a sensor with a strongly temperature-dependent property is required. This may be the resistance of a superconductor operated within its normal-to-superconductor transition (TES) or the magnetisation of a paramagnetic material situated in a weak magnetic field (MMC). Another property with strong temperature dependence is the magnetic penetration depth λ of a superconductor, which diverges as its critical temperature T_c is approached. Such magnetic penetration depth thermometers (MPTs) have already been developed [Nag12, Ban12], but have not yet reached the maturity of MMCs or TESs due to hysteretic effects [Ste13]. For thermometer readout, appropriate low-impedance readout circuits transform the microcalorimeter signal into a change of current or magnetic flux, which is subsequently measured by wideband superconducting quantum interference devices (SQUIDs) [Fag06]. These sensors can measure magnetic flux with utmost precision. Current applications for cryogenic microcalorimeters include astronomy [Bar18, Ban19], particle physics [Gas17, Kan17, Sin23], dark matter search [Rot18, vK23], radio-nuclide metrology [Loi18, Mül24], and many more. Another application with the potential to significantly benefit from microcalorimeters is X-ray emission spectroscopy (XES), both at synchrotron light sources and in a laboratory environment [Fri06, Dor16]. Here, the detection efficiency of microcalorimeter-based detection systems strongly relax the beam intensity requirements compared to state-of-the-art wavelength-dispersive X-ray spectrometers based on diffraction gratings or bent crystals [Uhl15]. This significantly eases measurements of strongly diluted or radiation sensitive samples. An additional advantage is that microcalorimeters can cover a wide energy range from 100 eV [Lee19] up to 100 keV [Nov15], including the entire tender X-ray range which is challenging to achieve with grating and crystal spectrometers [Uhl15]. At the time of writing, state-of-the-art TES- and MMC-based X-ray detectors achieve a remarkable energy resolution ΔE_FWHM of 0.72 eV for 1.5 keV photons [Lee15] and of 1.25 eV for 5.9 keV photons [Kra23], which comes close to wavelength-dispersive detectors. At the same time, the quantum efficiency of microcalorimeters is almost 100 % in this energy range, and hence out-competes wavelength-dispersive spectrometers by orders of magnitude. Despite the remarkable performance of both, MMCs and TESs, either detector type has yet to reach an energy resolution in the

range of 100 meV. Consequently, they are not yet suitable for applications requiring such a level of resolution, such as the investigation of vibrations or *d*-*d*-excitations in soft X-ray spectroscopy [But96], or resonant inelastic X-ray scattering [Ame11]. While development on MMCs and TESs is ongoing, we think it is beneficial to consider new microcalorimeter technologies. Against this background, we have developed a novel SQUID-based microcalorimeter called the λ-SQUID. Similarly to an MPT, it is based on the magnetic penetration depth λ of a superconductor operated just below its critical temperature T_c. A λ-SQUID mostly resembles a regular dc-SQUID, with the largest fraction of the device made from a superconducting material with a critical temperature $T_\mathrm{c} \gg T_0$ much larger than the operating temperature T_0 of the device. However, a section of the λ-SQUID loop with inductance L_λ (the λ-coil) consists of a different superconducting material with a much lower critical temperature $T_\mathrm{c}^\lambda \ll T_\mathrm{c}$. The operating temperature is selected such that $T_0 \lessapprox T_\mathrm{c}^\lambda$. A temperature-induced change of the magnetic penetration depth λ results in a redistribution of current running in the λ-coil. As a consequence, the mutual inductance M_in between the λ-coil and an input coil with inductance L_in carrying a constant dc current I_in is changed. This causes a change of the magnetic flux $\Delta\Phi = \Delta M_\mathrm{in} I_\mathrm{in}$ threading the λ-SQUID loop, which can be measured equivalently to a regular dc-SQUID.

Development of highly sensitive microcalorimeters alone is however not enough to realise next-generation experiments. Sophisticated superconducting electronics are required to read out the detectors without degrading the noise or bandwidth of the signals. In order to suppress the noise of the room-temperature readout electronics below that of the sensing SQUID, typically a two-stage arrangement is used. The output current signal of the sensing SQUID serves as input to a second SQUID operated as a highly sensitive low-noise amplifier [Dru96]. While this is a feasible approach for the readout of single detector channels or small arrays, the linear scaling of readout cost, complexity and heatload to the cryostat makes such an approach prohibitive for large detector arrays comprising hundreds or even thousands of detectors. To facilitate experiments with such large pixel counts, a variety of SQUID multiplexing schemes have been developed. These include time-division [Dor16], frequency-division using MHz [dH14, Ric21] or GHz carriers [Mat08, Hir13, Kem17], code-division [Mor16] or hybrid [Rei08, Irw18, Yu20, Sch22] multiplexing schemes. Out of these, microwave SQUID multiplexing [Mat08, Hir13, Kem17] (μMUXing) appears to be most suited for the readout of large and ultra-large scale cryogenic detector arrays. It does not require a restriction of the bandwidth per readout channel, and readout noise is, to first order, independent of the multiplexing factor. Microwave SQUID multiplexing relies on a large number of superconducting microwave resonators, each inductively coupled to an unshunted, non-hysteretic rf-SQUID. All resonator channels have a unique resonance frequency and are capacitively coupled to a single common transmission line carrying a comb of probe tone frequencies. Each carrier is matched to the resonance frequency of a specific resonator channel. The SQUID signals are thus transduced onto the amplitude and phase of the individual microwave carrier signals, and can be carried simultaneously along the single transmission line.

Resulting from the non-linearity of the Josephson equations describing the underlying physics of Josephson tunnel junctions and consequently the dependence of the rf-SQUID response on probe tone power [Weg22], μMUXes have intrinsically non-linear characteristics. Additionally, the non-zero response time of the microwave resonators must be taken into account. Within this thesis, we developed a model accounting for dynamic resonator effects up to first-order. Combined with the complexity of the FRM readout method typically used for linearisation and the large number of partially interdependent μMUX parameters, this makes using analytical methods for μMUX description or optimisation unfeasible. In order to realise next-generation highly multiplexed detector systems, however, it is paramount to optimise the design and readout of a μMUX. In this thesis, we hence present a simulation framework we have developed to explore the behaviour of a single μMUX resonator channel using numerical methods [Sch23]. Our simulations include the three most dominant noise sources, i.e. amplifier noise due to the cryogenic amplifier, resonator noise caused by coupling to two-level systems in its vicinity, and flux noise in the rf-SQUID. Both white and $1/f-$like noise spectra can be modelled. Flux ramp modulated readout [Mat12], even with a finite bandwidth of the flux ramp, and the finite resonator response time can be included. The dependence rf-SQUID response on probe tone power is implemented based on our most recent model [Weg22], and enables the simulations to take both finite probe tone powers and screening currents in the rf-SQUID loop into account.

In chapter 2, we begin by introducing the current state-of-the art of cryogenic microcalorimeters. We discuss different microcalorimeter types along with their strengths and weaknesses, as well as the SQUID readout and multiplexing schemes commonly applied in existing or planned experiments. We give a short summary of the thermodynamic description of cryogenic microcalorimeters, showing that their energy resolution is fundamentally limited.

In chapter 3, we introduce the concept of the λ-SQUID, along with an in-depth theory of operation. Using a custom software package based on sophisticated numerical methods, we detail the influence of the magnetic penetration depth λ on the mutual inductance between two parallel, straight inductors. This yields a robust understanding of the mechanism by which a λ-SQUID senses small changes in temperature. Furthermore, we show that in λ-SQUIDs, the proportionality of the flux signal $\Delta\Phi \propto I_{\mathrm{in}}$ to the dc input current yields a tunable gain, which we can adjust over a wide range even during device operation.

In chapter 4, we present the design and fabrication of first λ-SQUID prototypes. Based on our expertise on dc-SQUIDs, we have designed and manufactured λ-SQUIDs that utilise aluminium for the λ-coil, and niobium for the rest of the device. We detail the experimental methods with which we have characterised the devices. We present experimental data on the temperature-dependent mutual inductance M_{in}, and verify the agreement between this data and our expectations from the theory described in the previous chapter. We carefully test for hysteresis in the mutual inductance curves. Based on our measurements, we give detailed insight into the potential energy resolution of a fully functional λ-SQUID-based microcalorimeter, and demonstrate that it is at

least competitive to established microcalorimeter types.

We discuss design requirements for λ-SQUIDs to yield optimal temperature sensitivity in chapter 5. First, we consider the λ-coil forming the sensitive element from a general point of view, in order to conclude whether ideal values exist for its total inductance L_λ, the geometric volume V and the mutual inductance M_{in} to the input coil. Additionally, we use our software package introduced in chapter 3 to analyse the influence of the design of the λ-coil and input coil on the λ-SQUID temperature sensitivity. We focus on the width and thickness of the superconducting stripline that forms the λ-coil, and compare simulated mutual inductance curves to experimental data on λ-SQUID with varying λ-coil width to further verify our numerical approach. We remark how the λ-coil and input coil should be dimensioned to optimise temperature sensitivity, and conclude how future iterations of λ-SQUIDs should be designed. Finally, we present developments of technologies related to the λ-SQUID, like a concept for a λ-SQUID-based microbolometer.

In chapter 6, we give an introduction to microwave SQUID multiplexing, highlighting the principle of operation and outlining the physics. We recite the electronic behaviour of unshunted, non-hysteretic rf-SQUIDs inductively coupled to superconducting inductors. This is followed by a detailed derivation of our mathematical model for a superconducting lumped-element microwave resonator with a time-dependent total inductance, which takes dynamic effects into account up to the first order. After detailing the FRM method to linearise the output of a μMUX channel, we present the concept of HμMUX hybrid SQUID multiplexing. With experimental data from a prototype device, we demonstrate that HμMUX requires no additional technology compared to regular μMUX, neither for the device fabrication nor in terms of readout electronics. We then derive the potential performance of HμMUX compared to regular μMUX, where we focus on readout noise and bandwidth. This chapter concludes with a detailed description of the software framework algorithms and equations we have implemented for numerical μMUX simulation.

In chapter 7, we verify that our simulation framework works as intended by comparing simulation results to both, experimental data and theoretical considerations. We specify the default parameters used for all subsequent simulations, and then illustrate how the simulation software can be used to identify optimised parameters for the design and readout of a μMUX to minimise readout noise. Given the large configuration space, a full optimisation with regards to all parameters simultaneously is beyond the scope of this thesis, so we focus on the influence of the screening parameter β_{L}, the probe tone frequency f_{exc}, the probe tone power P_{exc} and the ratio η between maximum frequency shift $\Delta f_{\mathrm{res}}^{\mathrm{max}}$ and resonator bandwidth Δf_{BW} here. We continue with some exemplary additional uses of the simulation framework beyond optimisation. The modularity of our software allows it to be used for a variety of different applications. We present how we can model the non-linearity remaining after FRM, as well as the noise-shaping effects of FRM. Finally, we show that our simulation framework also easily allows us to study novel readout schemes without requiring the design or acquisition of any application-specific readout hardware.

2. Cryogenic Microcalorimeters: Current state of development

Cryogenic microcalorimeters have become key tools for several fields of physics, such as astronomy [Bar18, Ban19], particle physics [Gas17, Kan17, Sin23], dark matter search [Rot18, vK23], X-ray spectroscopy [Dor17, Ung24] or radio-nuclide metrology [Loi18, Mül24]. The family of these energy-dispersive single particle detectors includes devices such as semiconductor thermistors [McC93, Ban00], superconducting transition-edge sensors (TESs) [Irw05, Ull15], magnetic microcalorimeters (MMCs) [Fle05, Kem18] or magnetic penetration depth thermometers (MPTs) [Nag12, Ban12]. The presently mostly used technologies in the field are TES and MMCs, which have already proven remarkable performance and have been applied in various experiments. In this chapter, we will briefly introduce microcalorimeters in general, and MMCs and TESs in particular. We will also discuss SQUIDs, as they are commonly used to read out such detectors. Finally, we will give an overview over the multiplexing schemes that were developed to allow the readout of large arrays comprising hundreds of individual detectors.

2.1 Overview of existing microcalorimeter technologies

A detailed discussion of all existing cryogenic microcalorimeter technologies is beyond the scope of this thesis, but a basic understanding is nonetheless required to assess the viability of our novel detector concept. Before looking at specific realisations in more detail, we will first consider the microcalorimeter from a more abstract, thermodynamic point of view to gain some insight into their common fundamental principles and potential limitations.

2.1.1 Operation principle of cryogenic microcalorimeters

In figure 2.1(a), a schematic diagram of the thermodynamic systems comprising a microcalorimeter is depicted. Any microcalorimeter fundamentally consists of two components: A particle absorber with specific heat C_{abs}, and a temperature sensor with specific heat C_{sens}. Both components are in tight thermal contact with each other, represented by the thermal conductance G_{S}. Additionally, the absorber is coupled to a heat bath at temperature T_0 via the thermal conductance G_{B}. The thermal coupling between absorber and sensor is much larger than the coupling between absorber and heat bath, i.e. $G_{\mathrm{S}} \gg G_{\mathrm{B}}$. In thermal equilibrium, both, sensor and absorber, are at the temperature T_0 of the heat bath. When a particle is absorbed, it deposits an energy ΔE into the absorber. From the absorber, the deposited energy can flow to the sensor

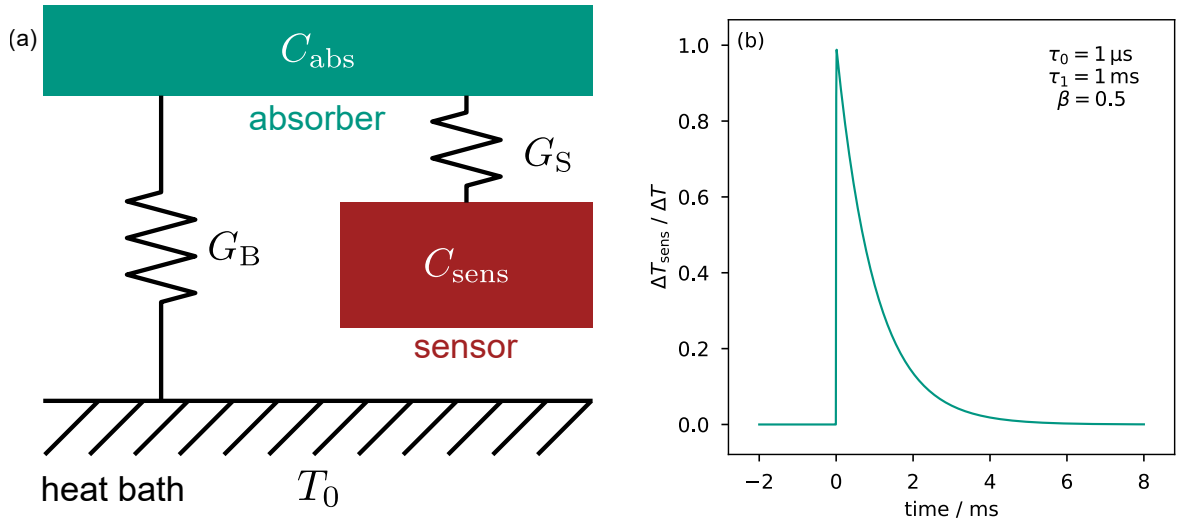


Fig. 2.1: (a) Simplified schematic diagram of a cryogenic microcalorimeter. The temperature sensor with specific heat C_{sens} is in strong thermal contact to the particle absorber with specific heat C_{abs} via the thermal conductivity G_{S}. In turn, the absorber is weakly coupled to a heat bath kept at temperature T_0 via the thermal conductance G_{B}. (b) Schematic depiction of the pulse shape of the temperature rise ΔT_{sens} experienced by the sensor upon absorption of a particle with energy ΔE in the absorber at time $t_0 = 0$. Here, a rise time $\tau_0 = 1\,\mu s$, decay time $\tau_1 = 1\,ms$ and specific heat ratio $\beta = 0.5$ were assumed.

via G_{S}, and to the heat bath via G_{B}. In the absence of noise, this is described by the differential equations [Fle05]

$$C_{\mathrm{sens}} \frac{\mathrm{d}T_{\mathrm{sens}}}{\mathrm{d}t} = -\left(T_{\mathrm{sens}}(t) - T_{\mathrm{abs}}(t)\right) G_{\mathrm{S}}, \tag{2.1}$$

$$C_{\mathrm{abs}} \frac{\mathrm{d}T_{\mathrm{abs}}}{\mathrm{d}t} = -\left(T_{\mathrm{abs}}(t) - T_{\mathrm{sens}}(t)\right) G_{\mathrm{S}} - \left(T_{\mathrm{abs}}(t) - T_0\right) G_{\mathrm{B}} + P(t), \tag{2.2}$$

where $P(t) = \Delta E \delta(t - t_0)$ represents the instantaneous energy input due to the absorption of a particle at time t_0. Since the thermal coupling to the sensor is much greater, the absorber and sensor quickly thermalise to the same temperature before a significant portion of the heat can flow to the heat bath. To understand the dynamics of a microcalorimeter, its rise time τ_0 and its decay time τ_1 are of major importance. They can be derived from equations 2.1 and 2.2 and are given by the expression [Fle05]

$$\tau_{0/1} = \frac{C_{\mathrm{abs}} G_{\mathrm{S}} + C_{\mathrm{sens}} \left(G_{\mathrm{S}} + G_{\mathrm{B}}\right)}{2 G_{\mathrm{S}} G_{\mathrm{B}}} \pm \sqrt{\frac{\left[C_{\mathrm{abs}} G_{\mathrm{S}} + C_{\mathrm{sens}} \left(G_{\mathrm{S}} + G_{\mathrm{B}}\right)\right]^2}{4 G_{\mathrm{S}}^2 G_{\mathrm{B}}^2} - \frac{C_{\mathrm{abs}} C_{\mathrm{sens}}}{G_{\mathrm{S}} G_{\mathrm{B}}}}. \tag{2.3}$$

The rise time τ_0 defines the time scale on which absorber and sensor thermalise, i.e the time scale on which energy flows from the absorber into the sensor. The temperature increase of the absorber-sensor system $\Delta T = \Delta E/(C_{\mathrm{abs}} + C_{\mathrm{sens}})$ is (to first order) proportional to the energy ΔE of the absorbed particle. Thus, the problem of measuring the energy of a particle reduces to a problem of precisely measuring the resulting temperature rise. To achieve this, we use a sensor made from a material with a strongly temperature dependent property. A number of possible physical effects may be used which result in a strongly temperature dependent observable or material property at cryogenic temperatures, giving rise to the several types of cryogenic microcalorimeters we will introduce later. The much longer decay time $\tau_1 \gg \tau_0$ specifies the time scale on which heat flows to the heat bath, i.e. how quickly the absorber-sensor system cools back down to the bath temperature T_0.

The pulse shape of the temperature rise resulting from the absorption of a particle with energy ΔE in the absorber is illustrated in figure 2.1(b). Resulting from the differential equations 2.1 and 2.2, it can be described by an exponential rise with rise time τ_0, where heat is transferred from the absorber to the sensor, and an exponential decay with the much slower decay time τ_1 during which the absorber and sensor cool back down to base temperature. The pulse shape of the additional energy E_{sen} in the sensor can be approximated by the equation [Fle05]

$$E_{\mathrm{sen}}(t) = \Delta E \beta \left(\mathrm{e}^{-t/\tau_1} - \mathrm{e}^{-t/\tau_0} \right), \tag{2.4}$$

$$\beta = \frac{C_{\mathrm{sens}}}{C_{\mathrm{sens}} + C_{\mathrm{abs}}}. \tag{2.5}$$

Here we introduced the ratio β of the sensor specific heat to the total heat capacity of the microcalorimeter. At finite temperatures, thermodynamic energy fluctuations between the different subsystems introduce a noise contribution that is independent of the type of thermometer and readout chain used, and which thus fundamentally limits the energy resolution of all microcalorimeters. This thermodynamic energy fluctuation noise is given by [McC05, Fle05]

$$S_{\mathrm{E,TD}}(f) = k_{\mathrm{B}} C_{\mathrm{sens}} T^2 \left[\frac{4\,(1-\beta)\,\tau_0}{1 + (2\pi\tau_0 f)^2} + \frac{4\beta\tau_1}{1 + (2\pi\tau_1 f)^2} \right] \tag{2.6}$$

for the typical situations $\tau_0 \ll \tau_1$ and $0.1 < C_{\mathrm{sens}}/C_{\mathrm{abs}} < 10$, which we will assume in the following. The energy resolution of a microcalorimeter is determined by

$$\Delta E_{\mathrm{FWHM}} = 2\sqrt{2\ln 2} \left[\int_0^\infty \frac{|p(f)|^2}{S_{\mathrm{E,tot}}(f)} \mathrm{d}f \right]^{-1/2}, \tag{2.7}$$

if optimal filtering is used [Fle05]. Here, $S_{\mathrm{E,tot}}(f)$ is the total energy noise, which includes but is generally not limited to the thermodynamic fluctuation noise $S_{\mathrm{E,TD}}(f)$. In real microcalorimeters additional sources of noise exist, e.g. from the readout chain

including SQUIDs and amplifiers. These additional contributions are specific to the calorimeter type and will be discussed later. The detector responsivity is the normalised Fourier space representation of the pulse shape previously introduced and has the form

$$|p(f)| = \frac{2\beta\tau_1}{\sqrt{1+(2\pi\tau_0 f)^2}\sqrt{1+(2\pi\tau_1 f)^2}}. \tag{2.8}$$

For calorimeters, the readout is typically much faster than the signal decay time τ_1. Calorimeters can thus be used to detect single absorption events. A variation of the concept, the cryogenic micro-bolometer, is operated at a much lower bandwidth to measure a continuous stream of incoming particles resulting in a time-constant deposited power. Here, the temperature of the detector is set by the incoming power and the heat flow via thermal conduction to the bath. Bolometers are applied to measure, for example, the energy of radiation such as the cosmic microwave background [Ade14]. For such applications, the low energy of individual photons makes single-particle detection unfeasible. While we will mention bolometers again later in this thesis, the main focus remains on microcalorimeters.

2.1.2 Magnetic Microcalorimeters

Magnetic microcalorimeters (MMCs) use a paramagnetic metallic material as their temperature sensor. Common sensor materials are gold or silver doped with small amounts of erbium [Kem18, Fri16]. The magnetisation of this sensor, when placed in a weak magnetic field, is strongly temperature dependent [Fle05]. This magnetisation change causes a change of magnetic flux threading a coil placed near it, which we can measure using a SQUID. A typical setup used to read out MMCs is schematically depicted in figure 2.2(a): Two independent sensor pixels are each coupled to a sensor coil with inductance L_M. The two sensor coils are connected to form a closed superconducting loop, which we prepare to carry a persistent field current I_F. This field current generates a weak magnetic field at the sensor pixels. Upon particle absorption in one of the pixels, its magnetisation changes, inducing a magnetic flux $\Delta\Phi_\mathrm{sen}$ in the sensor coil. Due to flux conservation in closed superconducting loops, a screening current ΔI_F in the loop results. The orientation of the two sensor coils is such that the sign of screening currents caused by one pixel is opposite to that of the other. The sign of the screening current thus gives information about the pixel in which the absorption occurred. For readout, an input coil with inductance L_in is connected to the two sensor coils, forming a superconducting flux transformer. Here, we also consider the parasitic inductance L_par resulting, for example, from bond wires between the MMC chip and a separate SQUID chip. Compared to the flux $\Delta\Phi_\mathrm{sen}$ induced by one of the sensor pixels, the magnetic flux $\Delta\Phi_\mathrm{SQ}$ induced into the SQUID loop is reduced by a factor of [Bur08]

$$\frac{\Delta\Phi_\mathrm{SQ}}{\Delta\Phi_\mathrm{sen}} = \frac{M_\mathrm{in}}{L_\mathrm{M} + 2\left(L_\mathrm{in} + L_\mathrm{par}\right)}. \tag{2.9}$$

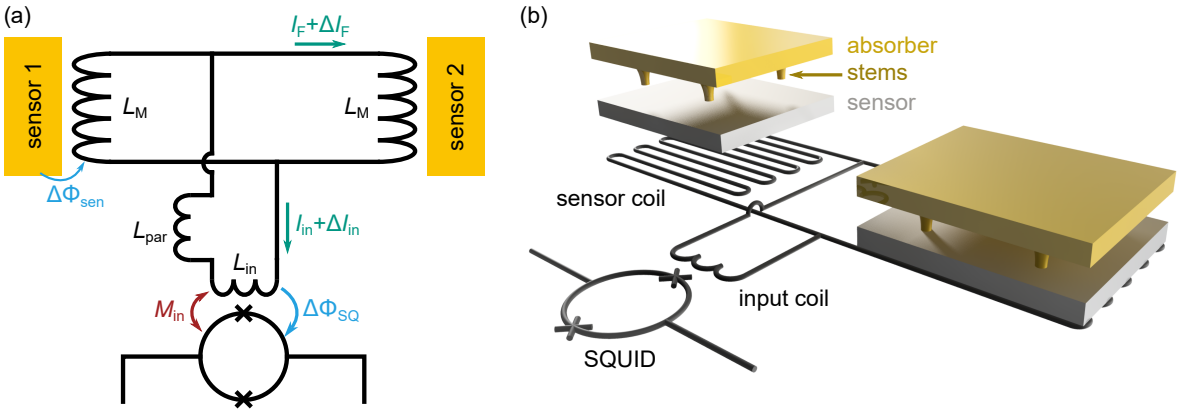


Fig. 2.2: (a) Schematic circuit diagram of a typical MMC readout arrangement. Two independent sensor pixels are coupled to a superconducting coil with inductance L_M each. Both coils form a closed superconducting loop carrying a persistent field current I_F, resulting in a weak magnetic field at the sensors. The magnetisation change resulting from a particle absorption in one pixel induces a flux change $\Delta\Phi_{sen}$ into the superconducting closed loop, causing a screening current ΔI_F. The sensor coils form a flux transformer together with the SQUID input coil with inductance L_{in} and the parasitic inductance L_{par}. The flux signal $\Delta\Phi_{SQ}$ induced into the SQUID results from the change of input current ΔI_{in} through the input coil. (b) Schematic render of an MMC pixel pair, superconducting flux transformer and SQUID. The sensor coils typically have a meander geometry, and sit underneath the sensor. The absorbers are placed on top of the sensors with stems to reduce the contact surface area.

Consequently, in such a geometry, the flux signal $\Delta\Phi_{SQ}$ measured by the SQUID is only on the order of a few percent of the flux signal $\Delta\Phi_{sen}$ originally caused by the sensor [Bur08, Bau22]. The advantage of this layout is that one SQUID can be used to read out two MMC pixels. Additionally, fluctuations of the bath temperature T_0 will cause pseudo-signals with same magnitude but opposite sign in the two pixels. Such temperature fluctuations will therefore not cause any screening currents ΔI_F in the closed superconducting loop formed by the two sensor coils. In figure 2.2(b), a schematic render illustrating an MMC pixel pair and superconducting flux transformer is shown. The meander-shaped sensor coils are placed underneath the paramagnetic sensor, separated only by a thin non-conducting layer for electrical isolation. The particle absorber, usually made from electroplated gold, sits atop the sensor and is freestanding on a few stems with small cross-section. By reducing the area of the interface between sensor and absorber, the loss of athermal phonons from the absorber to the substrate can be reduced, which could otherwise lead to undesired systematic errors in the measured energies [Fle09].

At the time of writing, MMCs manage outstanding energy resolutions of $\Delta E_{FWHM} = 1.25\,\text{eV}$ at photon energies of $5.9\,\text{keV}$ [Kra23], outperforming competing technologies in this energy range. They excel with short signal rise times (τ_0 on the order of $100\,\text{ns}$ [Kem18]) and unmatched linearity over a wide energy range [Zah24]. The tem-

perature dependent magnetisation of the sensor is well understood and stable over long periods of time. Downsides of this calorimeter type are the rigid cryogenic requirements, as the described level of sensitivity is only achieved at very low operating temperatures $T_0 \lesssim 20\,\mathrm{mK}$. Experiments taking advantage of MMCs must therefore be designed carefully with regards to heat load, thermalisation and cooling capacity. Additionally, for best performance, the SQUID readout must be impedance matched to the detector. Also the readout coil setup typically used to couple MMCs to the SQUIDs for readout results in a significant reduction in signal [Bur08, Bau22], leading to an increase in apparent SQUID noise. The contributions of the SQUIDs to the total system noise is thus difficult to suppress. All in all, MMCs offer remarkable performance at the price of challenging requirements on the surrounding systems which may be difficult to meet in restrictive, e.g. space- or power limited applications. Being a well-established microcalorimeter type, MMCs are used in several experiments like primary activity measurements [Loi18], determination of the neutrino mass [Gas17], search for neutrinoless double-β-decays [Kan17], calorimetric mass spectrometry on molecule fragments [Nov15], or for nuclear safeguards [Kim18].

2.1.3 Transition Edge Sensors

Another natural choice for a strongly temperature sensitive material property is the resistance of a superconducting material in its normal-to-superconducting phase transition. Transition edge sensors (TESs) make use of this effect, and have been developed into one of the most established types of cryogenic microcalorimeters [Irw05]. The sensor, a segment of a superconducting thin film, is operated near its transition temperature commonly employing electro-thermal feedback [Irw95, Irw05] to stabilise the sensor in the narrow temperature range where the resistance varies between zero and its normal value. This readout scheme is schematically depicted in figure 2.3(a). An operating current I_{ETF} is applied to a parallel connection of the TES and a bias resistor with resistance R_{B}. Since the bias resistance $R_{\mathrm{B}} \ll R_{\mathrm{TES}}$ is much lower than the resistance R_{TES} of the TES at its working point, the TES is effectively operated in voltage bias. The readout scheme is thus equivalent to the circuit diagram in figure 2.3(b). Due to this voltage bias, a current I_{TES} runs through the sensor, dissipating the Joule heating power P_{J}. Through coupling to the heat bath, the power P_{B} flows from the detector to the bath, and the signal power P results from absorbed particles. The temperature T of the TES is then defined by the differential equation

$$(C_{\mathrm{sens}} + C_{\mathrm{abs}})\,\frac{\mathrm{d}T}{\mathrm{d}t} = -P_{\mathrm{B}}(t) + P_{\mathrm{J}}(t) + P(t). \tag{2.10}$$

Without incoming radiation, i.e. $P = 0$, after a sufficiently long time a steady state results where the TES reaches a constant operating temperature T_{TES} where the Joule heating power input P_{J} equals the power P_{B} flowing to the heat bath.

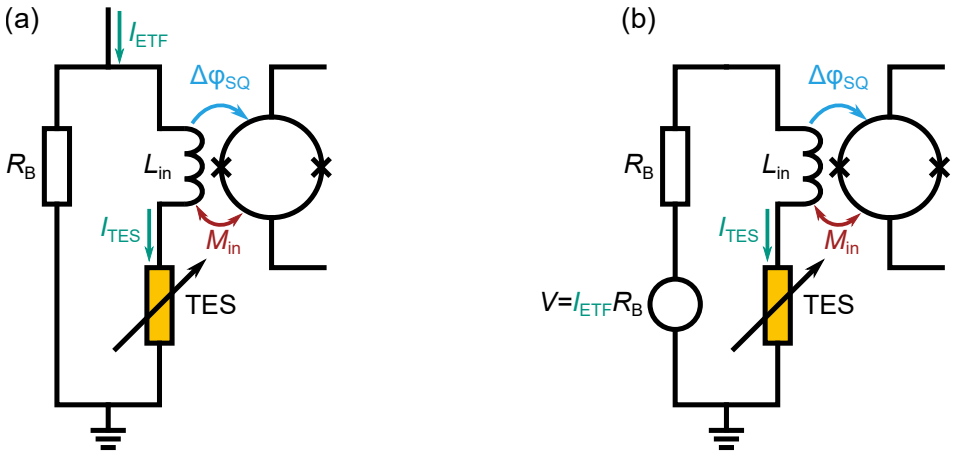


Fig. 2.3: (a) Schematic circuit diagram of a typical TES readout arrangement. An operating current I_{ETF} is applied. The TES, with resistance R_{TES} at its working point, is effectively operated in a voltage bias due to the bias resistor $R_{\mathrm{B}} \ll R_{\mathrm{TES}}$ connected in parallel to it. The circuit is thus electronically equivalent to the one depicted in (b). If the resistance of the TES changes due to a change in temperature, the resulting change of the current I_{TES} through a coil with inductance L_{in} is measured with a SQUID inductively coupled to it via the mutual inductance M_{in}.

Naturally, this operating temperature is above the temperature T_0 of the heat bath. Thus, requirements on the base temperature of the cryogenic system is less stringent for TESs compared to MMCs.

Upon particle absorption, the temperature of the sensor rises, increasing its resistance. In voltage bias, this causes a reduction of the current I_{TES} through the TES and the dissipated Joule heating power P_{J}. This negative feedback loop stabilises the TES at its desired working point in the normal-to-superconducting phase transition, and we can read out the current I_{TES} as a signal. To achieve this, we use a superconducting coil with inductance L_{in} connected in series with the TES. This input coil couples to a SQUID via the mutual inductance M_{in}, so changes in the feedback current I_{TES} can be measured sensitively. By making the mutual inductance M_{in} between the input coil and the SQUID loop large, we can ensure that the noise of the readout SQUID does not degrade the overall noise performance.

Noise in TESs is fundamentally limited by the thermodynamic energy fluctuations discussed in section 2.1.1, as well as Johnson noise due to their finite resistance and temperature [Irw05]. However, excess noise of practical TESs has been reported [Sei04, Lin04, Ull04, Jet09], so the energy resolution of real TESs has not yet reached their theoretical limit. At the time of writing, the sources of this excess noise are still being researched, but possible explanations include noise due to phase boundary fluctuations [Luu03], percolation noise [Bag09, Bra10] or mixed-down Johnson noise [Wes21].

Additionally, the power P_{J} dissipated by TES during operation causes a heat load which may be undesired for certain applications. Experiments based on TES include Lynx

for satellite-based X-ray spectroscopy [Ban19], the neutrinoless double-β-decay search experiment CUPID [Sin23] or BICEP2 [Ade14] for polarisation measurements of the cosmic microwave background. Some additional applications are the search for solar axions [Yag23], neutrino mass determination [RG13, Fav16], or X-ray absorption and emission spectroscopy [Dor17].

2.1.4 Magnetic Penetration-depth Thermometers

While TESs and MMCs account for the vast majority of cryogenic microcalorimeters used in experiments today, other types have been proposed and developed throughout the years. One such type is the magnetic penetration-depth thermometer (MPT), which makes use of the diverging magnetic penetration depth λ of a superconductor just below its transition temperature. A variety of geometries exist to make use of this observable, e.g. inductance bridge designs [McD87]. The most common type in recent developments, however, shares a lot of similarities with MMCs, but replacing the metallic paramagnetic sensor with a superconducting one. How the superconducting sensor shapes the externally applied magnetic field strongly depends on its penetration depth, again leading to a temperature sensitive flux density in a pick up coil coupled to a SQUID. This has some theoretical advantages: In MMCs, the limiting factor to the signal rise time τ_0 is the weak coupling between the electron system (which thermalises quickly after the absorption of a particle) and the system of magnetic spins in the sensor (which cause the measurable signal). In an MPT, the system of charge carriers is itself the one responsible for the signal, potentially significantly increasing the speed of the system. The low specific heat of superconductors relative to the paramagnetic sensor materials may also help to improve sensitivity. Attempts to develop this concept into competitive microcalorimeters to MMCs and TESs have so far been hindered by hysteresis [Ste13]. The calorimeter type we will introduce and thoroughly discuss in this thesis, the λ-SQUID, is also founded in the temperature dependence of the magnetic penetration depth. One may thus be inclined to include λ-SQUIDs in the MPT category. As will be presented later however, the underlying mechanism by which a change in penetration depth is transduced into a measurable signal differs considerably between typical MPTs and λ-SQUIDs. Nonetheless, the advantages of using a superconducting sensor material apply to λ-SQUIDs all the same.

2.2 dc-SQUID-based readout of cryogenic microcalorimeters

The remarkable sensitivity of SQUIDs, which can be as low as the quantum limit [Dru06], makes them suited for a variety of high-precision measurements. Additionally, the low impedance of the input coil of a current-sensing SQUID is particularly well adapted to the readout of low-impedance cryogenic microcalorimeters such as TESs or MMCs [McC05].

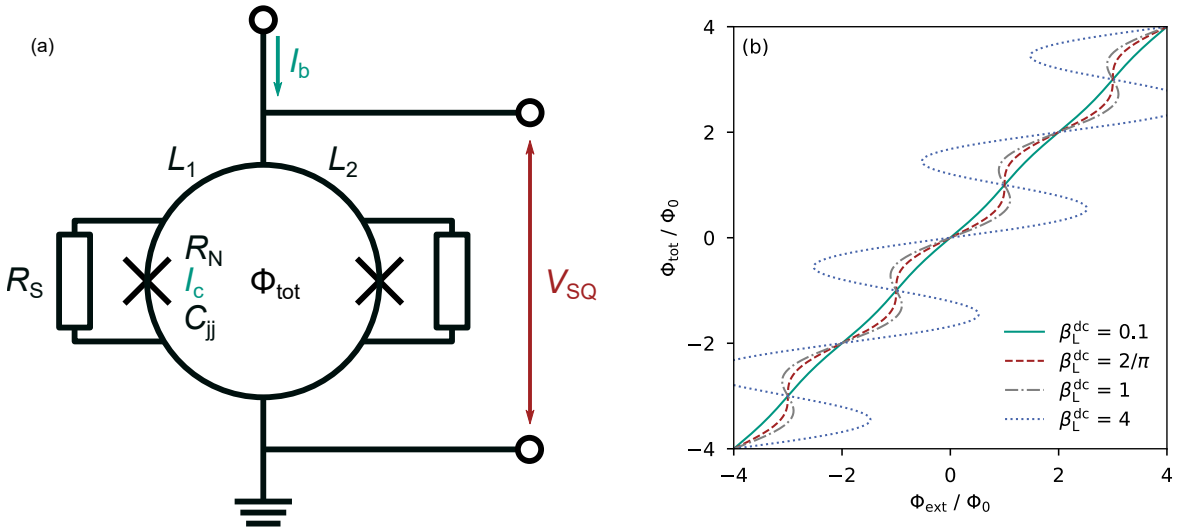


Fig. 2.4: (a) Schematic diagram of a resistively shunted dc-SQUID. A magnetic flux Φ_{tot} threads the SQUID loop with inductance $L_{\mathrm{SQ}} = L_1 + L_2$. The loop is interrupted by two identical Josephson tunnel junctions (represented by the $\times$ symbol) with critical current I_{c}. (b) Relation between the total flux Φ_{tot} threading the SQUID loop and the externally applied magnetic flux Φ_{ext}. For values of the screening parameter $\beta_{\mathrm{L}}^{\mathrm{dc}} \leq 2/\pi$, the relation is unique.

In the following we will quickly discuss the most relevant properties of SQUIDs, and specifically discuss their use for the readout of microcalorimeters.

2.2.1 Fundamentals of dc-SQUIDs

A dc-SQUID consists of a superconducting loop with inductance L_{SQ} interrupted by two resistively shunted Josephson tunnel junctions, as depicted in the simplified schematic circuit diagram 2.4(a). The total SQUID inductance $L_{\mathrm{SQ}} = L_1 + L_2$ is determined by the two "branches" of the SQUID. The inductances L_1, L_2 of the arms need not be identical, and asymmetric SQUIDs are very common in real applications. In the following we will however assume that both Josephson tunnel junctions are identical, i.e. they have the same critical current I_{c}, normal state resistance R_{N}, subgap-resistance R_{sg}, shunt resistance R_{S} and junction capacitance C_{jj}. We assume a current I_{b} through the SQUID and a voltage V_{SQ} across it, and describe the total magnetic flux threading the SQUID loop by Φ_{tot}.

In addition to the basic parameters describing the SQUID inductance and Josephson junctions, the behaviour of a SQUID is characterised by the screening parameter $\beta_{\mathrm{L}}^{\mathrm{dc}} = 2L_{\mathrm{SQ}}I_{\mathrm{c}}/\Phi_0$ and the junction's Stewart-McCumber parameter $\beta_{\mathrm{C}} = 2\pi I_{\mathrm{c}}R^2C_{\mathrm{jj}}/\Phi_0$ [Che04, Tes77]. Here, we have used the magnetic flux quantum $\Phi_0 \approx 2.0678 \times 10^{-15}$ Wb. The Stewart-McCumber parameter describes the damping of the Josephson junctions [Ste68, McC68]. For the case of weak damping, i.e. $\beta_{\mathrm{C}} \gg 1$,

once the junction is driven into the voltage state by increasing the applied current above its critical current $I_\mathrm{b} > I_\mathrm{c}$, it will remain in the voltage state even if the current is reduced to a value $I_\mathrm{r} < I_\mathrm{b} < I_\mathrm{c}$ below the critical current but above the retrapping current I_r. For such currents it depends on the history whether or not the junction is in the voltage state, thus causing a hysteretic behaviour [Ste68]. For strong damping $\beta_\mathrm{C} \ll 1$, the junction will immediately return to the zero voltage state once the applied current is reduced again $I < I_\mathrm{c}$, and the junction is non-hysteretic. For dc-SQUIDs, typically shunt resistors with $R_\mathrm{S} \ll R_\mathrm{N}$ are connected in parallel to the junctions to yield $\beta_\mathrm{C} \leq 1$. The SQUID screening parameter $\beta_\mathrm{L}^\mathrm{dc}$ describes the influence of screening currents running in the SQUID loop on the total magnetic flux Φ_tot. In general, any externally applied flux Φ_ext will result in screening currents in the SQUID, which in turn cause a flux contribution. The total flux Φ_tot hence has a non-trivial dependence on the externally applied magnetic flux [Che04]:

$$\frac{\Phi_\mathrm{tot}}{\Phi_0} = \frac{\Phi_\mathrm{ext}}{\Phi_0} - \frac{\beta_\mathrm{L}}{2} \sin\left(\pi \frac{\Phi_\mathrm{tot}}{\Phi_0}\right). \tag{2.11}$$

This relation between Φ_tot and Φ_ext is graphically depicted in figure 2.4(b) for various values of $\beta_\mathrm{L}^\mathrm{dc}$. In the limit of a vanishing screening $\beta_\mathrm{L}^\mathrm{dc} \ll 1$, we can neglect the contribution of the screening currents and the total flux $\Phi_\mathrm{tot} = \Phi_\mathrm{ext}$ threading the SQUID loop is given by the externally applied flux. As $\beta_\mathrm{L}^\mathrm{dc}$ increases, the screening flux becomes more and more relevant. In the limit $\beta_\mathrm{L}^\mathrm{dc} \to \infty$, a dc-SQUID behaves like a closed superconducting loop, screening any external flux to conserve a constant total flux $\Phi_\mathrm{tot} = \mathrm{const}$. The case of $\beta_\mathrm{L}^\mathrm{dc} \leq 2/\pi$ is of special interest: It is the largest value of the screening parameter for which the relation between Φ_ext and Φ_tot is unique. For larger values of the screening parameter, there are some regions of Φ_ext for which multiple values of Φ_tot exist, leading to a hysteretic behaviour of the dc-SQUID.

For real applications, numerical simulations have been used to assess that ideal SQUID performance is expected at non-negligible screening $\beta_\mathrm{L}^\mathrm{dc} \approx 1$ and finite damping $\beta_\mathrm{C} \lesssim 1$ [Tes77]. Under these conditions the dc-SQUID operates without hysteresis.

The measured current-to-voltage characteristic (IVC) of a dc-SQUID is exemplarily depicted in figure 2.5(a) for the two values $\Phi_\mathrm{tot} = n\Phi_0$ and $\Phi_\mathrm{tot} = (n + 1/2)\Phi_0$ of the magnetic flux threading the SQUID loop. For integer multiples of the flux quantum Φ_0, the critical current of the SQUID is maximised. The case of $\Phi_\mathrm{tot} = (n + 1/2)\Phi_0$ minimises the critical current.

To use the SQUID as a sensor for magnetic flux, two modes of operation are commonly employed. In current bias, a constant, suitable dc bias current I_b is applied. If the current is sufficiently large, i.e. $I_\mathrm{b} > I_{0,\mathrm{min}}$ with $I_{0,\mathrm{min}} = \min_{\Phi_\mathrm{tot}}(I_0)$, then the voltage V_SQ depends on the flux Φ_tot with a period length of one flux quantum Φ_0. The largest voltage swing is usually attained for $I_\mathrm{b} \gtrapprox I_{0,\mathrm{max}}$, resulting in a voltage to flux curve (VΦC) as shown in figure 2.5(b).

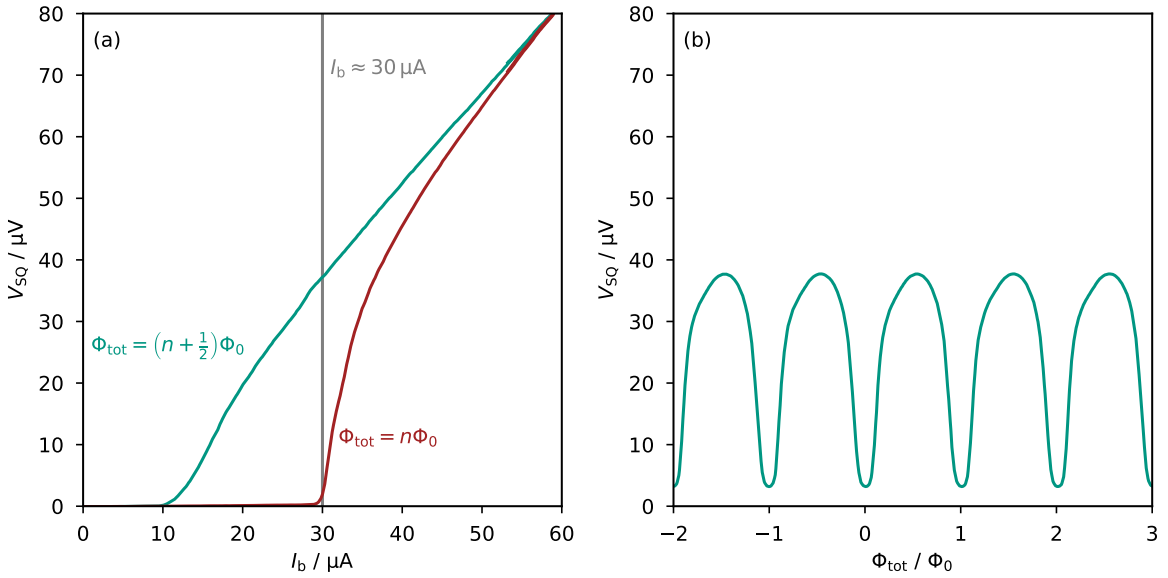


Fig. 2.5: (a) Current-to-voltage characteristic (IVC) of an exemplary dc-SQUID for the total flux states with maximum ($\Phi_{tot} = n\Phi_0$) and minimum ($\Phi_{tot} = (n + 1/2)\Phi_0$) critical current. (b) Voltage V_{SQ} across the same dc-SQUID versus total flux Φ_{tot} (VΦC) at a suitable bias current of $I_b \approx 30\,\mu A$. The characteristic response shows a periodicity with the flux quantum Φ_0.

In this configuration, the dc-SQUID behaves like a flux-to-voltage converter, and is usually characterised by a flux-to-voltage transfer coefficient

$$V_\Phi = \left| \frac{\partial V_{SQ}}{\partial \Phi_{tot}} \right|_{I_b = \text{const.}} \tag{2.12}$$

which specifies the slope of the VΦC at the respective choice of bias current I_b and total magnetic flux Φ_{tot}. As the VΦC is periodic, V_Φ varies strongly with Φ_{tot} and may even vanish. The flux states which maximise V_Φ typically occur around $\Phi_{tot} = (n \pm 1/4)\Phi_0$ for real SQUIDs.

In the case $\beta_L \approx 1$ and $\beta_C \approx 1$, the ideal flux to voltage transfer coefficient can be estimated by [Tes77]

$$V_\Phi = R/L_{SQ}. \tag{2.13}$$

Alternatively, the SQUID may be biased using a constant voltage V_{SQ}, and the current through the SQUID is measured. The resulting flux to current curve then depicts a periodic modulation similar to the VΦC discussed earlier.

At a finite temperature T, the resistive components of the shunted Josephson junctions depict the usual Johnson-Nyquist noise associated with ohmic resistors. In addition to

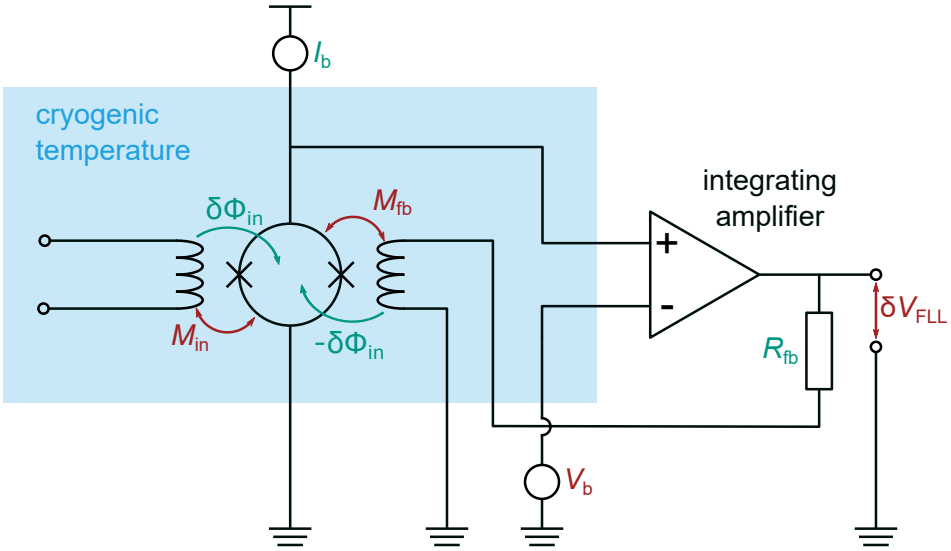


Fig. 2.6: Simplified schematic circuit diagram of a dc-SQUID operated in a flux locked loop (FLL). Any external flux signal $\delta\Phi_{\mathrm{in}}$, e.g. as induced by currents running through the input coil, is compensated by an equally large flux $-\delta\Phi_{\mathrm{in}}$ with opposite sign induced into the SQUID loop via the feedback coil. The SQUID therefore remains at its working point at all times, and the voltage V_{FLL} serves as output signal.

their inherent voltage noise, their current noise causes an effective flux noise due to the SQUID inductance, which in turn results in a voltage noise contribution [Che04]. This total voltage noise S_{VV}, and equivalently the total apparent flux noise S_Φ during read out of the dc-SQUID, limits its flux sensitivity. For the case with $\beta_{\mathrm{L}} \approx 1$ and $\beta_{\mathrm{C}} \approx 1$, the following simplified approximations suffice [Bru82]:

$$S_{\mathrm{VV}} = 18 k_{\mathrm{B}} T R, \tag{2.14}$$

$$S_\Phi = \frac{S_{\mathrm{VV}}}{V_\Phi^2}. \tag{2.15}$$

2.2.2 dc-SQUID detector readout

For practical applications, the periodic nature of the SQUID response (compare VΦC in figure 2.5(b)) poses an issue. One of the most common methods to linearise the output of a dc-SQUID is the so-called directly coupled flux locked loop (FLL) feedback circuit [Dru04], depicted schematically in figure 2.6. Here, the dc-SQUID is biased with a constant current I_{b}, and the voltage across the SQUID serves as one input of a integrating operational amplifier. The other input of the amplifier is fixed at a constant bias voltage V_{b}. At the output of the operational amplifier, the resulting voltage V_{FLL} causes a current through the feedback resistor R_{fb} and the feedback coil. The feedback coil in turn couples flux into the SQUID loop with the mutual inductance M_{fb}. By

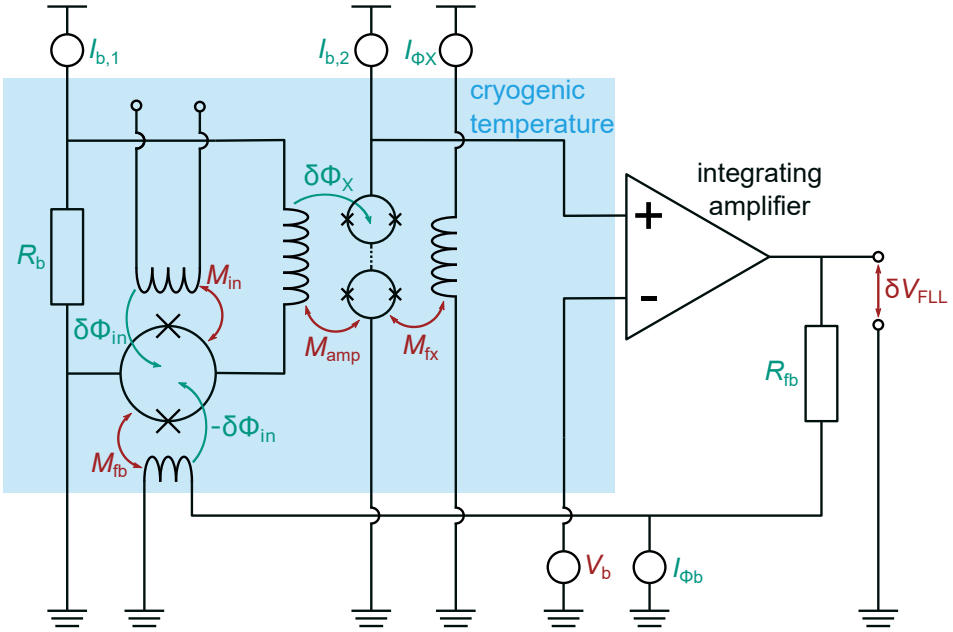


Fig. 2.7: Simplified schematic circuit diagram of a two-stage dc-SQUID setup operated in a flux locked loop (FLL). An array of dc-SQUIDs connected in series is used as a first low-noise amplifier stage to suppress the noise of the room-temperature readout electronics.

way of this feedback system, any change $\delta\Phi_{in}$ of the flux through the SQUID loop at a suitable working point results in a deviation of the SQUID voltage from the bias voltage V_b. This differential voltage at the amplifier input causes a voltage δV_{FLL} at its output, which in turn induces a feedback flux $\delta\Phi_{fb} = M_{fb}\delta V_{FLL}/R_{fb} = -\delta\Phi_{in}$ back into the SQUID loop. The negative feedback thus compensates any external flux signal and stabilises the dc-SQUID at the desired working point. The input flux can easily be derived from the voltage V_{FLL} at the amplifier output.

The integrating amplifier and other components required to operate a SQUID in FLL also contribute to noise. In the simple readout scheme discussed above, the noise contribution from the room-temperature electronics would actually dominate the total readout noise [Dru06]. In order to preserve the excellent sensitivity of the SQUID, an intermediate low-noise amplifier stage is required. One potential option to achieve the readout of a SQUID without degrading its noise performance is by using a two-stage SQUID setup [Wel93], where a series array of dc-SQUIDs is operated as an amplifier. Figure 2.7 depicts the simplified equivalent circuit diagram of such a setup.

With a suitably low value of the bias resistor R_b, the front-end SQUID is operated at a constant bias voltage. The current through it now depends on its flux state, and in turn induces a magnetic flux into the loops of the amplifier stage SQUID array. In a suitable configuration, the flux induced into the amplifier array exceeds the magnitude of the original signal flux by a factor of the flux gain $G_\Phi \lesssim \pi$ [Dru96]. Additionally, as the amplifier consists of multiple dc-SQUIDs connected in series, its output voltage at

a constant bias current exceeds that of a single SQUID proportionally, resulting in the amplifier-like characteristic of such a two-stage setup. Via the second SQUID stage, the signal from the front-end SQUID is amplified sufficiently that the room-temperature electronics no longer degrade the overall readout noise.

2.3 SQUID multiplexing techniques

Many modern experiments, e.g. in astronomy [Bar18, Ban19] or particle physics [Gas17], require hundreds or even thousands of individual detector pixels. Using individual two-stage dc-SQUID setups per readout channel becomes unfeasible at these scales, as the number of electrical wires from room temperature to the cryogenic setup and the number of room temperature electronics scale linearly with the pixel count. In this scenario, the system complexity, financial cost and heatload (both conductive and dissipative) become challenging as the number of pixels rises. To realise experiments with such large arrays, sophisticated SQUID multiplexing schemes have been developed and implemented successfully. We will discuss the most relevant of these methods in the following.

2.3.1 Time-division multiplexing

One commonly applied multiplexing scheme is time-division multiplexing (TDM) [Che99, Irw02, Dor16]. A simplified schematic circuit diagram is depicted in figure 2.8. In such a multiplexer, the parallel connection of a readout SQUID and a flux activated switch (FAS) form a unit cell, N of which are connected in series. A bias voltage V_b is applied across all N unit cells. When the FAS of a unit cell is closed, it shunts the respective readout SQUID. Thus, the FASs can be used to only apply the bias voltage to one readout SQUID at a time. By cycling through all N SQUIDs one after the other, each channel is read out consecutively. All N channels share one set of output lines and feedback lines, and one set of room temperature readout electronics. It is especially beneficial to operate a number M of such multiplexers simultaneously. In this case, we can route the addressing currents $I_{\mathrm{ad},i}$ through all M unit cells with the same index i, further reducing the required electrical connections per readout channel. For a total of $N \times M$ readout channels, we only need M output lines, feedback lines and readout electronics, as well as N lines for the addressing currents. The number of electrical connections in TDM thus scales with $\mathcal{O}(N + M)$, rather than with $\mathcal{O}(NM)$ as for non-multiplexed readout. Consequently, the system cost and complexity is greatly reduced. Since only M readout SQUIDs are operated at any time, the dissipated heat load is also reduced by a factor of N. The duty cycle of $1/N$ per readout channel however increases the effective bandwidth of the SQUID noise relative to the signal bandwidth. As a result, the SQUID noise is effectively increased proportional to $\sqrt{N}$, which must be considered when designing TDM systems. Additionally, the bandwidth of the dc-SQUID based amplifier stage fundamentally limits the total

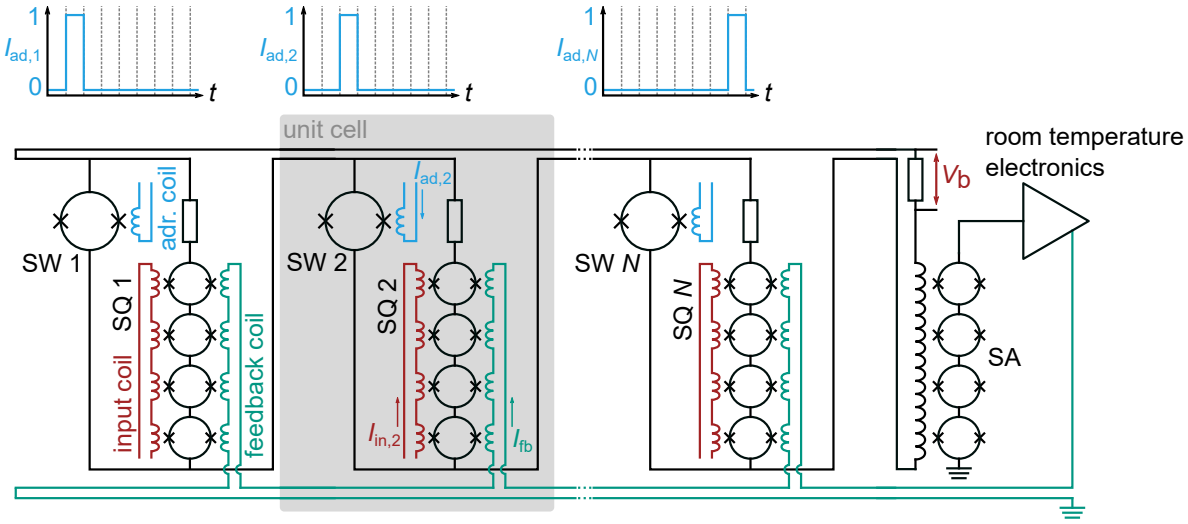


Fig. 2.8: Simplified schematic circuit diagram of a TDM scheme as presented in [Dor16, Rei19]. Each unit cell contains a readout SQUID (SQi) and a flux activated switch (SWi) connected in parallel. The input signals $I_{\mathrm{in},i}$ correspond to individual detector signals. A number N such unit cells are connected in series to the input of an amplifier SQUID (SA). The flux activated switches are used to apply a bias voltage V_b to only one readout SQUID at a time. Here, the readout SQUIDs and amplifier SQUID are realised as series arrays of multiple dc-SQUIDs. The switches SWi are operated (i.e. opened or closed) via the addressing current $I_{\mathrm{ad},i}$. All N channels share a common feedback line, one amplifier SQUID and one set of room temperature electronics.

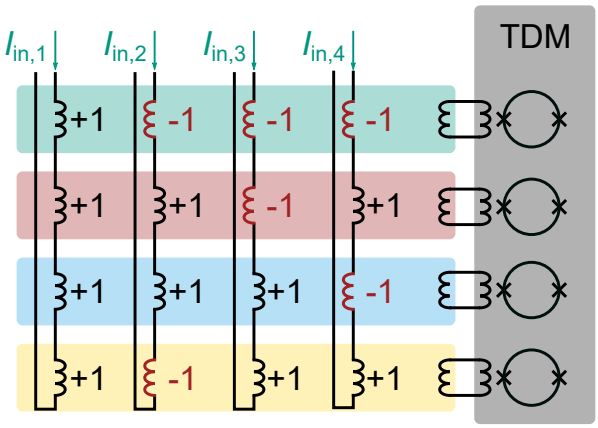


Fig. 2.9: Simplified schematic circuit diagram of a CDM scheme as presented in [Mor16]. The input signals $I_{\mathrm{in},i}$ correspond to individual detector signals. With a suitable arrangement of coils, each detector signal couples to every readout SQUID. The Walsh codes are encoded in the coupling polarity as indicated by ± 1. The individual readout SQUIDs are operated in a TDM scheme.

system bandwidth to the MHz range [Irw02]. While TDM has been successfully applied in a variety of experiments [Rei09, Dur23], multiplexing factors rarely exceed $N = 128$ [Prê16].

2.3.2 Code-division multiplexing

To mitigate the SQUID noise penalty of TDM, code-division multiplexing (CDM) was developed [Nie10]. In CDM, the output of a number N of pixels is connected in series for readout by a single amplifier. This again results in a reduction of required wires and room-temperature electronics much in the same way as TDM. Where both methods differ is that in CDM, all N pixels are operated at all times, rather than just one. In order to allow demultiplexing of the individual signals, the signal polarities of the individual pixels are periodically switched following specific Walsh codes. Each period (commonly referred to as a "frame") covers N switching cycles, and the pattern of polarities is unique for each of the N readout channels. After a full frame is recorded, simple arithmetic can be used to recover each individual pixel signal. To make efficient use of Walsh codes, N must be a power of 2. Since all pixels are read out all the time, the noise aliasing drawback of TDM does not affect CDM. To facilitate the required polarity switching, multiple techniques were developed. Either, N pixels are connected to a single SQUID for readout using a single-pole double-throw (SPDT) current-steering switch each. The SPDT itself consists of two purpose-specific SQUIDs, resistors and inductors, and allows to switch the polarity of the detector signal [Nie10]. Alternatively, N detectors may be connected to N SQUIDs for readout using a sophisticated network of inductors. The Walsh codes are "hard-coded" into this network such that each SQUID receives all detector outputs with a unique combination of polarities. Using a TDM method, one SQUID is read out at a time [Irw10, Mor16]. The simplified circuit diagram for the latter method is schematically depicted in 2.9, for a multiplexing factor of $N = 4$. The coupling polarities encode the Walsh codes, which allow for demultiplexing of the individual detector signals $I_{\mathrm{in},i}$. Regardless of the method used, CDM requires significantly more components at cryogenic temperatures compared to TDM, with sophisticated layout and wiring schemes. Since a dc-SQUID

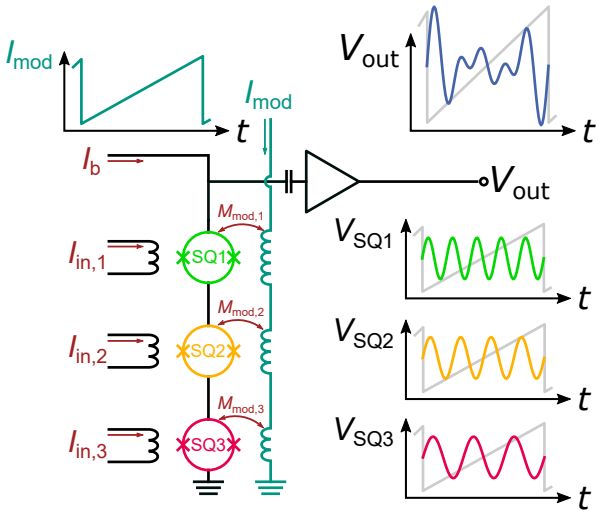


Fig. 2.10: Simplified schematic circuit diagram of an FDM scheme as presented in [Ric21]. Here, $N = 3$ dc-SQUIDs are connected in series. Their mutual inductances $M_{\mathrm{mod},i}$ are unique, so the applied flux ramp signal I_{mod} results in a unique modulation frequency for each SQUID. The individual SQUID responses act as carrier signals, and the input signals $I_{\mathrm{in},i}$ are encoded in the phase of the respective carrier.

array is commonly used as a first stage amplifier (compare subsection 2.2.2), the total bandwidth available to the entire multiplexer is in the MHz range. This sets a fundamental limit to the multiplexing factor N, depending on the bandwidth requirements per readout channel [Irw12]. In experiments, multiplexing factors as high as $N = 32$ have been realised [Mor16].

2.3.3 Frequency-domain multiplexing

Another approach encodes the signals of N detectors onto unique ac carrier signals in the MHz frequency range [dH14, Ric21]. All carriers can be superimposed onto a common transmission line, and a single amplifier and set of room temperature readout electronics is sufficient. Similar to CDM, transducing of the individual signals onto an ac carrier may happen at the detector level before SQUID readout [Yoo01] or during SQUID readout [Ric21]. The former requires fewer dc-SQUIDs to operate continuously in the cold reducing dissipated power, while the latter has fewer requirements regarding the design of the detector. A simplified schematic circuit diagram of an FDM is depicted in figure 2.10. Here, we show an FDM where the frequency encoding happens during SQUID readout. It uses a modulation coil coupled to all N readout SQUIDs, but with unique mutual inductances $M_{\mathrm{mod},i}$. A sawtooth-shaped flux ramp is applied to the modulation coil. Resulting from this flux ramp and the different mutual inductances $M_{\mathrm{mod},i}$, each of the N readout SQUIDs experiences a unique modulation frequency. Thus, the voltages $V_{\mathrm{SQ},i}$ across the SQUIDs act as carriers, typically in the MHz frequency range [Ric21]. The individual input signals are encoded in the phase of the respective carrier. Using common demodulation techniques, e.g. lock-in amplifiers or digital signal processing, the individual detector signals can be retrieved. Commonly, for MHz frequency carriers, the bandwidth limitation of the dc-SQUID based first amplifier stage again sets an upper bound to the total multiplexing factor N. Currently anticipated experiments aim for multiplexing factors on the order of $N = 40$ [Bar18].

2.3.4 Microwave SQUID multiplexing

To work around the bandwidth limit imposed by dc-SQUIDs, FDM with carrier frequencies in the GHz range has been developed [Irw04, Mat08, Hir13, Kem17]. While functionally similar to the FDM introduced previously, the implementation is significantly different. To differentiate between both methods, the term "microwave SQUID multiplexing" (μMUX) is generally applied. For μMUX, each readout channel consists of an rf-SQUID inductively coupled to a microwave resonator with a unique resonance frequency in the GHz range. The rf-SQUID behaves like a flux-dependent inductance, and via the mutual inductance between the resonator and itself influences the resonance frequency of the resonator. The range of resonance frequency modulation is typically of the same order as the resonator bandwidth, and may be as large as a few MHz depending on the application. Using a frequency spacing suitably larger than the resonator bandwidth, many such channels may be coupled to a common transmission line. By moving to microwave frequencies, the bandwidth limitations of the other multiplexing techniques is alleviated, enabling much larger multiplexing factors and/or larger signal bandwidths per channel. Therefore μMUX is the technology of choice for applications requiring hundreds or even thousands of detectors. As an example, for the ECHo experiment [Gas17], with a typical low-noise high electron mobility transistor (HEMT) amplifier with a bandwidth of $4 - 8\,\mathrm{GHz}$, a multiplexing factor of $N = 400$ with a per-channel signal bandwidth as large as $1\,\mathrm{MHz}$ is anticipated. We will discuss μMUX in much more detail in chapters 6 and 7, where we present our numerical software for the simulation and performance prediction of μMUX, and use it to find design parameters reducing their readout noise.

3. Theory of the λ-SQUID

In the previous chapter, we have briefly summarised the current state of the art of cryogenic microcalorimeters at the time of writing. We have seen that a readout channel usually consists of a microcalorimeter such as an MMC or TES, read out using a SQUID. The two most mature types of microcalorimeters have both achieved outstanding performance, with an energy resolution ΔE_{FWHM} of 0.72 eV for 1.5 keV photons [Lee15], and of 1.25 eV for 5.9 keV photons [Kra23]. Both provide a quantum efficiency close to 100 % in the respective energy range. However, both technologies have not yet reached the fundamental resolution limit set by thermodynamic fluctuation noise (see section 2.1.1). For MMCs, readout noise degrades the signal-to-noise ratio (SNR). In TESs, excess noise is present, potentially caused by phase boundary fluctuations or percolation noise. In addition to the ongoing developments on MMCs and TESs, it is thus worthwhile to consider additional detector technologies in an effort to find a technology potentially reaching the fundamental limit. In the following, we present a novel type of microcalorimeter, called λ-SQUID. Similar to MPTs, it relies on the magnetic penetration depth $\lambda(T)$ as the temperature sensitive physical parameter. In contrast to regular MPTs the sensing element is directly integrated into the loop of a dc-SQUID, to avoid transformer losses and ensure optimal signal.

3.1 The λ-SQUID: A superconducting microcalorimeter with in-situ tunable gain

A λ-SQUID, as schematically depicted in figure 3.1(a), largely resembles a conventional dc-SQUID coupled to an input coil L_{in} and a feedback coil L_{fb}. The input coil carries a dc current I_{in}. A majority of the device, including auxiliary inductors and the Josephson tunnel junction electrodes, is made from a superconducting material with a critical temperature $T_{\mathrm{c}} \gg T_0$ which far exceeds the operating temperature T_0 of the device. The so-called λ-SQUID, the section of the SQUID loop which couples to the input coil, is made from a different superconducting material with a much lower critical temperature $T_{\mathrm{c}}^{\lambda} \lessapprox T_0$. Thus, at the operating point, it is held just below its critical temperature, such that its magnetic penetration depth $\lambda(T)$ depicts a strong temperature dependence. This is clear from the temperature dependence of the magnetic penetration depth $\lambda(T)$, as displayed in figure 3.1(b). The Casimir-Gorter two-fluid model predicts that the temperature dependence of the magnetic penetration depth follows the relation [Dau48]

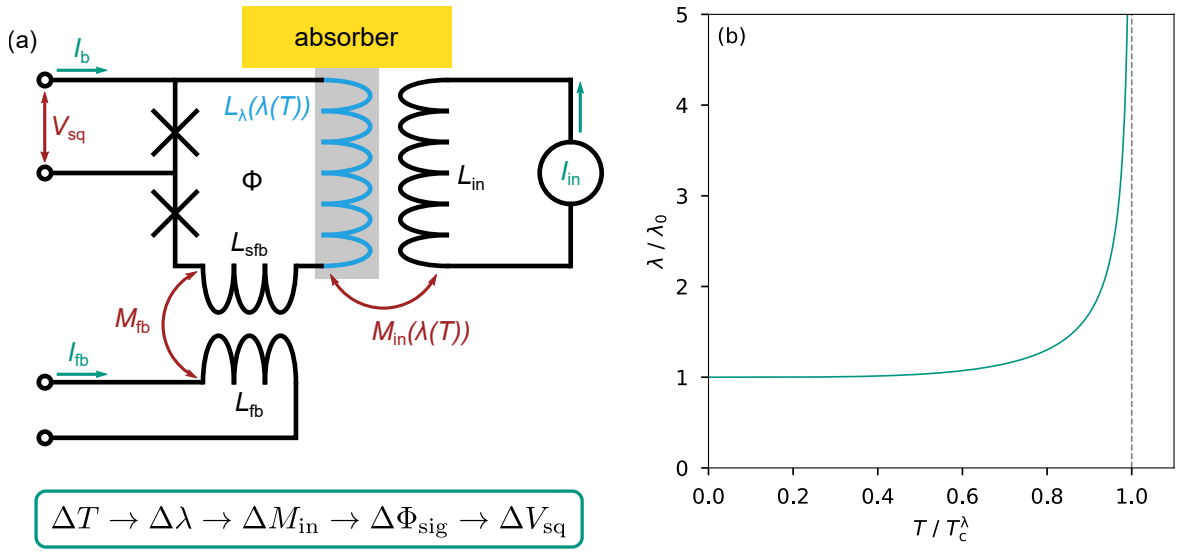


Fig. 3.1: (a) Simplified equivalent circuit diagram of a λ-SQUID. Inductors depicted in black are made from a superconducting material with critical temperature T_c. The λ-coil displayed in blue is made from a different superconducting material with critical temperature $T_c^\lambda \ll T_c$, and is in strong thermal contact with the absorber. The device is operated at a temperature $T_0 \lessapprox T_c^\lambda$. An input inductor with inductance L_{in} carries a constant current I_{in} and a temperature dependent mutual inductance $M_{in}(T)$ exists between it and the λ-coil. (b) Temperature dependence of the magnetic penetration depth λ given by equation 3.1. The magnetic penetration depth diverges at $T = T_c^\lambda$, and the curve becomes very steep at $T \lessapprox T_c^\lambda$.

$$\lambda(T) = \lambda(0)\sqrt{z(T)}, \tag{3.1}$$

$$z(T) = \left[1 - \tilde{t}(T)^4\right]^{-1}, \tag{3.2}$$

$$\tilde{t}(T) = \frac{T}{T_c^\lambda}, \tag{3.3}$$

where we have introduced the dimensionless scaling function $z(T)$ and the reduced temperature $\tilde{t}$.

If the temperature T of the λ-coil changes, this will result in a change in its magnetic penetration depth λ. This has a twofold effect on the inductance $L_\lambda = L_{\lambda,geo} + L_{\lambda,kin}$ of the λ-coil, which is comprised of a geometric contribution $L_{\lambda,geo}$ and a kinetic contribution $L_{\lambda,kin}$. The geometric inductance $L_{\lambda,geo}$ arises from the energy stored in magnetic fields induced by the currents within the conductor, while the kinetic contribution $L_{\lambda,kin}$ results from the kinetic energy of Cooper pairs. Firstly, the kinetic contribution depends directly on the magnetic penetration depth.

For conductors with lateral dimensions much smaller than their magnetic penetration depth, i.e. with a homogeneous current density distribution (CDD) in their cross-section, it can be approximated by [Mes69]

$$L_{\lambda,\mathrm{kin}} = \mu_0 \lambda^2 l/A \tag{3.4}$$

with the length l and cross-section area A of the conductor. Here, $\mu_0 = 1.256\,637\,\mathrm{N\,A^{-2}}$ is the vacuum permeability. In the case of a non-uniform CDD the relation is more complex. We will discuss appropriate numerical methods for the kinetic inductance for such situations in subsections 3.2.1 and 3.2.2. From equation 3.4, we can see that the kinetic contribution can vary greatly with temperature: $L_{\lambda,\mathrm{kin}}$ becomes even infinitely large as the magnetic penetration depth λ diverges. Altering the magnetic penetration depth also leads to a redistribution of current in the cross-section of the λ-coil. Qualitatively, it is easy to understand that the geometric self-inductance $L_{\lambda,\mathrm{geo}}$ results not from the geometry of a conductor itself, but rather from the path that the current takes. The CDD within the λ-coil consequently affects the geometric self-inductance $L_{\lambda,\mathrm{geo}}$ of the λ-coil, which in turn influences the mutual inductance M_{in} between the input- and the λ-coil. A simple analytic approach to describe this relation does not exist, and we will introduce robust numerical methods to study this effect in subsections 3.2.1 and 3.2.2. We will see in detail how this effect results in a temperature-dependent mutual inductance $M_{\mathrm{in}}(T)$ between the input- and the λ-coil. It is important to note that the relative influence of temperature on the geometric inductance $L_{\lambda,\mathrm{geo}}$ and mutual inductance M_{in} is generally much smaller compared to the effect on kinetic inductance $L_{\lambda,\mathrm{kin}}$.

The fundamental idea of the λ-SQUID is rather simple yet substantially different from the devices introduced in section 2.1. While the flux signal Φ_{sig} in the SQUID used for TES, MMC or MPT readout is governed by the change in signal current ΔI_{in} running in the signal coil, i.e. $\Delta\Phi_{\mathrm{sig}} = M_{\mathrm{in}}\Delta I_{\mathrm{in}}$, this relation is inverted for the λ-SQUID. Here, the temperature-sensitive element is the mutual inductance M_{in} between the input coil carrying the dc current I_{in} and the λ-coil. The flux signal is thus given by $\Delta\Phi_{\mathrm{sig}} = \Delta M_{\mathrm{in}} I_{\mathrm{in}}$, where we can freely choose I_{in} limited solely by the ampacity of the input coil. Even if the temperature-induced change in mutual inductance ΔM_{in} is fairly small, we can thus still achieve sufficient signal amplitudes $\Delta\Phi_{\mathrm{sig}}$ within the SQUID loop. Additionally, the proportionality of the signal with respect to the easily controllable input current gives the λ-SQUID an in-situ tunable gain factor.

By attaching a suitable particle absorber to the λ-coil, the absorption of a particle causes a temperature rise of this coil which is transduced into a change of inductance and consequently a change of magnetic flux within the SQUID loop. The latter can be sensed as a change of output signal of the SQUID. The feedback coil with inductance L_{fb} allows for additional control of the magnetic flux threading the SQUID loop by running a current I_{fb} through it. As we will see, this is essential for linearising the output of the λ-SQUID.

For the following discussion, we want to to assume a constant bias current. In this case, the relationship between the output signal voltage V_{SQ} and the temperature T is defined by the gain coefficient

$$\frac{\partial V_{\mathrm{SQ}}}{\partial T} = \frac{\partial V_{\mathrm{SQ}}}{\partial \Phi_{\mathrm{sig}}} \frac{\partial \Phi}{\partial T} = \frac{\partial V_{\mathrm{SQ}}}{\partial \Phi} \frac{\partial M_{\mathrm{in}}}{\partial T} I_{\mathrm{in}}, \tag{3.5}$$

where the flux-to-voltage transfer coefficient for an optimised dc-SQUID can be estimated by $\partial V_{\mathrm{SQ}}/\partial \Phi = R/L_{\mathrm{SQ}}$ [Tes77]. Here, L_{SQ} denotes the total SQUID inductance, and R the resistance of the shunted junctions. From equation 3.5, the tunability of the gain factor gets clearly apparent: With I_{in} being limited solely by the ampacity of the input coil, and the temperature dependence $\partial M_{\mathrm{in}}/\partial T$ depending on the operation temperature, the gain coefficient can be varied by both, the input current and operation temperature, over a wide range. Moreover, with a sufficient choice of the current I_{in}, the gain coefficient can be made suitably large, even if $\partial M_{\mathrm{in}}/\partial T$ itself is rather small. In addition, as the current I_{in} can be changed fast, e.g. by external control electronics, the gain can be tuned even in-situ, i.e. even during the acquisition of a detection event. This enables additional degrees of freedom during readout, e.g. by ensuring that the dynamic range of analogue to digital converters in the readout chain is always fully utilised.

3.2 Mutual inductance between parallel superconducting lines

As it is the basis of the operational principle of a λ-SQUID, it is crucial to describe and predict the mutual inductance between superconducting conductors. The loops of a λ-SQUID generally have a complex, three-dimensional shape, which makes an analytic (or even numerical) approach to this problem very challenging. In microfabricated thin-film electronics, such as the devices fabricated at IMS including, but not limited to, our λ-SQUIDs, the most common way to realise tightly coupled inductors is by placing the coils one atop the other in a washer-like geometry. The two coils with linewidths of the order of 10 µm are separated by a thin (order of 100 nm) layer of insulating material. Loop diameters are typically much larger than the linewidths. As a result, we can make the assumption that the sensing element (the λ-coil and the tightly coupled and hence physically close input coil) can be described with sufficient accuracy by long, straight, rectangular inductors with constant cross-sections and physical separation.

The task of computing the inductance of long, straight normal conductors and the mutual inductance between two long, parallel straight normal conductors is as old as the practical application of electricity. One of the earliest methods to solve this was presented by James Clerk Maxwell in 1872, and gives an exact solution only in the limit of infinite, perfectly straight conductors [Max72]. If the lengths and radii of bends are significantly larger than the lateral dimensions of the cross-section and spacing between conductors, this approach is still a reasonable approximation [Wea16].

For two parallel filaments, i.e. conductors with an infinitesimally small, point-like cross-section, their mutual inductance can be expressed as follows [Ros08, Wea16]:

$$M = \frac{\mu_0 l}{2\pi}\left[\ln\left(\frac{l}{D} + \sqrt{1+\left(\frac{l}{D}\right)^2}\right) - \sqrt{1+\left(\frac{D}{l}\right)^2} + \frac{D}{l}\right]. \tag{3.6}$$

Here, l is the length of the filaments, and D the distance between them (measured normal to the direction of the filaments). A similar expression can be found for any pair of two parallel conductors with constant, but otherwise arbitrary cross-sections. Here, the distance D between the filaments in equation 3.6 is simply replaced by the geometric mean distance (GMD) between the two cross-sections of the conductors. The problem of deriving their mutual inductance is thus reduced to a problem of computing the GMD between both conductors. Additionally, the self-inductance of a conductor can be computed similarly by using the GMD of its cross-section to itself.

For any two conductor cross-sections S_1 and S_2 in a plane, the geometric mean distance R between them can be computed with the following integral [Max72]:

$$\ln(R)\int dxdyd\xi d\eta = \int \ln\left(r(x,y,\xi,\eta)\right) dxdyd\xi d\eta \tag{3.7}$$

Here, we use the coordinates x and y to describe the points within cross-section S_1 and the coordinates ξ and η for the points within cross-section S_2. The euclidean distance between any two points (x,y) and (ξ,η) is

$$r(x,y,\xi,\eta) = \sqrt{(x-\xi)^2 + (y-\eta)^2}. \tag{3.8}$$

In this original definition of the GMD, all points within the cross-sections are weighted equally, since it was derived for normal metal conductors with a homogeneous current distribution across their cross-sections. It was later adapted for conductors displaying the skin effect by introducing weighting factors proportional to their non-uniform current density distributions [Aeb17]. While the original intention was to extend the GMD method to high frequency signals in normal metal conductors, we can nonetheless apply it to superconductors, provided we substitute an appropriate model for the current density distribution (CDD). If we assume that $j_1(x,y)$ and $j_2(\xi,\eta)$ are the current density distributions in the cross-sections S_1 and S_2, respectively, we can construct a weight function

$$g(x,y,\xi,\eta) = j_1(x,y)j_2(\xi,\eta). \tag{3.9}$$

Note that this weight function is not assumed to be normalised, which we need to keep in mind when computing the GMD.

We then obtain the following, more general expression for the weighted GMD R_{sc}:

$$\ln\left(R_{\mathrm{sc}}\right) \int g(x,y,\xi,\eta)dxdyd\xi d\eta = \int g(x,y,\xi,\eta) \ln\left(r(x,y,\xi,\eta)\right) dxdyd\xi d\eta. \tag{3.10}$$

Fundamentally, we can see from this expression that a change in the CDD also changes the effective distance between two conductors, even if their physical geometry remains unaltered. This is why the mutual inductance M_{in} between the λ-coil and an input coil changes with temperature. As the magnetic penetration depth $\lambda(T)$ of the λ-coil increases with temperature, the current density distribution within its cross-section is redistributed, leading to a different effective distance and thus different mutual inductance between both conductors.

Several numerical methods have been developed to calculate the CDD and inductance matrices of a system of rectangular conductors. Two such methods were published by Sheen *et al.* [She91] and Chang *et al.* [Cha81], both of which assume infinite, parallel, rectangular superconducting inductors. The cross-section of such an example system of conductors is depicted in figure 3.2(a). For both methods, the conductor cross-sections are then segmentised into a large number of small, rectangular segments. Here, the segmentation is done such that the CDD within each segment can be approximated as homogeneous. This is illustrated in figure 3.2(b). Both methods enforce the boundary condition that the sum of currents through all conductors vanishes, which we will come back to later. The methods differ in how the CDD and the inductance matrix is computed and which boundary conditions must be defined. Thus, both methods have some unique advantages depending on the application, but for certain input parameters they are expected to yield very similar results, which we can use to verify their correct implementation. To us, for a system of N coupled inductors, the inductance matrix $\underline{L}$ is the most valuable simulation result. Its elements $L_{k,l}$ represent the (mutual) inductance between conductors with the indices k and l, respectively. The CDD resulting from simulations using Chang's method are, as an example, depicted in figure 3.2(c).

We have implemented both simulation methods from scratch in a convenient Python library, along with methods to define and segmentise arbitrary conductor systems. This allows us to set up and compute simulations with either method with little effort. The software is easy to use even without in-depth knowledge of the underlying algorithms and may be applied even outside the scope of λ-SQUIDs in the future.

The functions to define a system of N conductors and segmentise them are shared between both methods. Figure 3.2(b) illustrates such a setup with three separate, segmentised conductors. It depicts a cross-sectional view of the conductor system. The areas of the individual segments need not be equal, and for most cases it is beneficial for the computing time to use denser segments where local changes in current density are especially large, e.g. at edges or corners. In our implementation, the number of segments along the x and y direction of each conductor can be chosen separately. They may be evenly distributed, but generally a non-homogeneous distribution is preferred. To achieve this, a user-specified arbitrary power law can be used for non-linearly spaced

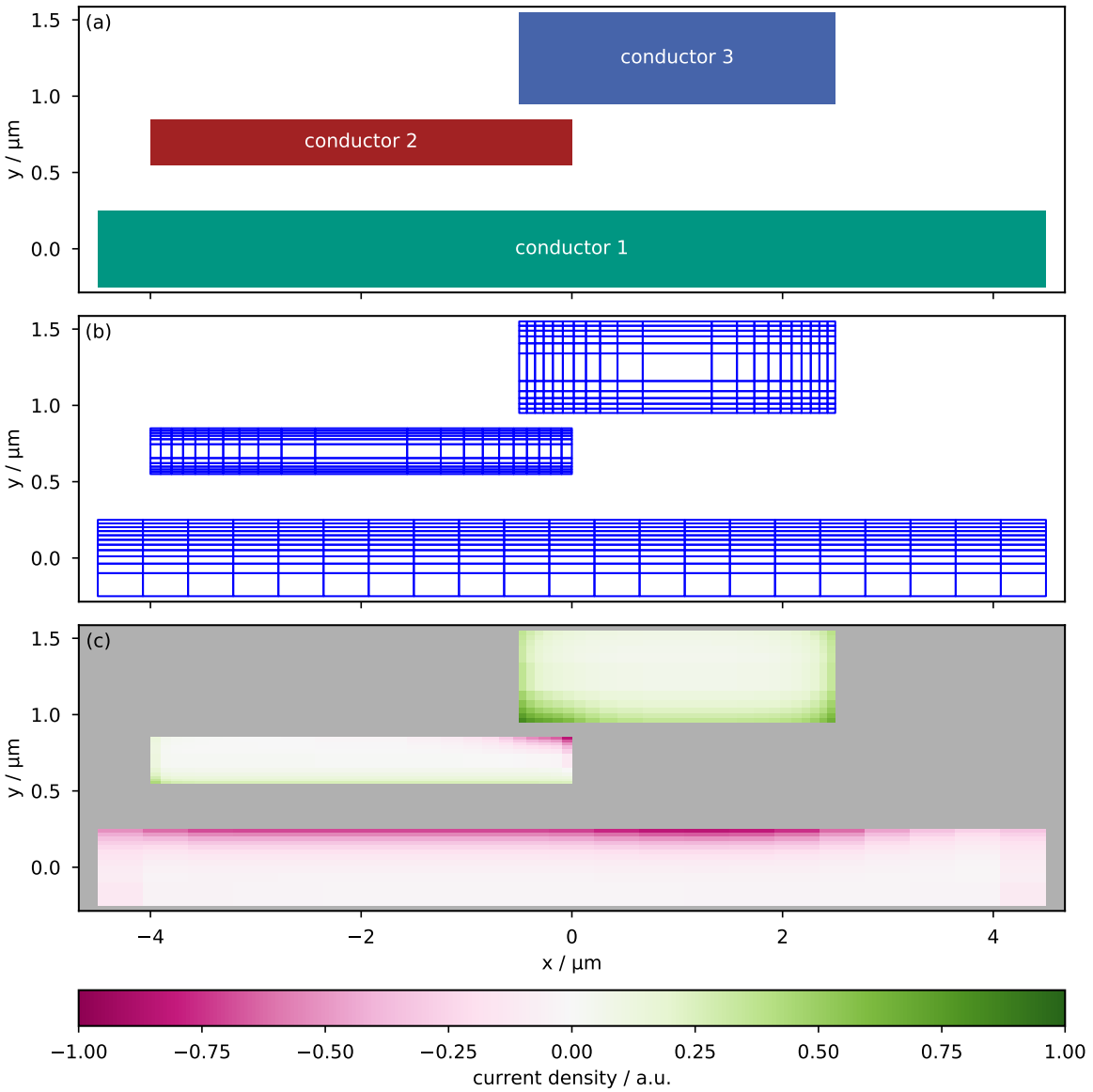


Fig. 3.2: (a) Cross-sectional view of a setup of three straight, infinitely long, parallel conductors with rectangular cross-sections. (b) Segmentised cross-section, where each conductor is separated into a large number of small segments. Segment areas need not be identical. (c) Simulation result for the CDD in the three-conductor setup using Chang's method. The simulation also yields the inductance matrix $\underline{L}$.

segments. Methods for denser segments at one or both edges or at the centre are available, and can be set independently for all axes of all conductors. The size of segments must be small enough for the assumption of a homogeneous CDD in each segment to be valid, but using small (i.e. too many) segments increases the computing time. Since electromagnetic fields of other conductors affect it, it is difficult to predict a priori where and how strongly the CDD changes locally within one conductor, and thus challenging to predict how finely the segmentation needs to be for a given conductor geometry. In practice, we have generally started with fairly coarse segmentation, and then repeated simulations for finer and finer segmentation. Once the inductance matrix $\underline{L}$ no longer significantly changes with finer segmentation, the settings were used for simulation runs of the same geometry.

We will not describe the specifics or implementation of each method here in detail. The reader may instead refer to the respective original publications. We will however outline the fundamental principles to give some insight into the strengths and weaknesses associated with each method.

3.2.1 Method of Sheen *et al.*

The method by Sheen *et al.* [She91] computes the CDD and inductance matrix via inductance partials, i.e. the geometric inductance contribution for each segment, and a complex self-impedance, i.e. ohmic conductive and kinetic inductive contributions for each segment. The latter only applies to a segment itself, since neither ohmic resistance nor kinetic inductance create a magnetic field that may couple to neighbouring segments. This is actually one strength of Sheen's method: It allows to define a normal resistance for each conductor as well as a signal frequency. Quasiparticle currents, as they occur for high frequency currents, can thus be modelled by this method. The inductance partials account for geometric inductance, and we hence must consider all segments simultaneously in the derivation. Sheen's method is an extension of Weeks' method [Wee79], which was originally developed for normal conductors at high frequencies. All segments within one conductor are treated as impedances connected in parallel. A voltage within each conductor (relative to a ground plane / return conductor at voltage 0) is defined, and currents in each segment result accordingly. The CDD is computed simply by normalising the currents with the area of each segment. Since the sum of all currents is forced to be zero, yet currents can not be controlled per conductor, the return paths for currents are difficult to specify in certain scenarios. If a ground plane exists and all signal lines use it as their return current path, this is no issue. By setting all signal lines to the same voltage one can ensure that no current from one signal line returns via another. However, for many of our designs, no common return path for all signal lines exist, and the inductor system generally comprises multiple galvanically isolated loops. If not handled carefully, currents may take different paths than intended, which can lead to unexpected results. To work around this inherent limitation, we introduced additional inductors to most simulations presented here using Sheen's method. By placing a copy of the intended setup at some

distance with reversed voltages, the symmetry of the problem should result in all return currents flowing in the mirror representation of the original signal line. This works well, however, it has one obvious drawback. Since the number of conductors (and thus segments) is doubled, the rank of all matrices generated during simulation doubles, resulting in four times as many values to be computed. The computational cost of each simulation increases accordingly. Additionally, the presence of the mirrored stack introduces an additional, asymmetric source of electromagnetic fields, leading to some asymmetry in the simulation results. This was considered to not be problematic since in real λ-SQUIDs, the loops themselves are not isolated, straight, infinite conductors, and the fields introduced by the mirrored conductor stack at an appropriate distance may actually be more representative of a cross-section of the real loop geometry. The inability to specify the total current per inductor makes Sheen's method less attractive for simulating the behaviour of λ-SQUIDs, but its capability to model quasiparticle currents at high signal frequencies makes this method suitable for other applications, e.g. for simulating microwave SQUID multiplexing.

3.2.2 Method of Chang *et al.*

Ten years earlier than Sheen *et al.*, Chang *et al.* [Cha81] proposed a method to numerically compute the CDD and inductance matrix for a system of parallel superconducting transmission lines with an approach based on minimising the total energy. The minimum of the energy stored in magnetic fields (geometric contribution) and kinetic energy of Cooper pairs (kinetic contribution) is found using a method of Lagrange multipliers. Contrary to Sheen *et al.*, the boundary conditions for the method of Chang *et al.* define the total current through each inductor. This makes it much easier to ensure that currents take the intended paths, and even allows to easily simulate setups where some conductors carry significantly larger currents than others. To make sure that all currents still add up to zero, a similar workaround as with Sheen's method may be employed. By mirroring the original stack of inductors at some distance with inverted currents, the vanishing total currents can be realised for any setup, albeit at the cost of computation time. One downside to Chang's method is the limitation to dc fields, as the influence of quasiparticles is neglected. For our specific use case this is of little importance, as both the field current running through the input coil and the bias current in the λ-SQUID-loop are constant in time, but it may be a drawback for other applications of the software package. Moreover, the condition of vanishing total currents is not met by default, but depends on the currents specified by the user during setup of the geometry. Failure to ensure that all currents must add to zero will result in faulty data, so the user must take care to prevent this by defining the setup appropriately.

Despite the different algorithms of the two methods, both require operations on matrices of similar size. In practice, neither method had significant speed benefits over the other, if the same setup and segmentation granularity were used.

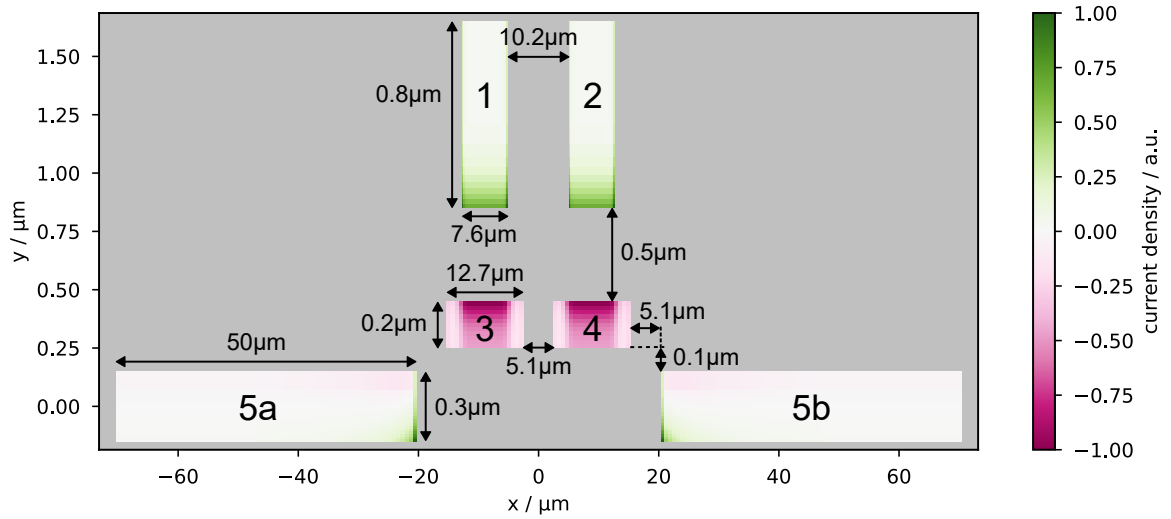


Fig. 3.3: Cross-section of the test geometry presented in [Cha81]. Conductors 1 and 2 have identical geometry and a penetration depth of $\lambda_1 = \lambda_2 = 0.119\,\mu\text{m}$. Likewise, conductors 3 and 4 share the same geometry and penetration depth $\lambda_3 = \lambda_4 = 0.137\,\mu\text{m}$. Conductors $5a$ and $5b$ are both part of the ground plane with a penetration depth $\lambda_{5a} = \lambda_{5a} = 0.086\,\mu\text{m}$. The colour represents the CDD, relative to the maximum value of each conductor, as derived by Chang's method.

3.2.3 Comparison and testing of Chang's and Sheen's methods

To verify our implementations of Sheen's and Chang's method, we have compared them both to each other and to the test geometry specified in [Cha81]. In figure 3.3, the test geometry is depicted as well as the CDD derived by Chang's method. The CDD is displayed by colour and units are relative to the largest value of the current density per conductor. The conductors 5a and 5b appear separate, but actually form one common ground plane. They are treated as a single conductor within the simulation software. We proceeded to use both the methods by Chang *et al.* and by Sheen *et al.* to derive the respective inductance matrices. In units of $\text{pH}\,\mu\text{m}^{-1}$, the inductance matrix derived by our implementation of Chang's method is

$$\underline{L}_{\text{sim}} = \begin{pmatrix} 0.484609 & 0.166276 & 0.424344 & 0.166488 \\ 0.166276 & 0.484551 & 0.166489 & 0.424285 \\ 0.424344 & 0.166489 & 0.452107 & 0.167091 \\ 0.166488 & 0.424285 & 0.167091 & 0.452047 \end{pmatrix}. \tag{3.11}$$

For comparison, the values given in the original publication [Cha81] are

$$\underline{L}_{\text{ref}} = \begin{pmatrix} 0.485818 & 0.165898 & 0.419594 & 0.166041 \\ 0.165898 & 0.485818 & 0.166041 & 0.419594 \\ 0.419594 & 0.166041 & 0.449334 & 0.166703 \\ 0.166041 & 0.419594 & 0.166703 & 0.449334 \end{pmatrix} \tag{3.12}$$

Note that the ground plane (conductors 51 and 5b) is assumed to form the return line for all 4 signal lines. Only self- and mutual inductances of/between the signal lines are computed, hence the inductance matrix has rank 4. A comparison of our results to those in Chang's original publication reveals an average deviation below 0.5 %. The relative deviation peaks at 1.1 % for the element $L_{1,3}$, and is below 0.5 % on average. The exact method used for segmentation is not specified in Chang's original publication, so both the number and distribution of segments is likely different from our simulation. This may be the cause for the deviation seen here. From this excellent agreement, we conclude that our implementation of Chang's method performs as intended. Additionally, we have performed the same simulation (i.e. identical setup and segmentation) with our implementation of Sheen's method. Relative deviation between our implementations of the two methods are on the order of $\mathcal{O}(10^{-12})$, likely due to floating point precision. It should be noted that Sheen's method requires a non-zero signal frequency to be defined. This simulation was performed assuming a frequency of 100 Hz, which is sufficiently low that the simulation results resemble the dc case.

In the later section 4.3.2, we will compare simulation results using Chang's method to experimentally acquired data on real samples. We will see there that the agreement is excellent also, which we interpret as another proof that our implementations can be utilised to determine the (mutual) inductances in stripline geometries.

3.2.4 Importance of the reference patch

Both simulation methods require the definition of a reference patch, i.e. one of the segments created during segmentation of the conductor setup will be used as a reference in all subsequent calculations. For example, in Sheen's method, all voltages will be relative to this reference patch. Since all currents must add to zero, the currents in the different segments can not be calculated independently. Instead, the current through the reference patch is defined by the currents in all other segments and the vanishing total current. The conductor containing this reference patch will automatically become a return line/ground plane, even if it carries no current. Coupling of the other conductors (referred to as "signal lines" in the respective original publications) to the ground plane is not evaluated, and the inductance matrix contains elements only for the signal lines. It is implied that all signal lines eventually connect to the ground plane. The choice of return patch (or, more precisely, the conductor which contains it) thus has an influence on the inductance matrix $\underline{L}$. Both methods were developed for conductor systems where a common ground plane forms the return path for all signal lines.

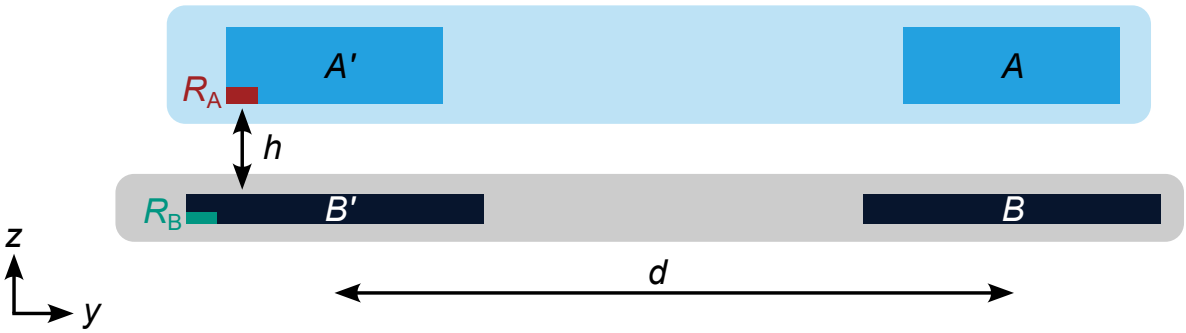


Fig. 3.4: Cross-section of a two-conductor system with conductors A and B. As explained in the main text, a copy of the system (conductors A' and B') is placed at a distance $d \gg h$, with separation h between conductors A and B. We assume A' is the return conductor for A (and B' for B), but that A and A' have no galvanic contact to B and B'. A fully accurate model would thus require a return patch R_A for the conductors A and A', and a separate return patch R_B for B and B'.

This, however, is not true for our case. As previously noted, we generally have galvanically separated inductors that do not share a common return line, and instead have a dedicated and unique return line each. It would therefore be more accurate to model the system with multiple, arbitrary reference patches. Attempts to generalise either Sheen's or Chang's method to include groups of inductors with arbitrary, galvanically separated return lines have not been successful so far, but efforts are ongoing.

As previously explained, both methods benefit from modelling both the original conductor system as well as a copy of it placed at some distance d, as presented in figure 3.4. Here, the original system consists of conductors A and B, with A' and B' comprising the copied system. In most of our scenarios, A and A' form a galvanically separate loop from B and B'. We would thus prefer to use two return lines (A' as return line for A, and B' as return line for B), and consequently the two reference patches R_A and R_B[1]. Thus, R_A would be the reference patch for any segment in A or A', and similarly R_B for any of the segments in B and B'. Using individual return patches (or return lines) is, however, not possible with the software in its current state, and so all conductors must share the same common reference patch. In the case of $d \gg h$ however, the error caused by using a single return patch (e.g. R_B) for all four conductors is negligible for the self- and mutual inductances of/between A and B. The errors in the copied stack A' and B' are much more significant, however these data are not relevant for our calculations. The separation h between the individual inductors within a system is usually $\mathcal{O}(100\,\mathrm{nm})$ due to the film thicknesses and alignment of inductors along the vertical axis, so a separation d of $\mathcal{O}(100\,\mu\mathrm{m})$ is deemed sufficient.

[1]Note that it is of no relevance where the reference patch R_A is placed within the conductor A'. Naturally, the same is true for R_B and B', or any reference patch and return line.

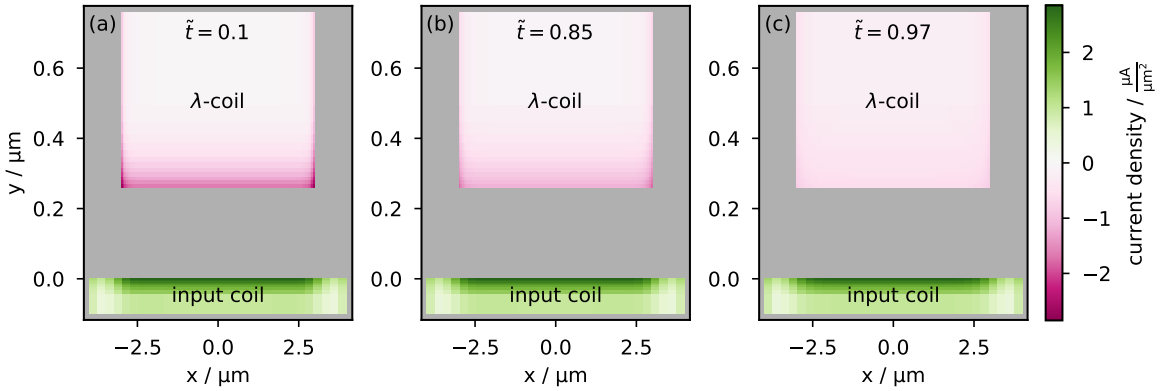


Fig. 3.5: Cross-section of the two-conductor stripline described in the main text. The CDD is depicted by colour, assuming a total current with amplitude 1 µA in each conductor, but with opposite signs. The temperature changes from $\tilde{t} = 0.1$ in (a) to $\tilde{t} = 0.85$ in (b) and $\tilde{t} = 0.97$ in (c). It is clearly visible that the CDD in the top conductor (λ-coil) becomes more homogeneous as the temperature increases. The CDD in the lower conductor (input coil) stays mostly unaltered, as its critical temperature $T_c = 9T_c^\lambda$ is much higher.

3.2.5 Temperature dependent mutual inductance of superconducting striplines

With numerical methods available to calculate the mutual inductance $M_{i,j}(\lambda_1(T), \lambda_2(T),...,\lambda_N(T)))$ for a given geometry of N rectangular conductors with magnetic penetration depths λ_i, $i,j = 1,2,...,N$, we can now quantise how the mutual inductances change with temperature. For simplicity, we will consider a geometry of only two conductors, which is representative of the geometry of the λ-coil of our prototype devices discussed in chapter 4. We will consider the influence of specific, geometric parameters on the temperature dependent mutual inductance in much greater detail in chapter 5, which is dedicated to optimising the performance of a λ-SQUID. Here we just want to highlight how a temperature induced change of the magnetic penetration depth leads to a change in mutual inductance M_{in}. For this example, we assume a simple geometry of a rectangular input coil with width $b_{\text{in}} = 8\,\mu\text{m}$, thickness $a_{\text{in}} = 100\,\text{nm}$, magnetic penetration depth $\lambda_1(0) = 50\,\text{nm}$ at zero temperature and critical temperature $T_c = 9T_c^\lambda$. The sensor coil has the width $b_{\text{sen}} = 6\,\mu\text{m}$, thickness $a_{\text{sen}} = 500\,\text{nm}$, penetration depth $\lambda_2(0) = 50\,\text{nm}$ and critical temperature T_c^λ. We assume that the temperature dependence of the magnetic penetration depth follows equation 3.1. The sensor inductor is placed above the input inductor, separated by $a_{\text{iso}} = 260\,\text{nm}$ of vacuum, since the magnetic influence of the isolating dielectric is assumed to be negligible. We set a total current of 1 µA per conductor, with a positive sign for the input coil and a negative sign for the sensor coil. We therefore assume opposing directions of current flow.

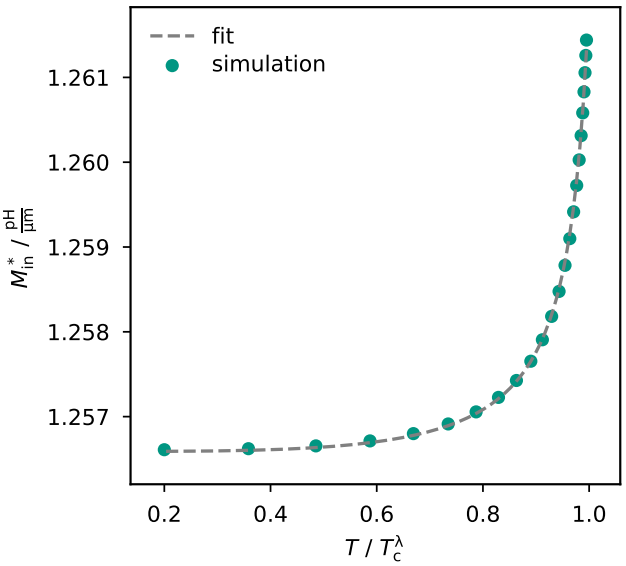


Fig. 3.6: Mutual inductance per unit length M^*_{in} versus temperature for the geometry depicted in figure 3.5. Due to a redistribution of the CDD within the cross-section of the sensor coil, the mutual inductance M^*_{in} increases with temperature. The function 3.13 used for the fit is detailed in the main text and describes the curve accurately.

In figures 3.5 (a) to (c), the CDD for our prototype geometry is displayed for three different temperatures $\tilde{t}$. In (a), the temperature is quite low with only $\tilde{t} = 0.1$. The magnetic penetration depth λ_2 of the sensor coil is much smaller than its physical dimensions, leading to an accumulation of current at the lower edge and corners of the conductor. The CDD in the sensor coil is strongly inhomogeneous, and focused near the edge facing the input coil due to the magnetic fields created by currents in the input coil. As the temperature increases to $\tilde{t} = 0.85$ in (b), the magnetic penetration depth of the sensor coil increases, resulting in a more homogeneous CDD in its cross-section with a less pronounced concentration at the lower corners. The critical temperature of the input coil is much larger, so little change is seen there. At a temperature of $\tilde{t} = 0.97$ (see figure 3.5(c)), the CDD within the sensor coil has homogenised even further. As implied by equation 3.10, the redistribution of the current density changes the effective distance between the two conductors, resulting in a change in mutual inductance. We will see later that this change can be both positive or negative depending on the geometry, and it can be difficult to predict intuitively. Using the numerical methods we have implemented, however, we can analyse this behaviour for any geometry within a couple of minutes of computing time.

The simulation results for the mutual inductance per unit length $\tilde{M}_{in}$ versus temperature acquired by Chang's method for our prototype geometry are depicted in figure 3.6. As alluded to in section 3.2.3, we would obtain the same results using Sheen's method for an equivalent setup. For the parameter set we assumed here, the mutual inductance increases with temperature. The change in the mutual inductance over the entire simulated temperature range is on the order $\mathcal{O}(1\,\%)$. As the change in mutual inductance results from the increasing magnetic penetration depth λ, it is not surprising to see that they follow a similar shape which is flat at low temperatures and increasingly steep as the critical temperature is approached.

We have performed a fit to the simulation data using the function

$$M_{\mathrm{in}}^{*}(T) = M_{\mathrm{in}}^{*}(0)\left[1 - a\left(1 - z(T)\right)\right]. \tag{3.13}$$

The choice of this fit function is not arbitrary. We can see from our simulations that the temperature-induced change of the mutual inductance is typically $\mathcal{O}(1\,\%)$, and thus relatively small. It is hence reasonable to assume that the mutual inductance can be expressed by a constant offset, given by its low-temperature value $M_{\mathrm{in}}^{*}(0)$, and some function $g(\lambda(T))$ describing the small influence of the magnetic penetration depth:

$$M_{\mathrm{in}}^{*}(T) = M_{\mathrm{in}}^{*}(0)\left[1 + g(\lambda(T))\right] \tag{3.14}$$

Even if the nature of this function $g(\lambda(T))$ is not known, we can nonetheless approximate it via a first-order Taylor expansion around zero temperature $T = 0$, i.e. $\tilde{t} = 0$ or $z = 1$. Because of how we defined $g(\lambda(T))$, we can immediately conclude $g(\lambda(0)) = 0$, so the approximation is given by

$$\begin{aligned} M_{\mathrm{in}}^{*}(T) &= M_{\mathrm{in}}^{*}(0)\left[1 + \frac{\partial g(\lambda(0))}{\partial \lambda}\left(\lambda(T) - \lambda(0)\right)\right] && (3.15)\\ &= M_{\mathrm{in}}^{*}(0)\left[1 + \frac{\partial g(\lambda(0))}{\partial \lambda}\frac{\partial \lambda(0)}{\partial z}\left(z(T) - 1\right)\right]. && (3.16) \end{aligned}$$

We can now associate the unknown, but temperature-independent term $\frac{\partial g(\lambda(0))}{\partial \lambda}\frac{\partial \lambda(0)}{\partial z} \equiv a$ with a constant, which then yields our fit function expressed in equation 3.13. From the excellent agreement between the fit function and our simulated data, we can conclude that the first-order Taylor expansion is sufficiently accurate. Over the course of this thesis, we will see that this function can describe a variety of both simulated and experimental data with excellent agreement, indicating its applicability over a wide range of geometries. Especially when considering the noise or sensitivity of a λ-SQUID, as can be seen from equation 3.5, the temperature derivative of the mutual inductance is highly relevant. By taking the temperature derivative of our fit function we can find

$$\frac{\partial M_{\mathrm{in}}^{*}}{\partial T} = \frac{M_{\mathrm{in}}^{*}(0)\, a}{T_{\mathrm{c}}^{\lambda}} \frac{4\tilde{t}^{3}}{\left(1 - \tilde{t}^{4}\right)^{2}}. \tag{3.17}$$

In addition to the temperature-dependent term on the very right hand side of this expression, we can see that this derivative is inversely proportional to the critical temperature T_{c}^{λ} of the sensor element, which describes the only material-dependent quantity. The influence of the coil geometry (both λ-coil and input coil) on the derivative $\partial M_{\mathrm{in}}^{*}/\partial T$ is thus entirely contained with in the product $M_{\mathrm{in}}^{*}(0)\, a$ of two fit parameters.

3.3 Noise analysis of the λ-SQUID

The energy resolution of a λ-SQUID operated as a microcalorimeter is limited by the total energy noise arising from various sources. In a suitable setup with a low-noise amplifier, e.g. an N dc-SQUID series array, two noise contributions dominate. On the one hand, energy fluctuations between the absorber, sensor and heat bath introduce a fundamental thermodynamic energy noise $S_{\mathrm{E,TD}}$. This type of noise is intrinsic to all systems of coupled thermal masses, and exists equivalently for all types of microcalorimeters including TESs and MMCs. We have already introduced this type of noise in chapter 2, and given equation 2.6 to describe it mathematically [McC05, Fle05].

Due to its similarity to a regular dc-SQUID, both in design and underlying physics, the voltage noise S_{VV} of a λ-SQUID follows the exact same equation 2.14. With the temperature-to-voltage gain coefficient $\partial V_{\mathrm{SQ}}/\partial T$ we introduced in equation 3.5 and the inverse total heat capacity $1/C_{\mathrm{tot}} = \partial T/\partial E$ of the λ-SQUID we can therefore compute the energy noise contribution $S_{\mathrm{E,SQ}}$ of the λ-SQUID itself:

$$S_{\mathrm{E,SQ}} = S_{\mathrm{VV}} \left(\frac{\partial V_{\mathrm{SQ}}}{\partial T} \frac{\partial T}{\partial E} \right)^{-2}. \tag{3.18}$$

The resulting energy resolution of a λ-SQUID can then be derived using equation 2.7 with the total noise $S_{\mathrm{E,tot}} = S_{\mathrm{E,TD}} + S_{\mathrm{E,SQ}}$ given by the two contributions discussed previously.

4. Prototype λ-SQUID-like devices

In this chapter, we present the fabrication of our first prototype devices to investigate the λ-SQUID concept experimentally. We discuss experimental results, compare them to theoretical predictions using Chang's numerical method, and finally use our data and simple SQUID theory to predict the potential energy resolution of a fully functional λ-SQUID microcalorimeter.

4.1 Fabrication technology

All devices discussed in this chapter were designed and manufactured in-house using the micro- and nanofabrication facilities at IMS. Since λ-SQUIDs share significant similarities with regular dc-SQUIDs, the fabrication of λ-SQUIDs can in large parts draw from our expertise in manufacturing dc-SQUIDs. The λ-SQUID fabrication process is thus based on our standard process for dc-SQUIDs, complemented by a sensor layer for the λ-coil.

The basis of the process is a Nb/Al-AlO_x/Nb trilayer. The trilayer is sputter deposited in-situ onto silicon substrates electrically insulated with a 250 nm thick wet-thermal SiO_2 layer. The two niobium layers of the trilayer serve as electrodes for the Josephson tunnel junctions and are separated by a thin layer of oxidised aluminium to form the tunnel barrier. The thickness of this tunnel barrier can be tuned by carefully adjusting the oxidation process setting the critical current density of the junctions.

The trilayer is deposited in the dc-magnetron sputter system UTS500[1]. It features a main chamber with 3-inch sputter sources for niobium and aluminium as well as a load lock fitted for both plasma cleaning and controlled static oxidation. Before the trilayer deposition starts, the original substrates are cleaned in the load lock with an rf-plasma at $P_{\mathrm{rf}} = 60\,\mathrm{W}$ in an Ar atmosphere at a pressure of $p_{\mathrm{Ar}} = 4\,\mathrm{Pa}$ for a duration of 3 min. This removes moisture adsorbed to the substrate surface. Then, the first niobium layer is deposited in the main chamber in an Ar atmosphere at a pressure of $p_{\mathrm{Ar}} = 1.11\,\mathrm{Pa}$ supplying a power of $P_{\mathrm{dc}} = 300\,\mathrm{W}$ to the dc-magnetron. A thickness of 100 nm is deposited at a rate of $\dot{n}_{\mathrm{Nb}} = 1.18\,\mathrm{nm\,s^{-1}}$. Immediately afterwards, the aluminium layer is sputtered at an Ar pressure of $p_{\mathrm{Ar}} = 0.93\,\mathrm{Pa}$ using a power of $P_{\mathrm{dc}} = 100\,\mathrm{W}$. We deposit a film thickness of 7 nm with a rate of $\dot{n}_{\mathrm{Al}} = 0.63\,\mathrm{nm\,s^{-1}}$. Subsequently, the aluminium layer is oxidised in the load lock. To ensure a high purity oxygen atmosphere, the load lock is purged with oxygen three times before the wafer is transferred into the load lock. The aluminium layer is oxidised for 3 h 30 min in a static oxygen atmosphere at a pressure of $p_{\mathrm{O2}} = 8\,\mathrm{Pa}$, to yield a critical current density of $j_{\mathrm{c}} = 30\,\mathrm{A\,cm^{-2}}$ for the Josephson tunnel junctions. After the oxidation, the second, 100 nm thick niobium

[1] This custom sputter system was purpose built at IMS

Tab. 4.1: Parameters for etching of Nb in the ICP-RIE and IMS-RIE dry-etching systems. The gas flow of process gasses (in sccm), total gas mixture pressure p_{process} (in Pa) and the radio frequency powers (in W) applied to the table and coupled into the plasma are included. In the ICP-RIE, a 15 s pre-clean before the actual etching is used. Determination of the etching endpoint is done optically via a laser (ICP-RIE) or by eye (IMS-RIE).

Process	Parameter	ICP-RIE	IMS-RIE
Pre-clean	Ar	50 sccm	
	O_2	5 sccm	
	p_{process}	2 Pa	
	table RF	50 W	
	plasma RF	600 W	
Nb-etch	SF_6	20 sccm	30 sccm
	O_2		6 sccm
	Ar	30 sccm	
	p_{process}	20 Pa	35 Pa
	table RF	60 W	
	plasma RF	300 W	100 W

layer is deposited. The deposition parameters are identical to the first Nb layer. During the entire process, the vacuum is not broken to ensure high quality interfaces between the individual layers of the trilayer.

To structure the top electrodes and define the size of the Josephson junctions, the trilayer is spin-coated with AZ-MIR 701[2] positive-tone photoresist. After a 90 s softbake at 90 °C the resist is exposed using the maskless direct laser writing system MLA 150[3], post-exposure baked at 110 °C for 90 s and subsequently developed for 90 s to 120 s in AZ-Developer diluted with ultra-pure water in a 1:1 ratio by volume. Depending on the batch, one of two systems for reactive ion etching (RIE) of the top niobium layer was used: Either a RIE system heavily modified in-house (IMS-RIE) or the state-of-the-art inductively coupled plasma (ICP) RIE system PlasmaPro 100 Cobra[4] (ICP-RIE) which belongs to the competence centre for High-resolution Superconducting Sensors (HSS). The respective parameters used for dry-etching of Nb are summarised in table 4.1.

The patterned top niobium layer serves as a hard mask for the subsequent aluminium wet etch. After the wafer surface has been wetted with water, a mixture of HNO_3 : CH_3COOH : H_3PO_4 : H_2O at a ratio of 1:1:16:2 by weight is added, and agitated until the end of the etch is visually confirmed. After stopping the etching process in ultra-pure water, the wafer is again structured with AZ-MIR 701. Next, the bottom Nb layer of the trilayer is etched using RIE. This layer which contains the bottom junction electrodes and electrical lines, e.g. sections of the SQUID loops and input coils. To electrically isolate the bottom Nb layer, two layers of rf-magnetron sputtered SiO_2 with a thickness of 125 nm each are used. Both layers are structured via lift-off with the negative-tone resist AZ nLOF 2020[5]. Softbake and post-exposure bake are at 110 °C for 5 min and 115 °C for 2 min, respectively. Development takes 60 s in undiluted AZ MIF 2026 developer. The deposition is performed in the in-house

[2]by Merck KGaA, Darmstadt, Germany, distributed by MicroChemicals GmbH, Ulm, Germany
[3]by Heidelberg Instruments Mikrotechnik GmbH, Heidelberg, Germany
[4]by Oxford Instruments Plasma Technology, Bristol, UK
[5]by Merck KGaA, Darmstadt, Germany, distributed by MicroChemicals GmbH, Ulm, Germany

built IDA-3 rf-magnetron sputter deposition system in an atmosphere of Ar and O_2 at partial pressures of $p_{Ar} = 0.36\,\mathrm{Pa}$ and $p_{O2} = 0.24\,\mathrm{Pa}$, respectively. The applied rf power is $P_{rf} = 120\,\mathrm{W}$, resulting in a deposition rate of $\dot{n}_{SiO2} = 31.25\,\mathrm{pm\,s^{-1}}$. Lift-off is performed in Micro D-350[6] DMSO-based stripper at an elevated temperature of 85 °C for at least 90 min before transferring to a megasonic bath[7]. Two baths, 10 min each, at $> 40\,^{\circ}\mathrm{C}$ are sufficient to remove all undesired SiO_2. Before blow-drying the wafer with nitrogen, one bath in acetone and two baths in isopropanol in the ultrasonic bath, two minutes each, ensure that all stripper residuals have been displaced. Using two isolation layers greatly increases reliability as is unlikely for damages or pinholes in both layers to occur at the same location. Additionally, it allows us to make the transitions onto or off of the isolation layers less steep, which is beneficial for the following electrical connection lines.

Next, a AuPd layer is deposited to form resistive elements such as shunt resistors. Structuring is performed with AZ nLOF 2020 using the same process as described before. The material is deposited in the home-made dc-magnetron sputter machine TGA, which features a 3" magnetron sputter source for AuPd and a smaller 2" magnetron sputter source for Nb. The AuPd layer is sandwiched between two very thin ($\approx 2\,\mathrm{nm}$) Nb layers, to ensure sticking and to offer protection from an ion gun cleaning process at a later step. The Nb is deposited in an Ar atmosphere at a pressure $p_{Ar} = 0.3\,\mathrm{Pa}$ to $0.35\,\mathrm{Pa}$, and deposition takes 6 s. The 130 nm thick AuPd layer itself is deposited at a pressure $p_{Ar} = 0.5\,\mathrm{Pa}$ with a deposition rate of $\dot{n}_{AuPd} = 0.903\,\mathrm{nm\,s^{-1}}$. Both depositions use the same sputter power of $P_{dc} = 70\,\mathrm{W}$. Lift-off is done in the same fashion as for the isolation layers.

The sensor layer (or layers) is done in the next step. For the majority of our prototype devices, an aluminium sensor layer was used, but especially in the future a bilayer or multilayer system may be used here. Aluminium has the advantage that its critical temperature $T_c^{Al} \approx 1.21\,\mathrm{K} \ll T_c^{Nb} \geq 8.9\,\mathrm{K}$ is sufficiently low compared to the Nb comprising the rest of the device. Hence, we can easily operate the prototypes near T_c^{Al}, while being far enough below T_c^{Nb}. Additionally, a deposition process for Al already existed at IMS, so its integration into the devices was easy to accomplish. Aluminium was deposited in the UTS500 as described for the trilayer, but with a thickness of 500 nm. We have used a lift-off process with AZ-nLOF 2020 resist for patterning. Lift-off itself was done in acetone rather than the DMSO-based stripper to avoid chemical degradation of the aluminium. Before megasonic agitation, the wafer was left in acetone at room temperature for at least 2 h. Two baths in the megasonic bath without heating for 10 min each followed by two 2 min baths in isopropanol in the ultrasonic bath were usually sufficient to remove most undesired aluminium. However, generally not all the aluminium was lifted entirely, causing a reduction in yield by roughly 10 %. More megasonic power could not be used without causing a significant amount of evaporation of acetone. During later batches of production, an additional, more powerful ultrasonic

[6] by Technic France, Saint-Denis, France, distributed by MicroChemicals GmbH, Ulm, Germany
[7] by SONOSYS Ultraschallsysteme GmbH, Neuenbürg, Germany

bath[8] became available. It was quickly found that an additional bath in acetone in this cleaner for 45 s at each of the three possible frequencies helps to significantly improve the lift-off quality, removing all undesired aluminium. The UTS500 sputter system as well as the small deposition systems IDA-1 and IDA-2 used for deposition of R&D materials at IMS have no ion gun to clean previous layers. Thus, in the design of the prototype devices, special care was taken to not include any vertical interconnects (VIAs) between the sensor layer and previous layers. Instead, the sensor layer is electronically connected only by the final Nb layer. This choice also allowed to easily integrate sensor layers deposited at other facilities, as all special cleaning procedures were postponed to the final Nb step, reducing the requirements set to the deposition system used for the sensor.

The final layer consists of Nb and contains electrical connections and inductor segments. It is deposited in the Univex 450 vacuum system which is fitted with 2" dc-magnetron sputter sources for Nb and Au as well as an ion gun for surface cleaning. Before deposition, a 5 min ion clean with a beam current of 20 mA and beam voltage of 275 V ablates approximately 10 nm of Nb from the exposed lower layers. This removes any surface oxides and other impurities and ensures a superconducting electrical interconnection between the different Nb layers. An argon pressure of $p_{\mathrm{Ar}} = 0.13\,\mathrm{Pa}$ is used for the ion clean. The final 700 nm thick Nb layer is deposited at $p_{\mathrm{Ar}} = 0.5\,\mathrm{Pa}$ using a dc power of $P_{\mathrm{dc}} = 60\,\mathrm{W}$, resulting in a deposition rate of $\dot{n}_{\mathrm{Nb}} = 0.34\,\mathrm{nm\,s^{-1}}$. The same lift-off process as for the sensor layer is used.

4.2 Experimental methods

All measurements were performed in a dilution refrigerator LD 250[9] at IMS which allows measurements at temperatures as low as 7 mK. For most of the experiments we have performed here, it was required to (smoothly) sweep temperatures from a few millikelvin to above the transition temperature of aluminium $T_{\mathrm{c}}^{\mathrm{Al}} \gtrapprox 1.2\,\mathrm{K}$, which exceeds the typical stable temperature range of dilution refrigerators. This was achieved by turning off the turbomolecular pump connected to the dilution unit, which increased the pressure at the still enough to operate the cryostat in temperatures well above 800 mK without having to take any mixture out of the circuit and into the storage tanks.

We have performed all measurements discussed in the following in a single-stage configuration, i.e. without using a SQUID-based amplifier stage. Instead, as depicted in figure 4.1(a), the device under test (DUT) was connected directly to the room temperature Magnicon XXF-1 SQUID electronics, using a cryogenic wiring harness of twisted pairs and triples[10] designed and fabricated in-house at IMS. The readout noise in this configuration is dominated by the SQUID electronics rather than the DUT (compare

[8] by ASONIC d.o.o., Ljubljana, Slovenia

[9] by Bluefors Oy, Helsinki, Finland

[10] Wire by ELSCHUKOM GmbH, Veilsdorf, Germany, made from 98 % Cu and 2 % Ni, with a diameter of 200 µm and a resistance of $2.01\,\Omega\,\mathrm{m^{-1}}$

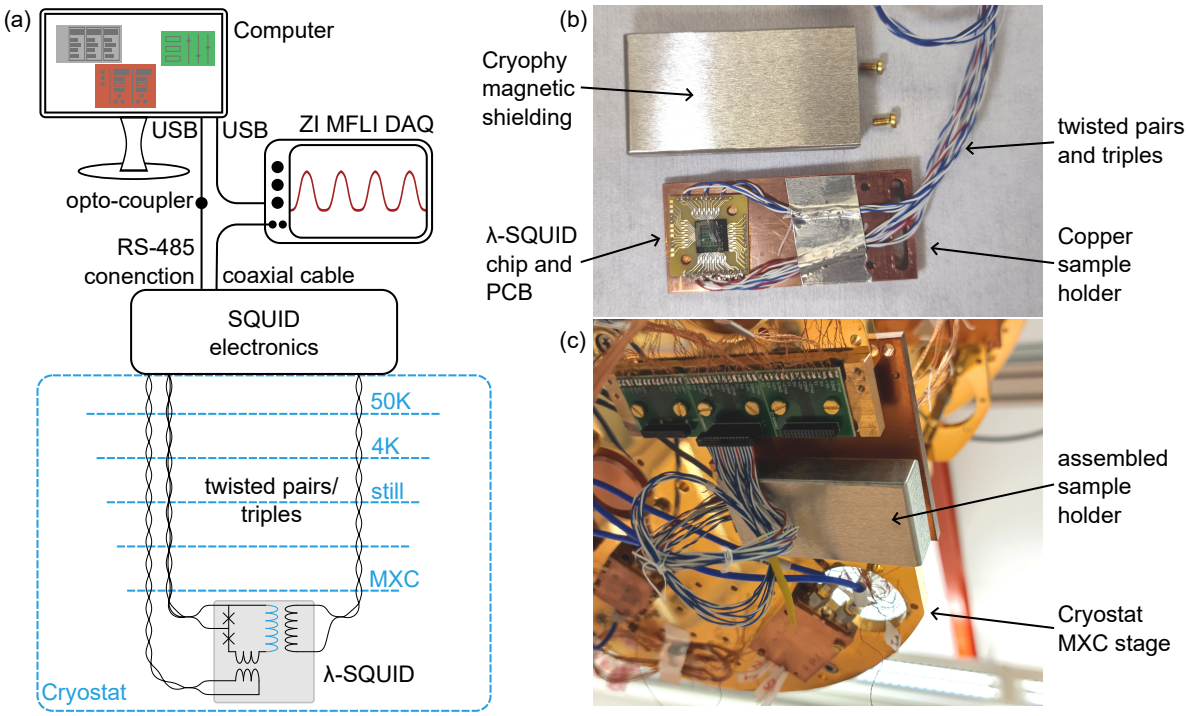


Fig. 4.1: (a) Schematic representation of the experimental setup used for characterising λ-SQUIDs. The λ-SQUID prototype is mounted to a sample holder and placed on the mixing chamber (MXC) stage of a dilution refrigerator. It is connected to the room-temperature SQUID electronics via twisted pairs and triples. Wires traversing any cryostat stage are thermalised on that stage to minimise conductive heatload to colder stages. The voltage across the λ-SQUID is recorded by a Zurich Instruments MFLI lock-in amplifier operated as a digital scope after preamplification in the SQUID electronics. A computer controls both the SQUID electronics and digital scope. (b) Disassembled sample holder for λ-SQUID chips. The chips are glued and wire-bonded to a PCB secured to a copper sample holder and shielded magnetically using a Cryophy shroud. (c) Assembled sample holder mounted to the MXC stage of our cryostat.

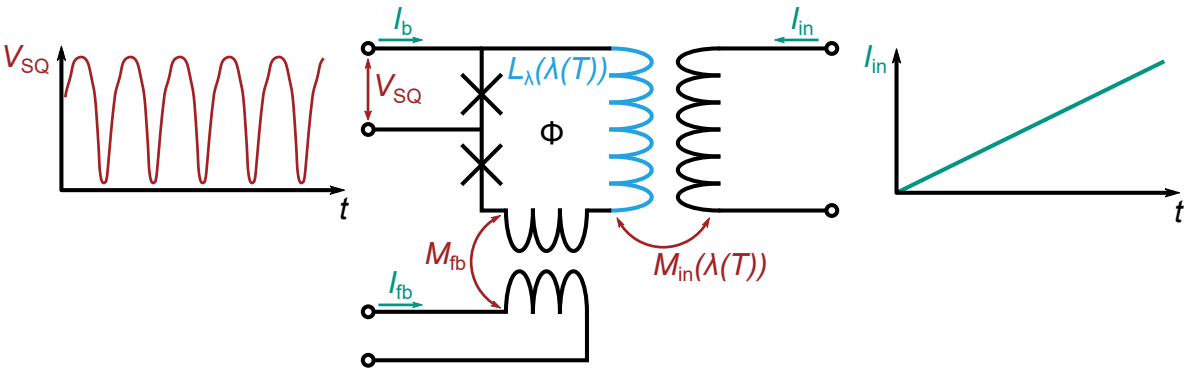


Fig. 4.2: Schematic of the static mutual inductance measurement method. We apply a linearly increasing input current I_{in} to the input coil of the λ-SQUID. The output voltage V_{SQ} depicts the typical periodic response. From the period length of this response and the corresponding current swing, we can derive the mutual inductance $M_{in}(T)$

section 2.2.2). For our measurements however, the noise performance was sufficient, especially since no noise measurements were performed. We chose the single-stage setup for its simplicity and ease of operation. Data was recorded using the digital scope mode of a MFLI[11] lock-in amplifier, and the entire measurement was controlled via a laptop. Using a mobile computer has the distinct advantage that it can be disconnected from mains power during data acquisition, eliminating a ground connection that may cause additional noise. Our setup is grounded solely via the MFLI lock-in amplifier during data recording in an effort to eliminate ground loops. The chips, each containing several λ-SQUIDs, were glued to a printed circuit board (PCB) using GE varnish and connected electronically using aluminium wire wedge-bonds. The PCB was mounted to a copper sample holder and enclosed in a Cryophy soft-magnetic shield to screen external magnetic fields, as depicted in the photograph 4.1(b). The assembled sample holder was then mounted to the mixing chamber stage of our cryostat (see photograph 4.1(c)) and connected to the wire harness using a 30-pin[12] connector.

The main purpose of the measurements was to study the temperature-dependent mutual inductance $M_{in}(T)$ between the λ-coil integrated into the SQUID-loop and the input coil. We have used two different measurement schemes, both with unique advantages and drawbacks.

4.2.1 Static mutual inductance measurements

For most of the measurements we performed, we have first characterised the DUT and subsequently operated it at its most suitable working point in a current-bias configuration. We recorded the voltage V_{SQ} across the λ-SQUID while linearly ramping up the current I_{in} running through the input coil, as illustrated schematically in figure 4.2.

[11] by Zurich Instruments AG, Zürich, Switzerland
[12] SFMC-115-01-L-D, .050" (1.27 mm), Tiger Eye™ system by Samtec, Santa Clara, CA, USA

From the periodicity of the characteristic SQUID response, the mutual inductance can be concluded:

$$M_{\mathrm{in}} = \frac{n\Phi_0}{\Delta I_{\mathrm{in}}}, \tag{4.1}$$

where ΔI_{in} describes the current swing in the input coil causing an integer number n of periods in the SQUID response.

As current source for the input coil current I_{in}, a Magnicon XXF-1 SQUID-electronics is used. A triangular signal with a 20 Hz repetition rate is applied. To measure the voltage V_{SQ} across the DUT, the voltage is first amplified with gain 2000 by the SQUID electronics and then recorded using the digital scope mode of a MFLI lock-in amplifier. All further data analysis is performed offline.

During data analysis, M_{in} was derived by fitting a sine-curve to the voltage data. Amplitude and offset of the sine were predetermined analytically from the data, so the only free parameters for the numerical fit were phase and frequency. To speed up the process further, a pre-estimate for the frequency for the first dataset is derived from the mutual inductance value M_{in} determined manually during DUT characterisation, and the phase is analytically estimated by demodulation of the response with the guessed frequency (compare equation 6.63 from section 6.6). For all further datasets, the previous fit results are used as initial estimates, since only small temperature changes occur between neighbouring datasets. Providing solid initial guesses for the free parameters helps to ensure a fast and robust convergence of the fitting algorithm.

This measurement type has the advantage of high accuracy. Since at each temperature, multiple scope shots can be acquired and averaged, the effective noise can be reduced. The temperature induced change in the mutual inductance M_{in} is rather small, so this provides an advantage. It should be mentioned that this mode of operation differs significantly from the way a λ-SQUID-based microcalorimeter would be operated: In a detector application, a constant input current would be maintained, rather than the linearly increasing current used here. Additionally, the static method is insensitive to the influence of the bias current on the total flux. Our λ-SQUIDs depict strong asymmetry, so the applied bias current I_{b} will cause some magnetic flux contribution due to the inductance L_{SQ} of the entire λ-SQUID-loop. As the temperature changes, the inductance L_λ of the λ-coil and consequently the total loop inductance L_{SQ} change as well. With a constant bias current, this will result in a temperature-dependent magnetic flux contribution. In the static measurement method, this pseudo-signal will cause a phase-shift of the periodic voltage response, but leave the periodicity unchanged. It will therefore not affect the values for the mutual inductance $M_{\mathrm{in}}(T)$ acquired in this way.

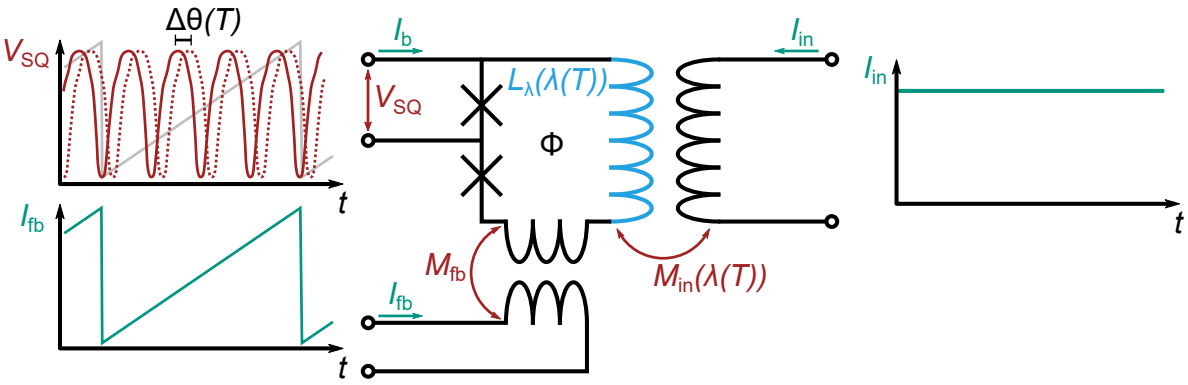


Fig. 4.3: Schematic of the FRM mutual inductance measurement method. We set a constant input current I_{in} running through the λ-SQUID input coil. We also apply a sawtooth-shaped flux ramp I_{fb} to the feedback coil. Depending on the mutual inductance $M_{\mathrm{in}}(T)$ between the λ-SQUID and the input coil, the output voltage response V_{SQ} is shifted by a phase $\Delta\Theta = 2\pi M_{\mathrm{in}}(T) I_{\mathrm{in}}/\Phi_0$.

4.2.2 Mutual inductance measurements using flux ramp modulation

During detector operation, the input current I_{in} would be constant in time, and the temperature dependent flux state of the λ-SQUID would be read out using a suitable method of linearisation, e.g. flux locked loop (FLL) [Dru04] or flux ramp modulation (FRM) [Ric21, Mat12]. While FLL has a noise advantage over FRM, it is sensitive to any voltage change across the device. As the temperature changes, so does the critical current of the Josephson tunnel junctions in the λ-SQUID. If the bias current I_{b} through the λ-SQUID is maintained at a constant value for the duration of the experiment, this temperature-induced shift in critical current causes an equally temperature-induced shift in voltage V_{SQ} across the λ-SQUID. Using FLL, it would be impossible to distinguish such a pseudo-signal from the voltage change due to a flux signal. This effect is expected to be rather small if the probed temperature range is sufficiently below the critical temperature of Nb (9.2 K) which comprises the Josephson junction electrodes. Thus, we expect this contribution to be negligible if the critical temperature T_{c}^{λ} of the λ-coil (and consequently the operating temperature T_0) are sufficiently low, and intend to use FLL for future devices using sensor materials with $T_{\mathrm{c}}^{\lambda} \leq 100\,\mathrm{mK}$. However, with our prototypes using aluminium for their λ-coil, we chose FRM as the method for linearisation to ensure this effect does not cause a systematic measurement error.

Here, a sawtooth-shaped flux ramp I_{fb} with amplitude $|I_{\mathrm{fb}}|$ and a sufficiently fast repetition rate f_{ramp} is applied to the feedback coil of the λ-SQUID, as illustrated schematically in figure 4.3. Over the course of one ramp segment, this leads to a linearly increasing magnetic flux through the λ-SQUID-loop. The modulation ramp amplitude is chosen such that the total flux induced per ramp segment is $\Delta\Phi_{\mathrm{mod}} = M_{\mathrm{fb}}\,|I_{\mathrm{fb}}| = n\Phi_0$ with $n \in \mathbb{N}$. The voltage V_{SQ} across the λ-SQUID changes accordingly and displays the typical periodicity. Thus, the voltage V_{SQ} modulates with a modulation frequency $f_{\mathrm{mod}} = f_{\mathrm{ramp}} M_{\mathrm{fb}}\,|I_{\mathrm{fb}}|\,/\Phi_0$. Any much slower additional flux signal Φ_{sig} causes a phase

shift $\Delta\Theta = 2\pi\Phi_{\mathrm{sig}}/\Phi_0$ of the periodic voltage response. Since the phase shift depends linearly on the magnitude of the signal flux, this serves as a way to linearise the SQUID response. Additionally, any temperature-induced shift in the λ-SQUID properties may cause a constant voltage offset or a change in the shape of the λ-SQUID response, but does not affect the phase shift $\Delta\Theta$. As a consequence, this method is insensitive to such shifts.

However, the quasi-static flux signal Φ_{sig} may have various sources: In addition to the desired signal induced via the input coil, any flux induced due to coupling of the total λ-SQUID inductance to the applied bias current will also contribute. Therefore we can use this measurement method to also analyse the pseudo-signal caused by this effect.

4.3 λ-SQUIDs with aluminium λ-coils

A vast majority of our λ-SQUID-like prototype devices were fabricated using aluminium as a sensor material, as an aluminium sputter deposition process was readily available at IMS, and since we could establish a process for realising reliable superconducting interconnections between aluminium and niobium with little effort. Within a few fabrication cycles, it was quickly established that the regular ion gun cleaning procedure used to remove the oxide layer from niobium is applicable to aluminium, too, which makes superconducting aluminium structures easy to integrate into the existing fabrication process for regular dc-SQUIDs based on a Nb/Al-AlO_x/Nb trilayer. Additionally, the critical temperature $T_{\mathrm{c}}^{\mathrm{Al}} \approx 1.2\,\mathrm{K}$ of aluminium is sufficiently below the critical temperature of niobium to easily facilitate all the measurements, even if sensor materials with lower T_{c}^{λ} are desired for actual sensor applications. In total, 6 batches of λ-SQUIDs with aluminium as a sensor material were produced over the course of this thesis, preceded by a vast number of test structures of various types. Variation between batches includes different stripline widths of the sensor- and input coil or the inclusion of on-chip heaters; otherwise all batches follow the same layout. In the following, we will discuss in detail the experimental results measured from these samples, and present their implications for future λ-SQUID developments.

4.3.1 Temperature-dependent mutual inductance M_{in}

Our first prototype devices were intended to give a proof of concept for the λ-SQUID. We wanted to verify experimentally that we can observe a temperature-dependent mutual inductance M_{in} in such devices, and use the gathered data to predict the potential performance of a λ-SQUID as a novel cryogenic microcalorimeter.

The design of our first prototype devices, exemplarily depicted in figure 4.4, is derived from one of our recent dc-SQUID designs for MMC readout. The SQUID comprises four parallel superconducting loops forming a parallel gradiometer. Each loop can be separated into two segments, an inner one which couples to the feedback coil and an

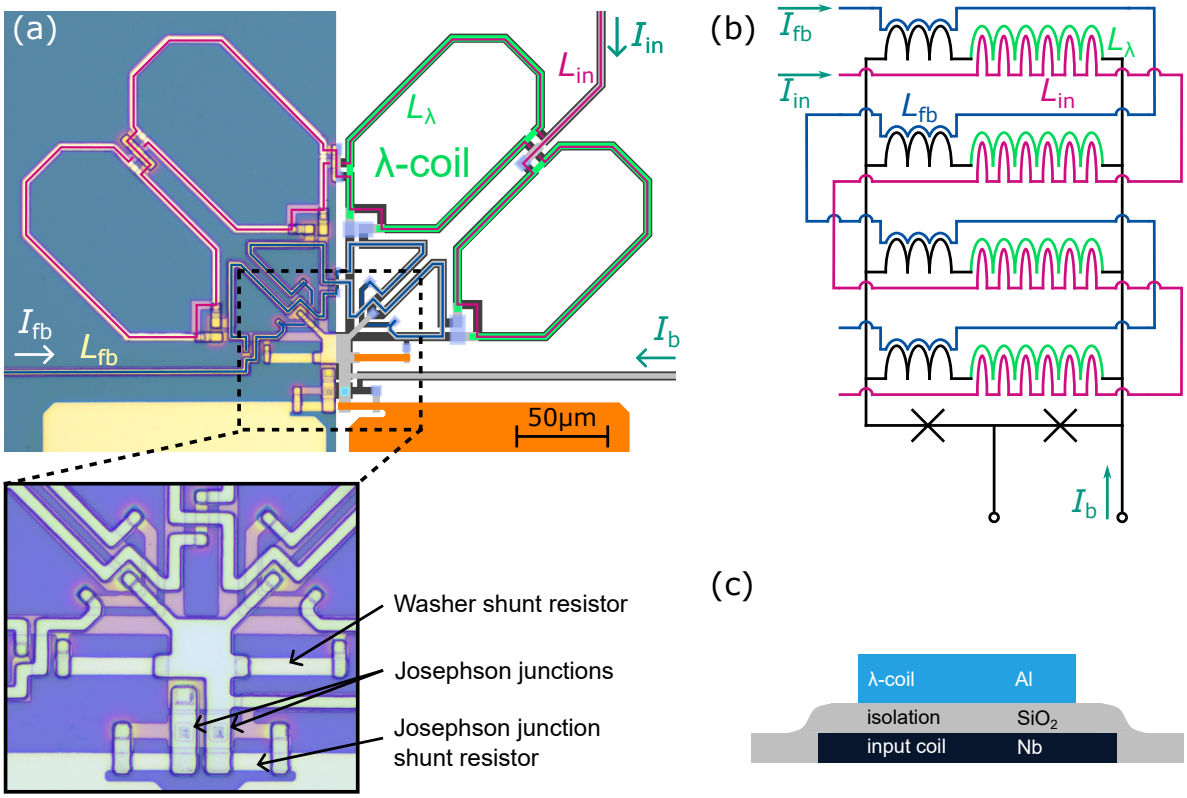


Fig. 4.4: (a) Micrograph (left) and design (right) of a λ-SQUID. The λ-SQUID consists of four washers, each coupled to a section of the input coil and the feedback coil. The aluminium λ-coil (green in the design and schematic, white in the micrograph) forms the largest portion of each washer and is placed on top of the input coil. The lines of the feedback- and input coil are traced in blue and magenta respectively. The bias line carrying the bias current I_b is depicted. The resistively shunted Josephson tunnel junctions are placed towards the centre of the device. Here, we can also see the shunt resistors placed in parallel to the four washers. (b) Equivalent circuit diagram of the λ-SQUID. The four washers form a parallel gradiometer. The respective input- and feedback coil segments are connected in series. (c) Cross-sectional view of the input coil and λ-coil.

outer one that couples to the input coil. These latter, outer loop segments form the λ-coil, the sensitive element of the device. With the exception of the λ-coil, the entire device including the Josephson junction electrodes and auxiliary inductors is fabricated from niobium, with a critical temperature ${T_c}^{\mathrm{Nb}} \approx 8.9\,\mathrm{K}$. The operating temperature T_0 is set by the critical temperature ${T_c}^{\mathrm{Al}} \approx 1.21\,\mathrm{K} \ll {T_c}^{\mathrm{Nb}}$ of the aluminium λ-coil, which is significantly lower than the critical temperature of the other components of the device. Parallel to the four washers, washer shunt resistors are placed to dampen resonances in the LC resonator circuit formed by the loop inductance L_{SQ} and the capacitance between the λ-SQUID-loop and the input and feedback coils [Enp86].

Using the simulation software InductEx[13], the inductances of the device were estimated to be $L_{\mathrm{SQ}} = 98\,\mathrm{pH}$ for the entire λ-SQUID loop, $L_{\mathrm{in}} = 1.16\,\mathrm{nH}$ for the input coil and $L_{\mathrm{fb}} = 379\,\mathrm{pH}$ for the feedback coil. The mutual inductances are $M_{\mathrm{in}} = 238\,\mathrm{pH}$ ($M_{\mathrm{in}}^{-1} = 8.7\,\mu\mathrm{A}/\Phi_0$) between λ-SQUID and input coil and $M_{\mathrm{fb}} = 54\,\mathrm{pH}$ ($M_{\mathrm{fb}}^{-1} = 38.3\,\mu\mathrm{A}/\Phi_0$) between λ-SQUID and feedback coil. With a Josephson junction area of $A_{\mathrm{jj}} = 20.25\,\mu\mathrm{m}^2$ and a targeted critical current density of $j_c = 30\,\mathrm{A\,cm^{-2}}$ we expect a critical current of $I_c = 6\,\mu\mathrm{A}$. By design, we anticipate a screening parameter of $\beta_{\mathrm{L}}^{\mathrm{dc}} = 0.57$. The shunt resistors are designed for a resistance $R_{\mathrm{S}} = 6.5\,\Omega$ each, which with a junction capacitance of $C_{\mathrm{jj}} \approx 0.8\,\mathrm{pF}$ yields a Stewart-McCumber parameter $\beta_{\mathrm{C}} = 0.62$. The input coil has a width of $b_{\mathrm{in}} = 5\,\mu\mathrm{m}$, while the λ-coil is slightly narrower at $b_{\mathrm{sen}} = 3.5\,\mu\mathrm{m}$ to avoid overlapping. The isolation layers are more prone to damage where they need to cover a step in a lower layer. We thus want to avoid having the λ-coil overlap the edges of the input coil underneath to ensure a reliable electrical isolation between them. Each batch contains a number of chips, each of which holds several individual λ-SQUIDs. The following measurements were performed on the specific λ-SQUID with the reference code LSQ_B04_C02_01C, a device from batch 4.

The voltage-current-characteristic (IVC) and the voltage to flux characteristic of this device are depicted in figures 4.5(a) and (b), respectively. Assuming identical Josephson junctions, the critical current of each was determined to be $I_c = 4.5\,\mu\mathrm{A}$, somewhat below the targeted value, most likely due to fabrication tolerances. The normal resistance is $R = 8.6\,\Omega$, which is above the targeted value, potentially due to deviations in the AuPd layer thickness. From the period length of the voltage modulation when increasing the current I_{in} in the input coil, we can determine an input mutual inductance of $M_{\mathrm{in}} = 227.4\,\mathrm{pH}$ ($M_{\mathrm{in}}^{-1} = 9.1\,\mu\mathrm{A}/\Phi_0$) at the cryostat base temperature of roughly 9 mK. A similar (undepicted) measurement of the output voltage V_{SQ} versus the applied feedback current I_{fb} yields a feedback coupling of $M_{\mathrm{fb}} = 50.1\,\mathrm{pH}$ ($M_{\mathrm{fb}}^{-1} = 41.3\,\mu\mathrm{A}/\Phi_0$). Relative deviations to the targeted values are thus 5 % and 8 % for the mutual inductances M_{in} and M_{fb}, respectively. This deviation is potentially caused by uncertainties in the widths of the striplines comprising the λ-SQUID washer, input coil and feedback coil due to fabrication tolerances.

Using the measurement methods described in section 4.2, the mutual inductance $M_{\mathrm{in}}(T)$ of this prototype device was measured over a wide temperature range spanning the

[13] by SUN Magnetics (Pty) Ltd, Stellenbosch, South Africa

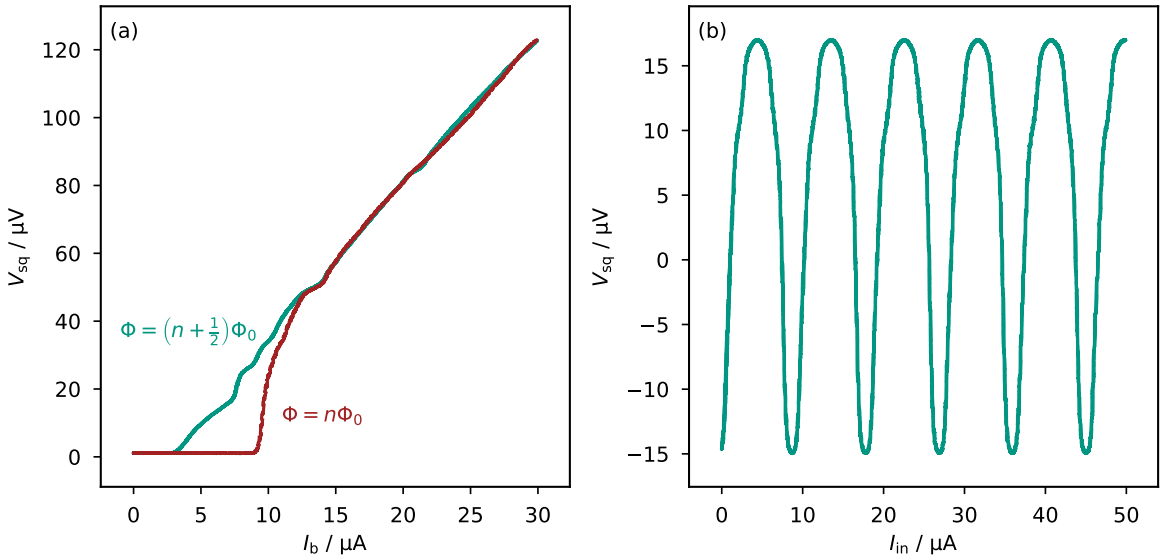


Fig. 4.5: (a) IVC of the λ-SQUID LSQ_B04_C02_01C for the flux states that minimise ($\Phi = (n + 1/2)\Phi_0$) and maximise ($\Phi = n\Phi_0$) the critical current. (b) Voltage V_{SQ} across the λ-SQUID versus the input current I_{in}. From the period length, the mutual inductance M_{in} can be estimated.

cryostat base temperature $< 10\,\mathrm{mK}$ up to above the critical temperature of the λ-coil $> 1.205\,\mathrm{K}$. Above this temperature, the λ-coil becomes normal conducting, interrupting the λ-SQUID loop. Quantum interference breaks down, and the flux-dependent periodic voltage response of the λ-SQUID is replaced by a flux-independent voltage.

Experimental data acquired using the static method is depicted in figure 4.6. Four curves measured with rising and six with falling temperatures make for a total of ten individual acquisitions. We have deliberately measured the mutual inductance multiple times and with alternating sign of temperature change in order to check for hysteresis in the curves. All curves overlap, not indicating any hysteresis. The qualitative agreement with the curves derived from our numerical models as presented in section 3.2 is also remarkable; we will analyse the quantitative agreement later. As expected, the curve starts out fairly flat at lowest temperatures, and increases in steepness as the critical temperature of the sensor material is approached. Across the measured temperature range the mutual inductance is increased by roughly 0.5 % in this device. While the magnetic penetration depth λ is expected to diverge near T_c^λ from the two-fluid model, the mutual inductance M_{in} can not become arbitrarily high: Once the magnetic penetration depth λ is much larger than the width of the sensor coil, the CDD in the sensor coil cross-section becomes homogeneous. Any further increase in λ would no longer affect the CDD or the mutual inductance M_{in}. We can thus predict that the mutual inductance will approach a fixed limit as the temperature gets increasingly close to the critical temperature T_c^λ of the sensor material. With a λ-coil width of $b_2 = 3.5\,\mu\mathrm{m}$ and assuming a zero-temperature magnetic penetration depth of $\lambda_{Al}(0) = 80\,\mathrm{nm}$ for our

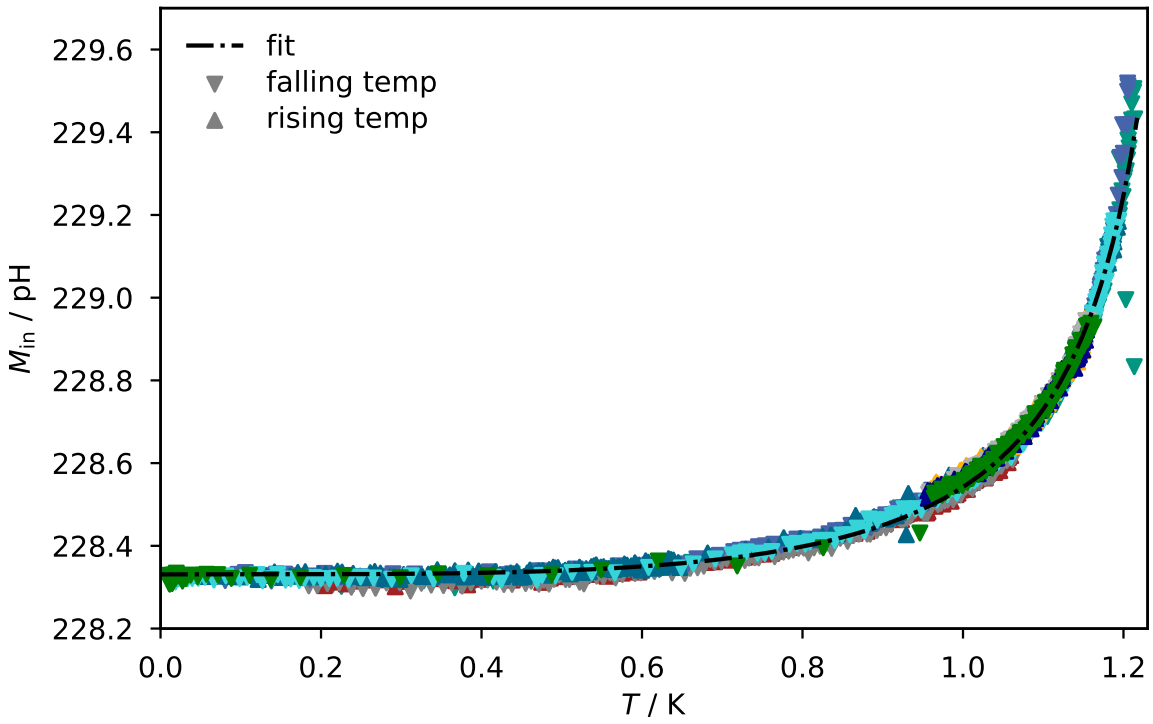


Fig. 4.6: Mutual inductance M_{in} versus temperature for the device with internal label LSQ_B04_C02_01C, acquired using the static measurement method (see section 4.2.1). Measurements were performed using both falling (▽, various colours) and rising (△, various colours) temperature. In total, we have acquired ten curves; six while cooling down and four while warming up. To all data simultaneously, a numerical fit according to equation 3.13 was performed.

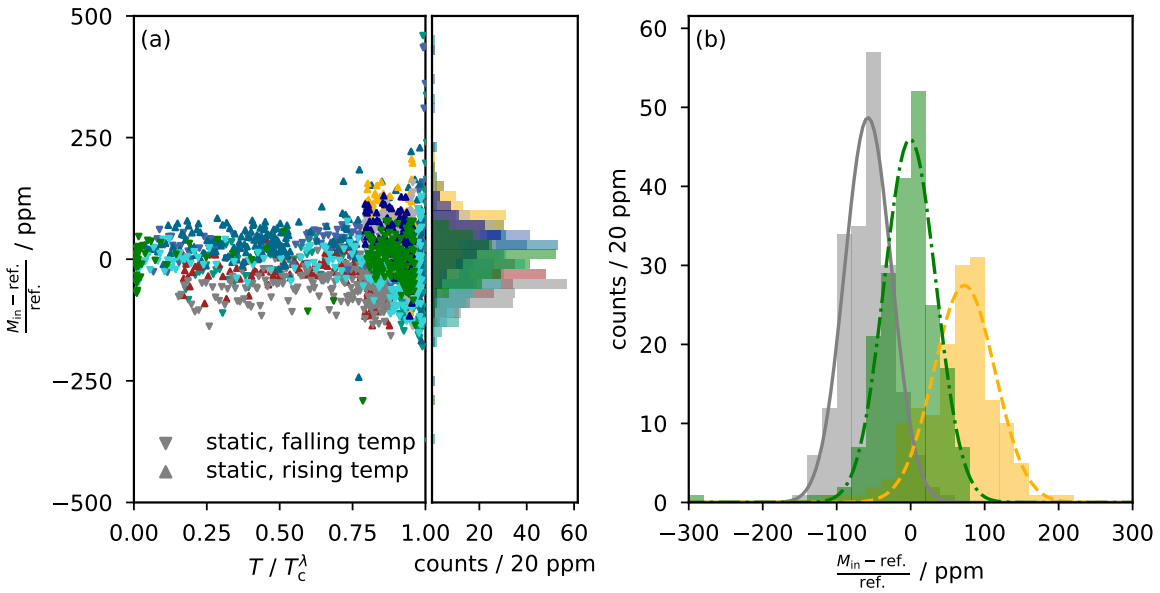


Fig. 4.7: (a) Deviation of measurements at rising and falling temperature from a single, common reference curve, versus temperature and in a histogram representation. Deviations between all curves are mostly below 250 ppm. (b) Three of the histograms of (a), including Gaussian fits. The means of each distribution are within the range ±100 ppm.

aluminium sensor material, the penetration depth would equal the sensor width at a temperature of 99.987 % of T_c^λ. This temperature range, starting only about 150 µK below the critical temperature of our aluminium sensor material, is extremely difficult to deliberately access experimentally in the given setup we have, and could not be probed explicitly. We have numerically fitted equation 3.13 to the dataset for further analysis. As explained in section 3.2.5, this function can be derived from simple theory and describes the expected mutual inductance curves exceptionally well. We can see a similarly excellent agreement here. We will use the fit parameters later for a discussion regarding the noise performance characteristics of the λ-SQUID concept.

For some microcalorimeter types using superconducting sensors, such as MPTs, hysteresis of the sensor response is a major challenge [Ste13]. Testing for such hysteresis is therefore of major importance when characterising our prototype devices. To quantify the deviation between the mutual inductance measurements using the static measurement method at rising and falling temperature, we have first defined a reference curve (ref.) using a smoothing spline fitted to all ten datasets simultaneously. We have then analysed the deviation of each dataset to this reference curve as presented in figure 4.7(a). we have also fitted a Gaussian to the resulting histograms of the deviation, as exemplarily shown in figure 4.7(b) for three of the curves. For a vast majority of data points, the relative deviation from the reference is below 250 ppm. Considering the histogram representation, we can see that the deviations can be accounted for by random noise, and the means of all distributions are within the range ±100 ppm. When

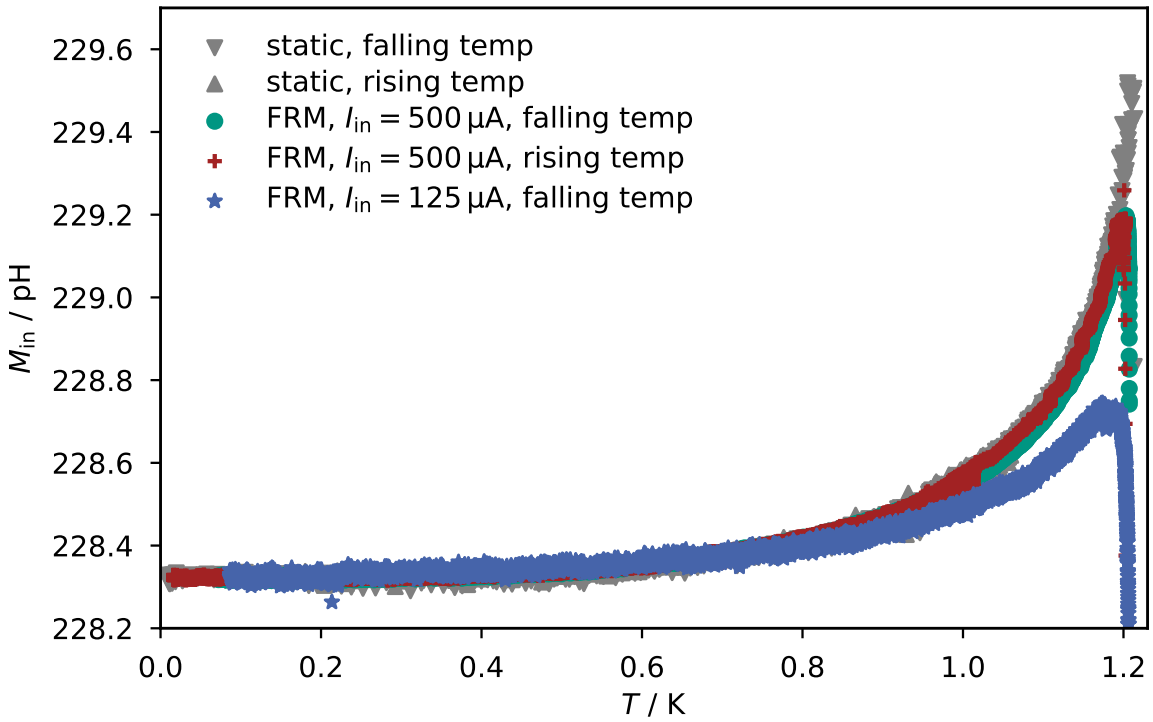


Fig. 4.8: Mutual inductance M_{in} versus temperature for the device with internal label LSQ_B04_C02_01C. Measurements performed with the FRM method using a constant input current of $I_{in} = 500\,\mu A$ at both increasing and falling temperature are shown, as well as a reference measurement using a lower input current of $I_{in} = 125\,\mu A$ at falling temperature. For comparison, the previously shown data from the static method are shown in grey.

considering the few outliers, it is important to keep in mind that the relevant temperature range exceeds 1 K, which is difficult to access in a dilution refrigerator. Above roughly 800 mK, the mixture in the dilution stage begins to change its phase, which can lead to sudden and rapid temperature jumps of the cryostat, especially while warming up. If the cryostat temperature changes too rapidly, a temperature offset between thermometer and device under test can result. Such jumps were present while acquiring the static measurements with rising temperature, leading to the few outliers at temperatures above 75 % of T_c^λ. During static measurements, the data points were acquired at constant time intervals. The fast change in temperature thus also results in much fewer data points in regions with such jumps.

To verify the data gathered with the static measurement method, we have also used the FRM method to probe the mutual inductance of the same device. We have measured mutual inductance curves again for both falling and rising temperature using the largest input current we can generate with our current source, which is $I_{in} = 500\,\mu A$. Additionally, we have acquired a curve at falling temperature using a much lower input current of $I_{in} = 125\,\mu A$, too. All these curves are plotted in figure 4.8. A few observations are

immediately apparent. Firstly, we can note the excellent agreement between the static and high-current FRM measurements over the vast majority of the temperature range. Close to $T_c^\lambda = 1.205\,\mathrm{K}$ however, the FRM curves depict a sudden change of direction and begin declining rapidly. This is even more noticeable in the reference curve measured with a reduced input current of $I_{in} = 125\,\mu\mathrm{A}$, which deviates from the static data already above 0.8 K. As detailed in section 3, both the kinetic ($L_{\lambda,kin}$) and geometric ($L_{\lambda,geo}$) contributions to the λ-coil inductance L_λ change with temperature. While only the geometric contribution $L_{\lambda,geo}$ has an influence on the mutual inductance M_{in}, the kinetic contribution actually experiences the stronger temperature-dependence, and can contribute a quasi-signal by coupling to currents running within the SQUID loop e.g. due to asymmetric bias currents. The λ-SQUID designs discussed in this thesis are exclusively asymmetric, i.e. the applied bias current I_b will inevitably cause some flux through the SQUID loop. In a static measurement, the pseudo-signal would only change the phase of the voltage modulation, but not its period length. The static method is thus insensitive to the pseudo-signal. When determining the mutual inductance using the FRM method however, we expect to see a contribution due to this pseudo-signal, since it is sensitive to any quasi-static magnetic flux contribution. We calculate the mutual inductance shift $\Delta M_{in} = \Delta\Phi_{sig}/I_{in}$ from the measured change in signal flux $\Delta\Phi_{sig}$ and the applied input current I_{in}, and therefore the same absolute pseudo-signal will cause a larger error to the mutual inductance determination if I_{in} is small. This is why the deviation caused by the pseudo-signal is larger in the curve acquired with a lower input current. While the bias current is considerably smaller than any input current typically applied, we must keep in mind that the pseudo-signal results also from the kinetic inductance $L_{\lambda,kin}$. While the geometric inductance will eventually saturate when the critical temperature is approached, the kinetic contribution will diverge similarly to λ. We thus conclude that for any input current I_{in} a temperature range exists above which the pseudo-signal due to the bias current and total λ-coil inductance becomes the dominating flux signal contribution. This temperature range, as previously noted, is expected to occur only extremely close to the transition temperature T_c^λ of the sensor material. We can push this range further towards higher temperatures by increasing the input current I_{in}. It is worth noting that, depending on the signs of the input current I_{in} and bias current I_b, the actual signal and pseudo-signal fluxes may or may not have the same sign. In this specific example shown here, the pseudo-signal has the opposite sign to the actual signal.

4.3.2 Comparison to simulated data

We can apply the numerical method by Chang *et al.* which we introduced in section 3.2 to compare our experimental results with simulated data of the respective λ-SQUID geometry.

The geometry of the λ-SQUIDs considered here features an input coil width and thickness of $b_{in} = 5\,\mu\mathrm{m}$ and $a_{in} = 100\,\mathrm{nm}$, a λ-coil width and thickness of $b_{sen} = 3.5\,\mu\mathrm{m}$ and $a_{in} = 500\,\mathrm{nm}$, and an isolation layer thickness of $a_{iso} = 260\,\mathrm{nm}$. We assume an

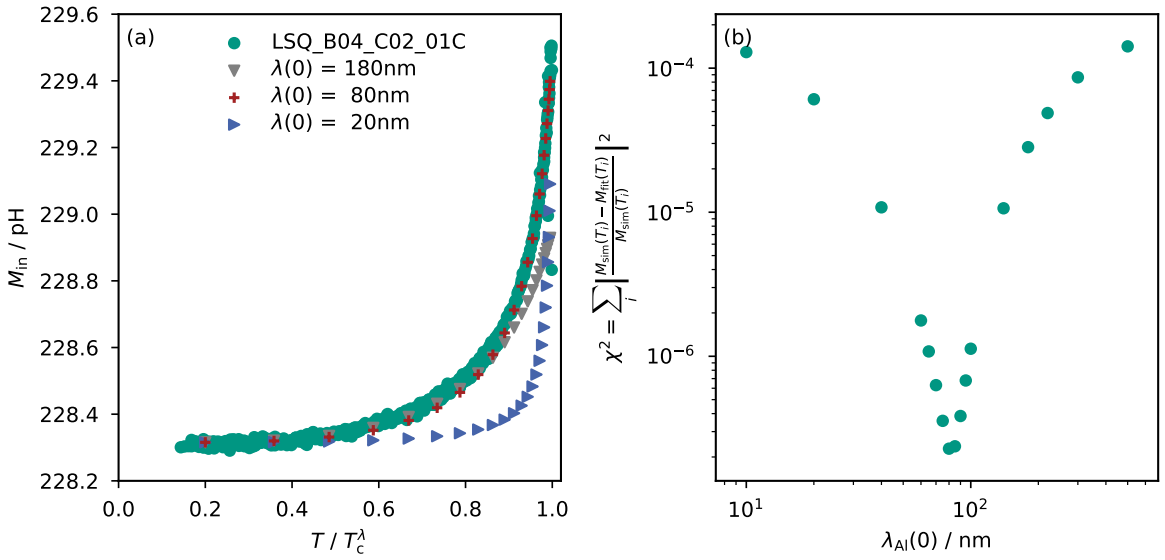


Fig. 4.9: (a) Measured dependence of the mutual inductance M_{in} on temperature of the λ-SQUID with internal label LSQ_B04_C02_01C as well as the expected dependence (based on simulations) for three different example values of the magnetic penetration depth $\lambda_{Al}(0)$ for the λ-coil. (b) Deviation between the simulated data and the fit of equation 3.13 to the measured data. At a penetration depth of $\lambda_{Al}(0) = 80\,\text{nm}$ the deviation is minimised.

almost temperature-independent magnetic penetration depth in the niobium input coil of $\lambda_{Nb} = 50\,\text{nm}$ over the relevant temperature range $10\,\text{mK} \leq T \leq 1.25\,\text{K}$. We will see later that this choice gave the best agreement between simulated and experimental data out of all tested values. The only free parameter left is the zero-temperature magnetic penetration depth $\lambda_{Al}(0)$ of the aluminium comprising the λ-coil. Since no previous measurements of the magnetic penetration depth of aluminium exist at IMS, we have used Chang's method to compute the temperature-dependent mutual inductance $M_{in}(T)$ for various values of $\lambda_{Al}(0)$ ranging from a very low 10 nm all the way up to 500 nm. Bulk aluminium has been reported to have a penetration depth of roughly 52 nm [Beh71]. With our dc-magnetron sputter deposited thin films, some deviation from the bulk value is to be expected. In figure 4.9(a), the simulated mutual inductance data for three example values of the magnetic penetration depth $\lambda_{Al}(0)$ of the λ-coil is depicted together with the experimental data of the λ-SQUID with the internal label LSQ_B04_C02_01C. For very large values of the penetration depth, e.g. $\lambda_{Al}(0) = 180\,\text{nm}$, the temperature-induced shift of the mutual inductance shows a much lower magnitude than we have measured. For very small values, e.g. $\lambda_{Al}(0) = 20\,\text{nm}$, the magnitude of the shift is again a little smaller than experimentally found, and the shape of the overall curve is more concave than the experimental data indicate. To find the most suitable value for the magnetic penetration depth $\lambda_{Al}(0)$, we have computed the reduced χ^2-sum of the simulated data to a fit of equation 3.13 to the measured curve. This deviation is depicted versus the value $\lambda_{Al}(0)$ in figure 4.9(b), where a clear

minimum at $\lambda_{\mathrm{Al}}(0) = 80\,\mathrm{nm}$ is found. We conclude that the experimental data of this prototype device can be best described assuming this value for the magnetic penetration depth of the aluminium sensor material, and will use this value in simulations going forward.

To obtain mutual inductance values from our simulations, the results must be multiplied with the length of the conductor. At a penetration depth of $\lambda_{\mathrm{Al}}(0) = 80\,\mathrm{nm}$, the length resulting in the depicted agreement is $l_{\mathrm{loop}}/2 = 159.7\,\mu\mathrm{m}$. The total centreline circumference of the aluminium λ-coil is 324 µm, of which 312 µm are placed atop the input coil. The length determined from the simulated data depicts excellent agreement, and equals half the centreline circumference of the λ-coil with a deviation of only 1.4 %. The factor one half arises since Chang's method by design also requires a return path for the current (see section 3.2.4). We therefore effectively simulate a slice through two input coil / λ-coil stacks, with one acting as the return current path for the other. The resulting inductance matrix is thus twice that of a single, isolated stack.

The observant reader may have noticed our choice for the niobium magnetic penetration depth of $\lambda_{\mathrm{Nb}} = 50\,\mathrm{nm}$ as rather odd, given that thin niobium films at IMS have been reported to have a magnetic penetration depth of $\lambda_{\mathrm{Nb}} \approx 100\,\mathrm{nm}$ at thicknesses of $a_{\mathrm{in}} = 100\,\mathrm{nm}$ [Gub05]. We have actually performed the procedure above for a couple different values of λ_{Nb}, including the values $\lambda_{\mathrm{Nb}} = 100\,\mathrm{nm}$ as reported in [Gub05] and $\lambda_{\mathrm{Nb}} \approx 170\,\mathrm{nm}$, which is commonly used for radio-frequency simulations at IMS. The resulting plots are depicted in figure 4.10 (a) and (b) for $\lambda_{\mathrm{Nb}} = 100\,\mathrm{nm}$ and in figure 4.10 (c) and (d) for $\lambda_{\mathrm{Nb}} \approx 170\,\mathrm{nm}$. It is apparent that, across the entire tested range of values for the penetration depth $\lambda_{\mathrm{Al}}(0)$ of the λ-coil, the agreement between experimental and simulated data is less good compared to the results presented in figure 4.9. While the best agreement resulted in a χ^2-sum of 2.28×10^{-7} for $\lambda_{\mathrm{Nb}} = 50\,\mathrm{nm}$, the values were considerably higher at 8.05×10^{-7} for $\lambda_{\mathrm{Nb}} = 100\,\mathrm{nm}$ and 3.08×10^{-6} for $\lambda_{\mathrm{Nb}} = 170\,\mathrm{nm}$ respectively. We have therefore decided to assume a magnetic penetration depth of $\lambda_{\mathrm{Nb}} = 50\,\mathrm{nm}$ for our simulations, as it yielded the best agreement to our experimental data. For the future, we plan a comprehensive investigation of the magnetic penetration depth of both, the niobium of the input coil and sensor material of the λ-coil using dedicated measurement techniques using, for example, a SQUID susceptometer.

We can conclude that we observe an excellent agreement between our experimental data and the simulation results from our implementation of Chang's method. With an appropriate choice of magnetic penetration depth $\lambda(0)$, both the absolute mutual inductance $M_{\mathrm{in}}(0)$ at low temperatures and the temperature-dependent change in mutual inductance are predicted correctly. We can thus assume that we have a robust theoretical understanding of the underlying mechanism leading to the observed mutual inductance curves, which is the basis for the λ-SQUID concept.

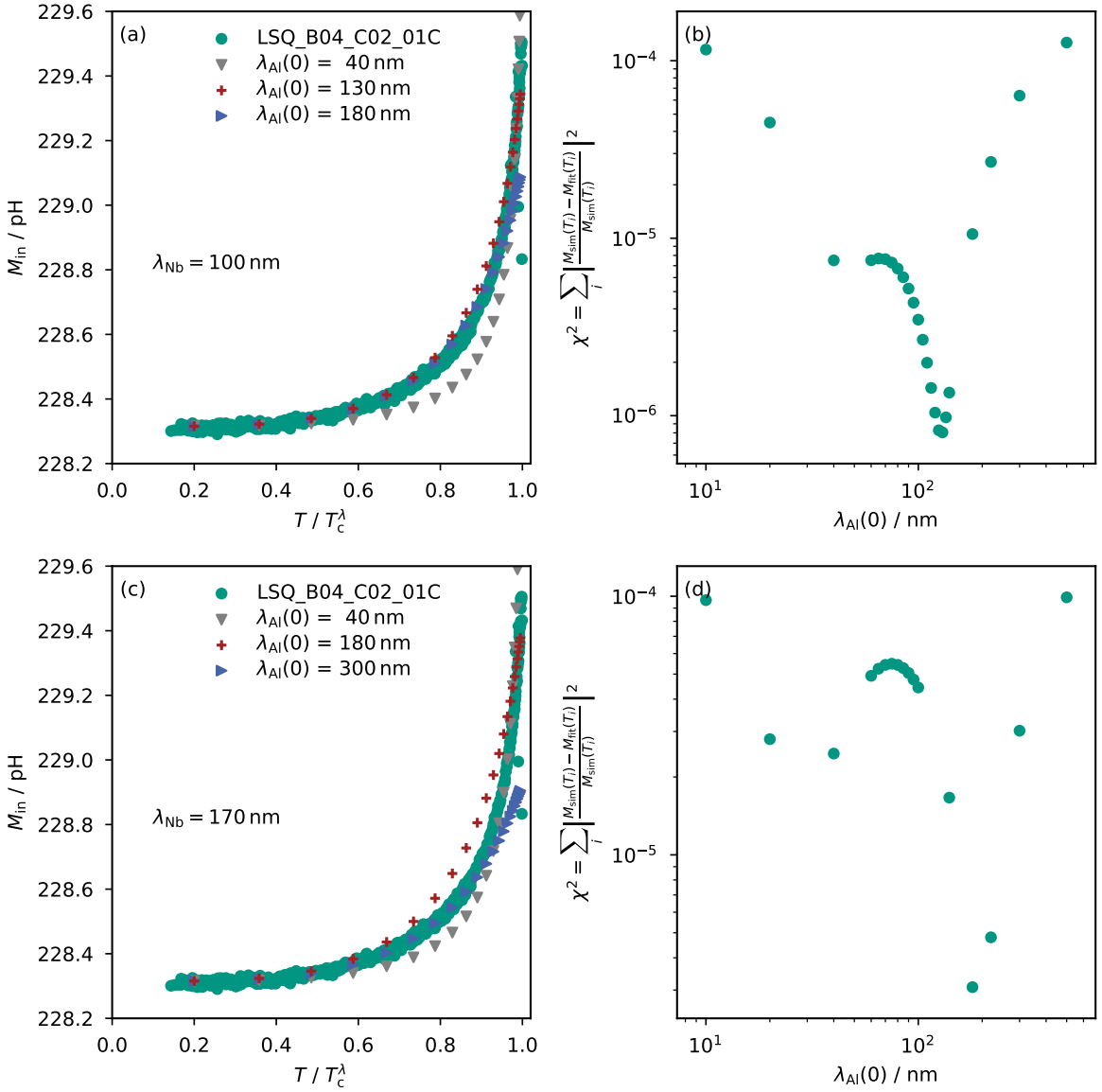


Fig. 4.10: (a),(c) Measured dependence of the mutual inductance M_{in} on temperature of the λ-SQUID with internal label LSQ_B04_C02_01C as well as the expected dependence (based on simulations) for three different example values of the magnetic penetration depth $\lambda_{Al}(0)$ for the λ-coil. (b),(d) Deviation between the simulated data and the fit of function 3.13 to the experimental data. For (a) and (b), we have used $\lambda_{Nb} = 100\,nm$ for the penetration depth in the niobium input coil as reported in [Gub05]. For (c) and (d), we have used a value of $\lambda_{Nb} = 170\,nm$ commonly used for radio frequency simulations at IMS.

4.3.3 Noise performance estimate

From the measured temperature dependence of the mutual inductance $M_{\mathrm{in}}(T)$ gathered from our prototype test devices, we can make some predictions regarding the potential energy resolution of a fully-fledged λ-SQUID-based microcalorimeter. As introduced in section 3.3, we can express the total energy noise $S_{\mathrm{E,tot}}$ of an λ-SQUID via the thermodynamic noise contribution $S_{\mathrm{E,TD}}$ and the SQUID-like noise contribution $S_{\mathrm{E,SQ}}$, assuming negligible readout chain noise:

$$
\begin{aligned}
S_{\mathrm{E,tot}} &= S_{\mathrm{E,SQ}} + S_{\mathrm{E,TD}} && (4.2)\\
S_{\mathrm{E,SQ}} &= S_{\mathrm{VV}} \left(\frac{\partial V_{\mathrm{SQ}}}{\partial T} \frac{\partial T}{\partial E} \right)^{-2}, && (4.3)\\
&= 18 k_{\mathrm{B}} T R \left(\frac{R}{L_{\mathrm{SQ}}} \frac{\partial M_{\mathrm{in}}}{\partial \tilde{t}} \frac{I_{\mathrm{in}}}{T_{\mathrm{c}}^{\lambda}} \frac{1}{C_{\mathrm{abs}} + C_{\mathrm{sens}}} \right)^{-2}, && (4.4)\\
S_{\mathrm{E,TD}} &= k_{\mathrm{B}} C_{\mathrm{sens}} T^2 \left[\frac{4\,(1-\beta)\,\tau_0}{1 + (2\pi\tau_0 f)^2} + \frac{4\beta\tau_1}{1 + (2\pi\tau_1 f)^2} \right] && (4.5)
\end{aligned}
$$

Here, we have assumed that the λ-SQUID has been designed like an optimised dc-SQUID with screening parameter $\beta_{\mathrm{L}}^{\mathrm{dc}} = 1$ and Stewart-McCumber parameter $\beta_{\mathrm{C}} = 1$ [Tes77]. The resistance R is the total resistance of one of the shunted Josephson junctions, and L_{SQ} is the total inductance of the λ-SQUID loop, including but not limited to the λ-coil.

For such an optimised device, the λ-SQUID gain coefficient $\partial V_{\mathrm{SQ}}/\partial T$ can be expressed as

$$
\frac{\partial V_{\mathrm{SQ}}}{\partial T} = \frac{R}{L_{\mathrm{SQ}}} \frac{\partial M_{\mathrm{in}}}{\partial \tilde{t}} \frac{I_{\mathrm{in}}}{T_{\mathrm{c}}^{\lambda}}, \tag{4.6}
$$

assuming the temperature dependence of the mutual inductance M_{in} depends only on the reduced temperature $\tilde{t} = T/T_{\mathrm{c}}^{\lambda}$, i.e. $\mathrm{d}M_{\mathrm{in}}/\mathrm{d}T = (\partial M_{\mathrm{in}}/\partial \tilde{t})(\mathrm{d}\tilde{t}/\mathrm{d}T)$. This assumption seems well justified, based on the fact that equation 3.13 introduced in section 3.2.5 describes both our experimental and simulated data exceptionally well, and satisfies the condition introduced above. Since the two-fluid model description of the temperature dependence of the magnetic penetration depth $\lambda(T)$ also predicts this scaling, we further have no reason to assume that $M_{\mathrm{in}}(T)$ would depict any other behaviour. This simplification neatly allows us to use the experimental data gathered on our prototype devices with aluminium λ-coils and extrapolate to materials with lower critical temperature T_{c}^{λ} of the sensor material. Doing so is crucial to gauge the potential performance of a fully-fledged λ-SQUID, since the operating temperature required with an aluminium λ-coil would exceed 1 K and result in thermal noise too large to be usable in a microcalorimeter application. From equation 4.6, it is immediately clear

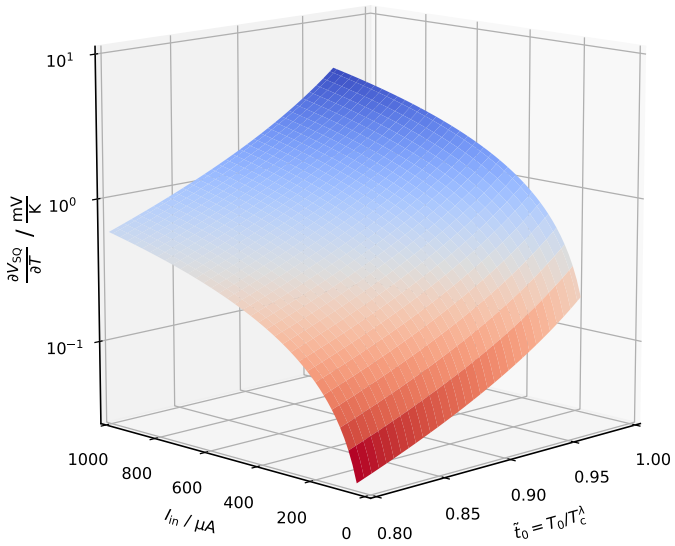


Fig. 4.11: Derived dependence of the gain coefficient $\partial V_{SQ}/\partial T$ on the input current I_{in} and the reduced operating temperature $\tilde{t}_0 = T_0/T_c^\lambda$, both of which we can adjust after device fabrication and even in-situ. $\partial M_{in}/\partial \tilde{t}$ was determined from experimental data on the device with internal label LSQ_B04_C02_01C, and a Josephson junction critical current $I_c = 5\,\mu A$, shunted junction resistance of $R = 5\,\Omega$ and sensor material critical temperature of $T_c^\lambda = 50\,mK$ were used.

that we have several ways to influence the gain coefficient, even after the device has been fabricated or even in-situ during device operation.

The most practical way is by tuning the input current I_{in}, which we can freely set using an external current source and which is limited solely by the ampacity of the input coil. Based on recent measurements on niobium deposited at IMS, we can expect an input coil ampacity exceeding 40 mA for the input coil geometry used in the devices considered here. Another way to adjust the gain coefficient is by altering the operating temperature T_0. As the mutual inductance curve gets steeper as we approach T_c^λ, reducing the operating temperature will reduce the gain coefficient $\partial V_{SQ}/\partial T$. This may be especially useful to increase the dynamic range of the detector, which is fundamentally limited by the tolerable temperature increase before superconductivity in the λ-coil breaks down. In figure 4.11, the gain coefficient $\partial V_{SQ}/\partial T$ is depicted versus the input current I_{in} and the reduced operating temperature $\tilde{t}_0 = T_0/T_c^\lambda$. The values were computed based on the mutual inductance curves of the device with the internal label LSQ_B04_C02_01C, from which $\partial M_{in}/\partial \tilde{t}$ was extracted by computing the derivative of the fit of equation 3.13 as shown in figure 4.6. To comply with the assumption of an optimised dc-SQUID, we have assumed a Josephson junction critical current of $I_c = 5\,\mu A$ and a shunted junction resistance of $R = 5\,\Omega$. For this example, a sensor material critical temperature of $T_c^\lambda = 50\,mK$ was used.

To predict the achievable energy resolution ΔE_{FWHM} we may expect from a fully functional λ-SQUID, we have used the gain coefficient values as presented in figure 4.11. An input current of $I_{in} = 3\,mA$ was assumed, which is considerably lower than the input coil ampacity but exceeds the maximum output current of the SQUID electronics

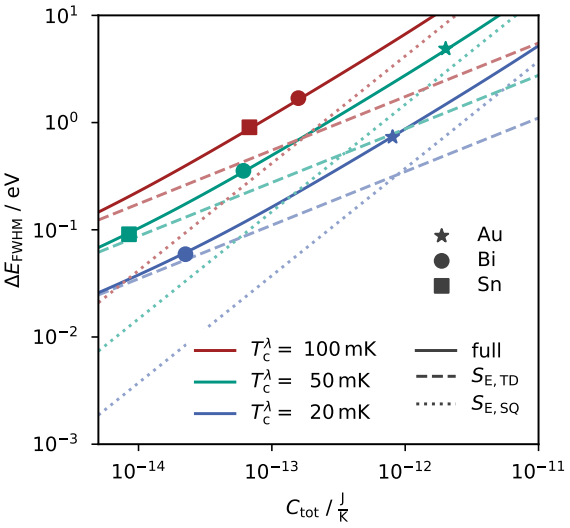


Fig. 4.12: Achievable energy resolution ΔE_{FWHM} versus total specific heat C_{tot} of a λ-SQUID-based microcalorimeter. The achievable energy resolution (solid line) is displayed as well as the effective energy resolutions if we consider only the thermodynamic noise $S_{\mathrm{E,TD}}$ (dashed) or only the SQUID-like noise $S_{\mathrm{E,SQ}}$ of the λ-SQUID (dotted), respectively. Curves for three values of $T_c^\lambda = 100\,\mathrm{mK}$ (red), $T_c^\lambda = 50\,\mathrm{mK}$ (green), and $T_c^\lambda = 20\,\mathrm{mK}$ (blue) at a constant input current of $I_{\mathrm{in}} = 3\,\mathrm{mA}$ are shown. Stars, circles and squares mark the full energy resolution when using absorbers made from Au, Bi and Sn, respectively, at the respective temperatures.

applied for our experiments. We used rise and decay times of $\tau_0 = 1\,\mu\mathrm{s}$ and $\tau_1 = 1\,\mathrm{ms}$ respectively, based on typical values for MMCs [Fle05]. Finally, we have assumed that the specific heat of the λ-coil always exactly equals that of the particle absorber, i.e. $C_{\mathrm{sens}} = C_{\mathrm{abs}}$. As we will show explicitly in section 5.1, this choice optimises the energy resolution of λ-SQUIDs. Based on these values, we can compute both, the thermodynamic and dc-SQUID-like energy noise contributions $S_{\mathrm{E,TD}}$ and $S_{\mathrm{E,SQ}}$ for any given value of the specific heat C_{abs} of the particle absorber and any critical temperature T_c^λ of the λ-coil. We can then calculate the resulting energy resolution ΔE_{FWHM} by solving the integral 2.7 numerically.

In figure 4.12, we have plotted the achievable energy resolution ΔE_{FWHM} versus the total specific heat $C_{\mathrm{tot}} = C_{\mathrm{abs}} + C_{\mathrm{sens}}$ for three values of the critical temperature of the λ-coil. The operating temperature is assumed to be $T_0 = 0.9 T_c^\lambda$. The achievable energy resolution is depicted by solid lines, while the limits imposed by the individual noise contributions are plotted as dashed ($S_{\mathrm{E,TD}}$) or dotted ($S_{\mathrm{E,SQ}}$) lines respectively. The different scaling of both contributions with total specific heat is clearly apparent (see equations 4.4 and 4.5). At low values of the total specific heat C_{tot}, thermodynamic noise fundamentally limits the energy resolution. As the specific heat increases, the SQUID-like noise contributions becomes more significant and begins to dominate. The crossing point where both noise contributions have an equal effect on the energy resolution shifts to larger values of the total specific heat as the critical temperature T_c^λ (and thus the operating temperature) of the device is reduced. As expected, a reduction in T_c^λ also leads to an improvement of noise overall.

As a specific example, we consider the three materials most commonly used for the particle absorbers in microcalorimeters, namely gold, tin and bismuth [Hor08, Bro08, Kra23]. An absorber area of $250\,\mu\mathrm{m} \times 250\,\mu\mathrm{m}$ is assumed. Absorber thicknesses d of 5 µm, 8.6 µm and 50 µm for gold, bismuth and tin respectively yield similar absorption efficiencies for

all materials, all of which exceed 98 % at photon energies up to 6 keV. The corresponding specific heat values resulting from such absorbers are marked in figure 4.12 by stars, circles and squares for Au, Bi and Sn, respectively, at the respective temperatures. We can see that the achievable energy resolution for a λ-SQUID with a suitable absorber and sensor material with critical temperature $T_c^\lambda \lessapprox 50\,\mathrm{mK}$ should surpass 400 meV. From these predictions, it is clear that the λ-SQUID as a concept is, from a standpoint of energy resolution, potentially competitive with mature microcalorimeter types such as MMCs or TESs. Moreover, the tunable gain coefficient $\partial V_{\mathrm{SQ}}/\partial T$ makes it rather easy to suppress the dc-SQUID-like noise contribution in a λ-SQUID sufficiently such that the energy resolution is dominated by thermodynamic noise that is intrinsic to all microcalorimeters. In our example here, a bismuth absorber at a temperature of 50 mK already has a much lower heat capacity than the cross-over point at which thermodynamic and dc-SQUID-like noise contribute equally to the energy resolution. Additionally, this cross-over point can easily be pushed further towards higher heat capacities by increasing the input current I_{in}.

It should be mentioned that a λ-SQUID with a bismuth absorber operated at 90 % of 50 mK with a specific heat of $6.12 \times 10^{-14}\,\mathrm{J\,K^{-1}}$ would experience a temperature increase of 2.62 mK (or just above 5 % of T_c^λ) upon absorption of a 1 keV photon. Such a large relative temperature change is expected to yield some nonlinearity, which may potentially be predicted theoretically and compensated for. The maximum dynamic range of this specific setup would be limited to photon energies of 1.9 keV, as the absorption of a higher energy particle would drive the λ-coil into the normal conducting state and the λ-SQUID would (temporarily) cease to function.

From the results presented in figure 4.12, it is immediately clear that we need to use a suitable material for the λ-coil with a critical temperature below $T_c^\lambda < 100\,\mathrm{mK}$ in order to construct a competitive microcalorimeter based on a λ-SQUID. Aluminium, while easy to deposit and integrate into the fabrication process, will not be sufficient.

4.4 λ-SQUIDs with Mo/AuPd bilayer λ-coils

With the need to use sensor materials for the λ-coil with a low critical temperature $T_c^\lambda < 100\,\mathrm{mK}$, the search for suitable candidates began. At IMS, no deposition for a suitable material existed, and it would have to be developed from the ground up. Based on our experiences with elemental aluminium as a sensor material, other elements with suitable critical temperatures such as hafnium (Hf, $T_c = 165\,\mathrm{mK}$), iridium (Ir, $T_c = 140\,\mathrm{mK}$) or tungsten (W, $T_c = 15\,\mathrm{mK}$) seem like a suitable choice. However, the deposition of these elements into thin films with homogeneous, reproducible properties is generally considered challenging [Lit05, Fer09, Hun18]. Considering materials successfully employed in TESs, bilayers of molybdenum and gold [Smi12] or molybdenum and copper [Gol11] offer the advantage of a tunable T_c by changing the thicknesses of the individual layers. In such bilayers, the proximity effect causes diffusion of charge carriers of the normal conducting metal into the superconductor and

vice-versa [Mar00, Fà19]. This results in a decrease of the effective critical temperature of the superconductor, depending on the layer thicknesses and the interface quality. Based on the additional degree of freedom introduced by the designable T_c and the fact that deposition processes for normal metals like Au and an AuPd alloy are already established at IMS, we decided to focus on bilayer (or multilayer) systems as potential sensor materials first.

The development of a reliable, repeatable deposition process for Mo/Au bilayers is, at the time of writing, still ongoing and the object of current research at IMS.

4.4.1 Integration of Mo/AuPd bilayers into the fabrication process

Before our own deposition process is ready and allows for fully in-house production of λ-SQUIDs with sub-100 mK sensor coils, colleagues at the Leibniz IPHT[14] in Jena kindly agreed to deposit some samples for us using their own Mo/AuPd bilayer process [Bou05]. The samples were fabricated at IMS up to the structuring of the sensor layer using a negative-tone resist for lift-off. They were then sent to IPHT for deposition, where sensor layer depositions for two batches of devices was performed. The two depositions differ in the thickness ratios to yield different critical temperatures T_c^λ: One deposition (batch 6 λ-SQUIDs) had a thickness of $t_{Mo} = 80\,nm$ for Mo and $t_{AuPd} = 20\,nm$ for AuPd. From data of IPHT we expect a critical temperature of $T_c^\lambda \approx 300\,mK$. The second deposition (batch 7 λ-SQUIDs) had a thickness of $t_{Mo} = 80\,nm$ for Mo and $t_{AuPd} = 60\,nm$ for AuPd, supposed to yield a critical temperature of $T_c^\lambda \approx 50\,mK$ to $T_c^\lambda \approx 100\,mK$. Such low T_c^λ are not commonly fabricated at IPHT, so the expected critical temperature is based on extrapolated data.

After deposition, the samples were shipped back to IMS, where they were immediately stored within a vacuum desiccator until further processing to prevent oxidation of the Mo/AuPd bilayers. Using test structures deposited simultaneously to the λ-SQUIDs, we first developed a process to fabricate superconducting interconnections between Nb deposited at IMS and the Mo/AuPd bilayers from IPHT. In figure 4.13(a), a micrograph of such a test structure is depicted, which contains a total of 16 interconnects, each with a $4\,\mu m \times 4\,\mu m$ contact area, connected in series. The Au passivation covering the entire structure will be discussed later and serves to prevent oxidation. Various ion-gun cleaning procedures were tested, and we could establish that cleaning times between 3 min and 10 min using the default beam voltage of 275 V and beam current of 20 mA in an argon atmosphere of 0.13 Pa all resulted in superconducting interconnections. This is apparent from the resistance versus temperature curves of the test structures presented in figure 4.13(b).

For the final λ-SQUID samples, a cleaning time of 5 min was used. Since the flanks of the bilayers are bare, oxygen can still access the Mo and cause oxidation. The same is true for any defects in the AuPd layer on top. In an effort to reduce the oxidation

[14] Leibniz-Institut für Photonische Technologien e.V. (IPHT), Albert-Einstein-Str. 9, 07745 Jena, Germany

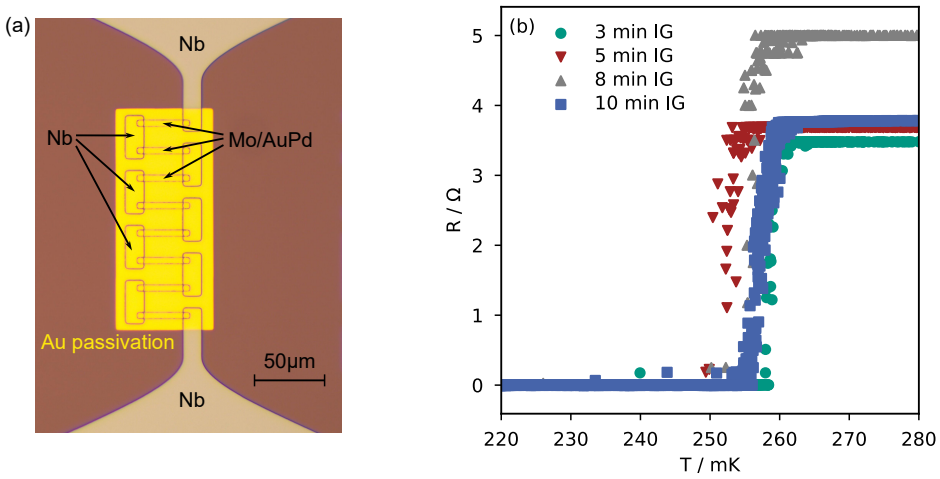


Fig. 4.13: (a) Micrograph of a test structure for Mo/AuP-Nb interconnects. Sixteen interconnects are connected in series, each with a 4 µm × 4 µm contact area. A Au passivation protects the Mo/AuPd from oxidisation. (b) Resistance versus temperature for interconnection test structures using a 80 nm/20 nm thick Mo/AuPd. Curves from devices with identical design but different ion gun (IG) cleaning time are depicted. All four displayed ion gun cleaning procedures yield superconducting connections.

during further processing and the use of the devices, an attempt was made to deposit an additional, 100 nm thick Au layer on top of the Mo/AuPd bilayers. By having this Au layer overlap, the flanks of the bilayers could be protected from oxidation, and defects in the AuPd layer would be covered also. The additional layer mostly contacts the normal-conducting AuPd, and no ion-gun cleaning before deposition was used to keep the interface transparency low. The influence of the Au passivation layer on the critical temperature of the bilayers was thus kept reasonable. From the resistance curves in figure 4.13(b), we can determine a critical temperature of $T_c^\lambda = 250\,\mathrm{mK}$ to $T_c^\lambda = 260\,\mathrm{mK}$ for the 80 nm/20 nm thick Mo/AuPd including passivation, for which IPHT had expected a critical temperature around 300 mK. Especially since a lower T_c^λ is not expected to hinder performance in λ-SQUIDs, we did not consider such a reduction to be problematic.

While the inclusion of a passivation layer was successful in all test structures, no attempt to fabricate them onto similarly dimensioned λ-coils of similar design was without flaws. In the λ-SQUIDs, the Au passivation partially peeled off of the bilayers as if layer adhesion was insufficient, as shown in figure 4.14. It is difficult to judge from these micrographs whether or not only the Au passivation has lifted, or if lower layers have lifted also. It could be feasible that during this process the AuPd layer atop the Mo might have been damaged as well. As we will see later, these λ-SQUIDs still depict a dc-SQUID-like behaviour, so there must be at least some superconducting Mo left to form the loops.

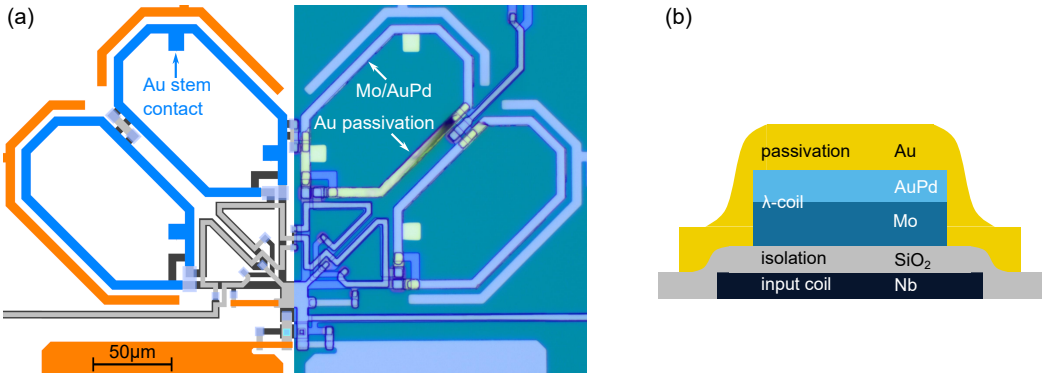


Fig. 4.14: (a) Design (left) and micrograph (right) of a λ-SQUID with a Mo/AuPd λ-coil. The design equals that of the devices discussed in section 4.3, but includes a Au passivation layer (blue in the design) covering the entire λ-coil. Square Au patches at the passivation layer were added to potentially be used as contacts for absorber stems. The Au is easily distinguishable by colour in the micrograph, and it is clearly visible that large sections of it have lifted off of the Mo/AuPd λ-coil and are missing. (b) Cross-sectional view of the intended stack comprising the input coil, the λ-coil and the Au passivation layer.

4.4.2 Temperature-dependent mutual inductance M_{in}

We used the static measurement method described in section 4.2.1 to acquire mutual inductance curves for some of the devices featuring an Mo/AuPd bilayer λ-coil deposited at IPHT. In figure 4.15(a) and (b), the mutual inductance M_{in} is displayed versus temperature for λ-SQUIDs with λ-coils made from 80 nm/20 nm thick Mo/AuPd and 80 nm/60 nm thick Mo/AuPd, respectively. All devices feature the same design and differ only in the thickness of the AuPd-layer in their Mo/AuPd bilayer λ-coils. The increased thickness of the AuPd (60 nm) results in a reduction of the sensor critical temperature T_{c}^{λ}: The dc-SQUID-like voltage modulation used to determine M_{in} in the static method breaks down above 260 mK for devices with 80 nm/20 nm thick Mo/AuPd, but already above 110 mK for devices with 80 nm/60 nm thick Mo/AuPd. More notably however, the all tested devices depict barely any temperature dependence of the mutual inductance M_{in}. While previous prototype devices with an aluminium sensor coil experienced a mutual inductance change on the order of 0.5 %, the largest modulation we have measured on the 80 nm/20 nm Mo/AuPd devices is 0.13 %. The characterised device with 80 nm/60 nm thick Mo/AuPd actually depicts no notable temperature dependence of the mutual inductance M_{in}.

For the devices with 80 nm/20 nm thick Mo/AuPd for their sensor coils, the shape of the mutual inductance curves depicts the expected shape at low temperatures $T \lessapprox 200$ mK, with a gradually increasing upwards slope. We have illustrated this using a guide-to-the-eye based on function 3.13 in figure 4.15(a). Thereafter, however, the mutual inductance curves flatten and eventually saturate or even decrease again. At the time of writing, we can not explain the origin of this deviation from the expected (and

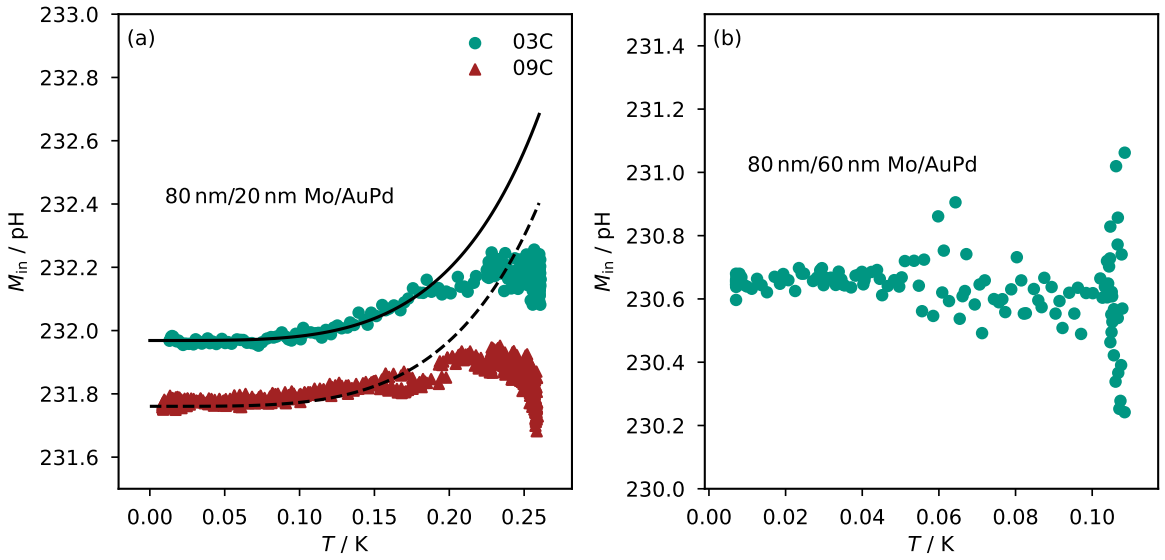


Fig. 4.15: Mutual inductance M_{in} versus temperature for (a) two λ-SQUIDs of the same chip (internal identification 03C and 09C) with 80 nm/20 nm thick Mo/AuPd and (b) a λ-SQUID with 80 nm/60 nm thick Mo/AuPd as sensor material. In (a), a guide-to-the-eye based on equation 3.13 to the data is depicted.

previously measured) behaviour. In section 4.3.1, we have introduced the pseudo-signal in asymmetric λ-SQUIDs due to coupling of the total λ-SQUID inductance to the bias current. While this pseudo-signal may cause such a deviation in the FRM method, the static method we have used here is insensitive to it. The kinetic contribution $L_{\lambda,\mathrm{kin}}$ to the inductance of the λ-coil may become dominating, but should not affect the mutual inductance determined using the static measurement method. From our simulations presented in section 4.3.2, we have seen that both, a very small and very large value of the magnetic penetration depth $\lambda(0)$ of the sensor material will lead to a much weaker thermal change of the mutual inductance. This might indicate that the Mo/AuPd used for the λ-coil here has a very different magnetic penetration depth $\lambda(0)$ compared to the aluminium previously used, and that the geometry of the λ-coil may have to be adjusted accordingly. The geometry of the λ-coil is, however, difficult to model using our numerical methods, since our implementations currently rely on a constant magnetic penetration depth throughout each material. For the Mo/AuPd bilayers this is likely not accurate, as the magnetic penetration depth in superconductor / normal conductor bilayers is highly non-trivial [Sim84]. The proper integration of complex sensor materials such as multilayer sandwiches into our implementation of Chang's and Sheen's numerical methods will be the subject of future work.

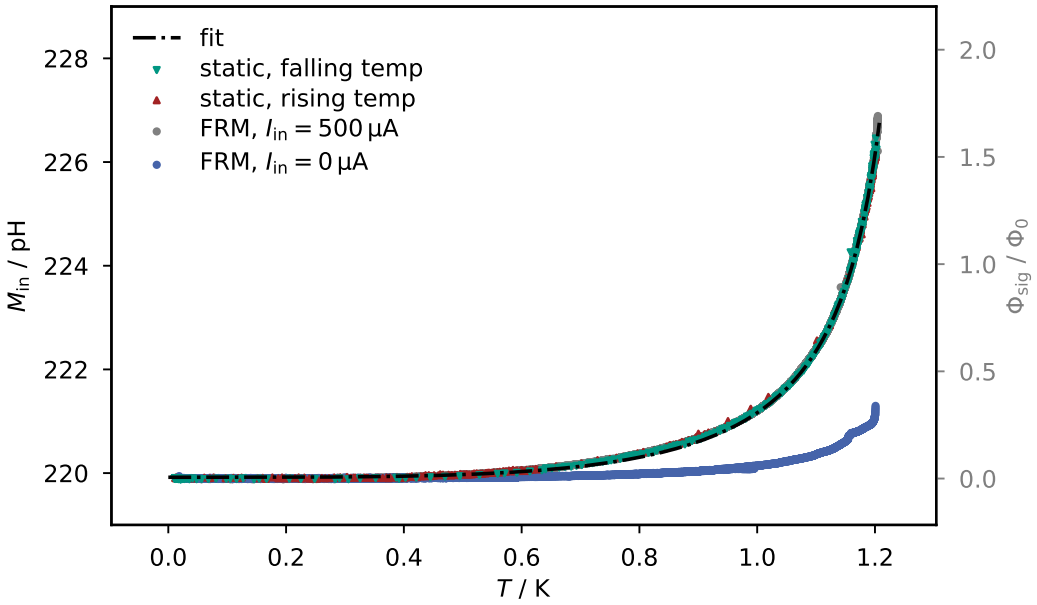


Fig. 4.16: Mutual inductance M_{in} versus temperature for the device with the internal label LSQ_B03_C01_01C. Measurements with the static method at both increasing and falling temperature are shown, as well as a FRM measurement using a constant input current of $I_{in} = 500\,\mu A$. The curves overlap, and are thus difficult to make out individually. To these data, equation 3.13 was fitted. The signal flux Φ_{sig} (right y-axis, grey) acquired during an FRM measurement with no input current $I_{in} = 0\,\mu A$ is depicted for reference.

4.5 Unexplained excess sensitivity in a singular λ-SQUID prototype

Within this thesis, we have fabricated a number of λ-SQUID prototypes using aluminium as a sensor material. The majority of characterised devices behaved like the λ-SQUID we have discussed in detail in section 4.3. We have seen in subsection 4.3.2 that we can reliably model and predict the temperature-dependent mutual inductance $M_{in}(T)$ of these devices. There are, however, still many things left for us to learn.

One curious example is the device with the internal label LSQ_B03_C01_01C, which features the exact same design with identical input- and λ-coil geometry as the λ-SQUID presented in section 4.3. The input coil is made from niobium while the λ-coil is made from aluminium. All layers where deposited in the same sputter systems using the same process parameters, and thus we would expect it to depict very similar mutual inductance curves as presented in section 4.3.

The mutual inductance curves for this device are plotted in figure 4.16. Interestingly, from the static measurements and the FRM data with an input current of $I_{in} = 500\,\mu A$, we can see that over the measured temperature range the mutual inductance is in-

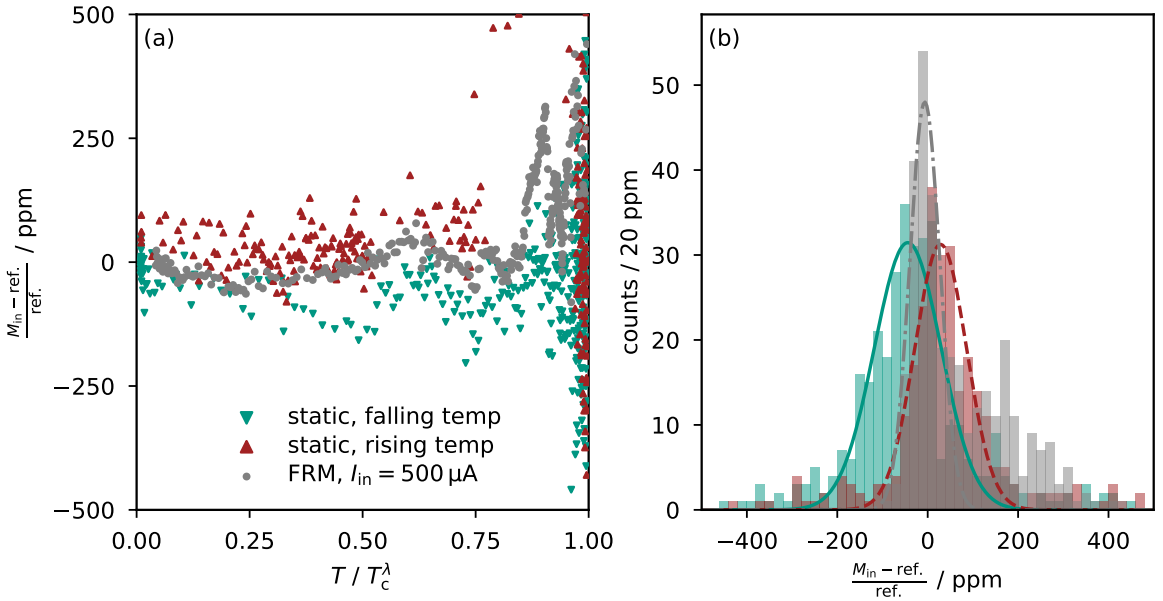


Fig. 4.17: Deviation of static measurements at rising and falling temperature and the FRM measurement at an $I_{in} = 500\,\mu A$ input current from a single, common reference curve, (a) versus temperature and (b) in a histogram representation. Fits of a Gaussian to the histrograms are shown as well. Deviations between all curves are mostly below 250 ppm. For the static measurement with rising temperature (red △), some uncommonly large deviation above 75 % of T_c^{λ} is present due to rapid changes in cryostat temperature.

creased by roughly 3 %, from 220 pH at base temperature to about 227 pH just below the transition. This marks a six-fold increase in temperature-induced mutual inductance shift compared to typical devices as presented in section 4.3. Using Chang's numerical method, we could not find any parameter set that resulted in such a significant mutual inductance modulation. We have not observed a response of a similar magnitude on any other device we have characterised, and do not currently understand where this comes from. A measurement error however seems unlikely, since mutual inductance curves acquired using both the static and FRM method overlap almost perfectly. It is fairly unlikely that independent measurement errors in both methods would lead to false but perfectly congruent results.

To study the influence of the quasi-signal, we have performed an additional FRM measurement without any applied input current $I_{in} = 0\,\mu A$ (blue curve in figure 4.16) on this device. All remaining signal flux Φ_{sig} (right-hand side y-axis) therefore has to result from internal currents in the λ-SQUID loop, or from some external source. Since the input current is zero, we can not calculate a corresponding mutual inductance in this specific case, so we have added a flux signal axis on the right of figure 4.16. As mentioned in section 4.3, the sign of the pseudo-signal relative to the intended signal depends on the sign of the bias- and input currents. Relative to the other measure-

ments presented in figure 4.16, we can see that here the pseudo-signal has a positive sign. However, the pseudo-signal is considerably smaller than the actual signal. We can therefore not identify any uncommonly large background signal, caused either by coupling of the bias current I_b to the total λ-SQUID inductance or any other source, that we might have falsely attributed to an uncommonly large mutual inductance response. We have also performed a statistical analysis of the mutual inductance curves measured on this device as presented in figure 4.17. Again, we can see little to no statistically relevant deviation between curves, as the outliers of the static measurement with rising temperature (△, red) above 75 % of T_c^λ can again be attributed to sudden temperature jumps of the cryostat. Except for the unusually strong temperature dependence of the mutual inductance, the device with internal label LSQ_B03_C01_01C therefore behaves exactly as expected.

Naturally, we would like to understand why this device depicts such a strong modulation. For the application in microcalorimeters it would be a huge benefit if we could reproduce a modulation this strong reliably, since the sensitivity of the device would be increased. Further study of this effect is the subject of future work.

5. Design considerations to optimise λ-SQUIDs

As the central sensing element, the λ-coil has an enormous influence on the performance of a λ-SQUID. Naturally, we want to understand what factors into the sensitivity and noise performance, and ultimately identify an optimal λ-coil design that maximises both. With the theory and numerical simulation tools discussed in chapter 3, we will now set out to first analyse the macroscopic layout (total inductance and volume) and later the microscopic design (specific transmission line geometry).

5.1 Generalised description of the λ-coil

Assuming a readout chain in which the noise of subsequent amplifiers do not affect the noise performance of the λ-SQUID, e.g. by using an N-dc-SQUID series array as a cryogenic amplifier, the energy resolution ΔE_{FWHM} of a λ-SQUID is set by two noise contributions. These are the thermodynamic energy fluctuations $S_{\mathrm{E,TD}}$ caused by random energy fluctuations among the absorber, sensor and heat bath, and the dc-SQUID-like noise contribution $S_{\mathrm{E,SQ}}$ from the λ-SQUID itself. In the following, we will derive the conditions for the λ-coil which minimise the λ-SQUID noise contribution $S_{\mathrm{E,SQ}}$.

For this derivation, we will assume a generalised λ-SQUID as schematically depicted in figure 5.1. For simplicity, the flux bias coil is neglected as it does not affect the sensitivity of the λ-SQUID. We consider that the λ-coil can be divided into small, identical unit elements, each with inductance $\tilde{L}$ and volume $\tilde{V}$. The λ-coil comprises N parallel rows of M unit elements in series each, resulting in $N \times M$ unit elements in total. Each unit element couples to a segment of the input coil with inductance $\tilde{L}_{\mathrm{in}}$ via a mutual inductance $\tilde{M}_{\mathrm{in}} = \kappa\sqrt{\tilde{L}\tilde{L}_{\mathrm{in}}}$. Here, κ is the geometric coupling factor. As a result, we can find the following relations for the total loop inductance L, the total volume V of the λ-coil, and the combined mutual inductance M_{in} between the λ-SQUID and the input coil:

$$L = \frac{K}{N}\tilde{L} = \nu\tilde{L}, \tag{5.1}$$

$$V = KN\tilde{V} = \mu\tilde{V}, \tag{5.2}$$

$$M_{\mathrm{in}} = K\tilde{M}_{\mathrm{in}} = \sqrt{\nu\mu}\tilde{M}_{\mathrm{in}}. \tag{5.3}$$

With only two free parameters (K and N), we see immediately that we can not choose all three quantities independently. To quantify the remaining degrees of freedom, we have introduced the parameters $\nu = K/N$ and $\mu = KN$ that define a specific layout

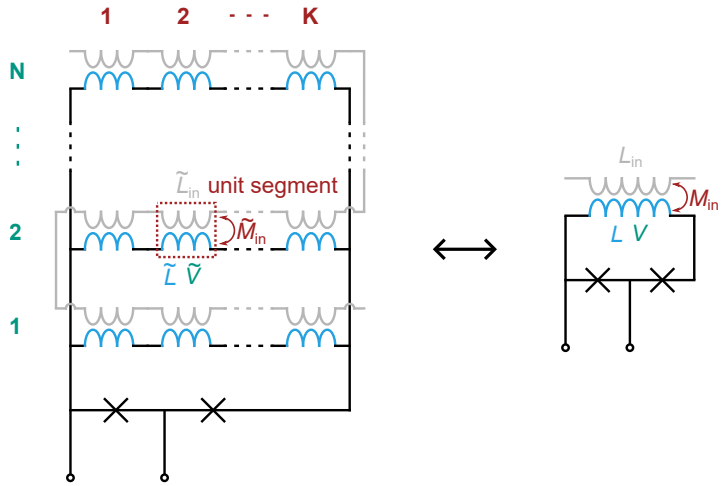


Fig. 5.1: Schematic circuit diagram of a generalised λ-SQUID. The SQUID loop consists of N identical segments connected in parallel, with each segment itself comprising K unit elements connected in series. One such unit element is framed in red. Each unit element has an inductance $\tilde{L}$ and volume $\tilde{V}$, and couples to a unit of input loop with inductance $\tilde{L}_{\mathrm{in}}$ with a mutual inductance $\tilde{M}_{\mathrm{in}}$. The total arrangement is equivalent to a single effective λ-coil with inductance L, volume V and mutual inductance M_{in} to an input coil with inductance L_{in}.

of the λ-coil. Relation 5.3 results from the usual definition of the mutual inductance as $M_{\mathrm{in}} = \kappa\sqrt{L L_{\mathrm{in}}}$, where we can use $L_{\mathrm{in}} = KN\tilde{L}_{\mathrm{in}} = \mu\tilde{L}_{\mathrm{in}}$ since all segments of the input coil are connected in series. We can use the geometry parameters ν and μ to express other relevant parameters: First, we assume that our λ-SQUID is optimised in terms of noise performance, i.e. the SQUID screening parameter is $\beta_{\mathrm{L}} = 1$ and the Stewart-McCumber parameter of the Josephson junctions is $\beta_{\mathrm{C}} = 1$ [Tes77]. Moreover, assuming an established fabrication process for Josephson junctions, the critical current is set by the junction area A_{jj} and the critical current density j_{c} via $I_{\mathrm{c}} = A_{\mathrm{jj}} j_{\mathrm{c}}$. The junction capacitance consequently is $C_{\mathrm{jj}} = A_{\mathrm{jj}} c^{\star}_{\mathrm{jj}} = I_{\mathrm{c}} c^{\star}_{\mathrm{jj}} / j_{\mathrm{c}}$, where $c^{\star}_{\mathrm{jj}}$ is the process-specific junction capacitance per unit area. From the conditions $\beta_{\mathrm{L}}, \beta_{\mathrm{C}} = 1$ we conclude:

$$I_{\mathrm{c}} = \left[\frac{\Phi_0}{2\tilde{L}}\right]\frac{1}{\nu}, \tag{5.4}$$

$$R = \left[\sqrt{\frac{2 j_{\mathrm{c}}}{\pi \Phi_0 c^{\star}_{\mathrm{jj}}}}\,\tilde{L}\right]\nu. \tag{5.5}$$

In both expressions, the term in brackets is independent of the specific design of the λ-SQUID, and depends only on fabrication parameters and the design of a unit element of the λ-coil. Softening the conditions $\beta_{\mathrm{L}}, \beta_{\mathrm{C}} = 1$ to allow for any other, fixed values introduces an additional layout-independent factor, and does not affect the dependence of I_{c} and R on the geometric parameters ν and μ.

The noise contribution $S_{\mathrm{E,SQ}}$ caused by the λ-SQUID, expressed in fluctuations of the energy content, is given by the expression 3.3

$$S_{\mathrm{E,SQ}} = S_{\Phi} \left(\frac{\partial \Phi}{\partial T} \frac{\partial T}{\partial E} \right)^{-2}. \tag{5.6}$$

Here, S_{Φ} denotes the magnetic flux noise of the SQUID. Moreover, $\partial\Phi/\partial T$ and $\partial T/\partial E = 1/C_{\mathrm{tot}}$ are the temperature-to-flux transfer coefficient of the λ-SQUID (see chapter 3) and the inverse total heat capacity of the detector, respectively. For an optimised dc-SQUID, the flux noise can be approximated by $S_{\Phi} \approx 18 k_{\mathrm{B}} T L^2/R$ at the operating temperature T [Che04]. The total heat capacity of the detector comprises both, the absorber and the λ-coil, i.e. $C_{\mathrm{tot}} = C_{\mathrm{abs}} + \mu \tilde{V} c$, with c the specific heat per unit volume of the sensor material comprising the λ-coil. The temperature-to-flux transfer coefficient $\partial\Phi/\partial T$ of the λ-SQUID is given by

$$\frac{\partial \Phi}{\partial T} = I_{\mathrm{in}} \frac{\partial M_{\mathrm{in}}}{\partial T} = \left[I_{\mathrm{in}} \frac{\partial \tilde{M}_{\mathrm{in}}}{\partial T} \right] \sqrt{\mu \nu}, \tag{5.7}$$

where, again, the term in brackets does not depend on the design of the λ-coil as a whole, but rather on the unit element. Using equations 5.4 and 5.5, we obtain the following expression for the noise contribution

$$S_{\mathrm{E,SQ}} = 18 k_{\mathrm{B}} T \sqrt{\frac{\pi \Phi_0 c_{\mathrm{jj}}^{\star}}{2 j_{\mathrm{c}}}} \tilde{L} \nu \left(\left[I_{\mathrm{in}} \frac{\partial \tilde{M}_{\mathrm{in}}}{\partial T} \right] \sqrt{\mu \nu} \frac{1}{C_{\mathrm{abs}} + \mu \tilde{V} c} \right)^{-2} \tag{5.8}$$

$$= \left[18 k_{\mathrm{B}} T \sqrt{\frac{\pi \Phi_0 c_{\mathrm{jj}}^{\star}}{2 j_{\mathrm{c}}}} \frac{\tilde{L}}{I_{\mathrm{in}}^2 \left(\frac{\partial \tilde{M}_{\mathrm{in}}}{\partial T} \right)^2} \right] \frac{\left(C_{\mathrm{abs}} + \mu \tilde{V} c \right)^2}{\mu} = \eta g(\mu). \tag{5.9}$$

Here, we have introduced the substitutions

$$\eta = \left[18 k_{\mathrm{B}} T \sqrt{\frac{\pi \Phi_0 c_{\mathrm{jj}}^{\star}}{2 j_{\mathrm{c}}}} \frac{\tilde{L}}{I_{\mathrm{in}}^2 \left(\frac{\partial \tilde{M}_{\mathrm{in}}}{\partial T} \right)^2} \right] \quad \text{and} \tag{5.10}$$

$$g(\mu) = \frac{\left(C_{\mathrm{abs}} + \mu \tilde{V} c \right)^2}{\mu}. \tag{5.11}$$

We see that $S_{\mathrm{E,SQ}}$ neatly separates into a term η which depends only on the unit element, but is independent of the specific layout of the λ-coil, and a function $g(\mu)$, which contains the dependence of the λ-SQUID noise $S_{\mathrm{E,SQ}}$ on the arrangement of unit elements that comprises the λ-coil. It is interesting to note that only the parameter μ appears, and that the parameter ν has dropped out. This can easily be understood as follows: An increase in ν causes a proportional increase in total inductance L and a

rise of $M_{\mathrm{in}} \propto \sqrt{\nu}$. While the latter results in an increase of detector signal, the former negatively affects the flux noise. Ultimately, the signal-to-noise ratio of the λ-SQUID remains unaltered by a change of the inductance L by varying the parameter ν as introduced above. This is a crucial result, as it allows us to set the inductance L of a λ-SQUID with respect to other boundary conditions (e.g. screening parameter or geometric constraints), which makes the design of an optimised device considerably less demanding.

To minimise the noise level $S_{\mathrm{E,SQ}}$, we only have to consider the design parameter μ. Since the prefactor η has no influence on this optimisation, we restrict our efforts to the function $g(\mu)$ and find

$$\frac{\partial g(\mu)}{\partial \mu} = \frac{2\left(C_{\mathrm{abs}} + \mu\tilde{V}c\right)c\tilde{V}}{\mu} - \frac{\left(C_{\mathrm{abs}} + \mu\tilde{V}c\right)^2}{\mu^2} \tag{5.12}$$

$$\frac{\partial^2 g(\mu)}{\partial \mu^2} = \frac{2\left(c\tilde{V}\right)^2}{\mu} - \frac{4\left(C_{\mathrm{abs}} + \mu\tilde{V}c\right)c\tilde{V}}{\mu^2} + \frac{2\left(C_{\mathrm{abs}} + \mu\tilde{V}c\right)^2}{\mu^3} \tag{5.13}$$

for its first and second derivatives, respectively. In this way, we find that the function $g(\mu)$, and thus the λ-SQUID energy noise contribution $S_{\mathrm{E,SQ}}$, has a minimum if the condition $\mu = \mu_{\mathrm{opt}}$ is satisfied, with

$$\mu_{\mathrm{opt}} c\tilde{V} = C_{\mathrm{sens}} = C_{\mathrm{abs}}. \tag{5.14}$$

Thus, we can conclude that the layout of the λ-coil should be chosen such that the total heat capacity of the λ-coil equals the absorber heat capacity, i.e. $C_{\mathrm{sens}} = C_{\mathrm{abs}}$. This resembles a well-known result for cryogenic microcalorimeters [McC05].

From this exercise we can draw two conclusions about the design of λ-SQUIDs. Firstly, the total inductance L of the entire loop does not affect the effective energy noise $S_{\mathrm{E,SQ}}$ of the device. Secondly, the total volume of the λ-coil should be chosen such that the heat capacity of the sensing element equals that of the absorber $C_{\mathrm{sens}} = C_{\mathrm{abs}}$ at the operating temperature. This suggests that we first dimension the absorber according to the intended application. The resulting specific heat C_{abs} then fixes the total volume $V_{\mathrm{sen}} = C_{\mathrm{abs}}/c$ of the sensing element. As the total inductance L is not relevant, we can distribute this volume into any number of identical, parallel loop segments (washers) as desired. This gives us a lot of freedom regarding the design of the λ-SQUID.

At this stage, however, it makes sense to consider the design of the unit elements. Using our optimisation condition, we can rewrite equation 5.8 as

$$S_{\mathrm{E,SQ}} = \left[72 k_{\mathrm{B}} T \sqrt{\frac{\pi \Phi_0 c_{\mathrm{jj}}^{\star}}{2 j_{\mathrm{c}}}} \frac{L_{\mathrm{w}} C_{\mathrm{w}}}{I_{\mathrm{in}}^2 \left(\frac{\partial M_{\mathrm{in,w}}}{\partial T}\right)^2}\right] C_{\mathrm{abs}} \tag{5.15}$$

Here we have introduced the washer inductance $L_\mathrm{w} = M\tilde{L}$, washer coupling $M_\mathrm{in,w} = M\tilde{M}_\mathrm{in}$, and washer heat capacity $C_\mathrm{w} = cM\tilde{V}$, which describe the parameters of each of the N parallel loop segments. This is convenient since these quantities are more tangible for a physical realisation than the unit segment parameters introduced before. It is clearly apparent that, still assuming a fixed Josephson junction fabrication process, the noise contribution $S_\mathrm{E,SQ}$ is minimised if the ratio

$$\zeta_\mathrm{w} = \frac{L_\mathrm{w} C_\mathrm{w}}{\left(\frac{\partial M_\mathrm{in,w}}{\partial T}\right)^2} \tag{5.16}$$

is as small as possible. We can thus use the ratio ζ_w as a figure of merit (FOM) to characterise a specific implementation of the λ-SQUID washer design. It becomes clear that the mutual inductance of the washer should be maximised for a given inductance and volume. Since $M_\mathrm{in} = \kappa\sqrt{LL_\mathrm{in}}$, maximising the geometric coupling κ is a natural way to improve performance. Most designs already achieve nearly optimal values of $\kappa \lessapprox 1$, however, leaving little room for further improvements. Likewise, the need to maximise the mutual inductance for a given volume can be understood intuitively, since it maximises the retrieved flux signal per unit volume. It is relevant to note that we can also express the FOM ζ_w using the (mutual) inductance and specific heat per unit length, assuming the λ-SQUID washer has a constant cross-section for its entire length. Using the quantities normalised to length is convenient when using the simulation methods introduced in section 3.2.

To conclude, it may be worth mentioning that we can see from equation 5.15, that the absolute noise $S_\mathrm{E,SQ}$ is minimised with respect to the junction fabrication process if the ratio $c^\star_\mathrm{jj}/j_\mathrm{c}$ is minimised. This can, for example, be realised by using cross-type Josephson junctions [Bau22] as currently under development at the IMS.

5.2 λ-coils with a stripline geometry

Following the rather abstracted considerations of the macroscopic λ-coil layout in the previous section, we will now use the numerical models presented in section 3.2.2 to identify criteria for optimising the microscopic design of the λ-coil / input coil combination. In the previous section, an abstract unit segment was introduced. In the limit of reducing this segment further and further, we naturally arrive at considering the design properties (i.e. (mutual) inductances and volume) per unit length. This ties in very well with Chang's numerical simulation method introduced in section 3.2.2, which returns the (mutual) inductances per unit length for a given cross-section through a system of infinitely long conductors.

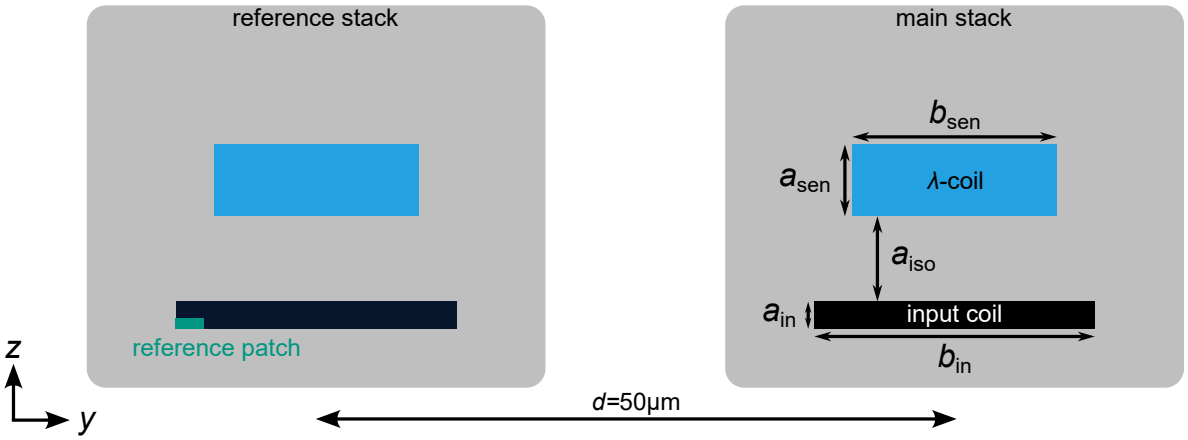


Fig. 5.2: Schematic cross-sectional view of the λ-coil (blue) and input coil (black) in a stripline geometry. Thickness and width of the λ-coil and input coil are a_{sen}, b_{sen}, a_{in} and b_{in}, respectively. Both conductors are separated by an isolation layer with thickness a_{iso}. To ensure zero total currents, a reference stack of conductors with identical geometry and inverted currents is placed at a distance $d = 50\,\mu\mathrm{m}$ from the main stack. The reference stack also contains the reference patch. For analysis, only the inductance matrix elements of the main stack are used. Currents flow in the x-direction, i.e. into (or out of) the page.

We can rewrite the FOM introduced in the previous section utilising the derivative of the fit function 3.17, and by normalising the (mutual) inductance and volume by a unit length:

$$\zeta = \frac{L^* A}{\left(M^*_{\mathrm{in}}(0)\, a\right)^2} (T_{\mathrm{c}})^2 \frac{\left(1-\tilde{t}^4\right)^4}{16\tilde{t}^6}. \tag{5.17}$$

Here, L^* is the λ-coil inductance per unit length, and $M^*_{\mathrm{in}}(0)$ is mutual inductance per unit length between the λ-coil and the input coil. The unitless sensitivity factor a describes how strongly the mutual inductance changes with temperature. We have deliberately dropped the specific heat c per unit volume of the λ-coil material, which is a material property without any dependence on geometry. It does thus not affect any of the following considerations. Furthermore, for a rectangular conductor, the volume per unit length is simply its cross-sectional area A. Using our implementation of Chang's numerical method, we can easily perform a run of simulations, and extract L^* and $M^*_{\mathrm{in}}(T)$ from the resulting inductance matrices. From a fit of function 3.17 to the latter, we can determine the fit parameters $M^*_{\mathrm{in}}(0)$, a and T_{c}. Using the known geometry of the conductors, we can then compute the FOM ζ. We thus have a way to predict the FOM ζ for any desired stripline geometry, and can employ it to search for geometries that minimise it. We deliberately leave the critical temperature T_{c} as a free fit parameter despite it being defined in the simulation, as the quality of the fits

is significantly improved. While this makes the evaluation of the simulated data more accurate, it means that we can not simply "drop" T_c from our FOM in equation 5.17. The value of T_c retrieved from the fit is generally a few percent larger than the value T_c^λ defined for the λ-coil in the simulations. As the derivative $\partial M_{in}/\partial T$ is temperature dependent, we need to agree on a value to perform this analysis. Here, we will derive the FOM for an operating temperature of $T_0 = 0.9T_c^\lambda$, which equals the example value we have used in the discussion potential noise performance in section 4.3.3. As long as the same operating temperature is used throughout, its specific value should have little effect on the conclusions we draw.

In this section, we will focus on simple stripline geometries as depicted in figure 5.2. Here, the entire geometric parameter space comprises the widths b_{sen}, b_{in} and thicknesses a_{sen}, a_{in} of the λ-coil and input coil, respectively, as well as the thickness a_{iso} of the isolation layer separating them. We will consider more complex arrangements in the next section, but even for this simple geometry a total of 5 parameters exist. Ideally one would optimise the entire parameter space simultaneously. This however would require a significant amount of computing time, and may be the topic of future work. Instead, we will focus on some of these parameters individually. This will already provide some useful insights into the effects of geometry on device sensitivity.

By the nature of Chang's numerical method, the total sum of all currents within the conductor system must vanish. As explained in section 3.2.4, we introduce a copy ("reference stack") of our original conductor system ("main stack"), with inverted currents placed a distance $d = 50\,\mu m$ from the main stack. This guarantees vanishing total currents and is reminiscent of the loop geometry of our test devices, where the loop diameter ($d = 68\,\mu m$) is of a similar magnitude. Finally, we will use the inductance matrix elements of the main stack for further analysis.

5.2.1 Variation of the sensor coil width

In order to verify our simulation software as described in section 3.2.2, and in order to investigate the influence of the λ-coil geometry on device performance, we have designed and fabricated prototype λ-SQUIDs with various widths of the λ-coil. Figures 5.3(a) to (c) show micrographs of such test devices. For the most part the devices again resemble the ones discussed previously in section 4.3. Similarly, their λ-coils are also made from Al. The design was modified slightly to allow for an input coil with a width of $b_{in} = 18\,\mu m$, on top of which a λ-coil of varying width could be placed. Devices with a λ-coil width of $b_{sen} = 2\,\mu m$, $b_{sen} = 8\,\mu m$, and $b_{sen} = 17.5\,\mu m$ were characterised using the static method. Using the geometry of these λ-SQUIDs, we have used our simulation software to compute the expected mutual inductance curves for the measured geometries. Here, we assumed magnetic penetrations depths of $\lambda_{in} = 50\,nm$ and $\lambda_{sen} = 80\,nm$ for input- and λ-coil, respectively. We found these values to best describe experimental data in section 4.3.2.

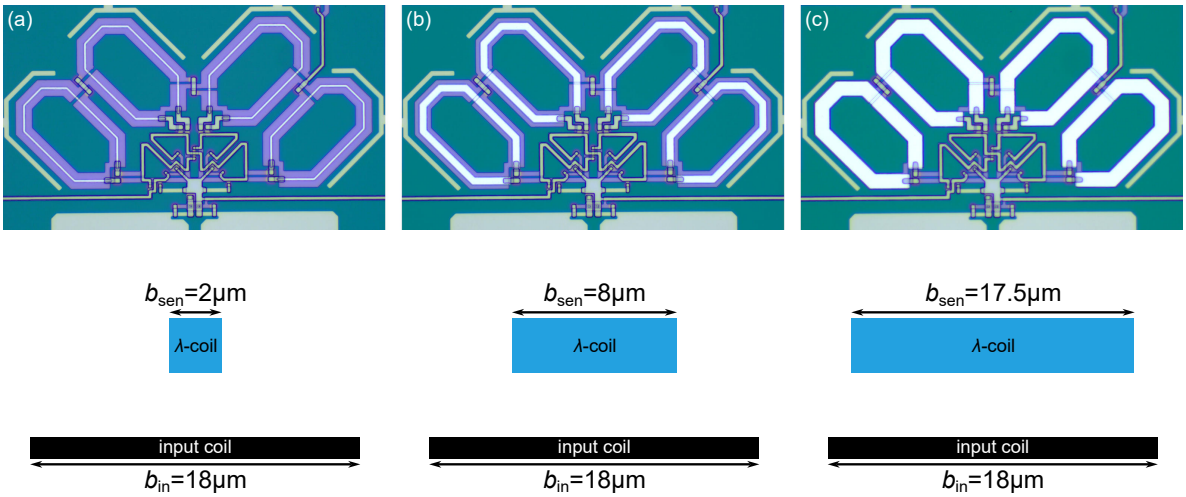


Fig. 5.3: Micrographs of three exemplary prototype devices with different λ-coil widths. The different widths, i.e. (a) $b_{sen} = 2\,\mu m$, (b) $b_{sen} = 8\,\mu m$, (c) $b_{sen} = 17.5\,\mu m$, of the Al λ-coils are easily discernible, while the input coil width is $b_{in} = 18\,\mu m$ for all devices. The cross-section through input- and λ-coil is depicted schematically below the micrographs.

Both, the experimental data and the simulation results, are graphically depicted in figures 5.4(a) to (c). To match simulation data and experimental data, we again had to multiply the mutual inductance per unit length returned by the numerical method by a length. As explained in section 4.3.2, this length is expected to equal half the loop circumference of one of the λ-SQUID washers. For the devices discussed here, the loop circumference determined by comparing simulated and experimental data was $l_{loop}/2 = 157.4\,\mu m$, $l_{loop}/2 = 157.1\,\mu m$ and $l_{loop}/2 = 156.9\,\mu m$ for the devices with $b_{sen} = 2\,\mu m$, $b_{sen} = 8\,\mu m$ and $b_{sen} = 17.5\,\mu m$ λ-coil width, respectively. This agrees very well with the design value of 312 µm, which neglects edge effects and the influence of bends. In general, we observe an excellent agreement between simulated and measured data. The mutual inductance curves agree in both direction of the inductance modulation (negative for the lower λ-coil widths, positive for $b_{sen} = 17.5\,\mu m$) and the magnitude of the temperature dependence. However, there are some notable differences between simulated and experimental data. With the devices featuring a $b_{sen} = 2\,\mu m$ and $b_{sen} = 8\,\mu m$ λ-coil width, at temperatures very close to the critical temperature T_c^λ the mutual inductance depicts an increase, even though the curves are decreasing for a vast majority of the temperature range. This inversion of the curve near T_c^λ is similar (albeit with different sign) to the sudden decrease near T_c^λ we have observed on our samples using a Mo/AuPd λ-coil (see section 4.4), and may potentially have the same origin. As explained above, the static measurement method is insensitive to the pseudo-signal induced by the bias current I_b coupling to the total λ-SQUID inductance, so the diverging kinetic inductance of the λ-coil is not a feasible explanation. The kinetic contribution $L_{\lambda,kin}$ of the λ-coil inductance will furthermore affect the screening currents within the λ-SQUID, but since these depend periodically on the external flux

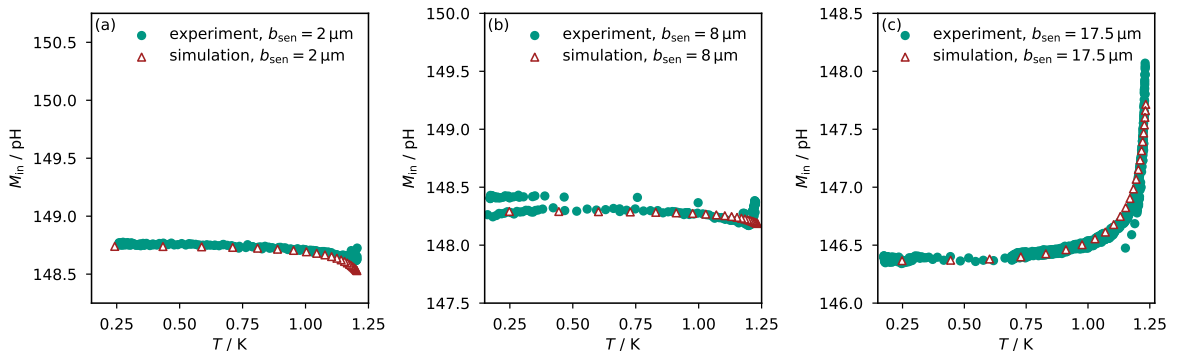


Fig. 5.4: Mutual inductance versus temperature for three exemplary test devices with different λ-coil widths (a) $b_{sen} = 2\,\mu m$, (b) $b_{sen} = 8\,\mu m$, (c) $b_{sen} = 17.5\,\mu m$. We show experimental data (green) measured using the static method as well as simulated data (red) of the respective geometry using Chang's method.

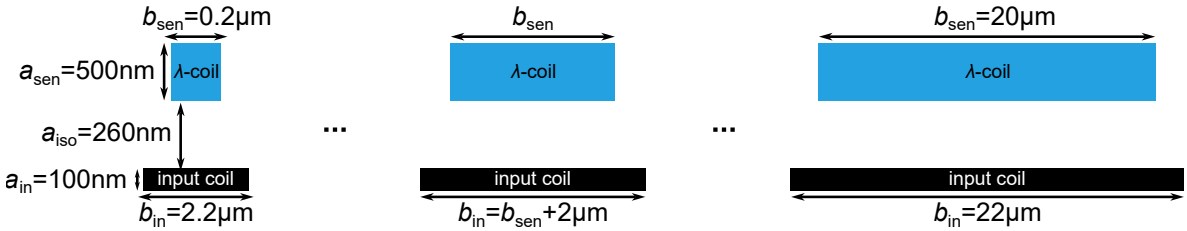


Fig. 5.5: Schematic cross-section illustrating the variation of the sensor coil width b_{sen}. To avoid overlapping edges, we ensured that the input coild width $b_{in} = b_{sen} + 2\,\mu m$ exceeds that of the λ-coil at all times.

they would only affect the shape of the voltage modulation, not its period length from which M_{in} is determined. Curiously, such an inversion is either not present in the device with a $b_{sen} = 17.5\,\mu m$ λ-coil width, or sufficiently small to not be visible. This behaviour was likewise not observed on our previous devices with aluminium λ-coils (see section 4.3). Nonetheless, over a large fraction of the relevant temperature range, the agreement between experiment and simulation is excellent. This experiment serves as another indication that our numerical simulation tools for the mutual inductance determination can predict and describe the experimentally observed behaviour with some confidence, at least with aluminium as the sensor material.

We can conclude that this data suggests that it seems beneficial to match the width of input coil and λ-coil, at least for the range of widths considered here. We will keep this result in mind and consider varying both, the widths of input- and λ-coil simultaneously in the next section.

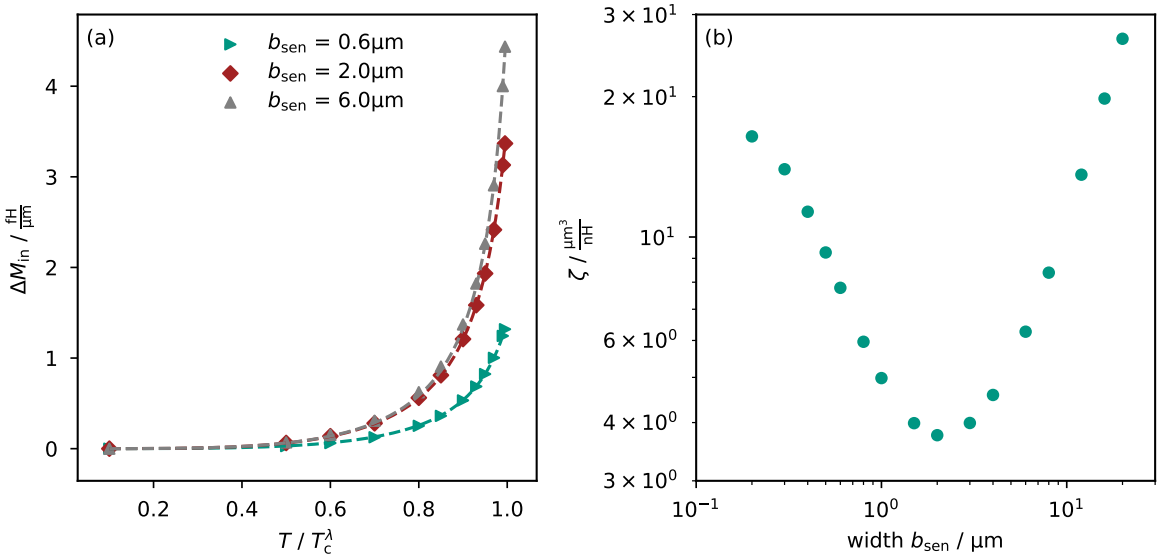


Fig. 5.6: (a) Simulated mutual inductance shift ΔM_{in} versus temperature for three example sensor widths. The dashed lines depict a fit of equation 3.13, from which the parameters $M_{in}^*(0)$ and a can be extracted. (b) FOM ζ versus the sensor width b_{sen}. A minimum around $b_{sen} \approx 2\,\mu m$ is apparent.

5.2.2 Variation of sensor- and input coil width

We have seen in the previous section that the width of the λ-coil should not be too different from the input coil. In this section, we will investigate the absolute dimensions by varying the width of both coils simultaneously, while keeping them similar. We have used our implementation of Chang's method to model a stripline geometry as depicted in figure 5.5. The sensor- and input coil thickness are $a_{sen} = 500\,nm$ and $a_{in} = 100\,nm$, respectively. Both are separated by a $a_{iso} = 260\,nm$ thick isolation layer. These dimensions are inspired by the those used for our test devices presented in chapter 4, where the λ-coil is placed on top of the input coil. To prevent overlap at the edges of the lower stripline, we have assumed that for any sensor coil width b_{sen}, the input coil width must be a little wider, i.e. $b_{in} = b_{sen} + 2\,\mu m$. This accounts, with some margin, for the alignment accuracy of the equipment available at IMS.

We have simulated the mutual inductance curves for a variety of 11 different λ-coil widths ranging from 100 nm up to 20 µm. The results are displayed in figure 5.6(a). For clarity, only three of the 11 curves are depicted. We have numerically fitted equation 3.13 to each dataset to extract the fit parameters $M_{in}^*(0)$, T_c and a required to derive the FOM ζ. For each sensor width, the resulting FOM ζ is plotted in figure 5.6(b).

It is immediately apparent that an optimal λ-coil width exists: The FOM ζ reaches a clear minimum around a width of $b_{sen} \approx 2\,\mu m$. It is easy to understand this relation intuitively: If the sensor width b_{sen} is extremely large, the currents will be concentrated mostly at the edges. Even if the magnetic penetration depth increases, the CDD will

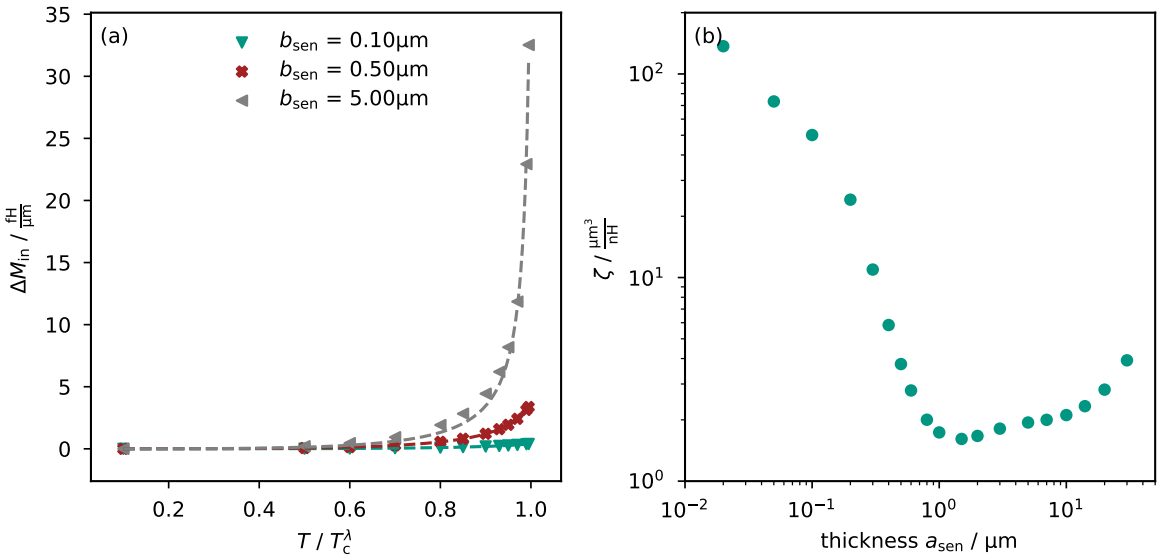


Fig. 5.7: (a) Simulated mutual inductance shift ΔM_{in} versus temperature for three example thicknesses of the λ-coil. The dashed lines depict a fit of equation 3.13, from which the parameters $M_{in}^*(0)$ and a can be extracted. (b) FOM ζ versus the λ-coil thickness a_{sen}. A broad minimum around a thickness of a few µm is observable.

not become significantly more homogeneous on the scale of the entire width. Thus, temperature only has a minor effect on the mutual inductance M_{in}, sensitivity is low and the FOM ζ is large. On the other hand, if the sensor width b_{sen} is very small, the CDD is already homogeneous even at very low temperatures. An increase in the magnetic penetration depth will affect neither the CDD nor the mutual inductance M_{in}. Again this results in a large value of the FOM ζ. It is therefore expected that an optimal value for the width b_{sen} of the λ-coil exists. For the geometry assumed here and a magnetic penetration depth of $\lambda(0) = 80\,nm$ of the sensor material, this optimum is at roughly $b_{sen} \approx 2\,\mu m$, but the value would likely change for a different sensor material.

5.2.3 Variation of the sensor coil thickness

Using the results from the previous section, we will now discuss the influence of the thickness a_{sen} of the λ-coil on sensitivity. We will assume a λ-coil and an input coil width of $b_{sen} = 2\,\mu m$ and $b_{in} = 4\,\mu m$, respectively. We found this width to yield the lowest FOM in the previous section. We keep the input coil and isolation thickness at $a_{in} = 100\,nm$ and $a_{iso} = 260\,nm$, respectively.

We have calculated mutual inductance curves for 19 thicknesses in the range from 20 nm to 30 µm. Three of these curves are depicted in figure 5.7(a). Again, we have fitted equation 3.13 to each curve for further analysis and computed the FOM ζ for each value of the thickness a_{sen}. The results are summarised in figure 5.7(b). As the sensor thickness increases, the FOM ζ is, at first, strongly reduced. Naturally, a change

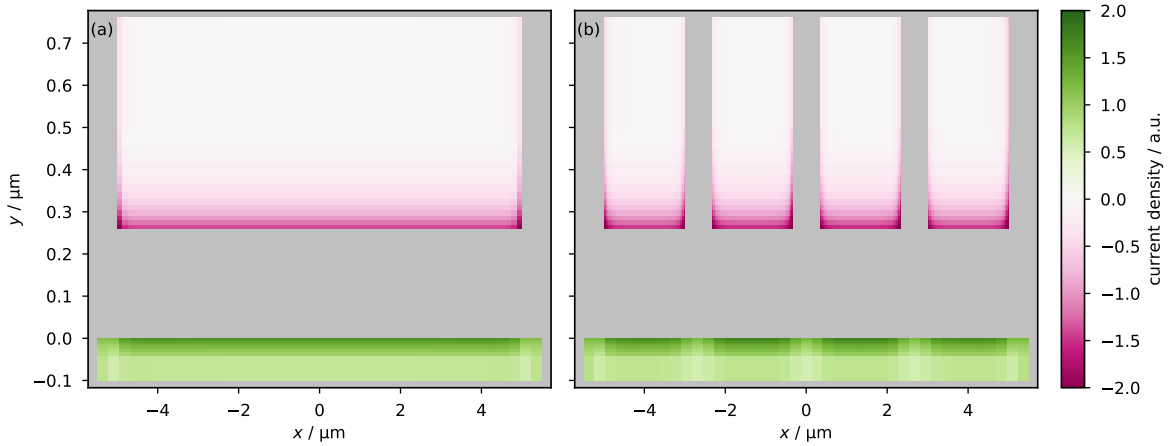


Fig. 5.8: Calculated example CDD for geometries with one (a) or four (b) windings of the λ-coil placed atop an input coil with a width of $b_{\mathrm{in}} = 12\,\mu\mathrm{m}$. The width of the λ-coil was adjusted such that it never overlaps the input coil.

in penetration depth can only affect the CDD in a significant way if the dimensions of the λ-coil cross-section are larger than the magnetic penetration depth λ. With $\lambda(0) = 80\,\mathrm{nm}$, as assumed here, it is therefore not surprising that a thickness of a few 100 nm is needed to yield a reasonable sensitivity. For larger thicknesses, a broad minimum exists. We can conclude that the sensor thickness should thus ideally be in the range of the order of 1 µm, not too different from our results regarding the ideal λ-coil width.

The fact that a large sensor thickness (compared to typical thin films) is ideal for λ-SQUID sensitivity is beneficial with respect to the thermal matching. As discussed in section 5.1, the total specific heat of the λ-coil should match that of the particle absorber. Since the absorber is generally rather thick (order µm) and made from a metal, we expect to require a similarly large total volume of the λ-coil. For a given total sensor volume, with a larger layer thickness the substrate area covered by the λ-coil can be lowered. This eases the design process of a suitably dimensioned λ-coil.

5.2.4 Variation of the number of sensor coil windings

The number of windings of the λ-coil with respect to the input coil is another free parameter that may influence the sensitivity of a λ-SQUID. For dc-SQUIDs, it is common to use multiple windings of the input coil in order to increase the coupling between the SQUID-loop and the input coil. To fit multiple turns of the input coil onto the SQUID loop, however, the linewidth of the input coil must be reduced. In previous sections, we have seen that it is beneficial for the input coil and λ-coil to have similar widths, however, using multiple turns improves the absolute mutual inductance. Which of the effects ultimately dominates is difficult to asses intuitively, but we can again use our simulation software to compare multiple configurations. For this, we have assumed a

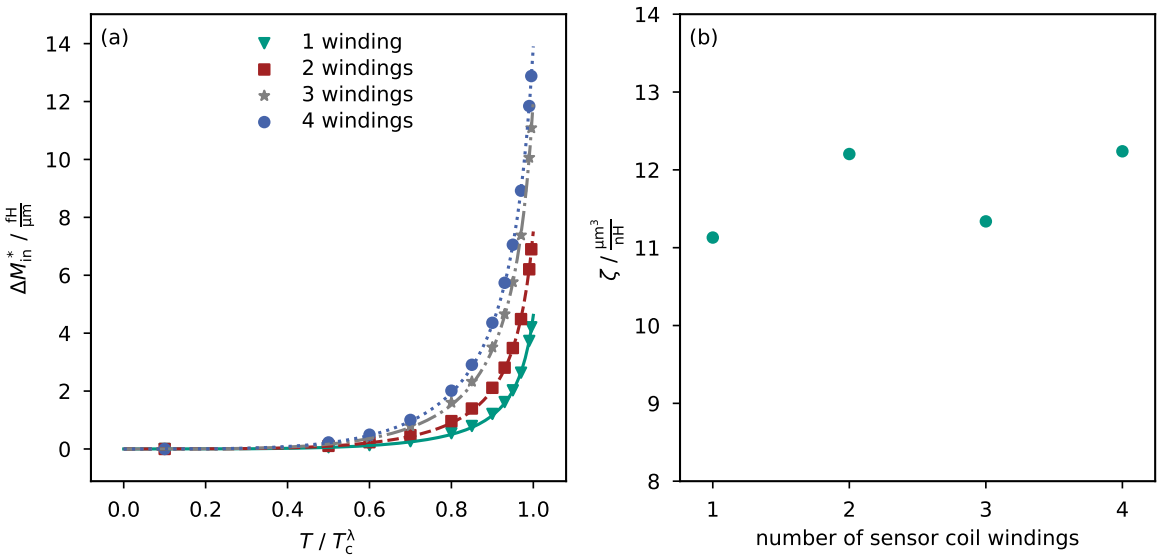


Fig. 5.9: (a) Change in mutual inductance versus temperature for different geometries with 1, 2, 3 or 4 windings of the λ-coil derived using Chang's numerical method. A fit of equation 3.13 to the data is used for further analysis. (b) FOM ζ for the four simulated geometries versus the number of λ-coil windings. Beyond some scattering, likely due to our specific geometries, the number of windings has little effect on the FOM.

geometry where an input loop of $b_{in} = 12\,\mu m$ width couples to one, two, three, or four windings of a λ-coil placed on top. A cross-section through such a geometry is displayed in figure 5.8 for two examples. The width of the sensor coil is adapted accordingly to not extend over the edges of the input coil, taking values of $b_{sen} = 10\,\mu m$, $b_{sen} = 4\,\mu m$, $b_{sen} = 3\,\mu m$ and $b_{sen} = 2\,\mu m$, for 1, 2, 3 and 4 windings, respectively. We have then used Chang's method to simulate the temperature-dependent mutual inductance M^*_{in} between the λ-coil and the input coil. After the inductance matrix was computed, we have assumed that all λ-coil windings are connected in series to derive the total (mutual) inductances of the λ-coil / input coil system.

The temperature-induced shift of the mutual inductance is plotted in figure 5.9(a) for four values of the number of λ-coil windings. Again, we have used a numerical fit of equation 3.13 to extract the fit parameters relevant to compute the FOM ζ, which is displayed versus the number of λ-coil windings in figure 5.9(b). Curiously, the number of windings seems to have a rather small effect on the FOM. Using four windings results in a FOM of $12.2\,\mu m^3/nH$, compared to the only marginally better FOM of $11.1\,\mu m^3/nH$ when using a single winding. Other simulated geometries have FOMs within that range, but no clear trend or dependency emerges. The observed fluctuations likely result from the specific geometries we chose, and small alterations in the width or spacing of the individual coil windings would result in slightly different FOMs. We can see from figure 5.9(a) that multiple, more narrow windings lead to a more significant increase of the mutual inductance with temperature. Connecting multiple, narrower lines in series,

however, increases the inductance of the sensor coil. From the definition of our FOM in equation 5.17, we can see that this will degrade the FOM. The area of all windings stays roughly the same in this example, so it seems that the gain in mutual inductance response is practically negated by a penalty to inductance, resulting in little net effect of the winding number on the FOM.

We can also make a comparison between the use of four λ-coil windings with $b_{\mathrm{sen}} = 2\,\mu\mathrm{m}$ width as discussed here with a single winding of a λ-coil with the same dimensions placed atop a narrower input coil, as presented in section 5.2.3. For the same sensor thickness of $a_{\mathrm{sen}} = 500\,\mathrm{nm}$, a narrow input coil and single λ-coil winding yield a FOM of $\zeta = 3.8\,\mu\mathrm{m}^3/\mathrm{nH}$ (compare figure 5.7(b)). Using four windings of the λ-coil on a wider input coil actually degrades the FOM to $\zeta = 12.2\,\mu\mathrm{m}^3/\mathrm{nH}$. Using single windings of a suitably narrow λ-coil and input coil thus yields much better sensitivity. Intuitively, we can understand this from the CDD in the input coil. If a wide input coil is used to couple to multiple windings on the λ-coil, then the same input current I_{in} is spread over a larger area. The input current CDD in the proximity of each λ-coil winding becomes less compared to using a single winding, which effectively reduces the mutual inductance M_{in}. In this specific example, using four windings of the λ-coil coupled to a common input coil results in an FOM roughly 3.2 times larger than coupling each of the windings to its own individual input coil, which agrees with the roughly 4 times reduction in current density per winding.

When constructing fully functional λ-SQUIDs in the future, one should therefore focus on simple stripline geometries of a single, narrow ($b_{\mathrm{sen}} \approx 2\,\mu\mathrm{m}$), thick ($a_{\mathrm{sen}} \gtrapprox 1\,\mu\mathrm{m}$) λ-coil on a suitably narrow ($b_{\mathrm{in}} \approx 4\,\mu\mathrm{m}$) input coil. One must keep in mind that the values specified here were derived assuming a magnetic penetration depth $\lambda(0) = 80\,\mathrm{nm}$ for the sensor material, which was found to describe experimental data on aluminium sensors well (see section 4.3.2). Different sensor materials with different magnetic penetration depths will likely result in different values for these parameters.

5.3 Future developments

The concept of the λ-SQUID developed over the course of this thesis was introduced in quite some detail. During this work, we also had some new ideas to take the concept further. While we did not pursue these ideas in the scope of this work, we will nonetheless mention them here as an outlook on future developments.

5.3.1 Microwave λ-SQUID Multiplexing

The μMUX multiplexing method using rf-SQUIDs and microwave resonators to transduce detector signals onto carrier signals in the GHz frequency range was already briefly introduced in section 2.3.4, and will be discussed in some detail in chapters 6 and 7. In favour of brevity we will not introduce it again here. Where typical μMUXing uses

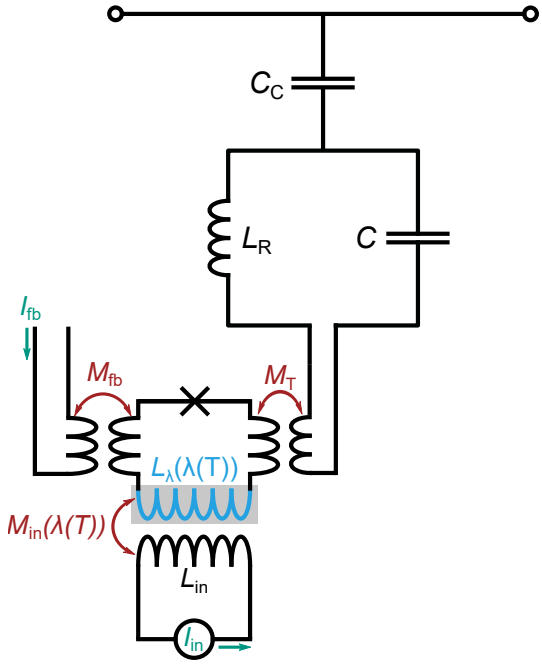


Fig. 5.10: Simplified equivalent circuit diagram of a single microwave λ-SQUID multiplexer channel. It resembles a resonator channel (see figure 6.2) of a typical μMUX, but replaces the rf-SQUID and detector by an rf-λ-SQUID. The device functions much like a regular μMUX channel, but relies on the temperature-dependent mutual inductance $M_{in}(T)$ between the rf-λ-SQUID and an input coil carrying a constant input current I_{in} to cause a flux change in the λ-SQUID. The flux signal is transduced onto a radio frequency carrier signal by a microwave resonator. For clarity, the particle absorber has been omitted.

an rf-SQUID reading out a cryogenic microcalorimeter such as an MMC or TES, one could potentially use an rf version of a λ-SQUID instead, as illustrated in figure 5.10. The detection principle is equivalent to the dc-λ-SQUIDs we have discussed so far: Upon particle absorption, the rise of detector temperature leads to an increase of the magnetic penetration depth $\lambda(T)$ in the λ-coil. The resulting change in the mutual inductance $M_{in}(T)$ between λ-coil and an input coil carrying a suitably large dc current I_{in} causes a change of the flux state of the λ-SQUID, which in this case can be read out by monitoring the power transmission $|S_{21}|^2$ of a sensibly chosen probe tone along the transmission line to which the resonator is coupled. This could facilitate the large multiplexing factors and total system bandwidths known from regular μMUXing with the stable operation, energy resolution and tunable gain of the λ-SQUID.

Originally, one major concern with using rf-λ-SQUIDs in a microwave multiplexer was a considerable reduction in internal quality factor Q_i at the operating temperature. During operation, a radio frequency signal couples into the SQUID loop. At the operating temperature near T_c^λ, the density of quasiparticles in the λ-coil is much larger than in a typical rf-SQUID loop operated in the mK temperature range. This could lead to losses at GHz frequencies, reducing the resonator's internal quality factor Q_i. Initial measurements on a first microwave λ-SQUID multiplexer, however, have indicated that the internal quality factors Q_i are not degraded much near (or even above) the critical temperature T_c^λ of the λ-coil. A lot of work will be needed to design and fabricate a microwave multiplexer incorporating rf-λ-SQUIDs as the sensitive element. Based on our current knowledge, however, it seems like a viable technology to facilitate highly multiplexed arrays of λ-SQUIDs for applications requiring hundreds (or potentially thousands) of detectors.

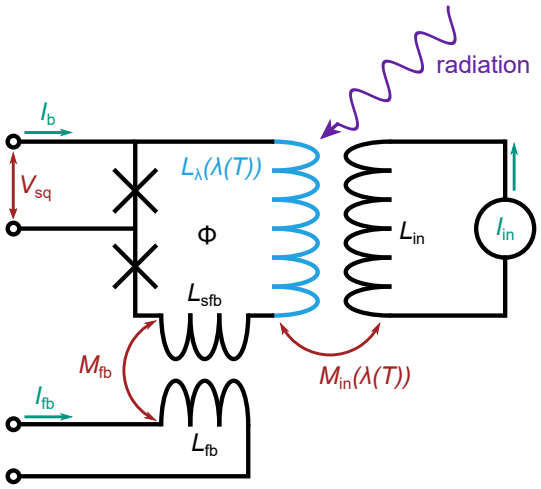


Fig. 5.11: Simplified equivalent circuit diagram of a λ-SQUID-based cryogenic bolometer. Rather than using a dedicated particle absorber, the geometry of the λ-coil is designed such that it can absorb incoming radiation directly.

5.3.2 Direct absorption λ-SQUID bolometer

So far, we have exclusively discussed the λ-SQUID as a potential cryogenic microcalorimeter. Due to their similarity, however, it is also feasible to construct bolometers based on λ-SQUIDs as illustrated in figure 5.11. For the application of a λ-SQUID as a bolometer in certain wavelength ranges, e.g. the infrared range, one may drop the absorber entirely. In a fashion similar to some designs of microwave kinetic inductance detectors (MKIDs), the λ-coil may be geometrically designed in such a way as to absorb the incoming radiation directly [Doy08], potentially with polarisation selectivity [Hub13]. The breaking of Cooper pairs due to the incoming radiation [Maz09] leads to an increase of the magnetic penetration depth λ in the illuminated inductor [Lon35, Tol22]. It was shown that this breaking of Cooper pairs is equivalent to an increase in temperature [Gao08], which causes a change of mutual inductance M_{in} by the mechanism we have introduced in section 3.2.5.

By not using an absorber, the specific heat of the detector can be reduced significantly, which has positive implications for the resolution. Additionally, the lack of an absorber streamlines the fabrication process, and no matching of specific heat between absorber and λ-coil is required. This point relaxes the conditions that have to be met during the design of the device. It might hence be worthwhile to further pursue the λ-SQUID concept as a direct absorption bolometer for radiation in the THz frequency range.

5.3.3 Superconducting Screening Thermometer

During the development of the λ-SQUID concept, an additional idea came up. One method for measuring magnetic penetration depth is the so-called two-coil method [Fio88], wherein an excitation coil and a sensing coil are placed on opposite sides of a large, thin sheet of the superconductor under test. An excitation current in the excitation coil results in a magnetic field which is shielded by the superconducting sheet such that the flux density at the sensing coil is significantly reduced. The

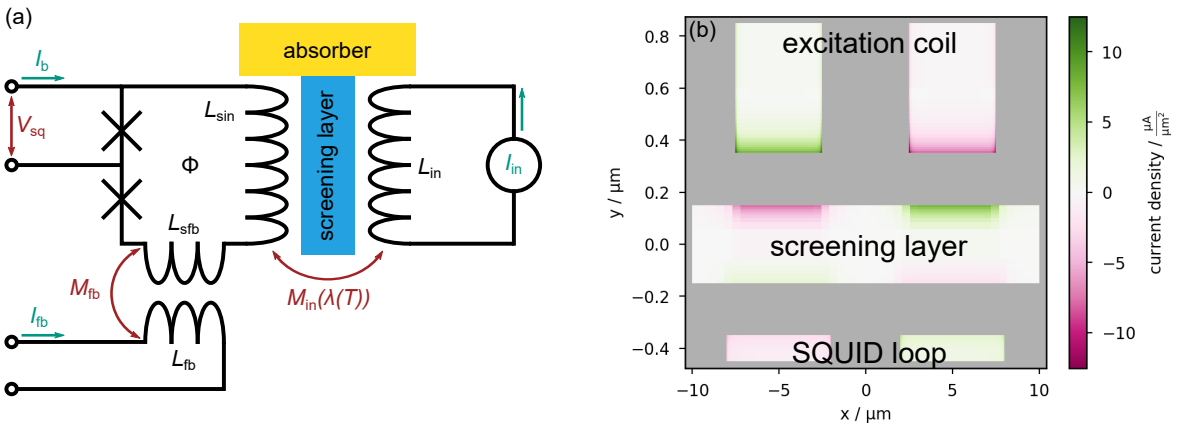


Fig. 5.12: (a) Schematic representation of a superconducting screening thermometer. A regular dc-SQUID and an excitation coil, both made from a material with $T_c \gg T_0$, are separated by a screening layer made from a different superconductor with $T_c^\lambda \lessapprox T_0$, resulting in a temperature-dependent mutual inductance $M_{in}(T)$. Here, T_0 is the operating temperature. (b) Cross-sectional view of two lines of the meander-shaped coils for both, the excitation coil (top) and SQUID loop (bottom), separated by the superconducting screening layer. Screening currents in the screening layer decrease the effect of the excitation coil magnetic field on the SQUID loop.

magnitude of the screening caused by the superconducting sheet depends on its thickness and, critically, on its magnetic penetration depth $\lambda(T)$. In addition to using this method to measure the magnetic penetration depth, one should be able to construct a thermometer by separating the loop of a SQUID (the sensing coil) and an excitation coil by a suitably dimensioned layer of superconductor with appropriate critical temperature, as schematically presented in figure 5.12(a). This configuration might have some advantages over the λ-SQUID design discussed above: Both the SQUID and excitation loop may be fabricated from an established, well-understood material (e.g. niobium) and operated well below transition temperature. The screening layer has a very simple geometry and requires no electrical connections of any kind, making it much simpler to integrate into the existing fabrication processes. The simple geometry may also help with thermalising the screening layer quickly over its entire area. The main upside, however, is that potentially, the modulation of the mutual inductance M_{in} may be significantly larger than the few percent seen for λ-SQUID in our early test devices. In this screening configuration, the mutual inductance may potentially vary from near-zero for total screening (i.e. $\lambda(T) \ll a_{scr}$ with thickness a_{scr} of the screening layer), to the fully unscreened value as the critical temperature T_c^λ of the screening layer is approached i.e. ($\lambda(T) \gg a_{scr}$). With the aforementioned two-coil method, variation of the mutual inductance of more than an order of magnitude have been reported [Fio88, He16].

We intend to construct both, the excitation coil and the SQUID loop as meander-shaped coils, one placed atop the other, separated by insulation layers and the superconducting

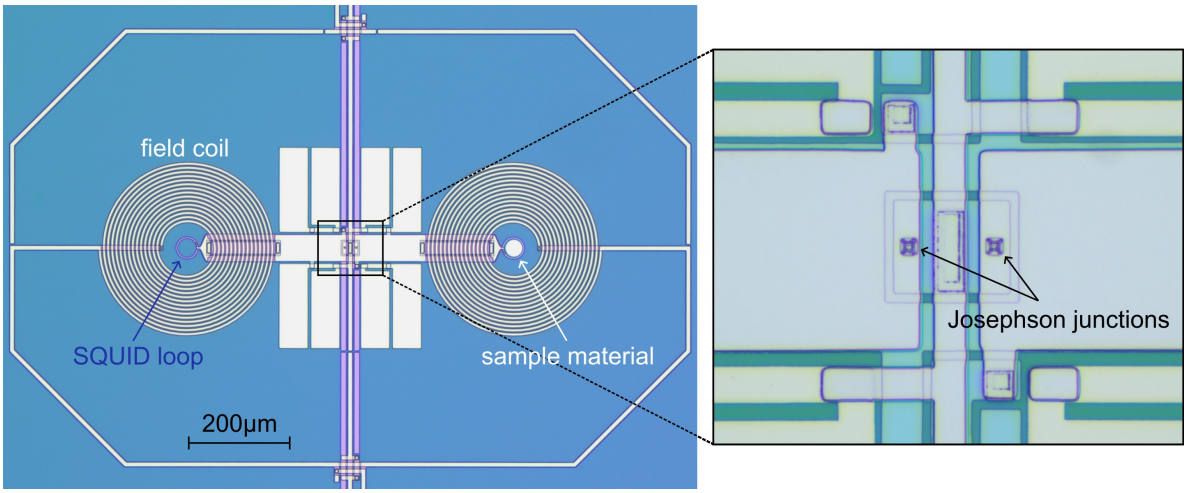


Fig. 5.13: Micrograph of a micro-susceptometer SQUID designed and fabricated at the IMS. The large, spiral field coils and the SQUID-loops placed at their centres are easy to make out. The Josephson junctions are at the centre of the device. The SQUID has almost perfect 180° rotational and mirror symmetry around two axes.

screening layer. In figure 5.12(b), we have depicted a cross-sectional view of a section of this geometry, including two lines of the meander-shaped coils for both, the excitation coil and SQUID loop. Neighbouring meander strips of the excitation coil carry the same current, but with opposite sign. We can see that screening currents within the screening layer result, effectively shielding the SQUID loop from the magnetic field induced by the excitation coil. As the temperature rises and the magnetic penetration depth $\lambda(T)$ in the screening layer approaches its thickness, we expect the screening currents to no longer screen the excitation coil field entirely, and some magnetic field will leak through to the SQUID loop. The magnitude of this leakage field depends on the temperature-dependent magnetic penetration depth $\lambda(T)$ in the screening layer, resulting in a temperature-dependent mutual inductance $M_{\mathrm{in}}(T)$.

We have already begun with the development of first prototype devices including an aluminium sensor layer. The more detailed study of this type of calorimeter, however, is beyond the scope of this work and will be the subject of future publications.

5.3.4 Micro-susceptometer SQUID

We have seen in section 4.3.2 that we still lack firm values for the magnetic penetration depths of niobium and aluminium, as we currently do not have an established experimental method to measure the magnetic penetration depth of superconducting materials. Over the course of this thesis, we have hence started development of a micro-susceptometer SQUID. Such a device is a highly sensitive tool to measure the magnetic properties of small samples (and especially thin films) in an applied magnetic field [Ket84, Can07].

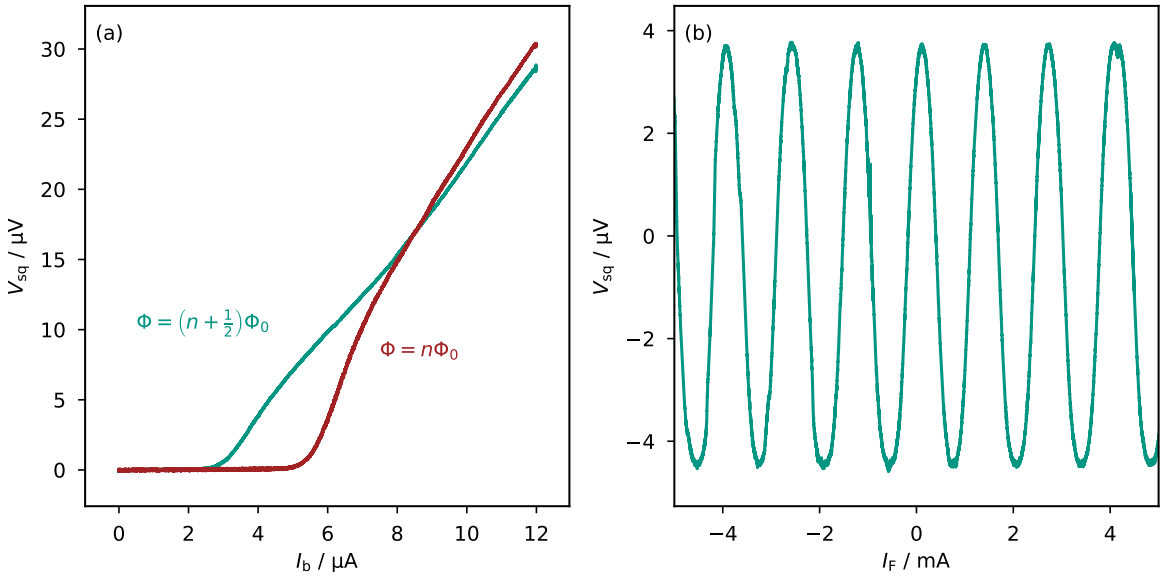


Fig. 5.14: (a) Current-voltage characteristic(IVC) of a micro-susceptometer SQUID for the two magnetic flux states $\Phi = n\Phi_0$ and $\Phi = (n + 1/2)\Phi_0$, maximising and minimising the critical current, respectively. (b) Voltage V_{SQ} across the device versus the applied field current I_F A field current of $I_F = 1.34\,\mathrm{mA}$ is required to induce a single flux quantum Φ_0.

Typically, a micro-susceptometer SQUID consists of two superconducting loops forming a serial gradiometer. Relative to their size, the loops are placed at a large distance from each other, in order to reduce crosstalk. The sample to be measured is placed within one of the two loops. A magnetic flux density can be applied using micro-fabricated on-chip field coils. Ideally, the susceptometer is fully symmetric such that without a sample, the applied magnetic field couples flux with exactly equal amplitude but opposite sign into the two SQUID loops, resulting in zero net flux. The presence of a sample with a non-zero magnetic susceptibility χ in one of the loops then introduces an asymmetry leading to a flux signal in the SQUID. The magnitude and sign of this signal is directly related to the sample geometry and its magnetic susceptibility. If the geometry of the sample is known, the sensitivity of a SQUID allows for a very accurate susceptibility measurement over a wide range of applied magnetic flux densities and frequencies from dc up to some 100 kHz. The temperature dependent magnetic properties of the sample material can be measured, too, naturally limited to ranges sufficiently below the critical temperature of the superconducting material comprising the micro-susceptometer SQUID.

To measure the magnetic properties of potential sensor materials for both, λ-SQUIDs and MMCs also being developed at IMS, we have started to develop our own micro-susceptometer SQUIDs. A micrograph of such a device designed and fabricated within this thesis is depicted in figure 5.13. Our design features two SQUID loops with a diameter of 40 µm and a centre-to-centre distance of 635 µm. Concentrically around each SQUID loop, a spiral field coil with 15 windings of 5 µm width at a 8 µm pitch is

located. The internal diameter of the field coil is 100 µm. Using the Biot-Savart law for an archimedian spiral, this geometry results in a magnetic flux density of $\mu_0 H = 96\,\mathrm{mT}$ at its centre if a field current of $I_\mathrm{F} = 100\,\mathrm{mA}$ is applied. With our device, the entire magnetic flux density range up to about 100 mT is therefore accessible. The layout features a near-perfect mirror symmetry along two axes, and likewise a near-perfect 180° rotational symmetry around its centre. For this, superfluous additional but galvanically unconnected shunt resistors and connection lines were included. Such symmetry is paramount to ensure that the applied magnetic field couples symmetrically into the two SQUID loops in the absence of a sample.

We have characterised a prototype of our micro-susceptometer SQUIDs without a sample to experimentally evaluate its symmetry. The acquired IVC is plotted in figure 5.14(a) for the two magnetic flux states $\Phi = n\Phi_0$ and $\Phi = (n + 1/2)\Phi_0$, maximising and minimising the critical current, respectively. The total SQUID inductance is, according to simulations using *InductEx*, $L_\mathrm{SQ} = 315\,\mathrm{pH}$. To yield a screening factor close to the ideal value $\beta_\mathrm{L} \approx 1$, a critical current of $I_\mathrm{c} = 3.3\,\mu\mathrm{A}$ per Josephson junction was intended. The real device depicts a somewhat lower value of around $I_\mathrm{c} = 2.6\,\mu\mathrm{A}$. The deliberate choice for an unusually large value of the screening parameter $\beta_\mathrm{L} \approx 1$ for a fabricated device is motivated by literature [Ket84], where successful micro-susceptometer SQUIDs have been made even with screening parameters exceeding unity. The measured device has a resistance of $R = 8\,\Omega$, which is close to the intended value of $7.4\,\Omega$ to result in a Stewart-McCumber-parameter $\beta_\mathrm{C} \approx 0.5$.

To probe the asymmetry of the SQUID loops with respect to the field coils, we have measured the voltage V_SQ across the device versus the applied field current I_F. The results are summarised in figure 5.14(b). From the periodicity of the response, we can deduce a residual mutual inductance between our micro-susceptometer SQUID and the filed coils of $M_\mathrm{F} = 1.54\,\mathrm{pH}$ ($M_\mathrm{F}^{-1} = 1.34\,\mathrm{mA}/\Phi_0$), which is about 30 times weaker still than the feedback coupling in our typical SQUIDs, despite the large number of windings of the spiral field coils and the large magnetic flux density they induce. Again using *InducEx* simulations, we can determine a coupling of $M_\mathrm{asym}^{-1} = 13.3\,\mu\mathrm{A}/\Phi_0$ between the SQUID and only one of the field coils, i.e. in a perfectly asymmetric configuration. We can thus estimate that the imbalance of our design is on the order of $M_\mathrm{asym}^{-1}/M_\mathrm{F}^{-1} = 0.01$, i.e. 1 %. This is of a similar order of magnitude as presented in [Ket84]

With the development of these micro-susceptometer SQUIDs, we intend to measure the magnetic properties of thin film samples of both superconducting and paramagnetic materials at cryogenic temperatures in the near future. This capability will be highly beneficial for the development of both, λ-SQUIDs and MMCs.

6. Microwave SQUID Multiplexing

Microwave SQUID multiplexing (μMUXing), as introduced in section 2, is a very promising technique for realising the simultaneous readout of hundreds to thousands of individual detector pixels. Taking a major role in future experiments, improving the performance of microwave SQUID multiplexers is the object of current research. In this chapter, we will give an introduction to the theoretical background regarding this multiplexing scheme. It will become apparent that analytical means will not suffice to properly model μMUXing and that numerical methods have to be applied instead.

The heart of any μMUX are a large number of rf-SQUIDs and superconducting microwave resonators. We will give a short overview concerning these devices and their operation here, but the detailed mathematical description will be presented in section 6.6 during the description of the simulation software and underlying algorithms to avoid repetition.

6.1 Inductively coupled non-hysteretic, unshunted rf-SQUIDs

Microwave SQUID multiplexers transduce a magnetic flux signal with a bandwidth in the range of 100 kHz to a few MHz into the side bands of a gigahertz carrier signal. The enormous bandwidth available in radio frequency systems allows for carrying a large number of readout signals on a single transmission line. One key element to achieve this is an rf-SQUID, which acts as a flux-dependent inductance due to the Josephson effects. It consists of a superconducting loop with inductance L_S interrupted by a single Josephson tunnel junction, the inductance of which is described by [Weg22]

$$L_\mathrm{jj}\left(\varphi_\mathrm{tot}\right) = \frac{L_\mathrm{j}}{\cos\left(\varphi_\mathrm{tot}\right)}. \tag{6.1}$$

with the Josephson inductance $L_\mathrm{j} = \Phi_0/(2\pi I_\mathrm{c})$ and critical current I_c. The phase $\varphi_\mathrm{tot} = 2\pi\Phi_\mathrm{tot}/\Phi_0$ that enters here relates to the total magnetic flux Φ_tot threading the SQUID loop. The inductance of the rf-SQUID can thus take a wide range of values, including infinite and negative ones, and displays the periodicity with flux of a single flux quantum Φ_0. Similar to dc-SQUIDs, the total flux depends not only on the externally applied flux but also on the screening current running in the SQUID loop. We can again introduce a screening parameter $\beta_\mathrm{L} = 2\pi L_\mathrm{SQ} I_\mathrm{c}/\Phi_0$ and express the total flux as

$$\varphi_\mathrm{tot} = \varphi_\mathrm{ext} - \beta_\mathrm{L}\sin\left(\varphi_\mathrm{tot}\right). \tag{6.2}$$

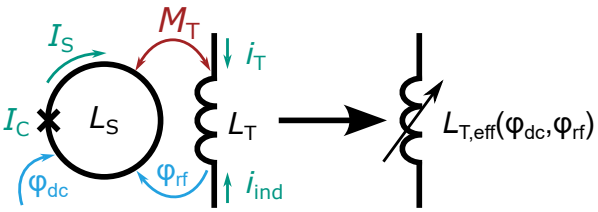


Fig. 6.1: Schematic circuit diagram of an rf-SQUID with loop inductance L_S and Josephson tunnel junction with critical current I_c coupled to an inductance L_T via the mutual inductance M_T. An rf current i_T induces a magnetic flux contribution φ_{rf} in the SQUID loop, in addition to a quasi-static external flux φ_{dc}. The circulating current I_s in the rf-SQUID loop induces a current i_{ind} back into the inductor. The whole circuit is electrically equivalent to a flux-dependent inductance $L_{T,eff}(\varphi_{dc},\varphi_{rf})$.

The relationship between total and external magnetic flux is unique up to screening parameters Hysteresis of $\beta_L < 1$. Above this limit, some ranges exist for which the same externally applied flux can lead to two or more possible values of the total flux, resulting in hysteretic behaviour of the rf-SQUID. In μMUX, non-hysteretic, unshunted rf-SQUIDs are used, i.e. $\beta_L < 1$ and $\beta_C \gg 1$. For the use in μMUXing, the rf-SQUID is inductively coupled to an inductor L_T via a mutual inductance M_T as schematically depicted in figure 6.1. Assuming an ac current i_T with angular frequency ω running in the inductance L_T, a flux signal φ_{rf} with the same frequency is induced into the SQUID loop. Assuming in addition a quasi-static external flux contribution φ_{dc}, we can express the time-dependent supercurrent $I_s(t)$ running in the rf-SQUID as [Weg22]

$$I_s(t) = -I_c \sin\left(\varphi_{dc} + \varphi_{rf}\sin(\omega t) + \beta_L \frac{I_s(t)}{I_c}\right) \tag{6.3}$$

which in turn induces an ac current i_{ind} back into the inductor L_T:

$$i_{ind}(t) = -\frac{M_T}{i\omega L_T}\frac{dI_s(t)}{dt}. \tag{6.4}$$

To any load connected to the inductance L_T, this has the effect that the circuit formed by the inductance L_T and the rf-SQUID is equivalent to a single inductor with the effective, flux-dependent inductance

$$L_{T,eff}(\varphi_{dc},\varphi_{rf}) = L_T - \Delta L_T(\varphi_{dc},\varphi_{rf}) = L_T\left(1 + \frac{i_{ind}(\varphi_{dc},\varphi_{rf})}{i_T}\right), \tag{6.5}$$

which is again periodic in φ_{dc} with a period of a single flux quantum. Thus, depending on the flux state of the rf-SQUID, the effective inductance is altered by an inductance shift $\Delta L_T(\varphi_{dc},\varphi_{rf})$. So far, no analytic expression for $L_{T,eff}(\varphi_{dc},\varphi_{rf})$ was found. Analytic solutions exist only for special cases, and a multi-term approximation has been derived for finite $0 \leq \beta_L \leq 0.6$ [Weg22]. We will briefly introduce them here.

6.1.1 Vanishing probe tone power $P_{\mathrm{exc}} \to 0$

For vanishing probe tone power, i.e. $\Phi_{\mathrm{rf}} \to 0$, an analytic solution for the inductance shift ΔL_{T} can be found [Weg22]:

$$\Delta L_{\mathrm{T}} = \frac{M_{\mathrm{T}}^2}{L_{\mathrm{S}}} \frac{\beta_{\mathrm{L}} \cos\left(\varphi_{\mathrm{tot}}\right)}{1 + \beta_{\mathrm{L}} \cos\left(\varphi_{\mathrm{tot}}\right)}. \tag{6.6}$$

In this special case we can neglect the radio-frequency flux contribution to φ_{tot}, but we need to keep in mind that screening currents within the SQUID loop cause a screening flux contribution. Here, the external flux equals the quasi-static contribution, i.e. $\varphi_{\mathrm{ext}} = \varphi_{\mathrm{dc}}$, and the resulting total flux φ_{tot} has to be determined using condition 6.2. While only valid for vanishing probe tone powers, this result is applicable to all values of the screening parameter β_{L}.

6.1.2 Vanishing screening currents $\beta_{\mathrm{L}} \to 0$

For vanishing screening currents within the SQUID loop, the the inductance shift ΔL_{T} takes the analytical form [Weg22]

$$\Delta L_{\mathrm{T}} = \frac{M_{\mathrm{T}}^2 \beta_{\mathrm{L}}}{L_{\mathrm{S}}} \frac{2J_1(\varphi_{\mathrm{rf}})}{\varphi_{\mathrm{rf}}} \cos\left(\varphi_{\mathrm{dc}}\right). \tag{6.7}$$

Since we neglect screening currents here, the total flux simply equals the external flux contributions $\varphi_{\mathrm{tot}} = \varphi_{\mathrm{dc}} + \varphi_{\mathrm{rf}}$. This solution is valid for all rf flux amplitudes φ_{rf} and thus all probe tone powers P_{exc}, but only in the limit of a vanishing screening parameter $\beta_{\mathrm{L}} \to 0$.

6.1.3 General case

Generally however, we can assume neither negligible probe tone power nor vanishing screening currents. In this case, no analytic solution has been found yet. Instead, one can find an approximate solution, which reads [Weg22]

$$\Delta L_{\mathrm{T}} = \frac{M_{\mathrm{T}}^2 \beta_{\mathrm{L}}}{L_{\mathrm{S}}} \frac{2}{\varphi_{\mathrm{rf}}} \sum_{i,j} a_{i,j} \beta_{\mathrm{L}}^{b_{i,j}} J_1(c_{i,j}\varphi_{\mathrm{rf}}) \cos\left(c_{i,j}\varphi_{\mathrm{dc}}\right) \tag{6.8}$$

with the coefficients $a_{i,j}$, $b_{i,j}$ and $c_{i,j}$ as listed in [Weg22]. Here, $J_1(x)$ denotes the Bessel function of the first kind. Currently, this expansion has been done to tenth order, yielding reasonable results for reasonably small screening parameters up to $\beta_{\mathrm{L}} \leq 0.6$. While limited to this range of the screening parameter, this expression is valid for all rf flux amplitudes φ_{rf}, and consequently all probe tone powers P_{exc}.

For the following section on microwave resonators it is important to remember that the rf-SQUID causes a modulation of the effective termination inductance $L_{\mathrm{T,eff}}(\varphi_{\mathrm{dc}},\varphi_{\mathrm{rf}})$, which we will use to describe the influence of the rf-SQUID on the resonator properties.

6.2 Single μMUX channel

Fundamentally, a single μMUX readout channel as we will consider it consists of a lumped-element resonator (LER) coupled to an rf-SQUID, as schematically depicted in figure 6.2(a). The resonator consists of an inductance $L = L_{\mathrm{R}} + L_{\mathrm{T}}$ and a capacitance C connected in parallel. The inductance is split between the main resonator inductance L_{R} and the coupling inductance L_{T} through which the coupling to the rf-SQUID is realised. A resistor R is included to account for losses within the resonator. For readout, the resonator is coupled to a superconducting transmission line with impedance Z_0 using a coupling capacitance C_{C}. Coupling to ground via the capacitance C_{para} may result from the parasitic capacitance due to the geometric arrangement of the lumped-element resonator. External coils coupled to the rf-SQUID can be used to induce flux into the SQUID loop: The input coil with inductance L_{in} and mutual inductance M_{in} to the rf-SQUID is connected to a detector (e.g. a TES or an MMC). Through this input coil, the detector signal is transduced into a flux φ_{sig} in the rf-SQUID. For linearisation, a modulation coil with inductance L_{mod} and mutual inductance M_{mod} is present. The modulation coils of all μMUX channels are connected in series, and carry the same modulation current I_{mod} supplied via room-temperature electronics. We will explain the method for linearisation and its consequences for μMUX operation in section 6.3. We have also discussed a very similar linearisation scheme for dc-SQUIDs in subsection 4.2.2.

The resonance frequency f_{res}, internal quality factor Q_{i}, coupling quality factor Q_{c}, loaded quality factor Q_{l} and resonance bandwidth Δf_{BW} of such a resonator are determined by its constituent components as follows [Mat11]:

$$f_{\mathrm{res}} = \frac{\omega_{\mathrm{res}}}{2\pi} = \frac{1}{2\pi\sqrt{L\,(C + C_{\mathrm{C,eff}})}} \tag{6.9}$$

$$Q_{\mathrm{i}} = \frac{R}{\omega_{\mathrm{res}} L} \tag{6.10}$$

$$Q_{\mathrm{c}} = \frac{2}{Z_0 \omega_{\mathrm{res}}^3 L C_{\mathrm{C}}^2} \tag{6.11}$$

$$\frac{1}{Q_{\mathrm{l}}} = \frac{1}{Q_{\mathrm{c}}} + \frac{1}{Q_{\mathrm{i}}} \tag{6.12}$$

$$\Delta f_{\mathrm{BW}} = \frac{f_{\mathrm{res}}}{Q_{\mathrm{l}}} \overset{Q_{\mathrm{i}} \gg Q_{\mathrm{c}}}{\approx} \frac{f_{\mathrm{res}}}{Q_{\mathrm{c}}}. \tag{6.13}$$

Here, the effective coupling capacitance results from the pure coupling- and parasitic

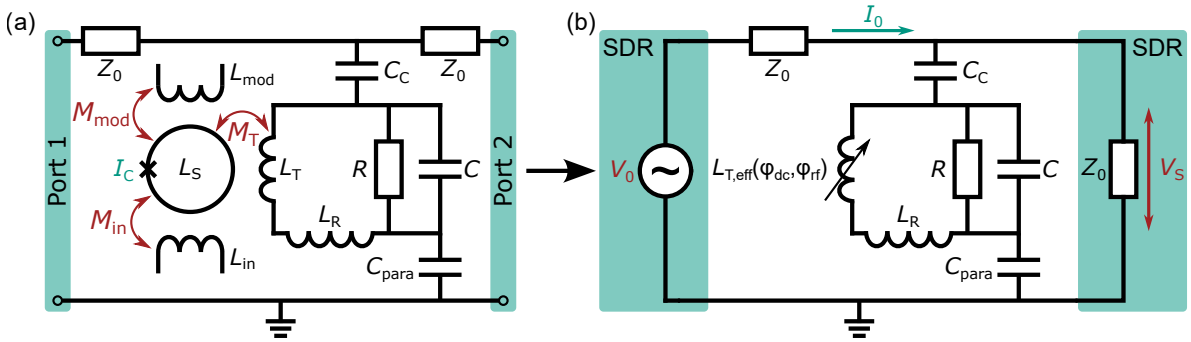


Fig. 6.2: (a) Schematic circuit diagram of a single μMUX readout channel, comprising a lumped element resonator capacitively coupled to a transmission line and inductively coupled to an rf-SQUID. The LER itself consists of an inductance $L = L_R + L_T$, capacitance C and resistance R connected in parallel. It is coupled to the transmission line via the effective capacitance $C_{C,eff} = (C_C^{-1} + C_{para}^{-1})^{-1}$. The rf-SQUID is formed by a superconducting loop with inductance L_S and an unshunted Josephson junction with critical current I_c. The mutual inductance between the SQUID loop and the coupling coil of the resonator is M_T. External coils coupled to the rf-SQUID can be used to induce flux into the SQUID loop: An input coil with inductance L_{in} and mutual inductance M_{in} to the rf-SQUID, and a modulation coil with inductance L_{mod} and mutual inductance M_{mod}. (b) Simplified circuit diagram of a single μMUX channel. The circuit of the termination inductance L_T coupled to the rf-SQUID is substituted by the flux-dependent tunable effective inductance $L_{T,eff}(\varphi_{dc},\varphi_{rf})$. For readout, we use a software-defined radio system (SDR) to apply an rf voltage V_0 at port 1, and to measure the transmitted signal voltage V_S at port 2.

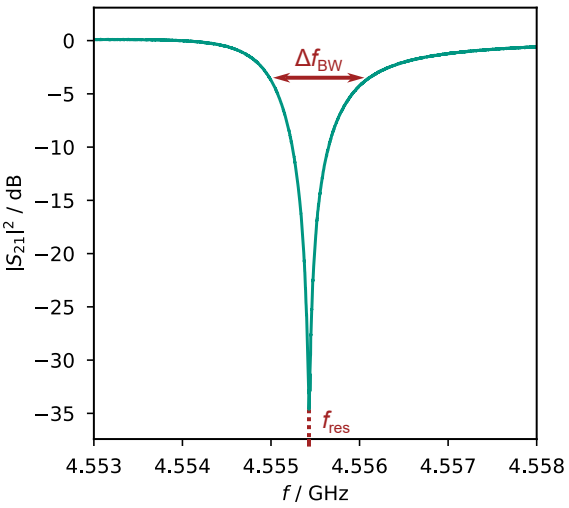


Fig. 6.3: Power transmission spectrum $|S_{21}|^2$ of a resonator channel fabricated and measured at IMS. At the resonance frequency $f_{\mathrm{res}} = 4.555\,27\,\mathrm{GHz}$, the transmitted power is at minimum and most of the incident power is reflected. The width of the resonance dip at $-3\,\mathrm{dB}$ relative to the baseline defines the resonator bandwidth $\Delta f_{\mathrm{BW}} = 1.03\,\mathrm{MHz}$.

capacitances $C_{\mathrm{C,eff}} = (C_{\mathrm{C}}^{-1} + C_{\mathrm{para}}^{-1})^{-1}$. In real resonators, the losses described by the internal quality factor Q_{i} are mainly caused by quasiparticle losses, radiation and coupling to two-level systems (TLS) in the vicinity of the resonator [Gao07]. In case of strong coupling, i.e. $Q_{\mathrm{i}} \gg Q_{\mathrm{c}}$, the bandwidth Δf_{BW} of the resonance can be set by dimensioning the coupling capacitance accordingly, as seen from equations 6.11 and 6.13. One important property of such a channel is its power transmission spectrum $|S_{21}(f)|^2$, which quantifies the ratio of power of an incoming probe tone with frequency f at port 1 and the resulting transmitted power of the outgoing probe tone at port 2. The power transmission spectrum $|S_{21}(f)|^2$ of such a channel is exemplarily depicted in figure 6.3. On resonance, the transmitted power is at minimum and most of the incident power is reflected. The depth of the resonance depends on the internal- and loaded quality factors: $\left|S_{21}{}^{\mathrm{min}}\right|^2 = Q_{\mathrm{l}}^2/Q_{\mathrm{i}}^2$. Lower internal losses, i.e. higher value of Q_{i}, result in a greater resonance depth. The bandwidth Δf_{BW} of the resonator is measured at $-3\,\mathrm{dB}$ below the baseline.

Deriving an expression for the transmission $S_{21}(f)$ as seen in this spectrum is quite challenging, considering that the resonance frequency of a μMUX channel changes in time. If the change in resonance frequency is sufficiently rapid, we can no longer assume an infinitely fast response time of the resonator. To accurately model lumped-element resonators in a μMUX operated near its bandwidth limit, we must therefore develop a model that takes the finite resonator response time into account.

6.2.1 Dynamical lumped element resonator model

To derive an analytical expression for the time-dependent transmission $S_{21}(t)$, we will replace the rf-SQUID and coupling inductance by the effective inductance $L_{\mathrm{T,eff}}$, as depicted in figure 6.2(b). The effective inductance $L_{\mathrm{T,eff}}$ depends on the non-static magnetic flux through the SQUID, and thus also on time. Furthermore, we assume that we apply a microwave voltage V_0 with amplitude $|V_0|$ and angular frequency ω to

port 1, causing an ac current I_0. We measure the transmitted output voltage V_S at port 2 using a voltmeter which is impedance-matched to the transmission line impedance Z_0. From the output voltage V_S, we can derive the transmission parameter $S_{21} = 2V_\mathrm{S}/V_0$.

For the derivation of the transmission coefficient S_{21} of a lumped element resonator as shown in figure 6.2(b), it is convenient to use the impedances in their operator forms, where we will use the convention $D \equiv \frac{\mathrm{d}}{\mathrm{d}t}$ for the operator of the time derivative. For inductances and capacitances respectively this yields:

$$Z_L = LD + \dot{L} \tag{6.14}$$

$$Z_C = \frac{1}{CD} \tag{6.15}$$

We then can derive the current I_0 using Ohm's law and the Kirchhoff rules as follows:

$$I_0 = V_0 \left(\frac{P + Z_0 Q}{Z_0 \left(2P + Z_0 Q\right)} \right). \tag{6.16}$$

With the substitutions:

$$\begin{aligned} P &= D^2 + \frac{1}{R\left(C_{\mathrm{C,eff}} + C\right)} \left[1 + R\left(C_{\mathrm{C,eff}} + C\right) \frac{\dot{L}}{L} \right] D \\ &\quad + \frac{1}{L\left(C_{\mathrm{C,eff}} + C\right)} \left[1 + \frac{\dot{L}}{R} \right] \end{aligned} \tag{6.17}$$

$$\begin{aligned} Q &= \frac{C_{\mathrm{C,eff}} C}{C_{\mathrm{C,eff}} + C} D^3 + \frac{C_{\mathrm{C,eff}}}{R\left(C_{\mathrm{C,eff}} + C\right)} \left[1 + RC \frac{\dot{L}}{L} \right] D^2 \\ &\quad + \frac{C_{\mathrm{C,eff}}}{L\left(C_{\mathrm{C,eff}} + C\right)} \left[1 + \frac{\dot{L}}{R} \right] D. \end{aligned} \tag{6.18}$$

Due to the presence of the time derivative operator D, also the terms P and Q are practically operators.

Using equation 6.16 and Kirchhoff's laws we can find the following expression by introducing the output voltage V_{S}:

$$PV_0 = (2P + Z_0 Q)\, V_{\mathrm{S}}, \tag{6.19}$$

which we will use in the next step to express the transmission coefficient S_{21}. In order to do this, we will again introduce substitutions:

$$\begin{aligned} X &\equiv \frac{C_{\mathrm{C,eff}} C}{(C_{\mathrm{C,eff}} + C)} \qquad A \equiv \frac{1}{R\,(C_{\mathrm{C,eff}} + C)} \\ Y &\equiv \frac{C_{\mathrm{C,eff}}}{R\,(C_{\mathrm{C,eff}} + C)} \qquad B \equiv \frac{1}{L\,(C_{\mathrm{C,eff}} + C)} \\ Z &\equiv \frac{C_{\mathrm{C,eff}}}{L\,(C_{\mathrm{C,eff}} + C)}. \end{aligned}$$

Using these and the relation $V_{\mathrm{S}} = S_{21} V_0/2$ we can expand equation 6.19 into

$$\begin{aligned} \Big[Z_0 X D^3 + \left(2 + Z_0 \left(Y + X\frac{\dot{L}}{L}\right)\right) \quad D^2 \\ + \left(2\left(A + \frac{\dot{L}}{L}\right) + Z_0\left(Z + Y\frac{\dot{L}}{L}\right)\right) D + 2\left(B + A\frac{\dot{L}}{L}\right)\Big] \quad S_{21} V_0 \\ = 2\left[D^2 + \left(A + \frac{\dot{L}}{L}\right) \quad D \quad + \left(B + A\frac{\dot{L}}{L}\right)\right] V_0, \end{aligned}$$

which is a rather cumbersome expression to deal with. Applying the differentiation operator and rearranging the terms then finally yields the third-order differential equation:

$$N_4 D^3 S_{21} + N_3 D^2 S_{21} + N_2 D S_{21} + N_1 S_{21} = N_0 \tag{6.20}$$

with the coefficients

$$
\begin{aligned}
N_4 &= [Z_0 X] && (6.21)\\
N_3 &= \left[3\mathrm{i}\omega Z_0 X + \left(2 + Z_0\left(Y + X\frac{\dot{L}}{L}\right)\right)\right] && (6.22)\\
N_2 &= \left[-3\omega^2 Z_0 X + 2\mathrm{i}\omega\left(2 + Z_0\left(Y + X\frac{\dot{L}}{L}\right)\right)\right. && (6.23)\\
&\quad \left. + \left(2\left(A + \frac{\dot{L}}{L}\right) + Z_0\left(Z + Y\frac{\dot{L}}{L}\right)\right)\right]\\
N_1 &= \left[-\mathrm{i}\omega^3 Z_0 X - \omega^2\left(2 + Z_0\left(Y + X\frac{\dot{L}}{L}\right)\right)\right. && (6.24)\\
&\quad + \mathrm{i}\omega\left(2\left(A + \frac{\dot{L}}{L}\right) + Z_0\left(Z + Y\frac{\dot{L}}{L}\right)\right)\\
&\quad \left. + 2\left(B + A\frac{\dot{L}}{L}\right)\right]\\
N_0 &= -2\omega^2 + 2\mathrm{i}\omega\left(A + \frac{\dot{L}}{L}\right) + 2\left(B + A\frac{\dot{L}}{L}\right). && (6.25)
\end{aligned}
$$

This third-order differential equation fully describes the transmission coefficient $S_{21}(t)$ of a superconducting lumped-element resonator as shown in figure 6.2(b). Working with such a formidable expression is not particularly convenient, and we will simplify it significantly in the following. First, we will consider the steady state. If all parameters are constant, a steady state value S_{21}^{SS} of the transmission coefficient will be assumed after a sufficiently long time. In the steady state, all derivatives of S_{21} vanish and equation 6.20 simplifies to:

$$N_1 S_{21}^{\mathrm{SS}} = N_0. \tag{6.26}$$

Conveniently, we can also neglect the time-derivative $\dot{L} = 0$ of the inductance L in the steady state. This yields:

$$S_{21}^{\mathrm{SS}} = \frac{-2\frac{\omega^2}{\omega_{\mathrm{res}}^2} + 2\mathrm{i}\omega\frac{L}{R} + 2}{-2\frac{\omega^2}{\omega_{\mathrm{res}}^2} + 2\mathrm{i}\omega\frac{L}{R} + 2 - \mathrm{i}\omega^3 Z_0 C C_{\mathrm{C,eff}} L - \omega^2 Z_0 C_{\mathrm{C,eff}}\frac{L}{R} + \mathrm{i}\omega Z_0 C_{\mathrm{C,eff}}} \tag{6.27}$$

By using the definitions for the macroscopic device parameters introduced previously, this result can be approximated to the steady state solution

$$S_{21}^{\mathrm{SS}} \approx \frac{\frac{Q_\mathrm{l}}{Q_\mathrm{i}} + 2\mathrm{i}Q_\mathrm{l}\frac{f-f_\mathrm{res}}{f_\mathrm{res}}}{1 + 2\mathrm{i}Q_\mathrm{l}\frac{f-f_\mathrm{res}}{f_\mathrm{res}}}, \tag{6.28}$$

which is a much more manageable expression. However, the steady state approximation will not suffice for our applications regarding high-bandwidth μMUX readout, and we need to consider the dynamics of a lumped element resonator also. Going back to the full differential equation, we can use the steady state solution in conjunction with the approximating assumption that the resonator is lossless and neglect all higher order terms of the differential equation except for the first order to get the following expression:

$$DS_{21} = \frac{N_1}{N_2}\left(S_{21}^{\mathrm{SS}} - S_{21}\right). \tag{6.29}$$

To solve this expression we will furthermore make the assumption that the derivative of the inductance L is small compared to L itself: $\dot{L}/L \approx 0$. Expressing the prefactor in the macroscopic parameters then yields:

$$\begin{aligned} \frac{N_1}{N_2} &= \mathrm{i}\omega + \frac{2\mathrm{i}Z_0\omega^3 C C_{\mathrm{C,eff}} L + 2\omega^2\left(C + C_{\mathrm{C,eff}}\right)L + 2}{-3Z_0\omega^2 C C_{\mathrm{C,eff}} L + 4\mathrm{i}\omega\left(C + C_{\mathrm{C,eff}}\right)L + Z_0 C_{\mathrm{C,eff}}} && (6.30)\\ &\approx \pi\Delta f_{\mathrm{BW}} + \mathrm{i}\left(\omega_\mathrm{res} - \omega\right) && (6.31) \end{aligned}$$

This brings us to a first-order differential equation for the transmission parameter S_{21}:

$$DS_{21}(t) \approx \left(\mathrm{i}\left(\omega_\mathrm{res}(t) - \omega\right) - \pi\Delta f_{\mathrm{BW}}\right)\left(S_{21}(t) - S_{21}^{\mathrm{SS}}(t)\right). \tag{6.32}$$

Here, $S_{21}^{\mathrm{SS}}(t)$ is the steady state solution for the parameter values at time t. Since the numerical methods for solving differential equations are rather demanding in terms of computation time, an iterative approximation to this is more useful for simulations. We can easily see that in the case of a constant value of $S_{21}^{\mathrm{SS}}(t) = S_{21}^{\mathrm{SS}} = const.$, the differential equation has the following solution:

$$S_{21}(t) \approx S_{21}^{\mathrm{SS}} + \left(S_{21}(0) - S_{21}^{\mathrm{SS}}\right)\mathrm{e}^{-\pi\Delta f_{\mathrm{BW}}t + \mathrm{i}(\omega_\mathrm{res} - \omega)t}. \tag{6.33}$$

Even though this assumption is not true in general, it is approximately true on sufficiently small timescales. If $S_{21}^{\mathrm{SS}}(t)$ is approximately constant on a timescale Δt, we can apply expression 6.33 iteratively to data points at time intervals Δt. In this way, we can generate transmission time traces of arbitrary length.

6.3 Readout and linearisation

We have seen from equation 6.9 that the shift of the effective termination inductance $L_{\mathrm{T,eff}}$ causes a shift in the resonance frequency $f_{\mathrm{res}}(\varphi_{\mathrm{dc}}) = f_{\mathrm{res,0}} + \Delta f_{\mathrm{res}}(\varphi_{\mathrm{dc}})$ around the unaltered resonance frequency $f_{\mathrm{res,0}}$, i.e. of the bare resonator without an rf-SQUID present. This shift will generally take both, positive and negative values and displays a periodicity with one flux quantum, as we can see in figure 6.4(a). Here, the flux dependent resonance frequency f_{res} of a single μMUX channel is shown schematically.

The transmission spectra corresponding to the colour-highlighted points are plotted in figure 6.4(b). Naturally, as the resonance frequency shifts with magnetic flux, so does the characteristic resonance dip in the transmission spectrum. As the flux signal is encoded in the resonance frequency f_{res} of the microwave resonator, one way to read out the signal would be to measure a full transmission spectrum across the entire frequency range covered by the modulation, and then determine the actual resonance frequency. This would, however, take a meaningful amount of time and would thus limit the measurement bandwidth. Instead, the transmission $S_{21}(f_{\mathrm{exc}})$ is monitored at a suitably chosen probe tone with frequency f_{exc}. While readout schemes exist where the probe tone is varied with time, e.g. tone-tracking [Yu23], we will in the following generally assume it to be constant in time. A suitable probe tone for this exemplary μMUX channel is marked by a grey line, and lies just above the largest resonance frequency reached during modulation.

The transmission $|S_{21}(f_{\mathrm{exc}})|^2$ at the fixed probe tone frequency f_{exc} also changes with the magnetic flux Φ_{dc} threading the rf-SQUID-loop. This finally yields the flux-dependent transmission $|S_{21}(f_{\mathrm{exc}})|^2$ at the probe tone frequency as displayed in figure 6.4(c). It displays the same periodicity of one flux quantum Φ_0 as the resonance frequency, and can be easily measured using a single, constant probe tone.

To efficiently multiplex the readout of a large number of detectors, we can take a large number $N \in \mathbb{N}$ of μMUX channels, each with a unique resonance frequency, and couple them to the same transmission line. Such a configuration is schematically depicted in figure 6.5. A comb of probe tone frequencies f_i, $I = 1,...,N$ is applied to the transmission line input, and the transmission of each probe tone is monitored at the output. By selecting a sufficient spacing between individual resonance frequencies, the crosstalk between channels can be reduced. In this way, a single coaxial transmission line, modulation line and amplifier can be used to read out up to several hundred detectors simultaneously.

With an appropriate choice of f_{exc}, the resulting transmission data $S_{21}(f_{\mathrm{exc}})$ depicts the largest possible peak-to-peak amplitude. It is, however, still periodic, and thus only linear for a small range of the input signal. To apply multiplexing for the readout of detectors with potentially large flux signals, we must therefore linearise the output. One common method to achieve this is flux ramp modulation (FRM) [Mat12], for which a sawtooth-shaped modulation current signal with peak-peak amplitude $I_{\mathrm{mod}}^{\mathrm{max}}$ and repetition rate f_{ramp} is applied to the modulation coil. The ramp repetition rate defines

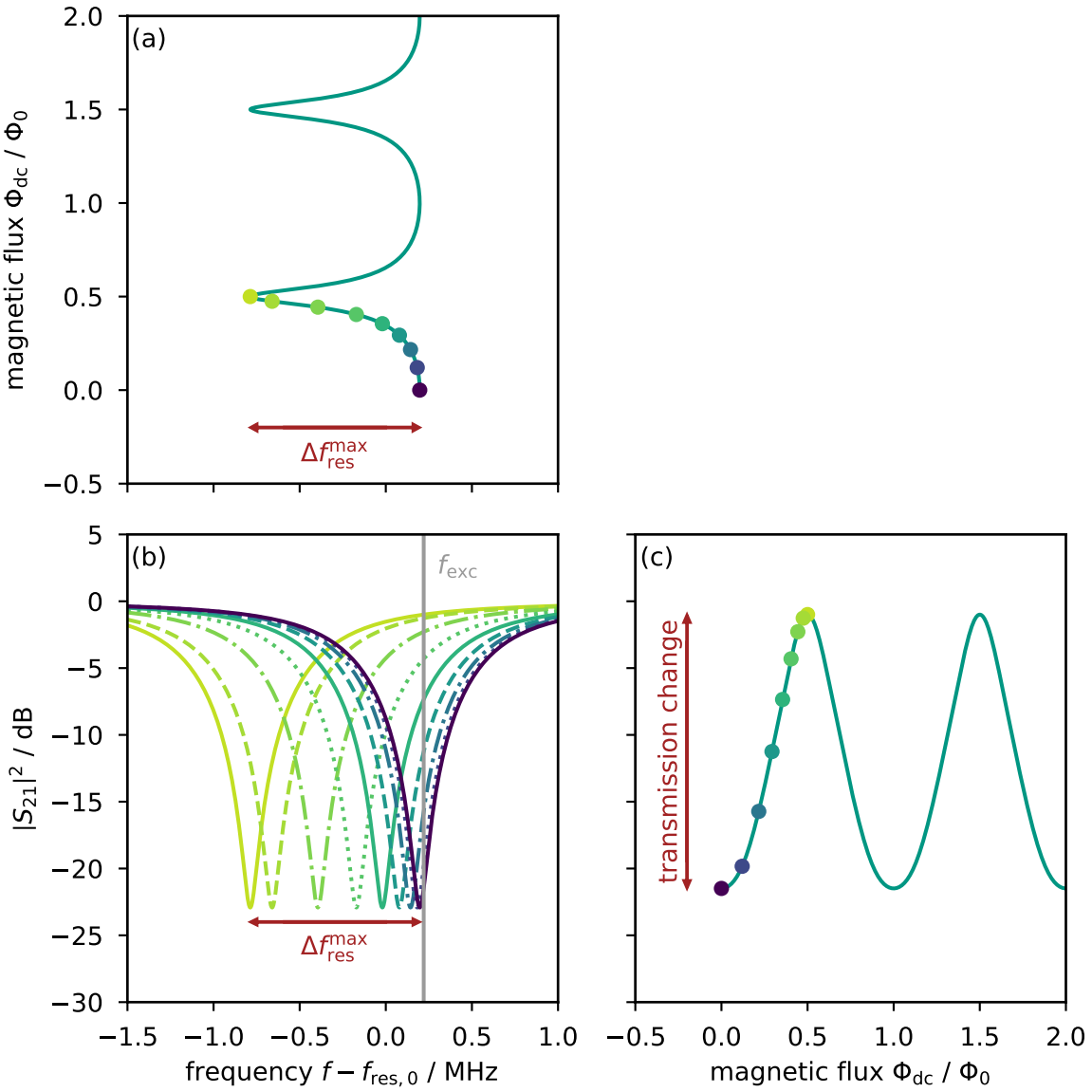


Fig. 6.4: (a) Resonance frequency f_{res} of a μMUX channel versus the magnetic flux Φ_{dc}. The resonance frequency is modulated periodically around the unloaded value $f_{\mathrm{res},0}$. The amplitude of this modulation $\Delta f_{\mathrm{res}}^{\mathrm{max}} = 1\,\mathrm{MHz}$ is much smaller than the unloaded resonance frequency, which is in the GHz range. Some points along the first semi-period are marked in colour. (b) Transmission spectra $|S_{21}|^2$ for the colour-marked flux states of (a). Due to the resonance frequency modulation, the minima of the spectra are shifted accordingly. A suitable probe tone frequency f_{exc} for readout is marked in grey. (c) Transmission $|S_{21}(f_{\mathrm{exc}})|^2$ at the probe tone frequency versus magnetic flux Φ_{dc}. The same flux states from (a) and (b) are also highlighted here. The periodic dependence of the transmission on the magnetic flux is easily discernible. For these plots, we have assumed a resonance frequency of $f_{\mathrm{res},0} = 4\,\mathrm{GHz}$, a bandwidth and resonance frequency shift of $\Delta f_{\mathrm{BW}} = \Delta f_{\mathrm{res}}^{\mathrm{max}} = 1\,\mathrm{MHz}$, a SQUID screening parameter of $\beta_{\mathrm{L}} = 0.6$ and a probe tone power of $P_{\mathrm{exc}} = -70\,\mathrm{dBm}$.

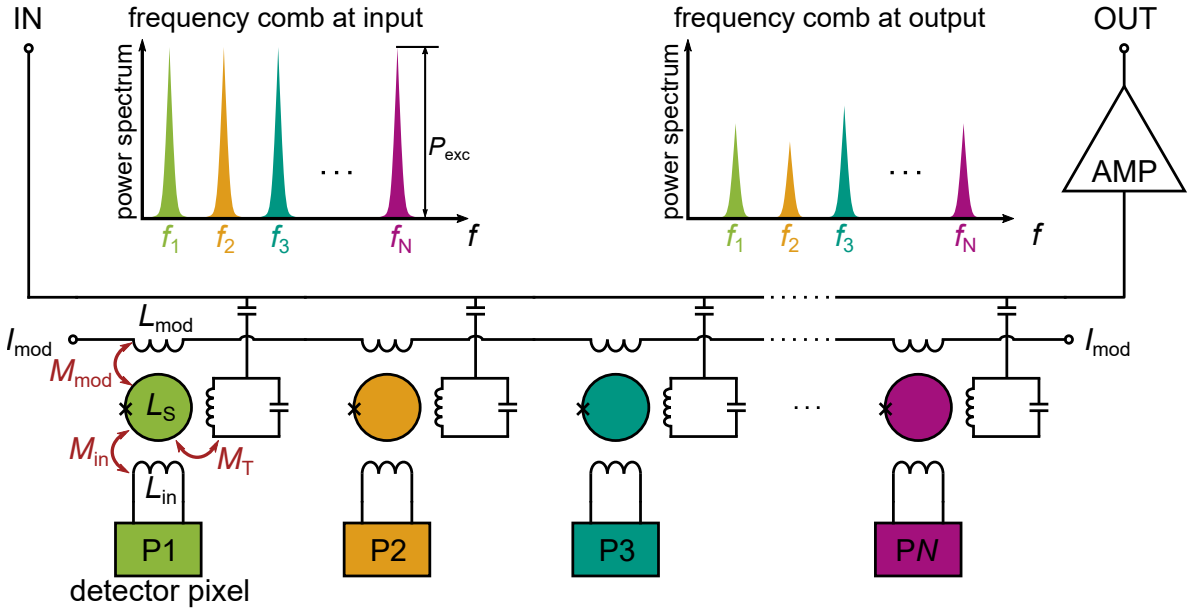


Fig. 6.5: Simplified schematic diagram of a μMUX, consisting of N readout channels. All channels are connected to the same transmission line and modulation line, and to a distinct detector. Each channel has a unique resonance frequency, and is probed using a suitably chosen probe tone. Consequently, a comb of N unique probe tones is applied to the input of the transmission line. At its output, the microwave signals are amplified by an amplifier, and the transmission of each probe tone is measured to deduce the signal of the respective detector pixel.

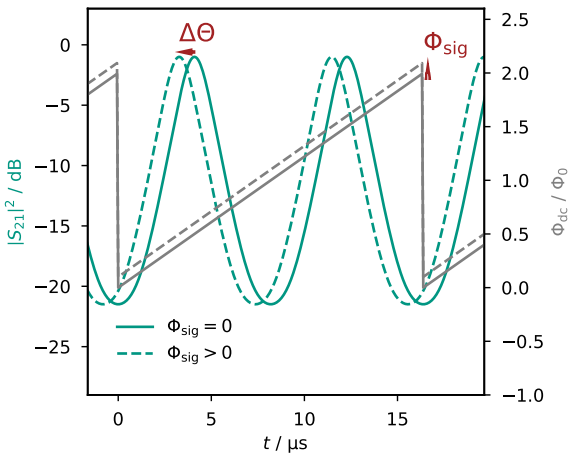


Fig. 6.6: Transmission $|S_{21}(f_{exc})|^2$ (green, left y-axis) and dc-flux $\Phi_{dc} = \Phi_{mod} + \Phi_{sig}$ (grey, right y-axis) versus time. The modulation amplitude is $A_{mod} = 2$, i.e. one modulation flux ramp induces $2\Phi_0$, resulting in two periods of transmission modulation per ramp segment. Even though the relation between transmission and flux is non-linear, the phase shift $\Delta\Theta$ of the transmission modulation depends linearly on the external signal $\Delta\Phi_{sig}$.

the sampling rate of the flux signal to be measured, and must be chosen accordingly. The current amplitude $I_{\mathrm{mod}}^{\mathrm{max}}$ is chosen such that it induces an integer multiple of flux quanta per ramp segment, i.e. $I_{\mathrm{mod}}^{\mathrm{max}} M_{\mathrm{mod}} = A_{\mathrm{mod}} \Phi_0$ with $A_{\mathrm{mod}} \in \mathbb{N}$. Due to the periodicity of the flux-dependent resonance frequency shift, this leads to a periodic modulation of the resonance frequency $f_{\mathrm{res}}(t)$ with frequency $f_{\mathrm{mod}} = f_{\mathrm{ramp}} I_{\mathrm{mod}}^{\mathrm{max}} M_{\mathrm{mod}} / \Phi_0 = A_{\mathrm{mod}} f_{\mathrm{ramp}}$. With a properly selected probe tone frequency f_{exc} this results in a modulation of the transmission $S_{21}(t)$ with the same frequency f_{mod}, as illustrated in figure 6.6. Any additional flux signal Φ_{sig}, which we assume to be quasi-static with respect to the ramp repetition rate f_{ramp}, causes a quasi-constant flux offset across the entire ramp segment, resulting in phase shift $\Delta\Theta = 2\pi\Phi_{\mathrm{sig}}/\Phi_0$ of the periodic transmission response. We can determine this phase shift by demodulating the transmission response with the modulation frequency f_{mod}. Determining the phase for each ramp segment finally yields a signal flux time trace. The relation between phase shift and signal flux linearises the signal, while the only hardware requirement at cryogenic temperatures is the additional modulation coil coupled to the rf-SQUID loop. Since the flux ramp signal is identical for all readout channels, they can all be connected in series, requiring only one additional pair of wires between room temperature and the cryogenic stage regardless of the pixel count. FRM is thus highly suited to read out large systems of multiplexed detectors. One downside is the reduction in measurement bandwidth. A suitably large number of data points per ramp segment is required to effectively determine the phase shift during demodulation, however each ramp segment only yields a single signal data point. The effective measurement bandwidth is thus reduced by a factor $W = f_{\mathrm{s}}/f_{\mathrm{ramp}}$, where f_{s} is the sampling rate of the data acquisition system (DAQ). Additionally, the reduction in SNR caused by using the entire transmission response may increase the noise: From figure 6.6, it is apparent that $S_{21}(\Phi)$ is nearly sinusoidal, with steep sections where the flux-to-transmission transfer coefficient $K_\phi(\phi) = (\partial\,|S_{21}(\phi)|\,/\partial\phi)$ is large and regions close to the extrema where $K_\phi(\phi)$ is small or even zero. This leads to an effective value of the transfer coefficient which is smaller than the maximum value. For non-FRM-linearised, i.e. open-loop readout, the working point would be chosen such that $K_\phi(\phi)$ is maximised. The reduction in the effective transfer coefficient for FRM yields a lower SNR and therefore, after demodulation, a penalty to the noise contributions which occur in the readout chain after the multiplexer, e.g amplifier noise. Since in most contemporary systems the dominant noise source is indeed the cryogenic amplifier, this is a notable effect in current systems. The amplifier noise is effectively increased by the degradation factor

$$c_{\mathrm{deg_t}} = \sqrt{\frac{\left(K_\phi^{\mathrm{max}}\right)^2}{\langle K_\phi^2 \rangle}} \quad \text{with} \quad \langle K_\phi^2 \rangle = \frac{1}{2\pi} \int_0^{2\pi} \left(\frac{\partial\,|S_{21}(\phi)|}{\partial\phi} \right)^2 d\phi. \tag{6.34}$$

During demodulation, typically only the phase of the sinusoidal contribution with frequency f_{mod} is determined. For not entirely sinusoidal signals, this leads to an effective loss of signal power due to the existence of higher modes. Again this leads to a noise degradation by a factor of

$$c_{\mathrm{deg_p}} = \frac{\sum_k |a_k|^2}{|a_{\mathrm{base}}|^2}. \tag{6.35}$$

where a_k are the coefficients of the Fourier transform of the transmission response, and a_{base} is the Fourier coefficient with the frequency f_{mod} which is used for phase determination. Finally, we typically cut some data points at the start and end of each ramp segment to avoid transients from negatively affecting demodulation. Thus, only a fraction $\alpha < 1$ of each ramp segment is used for evaluation, further degrading the noise by $c_{\mathrm{deg_a}} = \sqrt{\alpha}$ [Mat12]. When using FRM compared to open loop, the readout noise is thus degraded by a factor of $c_{\mathrm{deg}} = c_{\mathrm{deg_t}} c_{\mathrm{deg_a}} c_{\mathrm{deg_p}}$. This degradation is minimal for a perfectly sinusoidal, non-cropped transmission modulation, forming a lower bound for real signals of $c_{\mathrm{deg}} \geq \sqrt{2}$. Another, generally beneficial side-effect of FRM is its insensitivity to excess low-frequency noise added at the resonator (or at the amplifier). Such noise may arise in μMUX due to two-level tunnelling systems (TLS) in the vicinity of the microwave resonator [Gao07]. Any excess noise at frequencies much below the ramp reset rate f_{ramp} effectively causes, over a single ramp segment, a constant offset. This offset however has little influence on the phase shift $\Delta\Theta$ determined during demodulation, and is thus inconsequential for the resulting output signal.

6.4 Hybrid microwave SQUID multiplexing

In an effort to improve multiplexing performance, one can combine multiple multiplexing techniques [Rei08, Irw18, Yu20]. At the time of writing, one problem of μMUX is the fabrication tolerances of the microwave resonators, which results in an undesired frequency spread. To control crosstalk between individual channels, it is paramount to ensure a sufficient frequency spacing between neighbouring resonators. This is usually expressed with the guard factor $\eta_{\mathrm{BW}} = (f_{\mathrm{res}i+1} - f_{\mathrm{res}i})/\Delta f_{\mathrm{BW}}$, given by the ratio of the distance $f_{\mathrm{res}i+1} - f_{\mathrm{res}i}$ between neighbouring resonators in frequency space and the resonator bandwidth Δf_{BW}. Usually, a guard factor $\eta_{\mathrm{BW}} = \mathcal{O}(10)$ is sufficient to limit crosstalk to tolerable levels. The frequency spread due to fabrication tolerances thus effectively sets a lower limit to the spacing of resonators in frequency space. For applications where only small bandwidths per channel suffice (e.g. bolometers), this means that the total multiplexing factor may be limited by fabrication accuracy rather than feedline signal capacity. Naturally, this is highly undesirable. At the IMS, we have developed a hybrid multiplexing scheme (HμMUX) [Sch22] which combines the previously described microwave SQUID multiplexing with flux ramp modulation multiplexing [Ric21]. The latter is a method of MHz frequency multiplexing previously applied to dc-SQUIDs.

One resonator channel of a HμMUX is schematically depicted in figure 6.7. In contrast to μMUX, it is important to note that a single resonator channel now comprises multiple readout channels. The fundamental idea of HμMUX is simple. If fabrication tolerances limit the total number of resonator channels which can be coupled to the

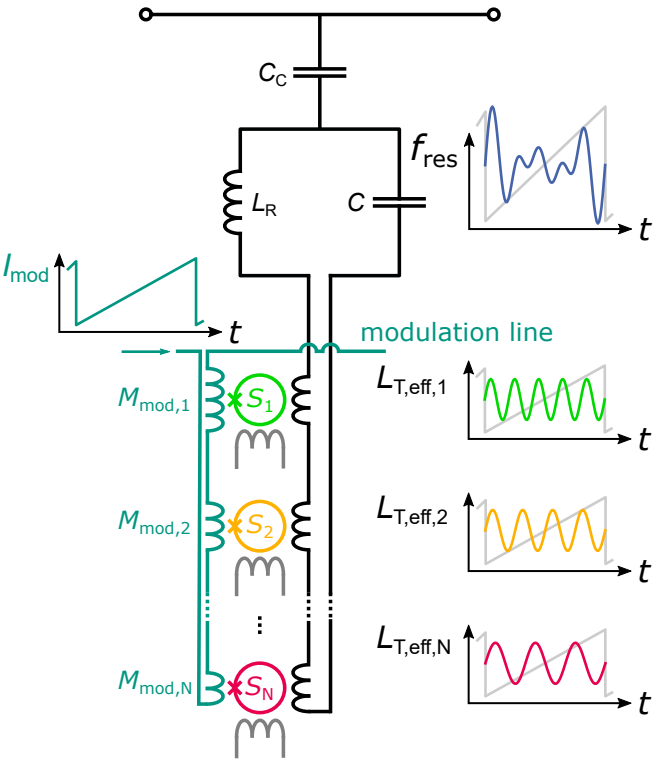


Fig. 6.7: Schematic circuit diagram of a single HμMUX resonator channel. The resonator is coupled to a number of N identical rf-SQUIDs. Each SQUID experiences a unique modulation amplitude $A_{\mathrm{mod}i}$ during FRM, leading to a unique modulation frequency $f_{\mathrm{mod}i}$. From the modulation of the resonance frequency f_{res}, caused by all SQUIDs combined, the individual signals can be recovered via demodulation with the respective modulation frequencies.

same transmission line, then we can only increase the multiplexing factor further by increasing the readout channels per resonator. To do this, we couple a number N of rf-SQUIDs to the same resonator. Much like a regular μMUX, we use FRM to linearise the HμMUX output. By carefully choosing the mutual inductance $M_{\mathrm{mod}i}$, $i \in [1,N]$ between each of these SQUIDs and the modulation line, we can make sure that the modulation frequencies $f_{\mathrm{mod}i} = f_{\mathrm{ramp}} M_{\mathrm{mod}i} I_{\mathrm{mod}}^{\mathrm{max}} / \Phi_0 = A_{\mathrm{mod}i} f_{\mathrm{ramp}}$ of all SQUIDs are unique. During the FRM demodulation step, we can demodulate the resulting signal with each modulation frequency $f_{\mathrm{mod}i}$ to retrieve the respective signal. HμMUX therefore increases the multiplexing factor by a factor of N compared to a regular μMUX using the same number of microwave resonators.

Another meaningful advantage of HμMUX is that no special readout electronics are needed beyond an SDR system as required for regular μMUX. Only minor modifications to software are required to demodulate the transmission time trace with respect to several unique frequencies, rather than just as single one.

6.4.1 First HμMUX device and multiplexed readout

To verify the feasibility of HμMUX, especially without requiring additional readout hardware, we have designed and fabricated a prototype as depicted in figure 6.8. Each resonator channel consists of a superconducting lumped-element resonator comprising the meander-shaped resonator inductance L_{R}, coupling inductance L_{T} and interdigital capacitance C. The latter was tuned appropriately in dependence on the designed res-

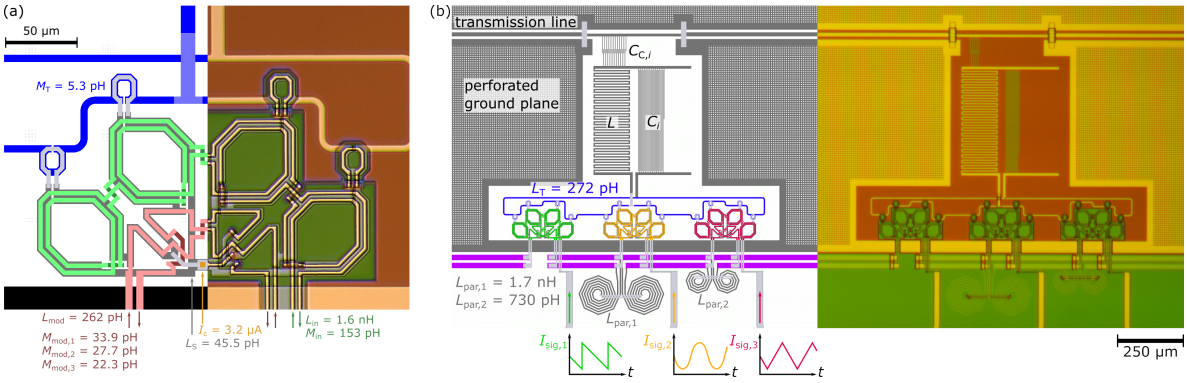


Fig. 6.8: (a) Layout (left) and micrograph (right) of a single non-hysteretic unshunted rf-SQUID, as it was used in our HμMUX prototype. The rf-SQUID comprises four loops connected in parallel. The load inductor L_T (blue, top), input coil L_in (green, middle) and modulation coil L_mod (red, bottom) are placed above or below the SQUID loops. The designed (mutual) inductance values are displayed. (b) Layout (left) and micrograph (right) or a single resonator channel each. One lumped-element resonator couples to $N = 3$ rf-SQUIDs, thus forming 3 readout channels. To tune the modulation amplitudes $A_{\mathrm{mod},i}$, coils with inductances $L_{\mathrm{par},1}$ and $L_{\mathrm{par},2}$ in parallel to the modulation coils of the rf-SQUIDs with indices 2 and 3 are used, respectively. The three independent SQUIDs are colour coded for easy distinction.

onance frequency in the range of 4 GHz to 4 GHz. The bandwidth of the resonance is set via the coupling capacitance C_C between the resonator and the coplanar waveguide transmission line. The latter carries the probe tones from room temperature to the device and enables readout. The coupling inductance couples to $N = 3$ rf-SQUIDs, each with loop inductance $L_\mathrm{S} = 45.5\,\mathrm{pH}$ and an unshunted Josephson tunnel junction with critical current $I_\mathrm{c} = 3.2\,\mu\mathrm{A}$. The loop consists of four washers connected to form a parallel gradiometer, minimising the influence of magnetic background fields. The three SQUIDs are identical in design, and the mutual inductances $M_{\mathrm{mod},i}$ were adjusted by connecting inductors in parallel to the modulation coils L_mod of each SQUID. These resulted in mutual inductances of $M_{\mathrm{mod},1} = 33.9\,\mathrm{pH}$, $M_{\mathrm{mod},2} = 27.7\,\mathrm{pH}$ and $M_{\mathrm{mod},3} = 22.3\,\mathrm{pH}$, respectively.

For the measurement, we have mounted the prototype device into a dipstick measurement setup and submerged it in liquid helium. The chip was electronically connected to a printed circuit board using ultra-sonic wire bonding of aluminium wire. Strict limitations of the size of the setup did not allow for a cryogenic amplifier stage, so only room-temperature amplification was possible.

To characterise the device, we first used a vector network analyser to acquire transmission spectra on a HμMUX resonator channel. From these transmission spectra, the resonance frequency f_res was determined. We then applied a constant current to the modulation coil, leading to magnetic flux coupling into the individual SQUIDs. In this way, we recorded the resonance frequency f_res versus the applied modulation current

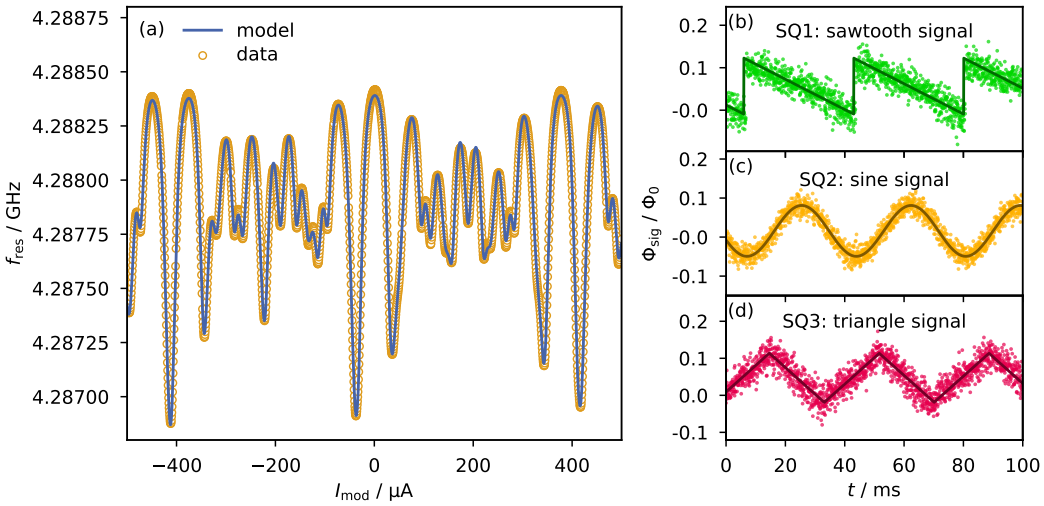


Fig. 6.9: (a) Resonance frequency f_{res} of a HμMUX resonator channel versus the modulation current I_{mod}. The resulting modulation results from all three rf-SQUIDs coupled to the resonator, and can be described very accurately by a superposition of the individual resonance frequency shifts of all SQUIDs (blue line) resulting from equation 6.8. (b)-(d) Demodulated test signals Φ_{sig} injected into the SQUID "SQi" via its input coil. All three signals were acquired on a single HμMUX resonator channel, and the shape of the applied test signals (solid lines) are easily recognisable.

I_{mod} as plotted in figure 6.9(a). While the resonance frequency modulation caused by each rf-SQUID individually is somewhat reminiscent of a sine curve, the total modulation in a HμMUX resonator channel results from all N SQUIDs simultaneously. Due to their different mutual inductances $M_{\mathrm{mod},i}$ to the modulation coil, the period length of all SQUIDs is unique, and the resulting total frequency modulation is thus a superposition of the N sine-like individual SQUID responses. We can use equation 6.8 for each SQUID and fit it to the data, and see that our multiplexer model originally developed for regular μMUX easily extends to HμMUX also. We can thus reliably predict the behaviour of HμMUX with the same level of confidence.

Additionally, we have used our SDR system to actually operate a HμMUX resonator channel. We have applied a modulation ramp and continuously monitored the transmission at a suitable probe tone frequency. Transmission data recording was done via the SDR system, but demodulation of the transmission time trace was performed offline. We have applied distinct test signals to the input coils of all 3 rf-SQUIDs connected to one resonator, and the signal time traces retrieved after demodulation are depicted in figure 6.9(b). We can easily differentiate the signal shapes, even though the lack of a cryogenic amplifier resulted in significant noise. This noise makes an assessment of crosstalk between the channels difficult, but we can estimate an upper bound of 1.1 %. We have thus successfully demonstrated the operation of a HμMUX, without any hardware requirements beyond those of regular μMUX.

6.4.2 Bandwidth and noise performance of HμMUX compared to μMUX

Regarding the potential performance of HμMUX, especially when comparing to regular μMUX, we can use some general considerations to draw some important conclusion with respect to multiplexing factor, per-channel bandwidth and readout noise. We have already established that the modulation frequencies $f_{\mathrm{mod}\,i} = A_{\mathrm{mod}\,i} f_{\mathrm{ramp}}$ of all N rf-SQUIDs of the same resonator channel must be unique. Since the ramp reset rate f_{ramp} is fixed, this necessitates unique modulation amplitudes $A_{\mathrm{mod}\,i}$. Additionally, as presented in section 6.3, FRM linearisation requires an integer-valued modulation amplitude, i.e. $A_{\mathrm{mod}\,i} \in \mathbb{N}$. Furthermore we want to ensure that no two modulation amplitudes are integer multiples of one another. Otherwise higher harmonics in the response of one channel may lead to excessive crosstalk in another. This brings us to the conclusion:

$$A_{\mathrm{mod},1} < A_{\mathrm{mod},2} < ... < A_{\mathrm{mod},N} < 2A_{\mathrm{mod},1}. \tag{6.36}$$

Here, we assume for simplicity that the entirety of each ramp segment is used for demodulation. After demodulation, we acquire one signal data point per ramp segment. The measurement bandwidth is hence defined by the ramp reset rate f_{ramp}, which we want to maximise. Due to the finite response time of the microwave resonator, all modulation frequencies must be below the limit frequency f_{lim} above which the resonator can no longer adequately follow the modulation. Consequently, the modulation amplitudes $A_{\mathrm{mod},i}$ must be as small as possible. Given the restrictions of unique and integer valued modulation amplitudes, we can conclude that ideally we choose the difference between neighbouring amplitudes as the smallest integer, i.e. unity: $A^{\mathrm{min}}_{\mathrm{mod},i+1} - A^{\mathrm{min}}_{\mathrm{mod},i+1} = 1$. This leads to a natural choice of modulation amplitudes:

$$\begin{aligned} A^{\mathrm{min}}_{\mathrm{mod},N} + 1 &\stackrel{!}{=} 2A^{\mathrm{min}}_{\mathrm{mod},1} && (6.37)\\ \rightarrow A^{\mathrm{min}}_{\mathrm{mod},1} + N &\stackrel{!}{=} 2A^{\mathrm{min}}_{\mathrm{mod},1} && (6.38)\\ \rightarrow A^{\mathrm{min}}_{\mathrm{mod},1} &\stackrel{!}{=} N && (6.39)\\ \rightarrow A^{\mathrm{min}}_{\mathrm{mod},i} &\stackrel{!}{=} N + (i-1). && (6.40) \end{aligned}$$

The ramp reset rate f_{ramp}, and equivalently the measurement bandwidth, is ultimately limited by the largest of all modulation frequencies, i.e. $f_{\mathrm{mod}\,N}$. This yields the relation

$$f_{\mathrm{mod},N} = A_{\mathrm{mod},N} f_{\mathrm{ramp}} = (2N-1)\, f_{\mathrm{ramp}} \stackrel{!}{=} f_{\mathrm{lim}} \propto \Delta f_{\mathrm{BW}}, \tag{6.41}$$

where we used that the limit frequency f_{lim} of a microwave resonator is proportional to its bandwidth Δf_{BW}. As a figure of merit, it makes sense to consider the bandwidth per readout channel (equivalent to the ramp reset rate f_{ramp}) and number of readout

channels per unit frequency ρ_{SQ} not independently, but rather the product of both. We can choose to divide the total signal capacity Δf_{tot} of the feedline either into many channels, each with a certain bandwidth, or into fewer channels with a respectively larger bandwidth each. It strongly depends on the application which approach is more suitable. As a result, it makes sense to consider the product $f_{\mathrm{ramp}}\rho_{\mathrm{SQ}}$ instead, which we can understand as a sort of measure for how efficiently we utilise the signal capacity of the feedline.

We can express the density of readout channels in frequency space $\rho_{\mathrm{SQ}} = N_{\mathrm{SQ}}/\Delta f_{\mathrm{tot}} = N/(\eta_{\mathrm{BW}}\Delta f_{\mathrm{BW}})$ either with the total number N_{SQ} of readout channels and the total feedline signal capacity Δf_{tot}, or on a per-resonator basis using the number N of readout channels per resonator, the resonator bandwidth Δf_{BW} and the guard factor η_{BW} required to limit interchannel crosstalk. Using this we can find that

$$(2N-1)\, f_{\mathrm{ramp}} \propto \Delta f_{\mathrm{BW}} \propto \frac{N}{\rho_{\mathrm{SQ}}}, \tag{6.42}$$

from which we can immediately conclude

$$f_{\mathrm{ramp}}\rho_{\mathrm{SQ}} \propto \frac{N}{(2N-1)} = \begin{cases} 1 & \text{for} \quad N = 1, \\ \frac{1}{2} & \text{for} \quad N \to \infty. \end{cases} \tag{6.43}$$

The bandwidth available on the transmission line is thus most efficiently utilised for $N = 1$, i.e. only one rf-SQUID per resonator, which is just regular μMUX. The largest penalty to efficiency is 1/2 and occurs in the limit of $N \to \infty$, i.e. an infinite number of rf-SQUIDs coupled to a single resonator. This penalty results because in HμMUX, we can no longer use the minimum feasible (i.e. most efficient) modulation amplitude $A_{\mathrm{mod}} = 1$ for all readout channels. The need for unique modulation amplitudes for the N rf-SQUIDs of a single resonator channel forces us to use higher, less efficient modulation amplitudes for some of them. While HμMUX does lead to a reduction in bandwidth efficiency, the fact that this penalty never exceeds 1/2 makes it a worthwhile trade-off for any application where the multiplexing factor limitation imposed by fabrication tolerances is even more significant.

In addition to the bandwidth, we will analyse the influence of amplifier noise in HμMUX. With regard to this, the flux-to-voltage transfer coefficient

$$V_{\Phi}^{\mathrm{max},i} \propto \frac{\Delta f_{\mathrm{res}}^{\mathrm{max},i}}{\Delta f_{\mathrm{BW}}}\sqrt{P_{\mathrm{exc}}} \tag{6.44}$$

is of major importance. Here, $\Delta f_{\mathrm{res}}^{\mathrm{max},i}$ denotes the maximum resonance frequency shift caused by the rf-SQUID with index i, and P_{exc} is the probe tone power.

Assuming all N SQUIDs contribute equally to the total resonance frequency shift $\Delta f_{\mathrm{res}}^{\mathrm{max,tot}} = \sum \Delta f_{\mathrm{res}}^{\mathrm{max},i}$, i.e. that $\Delta f_{\mathrm{res}}^{\mathrm{max},i} = f_{\mathrm{res}}^{\mathrm{max,tot}}/N$ regardless of the index i, and keeping in mind that we need to keep the total resonance frequency shift $\Delta f_{\mathrm{res}}^{\mathrm{max,tot}} \propto \Delta f_{\mathrm{BW}}$ independently of the number N of rf-SQUIDs, we can conclude

$$V_{\Phi}^{\mathrm{max},i} \propto \frac{\sqrt{P_{\mathrm{exc}}}}{N}. \tag{6.45}$$

In the cases where HμMUX makes sense, i.e. applications requiring a very large number of readout channels, the total power $P_{\mathrm{exc,tot}} = N_{\mathrm{res}} P_{\mathrm{exc}}$ of all probe tones is usually limited by the saturation power of the HEMT amplifier, rather than the ideal readout power for each resonator channel. We have introduced the total number N_{res} or resonators here. With HμMUX, we can read out the same number of channels compared to regular μMUX using N times fewer resonators. This allows us to increase the probe tone power P_{exc} proportionally without altering $P_{\mathrm{exc,tot}}$, and thus without overloading the HEMT amplifier. In this scenario, the flux noise per readout channel caused by the HEMT is given by

$$\sqrt{S_{\Phi,\mathrm{HEMT},i}} = \sqrt{N}\sqrt{S_{\Phi,\mathrm{HEMT}}}, \tag{6.46}$$

where $\sqrt{S_{\Phi\mathrm{HEMT}}}$ is the HEMT flux noise contribution for a regular μMUX channel with equivalent parameters. We can see that HμMUX also causes a noise penalty compared to regular μMUX. Intuitively this can be easily understood, as the transmission modulation caused by a resonator is now divided between N readout channels, decreasing the SNR for each SQUID.

6.5 Overview of the software framework for μMUX simulation

The mathematical description of a μMUX channel, as we will see in this chapter, makes an analytic prediction of electronic behaviour or noise performance unfeasible. Instead, we have developed and implemented a numerical method to generate a time-discrete transmission time trace $S_{21,k} = S_{21}(t_k)$ with $k = 0,...,N-1$ and $N \in \mathbb{N}$ at equidistant points t_k in time. This time trace $S_{21,k}$ represents a discrete version of the time-dependent, complex-valued transmission parameter $S_{21}(t)$ of a single μMUX channel as sampled in a real setup using a data acquisition system running with sampling rate $f_{\mathrm{s}} = 1/(t_k - t_{k-1})$. We then treat this artificial time trace in the same way as experimental data. By numerically simulating any measurement on a μMUX channel with predefined device- and readout parameters, we can asses a variety of performance characteristics, such as readout noise or maximum bandwidth.

Figure 6.10 depicts a flowchart outlining the structure of our simulation framework to perform a single simulation run yielding the transmission time trace $S_{21}(t_k)$ for a given set of parameters. This time trace is analysed using a modified Welch's method (for

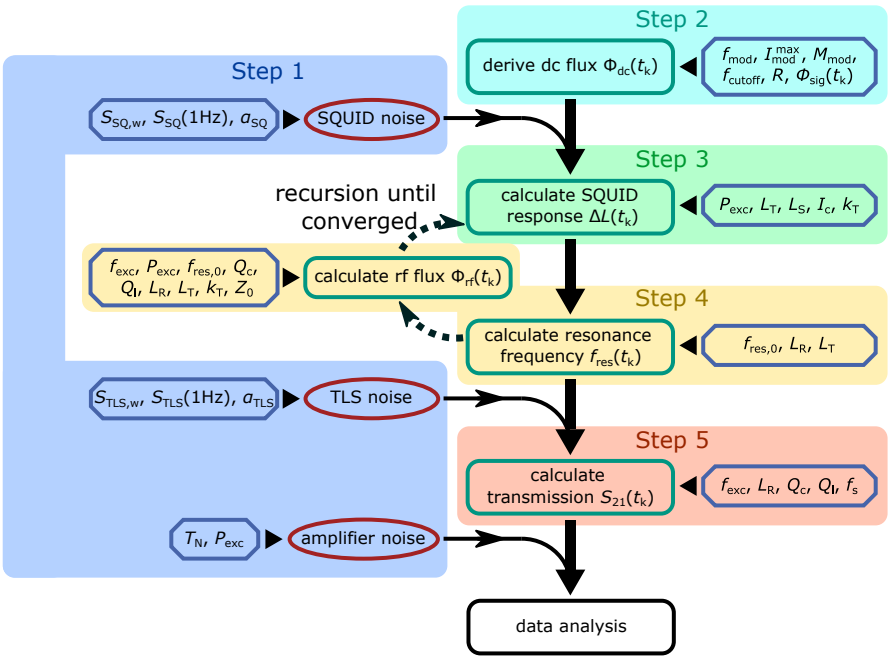


Fig. 6.10: Flowchart outlining the structure of our simulation framework. Blue octagons represent user specified input parameters, red ovals depict noise generators and green boxes numerical calculations. The individual steps as well as the meaning of the different symbols and variables are explained in the main text.

details see section 6.6) to determine the magnetic flux noise spectral density. In the following, we give a short overview of the basic workflow of such a single simulation run. In section 6.6, we then comprehensively discuss the individual steps including the developed algorithms and underlying equations.

6.5.1 Generation of noise traces

In step 1, we generate quasi-random noise time traces. The current implementation includes the three most dominant noise sources, i.e. amplifier noise added along the entire output signal path, two-level system (TLS) noise of the readout resonators affecting the resonance frequency as well as magnetic flux noise of the SQUID (SQ). We assume the amplifier noise to be white, with a magnitude calculated according to the predefined effective noise temperature T_N of the readout system as well as the readout power P_{exc}. For both, TLS noise and SQUID magnetic flux noise, we assume the noise to comprise a frequency-independent white and a frequency-dependent $1/f^{\alpha}$-like contribution. Either noise trace is hence generated according to three input parameters $S_{i,w}$, $S_i(1\,\mathrm{Hz})$ and α_i with $i \in \{\mathrm{TLS}, \mathrm{SQ}\}$ determining the resulting noise spectral density $S_i = S_{i,w} + S_i(1\,\mathrm{Hz})/f^{\alpha}$. As such, $S_{i,w}$ represents the amplitude of the white noise contribution and $S_i(1\,\mathrm{Hz})$ the amplitude at a frequency of $f = 1\,\mathrm{Hz}$ and the exponent α of the $1/f^{\alpha}$-like contribution. We have kept the code intentionally modular, so only

minor modifications are required to include arbitrary noise spectra of different shapes, e.g. ones measured experimentally.

6.5.2 Calculation of the quasi-static magnetic flux threading the the SQUID loop

In the second step, we compute the quasi-static flux Φ_{dc}. The total magnetic flux threading the SQUID loop is composed of three contributions, i.e. the actual input signal Φ_{in}, the sawtooth-shaped flux ramp Φ_{mod} as well as the magnetic flux Φ_{rf} induced by the microwave signal within the readout resonator. While not strictly static, the input signal and the flux ramp change much slower compared to the flux induced by the microwave signal. For this reason, we denote the first two contributions as 'dc-flux' $\Phi_{\mathrm{dc}} = \Phi_{\mathrm{in}} + \Phi_{\mathrm{mod}} + \Phi_{\mathrm{N}}$. It is composed of the preset noise-free input signal, the noise-free flux ramp signal as well as the flux noise time trace derived in the previous step (see section 6.5.1). One may assume the quasi-random noise Φ_{N} to not qualify as dc, given its uniform spectral density. However we generate noise with no spectral component above the Nyquist frequency of $f_{\mathrm{s}}/2$ with respect to the sampling rate $f_{\mathrm{s}} \ll f_{\mathrm{res}}$, which is typically $\mathcal{O}(10\,\mathrm{MHz})$, more than two orders of magnitude less than the resonance frequency. The sampling rate defines the time interval between data points in the generated transmission time trace $S_{21}(t_k)$, before a potential demodulation for FRM. Both, open-loop and FRM readout, can be modelled using our simulation framework, depending on the chosen input parameters. For open-loop readout, the modulation signal takes a predefined constant value representing a static magnetic flux bias. For flux ramp modulation, the flux signal is time-dependent and takes the shape of a sawtooth signal with ramp reset rate f_{ramp} and amplitude $\Phi_{\mathrm{mod}}^{\mathrm{max}} = M_{\mathrm{mod}} I_{\mathrm{mod}}^{\mathrm{max}}$. Here, $I_{\mathrm{mod}}^{\mathrm{max}}$ denotes the amplitude of the current running through the modulation coil and M_{mod} the mutual inductance between SQUID and modulation coil. Optionally, a Butterworth low-pass filter with predefined filter order R and cutoff frequency f_{cutoff} can be applied to the flux ramp signal to mimic a real system with finite bandwidth, resulting in ramp resets with finite steepness and transients in the transmission response.

6.5.3 Derivation of the effective inductance shift

The time-dependent shift $\Delta L_{\mathrm{T},k}$ of the inductance of the readout resonator, caused by the flux-state of the rf-SQUID, is difficult to calculate for the general case. For this third step, our simulation framework provides three methods to compute $\Delta L_{\mathrm{T},k}$, depending on the assumptions we can make about the setup. Analytical solutions were implemented for the cases of either very weak, i.e. negligible probe tone power P_{exc}, or very small, i.e. vanishing screening currents in the SQUID loop. In the general case of non-negligible probe tone power and finite screening currents, we use a tenth-order approximation, which is valid for values of the screening parameter up to $\beta_{\mathrm{L}} \leq 0.6$ [Weg22]. The latter two methods requires the self-consistent solution of an implicit equation, and can thus not be computed directly. Instead, a numerical recursive approach is required. We will

describe this in more detail in section 6.6.2. Relevant input parameters in this step are the SQUID inductance L_S, the critical current I_c, the geometric coupling parameter k_T between resonator and SQUID as well as the mutual inductance M_mod between modulation coil and SQUID. The flux state of the SQUID is set by the dc flux Φ_dc derived in the previous step as well as the radio frequency contribution Φ_rf induced by the current flowing within the resonator.

6.5.4 Calculation of the actual resonance frequency

In step 4, the time-dependent resonance frequency shift $f_{\mathrm{res},k}$ resulting from the effective inductance shift ΔL_T is derived. In addition to TLS noise, which causes a statistic fluctuation of the resonance frequency, the resonator parameters specified by the user enter. These include the unloaded resonance frequency $f_{\mathrm{res},0}$, the resonator inductance L_R, the coupling inductance L_T, the coupling quality factor Q_c, the loaded quality factor Q_l and the impedance Z_0 of the transmission line. Depending on the method used to derive the inductance shift ΔL_T, this step may also have to be computed iteratively. For a non-negligible probe tone power P_exc, the shift ΔL_T depends on the circulating currents in the resonator. These in turn depend on the relative positions of shifted resonance frequency f_res and fixed probe tone f_exc. As the resonance frequency f_res in turn depends on the inductance shift ΔL_T, we come full circle, and the equations can not be solved analytically. Once the resonance frequency f_res is calculated, the effective resonance frequency noise caused by TLS is added to yield the time trace of the resonance frequency $f_{\mathrm{res},k}$.

6.5.5 Derivation of the transmission coefficient

Finally, in step 5, all results from previous steps are combined, yielding the transmission time trace $S_{21,k}$. To maximise the measurement bandwidth, the ramp reset rate f_ramp and consequently the modulation frequency f_mod are usually set to approach the upper limits set by the resonator bandwidth. Thus, we need to take the finite settling time of the resonator into account when computing the transmission time trace $S_{21,k}$. In our simulation framework, the non-equilibrium dynamics of the superconducting lumped-element resonator is modelled by a first-order approximation. Adding amplifier noise to the complex transmission coefficient $S_{21,k}$ yields the final simulation output, which can subsequently be treated much the same way as regular experimental data for further analysis.

6.6 Detailed description of the simulation framework

The method used to generate noise time traces in the first step is identical for all three noise contributions and only differs by using different power spectral densities (PSDs). For a given PSD $\hat{S}_\mathrm{x}(f)$ of zero-mean noise of any observable X, the goal is to synthesise

a quasi-random time-discrete noise time trace x_k at equidistant time points $t_k = k/f_\mathrm{s}$ sampled with the sampling rate f_s. Here, $k = 0,...,N-1$ is the data point index and $N \in \mathbb{N}$ the total length of the dataset. We begin by generating noise coefficients $\hat{a}_j$ in frequency space with amplitudes

$$|\hat{a}_j| = \begin{cases} \sqrt{\hat{S}_\mathrm{x}(f_\mathrm{s}\frac{j}{N})} & \text{for } j = -\frac{N}{2}, -\frac{N}{2}+1,...,+\frac{N}{2}-1 \\ 0 & \text{for } j = 0 \end{cases} \tag{6.47}$$

as well as quasi-random phases θ_j following a uniform distribution

$$\hat{a}_j = |\hat{a}_j|\, \mathrm{e}^{\mathrm{i}\theta_j}, \quad \theta_j \in [0,2\pi)\,. \tag{6.48}$$

The quasi-random phases introduce the element of randomness that differentiate noise from non-statistical signals. The amplitude of the coefficients $\hat{a}_j$ must be well-defined to yield our desired PSD, but the phases are deliberately randomised to generate uncorrelated noise time traces. We use a quasi-random approach in our software, since it is much faster and true randomness is not required. We employ the permuted congruential generator PCG64, as implemented in the Python library *numpy*. The noise coefficient $\hat{a}_0$ at zero frequency must vanish to ensure zero-mean noise, regardless of the targeted noise spectral density. Using an inverse fast Fourier transform (FFT) yields a complex-valued discrete noise time trace:

$$x_k = \sqrt{\frac{f_s}{2}} \sum_{j=-N/2}^{N/2-1} \mathrm{e}^{2\pi\mathrm{i}\frac{jk}{N}} \hat{a}_j, \quad k = 0,...,N-1. \tag{6.49}$$

In case that real-valued noise is needed, the sum of the real and imaginary parts of each x_k is used. The spectral density of the noise remains the same. In the simulations, the transmission noise caused by the amplifier is complex-valued, whereas the flux noise in the SQUID and the resonance frequency noise are real-valued.

The noise time traces are generated first as they are crucial for the derivation of all intermediate results. Next we compute the external quasi-static flux contribution $\varphi_{\mathrm{dc},k} = \varphi_{\mathrm{sig},k} + \varphi_{\mathrm{mod},k} + \delta\varphi_k$, which in turn comprises the signal time trace $\varphi_{\mathrm{sig},k}$ defined as an input by the user, the modulation flux $\varphi_{\mathrm{mod},k}$ induced by the modulation coil and the effective magnetic flux noise $\delta\varphi_k$ of the SQUID. As illustrated previously, the noise time trace contains no frequency contributions above $f_\mathrm{s}/2$ and is thus treated as quasi-static with respect to the resonance frequency f_res.

In a microwave SQUID multiplexer operated with flux ramp modulation, a sawtooth-shaped modulation current I_mod is applied to the modulation coil. The mutual inductance between SQUID loop and modulation coil is M_mod, leading to a modulation flux $\varphi_\mathrm{mod} = 2\pi M_\mathrm{mod} I_\mathrm{mod}/\Phi_0$. In the simulation framework, a modulation current time trace $I_{\mathrm{mod},k}$ is generated using a predefined ramp repetition rate f_ramp and ramp amplitude $I_\mathrm{mod}^\mathrm{max}$. In software, a sawtooth shape with infinitely steep resets and perfectly linear ramp segments can be generated effortlessly. However, to mimic real electronics, we

include the possibility to apply a Butterworth low-pass filter to the time trace $I_{\mathrm{mod},k}$ to emulate the finite bandwidth of real signal generators and transmission lines. If the simulation is run with open-loop readout, the modulation flux is assumed to be constant, i.e. $\varphi_{\mathrm{mod},k} = \varphi_{\mathrm{bias}} = \mathrm{const.}$. The bias flux is then typically chosen such that the transfer coefficient $K_\phi(\Phi) = (\partial \left|S_{21}(\Phi)\right| / \partial\Phi)$ is maximised: $K_\phi(\Phi_{\mathrm{bias}}) = K_\Phi^{\mathrm{max}}$.

The method to derive the time trace $f_{\mathrm{res},k}$ of the resonance frequency depends on the actual device parameters. This results in different expressions for the inductance shift ΔL_{T} with varying numerical complexity. We hence choose the actual method on the basis of the predefined device parameters.

6.6.1 Vanishing probe tone power $\Phi_{\mathrm{rf}} \to 0$

The analytic solution for the inductance shift ΔL_{T} at vanishing probe tone powers, i.e. $\Phi_{\mathrm{rf}} \to 0$, is given by expression 6.6. To evaluate this expression, the total magnetic flux φ_{tot} threading the SQUID loop must be determined. We can neglect the radio-frequency contribution $\varphi_{\mathrm{rf}} \to 0$ in this special case, but due to screening currents within in the SQUID loop, the total flux is given by the expression [Weg22]

$$\varphi_{\mathrm{tot}} = \varphi_{\mathrm{dc}} - \beta_{\mathrm{L}} \sin\left(\varphi_{\mathrm{tot}}\right). \tag{6.50}$$

Despite being an implicit equation, this relation is unique for $\beta_{\mathrm{L}} < 1$ and can be inverted to yield the explicit expression

$$\varphi_{\mathrm{dc}} = \varphi_{\mathrm{tot}} + \beta_{\mathrm{L}} \sin\left(\varphi_{\mathrm{tot}}\right) \tag{6.51}$$

which we can evaluate at a sufficiently large number of linearly spaced nodes $\varphi_{\mathrm{tot},j} \in [0,2\pi)$, yielding an equal number of points $\varphi_{\mathrm{dc},j}$. Since the relation is unique, a cubic spline interpolation to the dataset can be performed, yielding an interpolation function $f(\varphi_{\mathrm{dc}})$ such that $f(\varphi_{\mathrm{dc},j}) = \varphi_{\mathrm{tot},j}$. Moreover, as $\Delta L_{\mathrm{T}}(\varphi_{\mathrm{tot}})$ is 2π-periodic, the restriction to nodes $\varphi_{\mathrm{tot},j}$ on the interval $[0,2\pi)$ is sufficient. Using the interpolation function $f(\varphi_{\mathrm{dc}})$, we calculate the $\varphi_{\mathrm{tot},k}$ for each value of $\varphi_{\mathrm{dc},k}$ for the given time trace which is used in the subsequent evaluation of equation 6.6 to obtain an inductance shift time trace $\Delta L_{\mathrm{T},k}$. Once the inductance shift has been calculated, the resulting resonance frequency time trace $f_{\mathrm{res},k}$ is derived using the expression

$$f_{\mathrm{res},k} = f_{\mathrm{res},0} \left(1 - \frac{\Delta L_{\mathrm{T},k}}{L_{\mathrm{R}} + L_{\mathrm{T}}}\right)^{-\frac{1}{2}}. \tag{6.52}$$

Though this method can be applied for negligible probe tone powers only, it is valid for any value of the screening parameter $\beta_{\mathrm{L}} < 1$.

6.6.2 Vanishing screening currents $\beta_\mathrm{L} \to 0$

For vanishing screening currents within the SQUID loop, we can use expression 6.7 for the inductance shift ΔL_T. At non-zero probe tone powers P_exc, currents running within the inductor L_T induce a non-negligible radio frequency flux contribution with amplitude φ_rf into the SQUID loop. The inductance shift ΔL_T thus depends on the energy stored within the resonator, which in turn depends on the difference between the resonance frequency f_res and the frequency of the probe tone f_exc. Since the resonance frequency depends on ΔL_T, the solution to equation 6.7 can not be calculated directly. The radio frequency flux amplitude is given by $\varphi_\mathrm{rf} = 2\pi M_\mathrm{T} I_\mathrm{T}/\Phi_0$. Here, $M_\mathrm{T} = k_\mathrm{T}\sqrt{L_\mathrm{T} L_\mathrm{S}}$ denotes the mutual inductance between SQUID loop and the load inductor and I_T is the amplitude of the microwave current running in the inductor L_T. The latter is calculated using the analytical expression [Ahr22]

$$I_\mathrm{T}(f_\mathrm{exc}) = \sqrt{2P_\mathrm{exc}Z_0}\frac{2\pi f_\mathrm{exc}\sqrt{\frac{2}{Z_0(2\pi f_\mathrm{res})^3 L Q_\mathrm{c}}}}{\left(2i - 2\pi f_\mathrm{exc}\sqrt{\frac{2}{Z_0(2\pi f_\mathrm{res})^3 L Q_\mathrm{c}}}Z_0\right)\left(\frac{f_\mathrm{exc}^2}{f_\mathrm{res}^2} - 1\right) + \frac{f_\mathrm{exc}^3}{f_\mathrm{res}^3}\frac{2}{Q_\mathrm{c}}}. \tag{6.53}$$

To derive the resonance frequency time trace $f_{\mathrm{res},k}$, we first evaluate equation 6.7 with some initial (likely very inaccurate) guess of the radio frequency flux, in our case $\varphi_{\mathrm{rf},k}^{(0)} = 0$. We use equation 6.52 to then compute a first (and just as inaccurate) guess $f_{\mathrm{res},k}^{(0)}$ of the resonance frequency time trace. We can use this however to improve our estimate of the radio frequency flux amplitude $\varphi_{\mathrm{rf},k}^{(1)}$ by using equation 6.53. This in turn leads us to an improved guess of the resonance frequency $f_{\mathrm{res},k}^{(1)}$. In this way, we can increase the fidelity of our estimates with each iteration, provided the series converges towards a stable solution, until subsequent results for the resonance frequency have a sufficiently small deviation:

$$\varphi_{\mathrm{rf},k}^{(0)} = 0 \quad \forall\ k, \tag{6.54}$$

$$\hat{f}_{\mathrm{res},k}^{(m)} = \widetilde{f_\mathrm{res}}(\varphi_{\mathrm{dc},k}, \varphi_{\mathrm{rf},k}^{(m)}), \tag{6.55}$$

$$\varphi_{\mathrm{rf},k}^{(m+1)} = \widetilde{\varphi_\mathrm{rf}}(\hat{f}_{\mathrm{res},k}^{(m)}, f_{\mathrm{exc},k}). \tag{6.56}$$

up until

$$\sum_{k=0}^{N} \frac{\hat{f}_{\mathrm{res},k}^{(M)} - \hat{f}_{\mathrm{res},k}^{(M-1)}}{\hat{f}_{\mathrm{res},k}^{(M)}} \leq \epsilon_\mathrm{f} \tag{6.57}$$

at some $M \in \mathbb{N}$ for a given maximum tolerable difference ϵ_f. The result $f_{\mathrm{res},k} \equiv f_{\mathrm{res},k}^{(M)}$ is the resonance frequency time trace used for the remaining part of the simulation run. In this description, $\widetilde{f_\mathrm{res}}(\varphi_\mathrm{dc}, \varphi_\mathrm{rf})$ refers to equations 6.52 and 6.7, and $\widetilde{\varphi_\mathrm{rf}}(f_\mathrm{res}, f_\mathrm{exc})$ follows from equation 6.53. Naturally, this method only works if the series $\hat{f}_{\mathrm{res},k}^{(m)}$ converges, which has been the case for all reasonable choices of simulation parameters we have tested so far.

6.6.3 General case

In the most general case however, both the screening parameter β_L and the probe tone power P_exc take non-zero values. While no analytic solution has yet been found, we can use the approximate multi-term expression 6.8. This tenth-order expansion is valid up to values of $\beta_\mathrm{L} \leq 0.6$ for the screening parameter, and arbitrary probe tone powers P_exc.

Here, we again face the issue of implicitness, as the inductance shift ΔL_T depends on itself via the radio frequency flux amplitude φ_rf and the resonance frequency f_res much like in the previous section. Thankfully, the same recursive method can be applied here also, with the single difference that equation 6.8 is used instead of equation 6.7.

Once the resonance frequency time trace $\hat{f}_{\mathrm{res},k}$ has been derived using the most appropriate method, the effective resonance frequency noise $\delta f_{\mathrm{res},k}$ is added, representing the noise contribution of two-level systems within the resonator. The noisy resonance frequency trace $f_{\mathrm{res},k} = \hat{f}_{\mathrm{res},k} + \delta f_{\mathrm{res},k}$ is then used to calculate the transmission time trace $\hat{S}_{21,k}$.

Assuming a sufficiently slow modulation of the resonance frequency, the transmission of a resonator can be approximated by the steady-state expression 6.28. To maximise the measurement bandwidth, we typically choose the flux ramp repetition rate f_ramp as high as possible while maintaining a tolerable level of noise degradation. We will discuss the nature of this degradation and upper limits to f_ramp later, but for now it is important to understand that a fast modulation of the resonance frequency is common (and intentional) in real μMUX applications. The quasi-static approximation then no longer suffices, and we must take the finite resonator bandwidth into account as detailed in section 6.2.1. In a first-order approximation, we can describe the time-dependent transmission coefficient by expression 6.33 and rearrange it slightly:

$$\begin{aligned} S_{21}(t_0 + \Delta t) &\approx S_{21}^\mathrm{SS}(t_0 + \Delta t) \\ &+ \left[S_{21}(t_0) - S_{21}^\mathrm{SS}(t_0 + \Delta t)\right] \mathrm{e}^{-\pi[\Delta f_\mathrm{BW} - 2\mathrm{i}(f_\mathrm{res} - f_\mathrm{exc})]\Delta t}. \end{aligned} \tag{6.58}$$

In case that the initial value of $S_{21}(t_0)$ at a time t_0 is known, the transmission parameter $S_{21}(t_0 + \Delta t)$ at time $t + \Delta t$ can be derived with expression 6.58. Applying this method over and over again allows generating a time trace of arbitrary length, covering an arbitrary time span. It is worth mentioning that this approximation is only valid assuming S_{21}^SS to be quasi-static on the time scale Δt, which we can always ensure by making Δt sufficiently small. In the simulation, we use the steady state value $\hat{S}_{21,0} = S_{21}^\mathrm{SS}(t_0)$ for the initial time t_0 as starting value. The time interval $\Delta t = t_{k+1} - t_k = 1/f_\mathrm{s}$ is given by the sampling rate f_s:

$$\hat{S}_{21,0} = \hat{S}_{21,0}^\mathrm{SS}, \tag{6.59}$$

$$\hat{S}_{21,k+1} = \hat{S}_{21,k+1}^\mathrm{SS} + \left(\hat{S}_{21,k} - \hat{S}_{21,k}^\mathrm{SS}\right) \mathrm{e}^{-\pi\left[\Delta f_\mathrm{BW} - 2\mathrm{i}\left(f_{\mathrm{res},k} - f_{\mathrm{exc},k}\right)\right]\Delta t}. \tag{6.60}$$

Finally, transmission noise $\delta S_{21,k}$ is added, representing amplifier noise caused by the HEMT amplifier, yielding the final simulation output

$$S_{21,k} = \hat{S}_{21,k} + \delta S_{21,k}. \tag{6.61}$$

Here, the relation between the transmission noise spectral density $\hat{S}_{\mathrm{S21}}$ and the system noise temperature T_{N} is given by:

$$\sqrt{\hat{S}_{\mathrm{S21}}} = 2\sqrt{\frac{2k_{\mathrm{B}}T_{\mathrm{N}}}{P_{\mathrm{exc}}}}. \tag{6.62}$$

This transmission time trace $S_{21,k}$ resembles a measurement with a μMUX device with the given parameters, including noise, resonator latency and, if desired, transients due to finite bandwidth of the flux modulation ramp. The transmission time trace $S_{21,k}$ thus closely resembles a time-discrete dataset acquired during a measurement on a real device. Demodulation of the transmission time trace yields the output signal flux $\varphi_{\mathrm{out},j}$

$$\varphi_{\mathrm{out},j} = \arctan\left[\frac{\sum_{k=jW}^{(j+1)W-1} \sin\left(2\pi j f_{\mathrm{mod}}/f_{\mathrm{res}}\right)|S_{21,k}|}{\sum_{k=jW}^{(j+1)W-1} \cos\left(2\pi j f_{\mathrm{mod}}/f_{\mathrm{res}}\right)|S_{21,k}|}\right], \tag{6.63}$$

in case that flux ramp modulation is used. Here, $f_{\mathrm{mod}} = f_{\mathrm{ramp}} M_{\mathrm{mod}} I_{\mathrm{mod}}^{\mathrm{max}}/\Phi_0$ denotes the modulation frequency, and $W = f_{\mathrm{s}}/f_{\mathrm{ramp}}$ is the number of data points in between two resets of the modulation ramp. Obviously, the resulting signal time trace $\varphi_{\mathrm{out},j}$ has a factor of W fewer points than the transmission time trace $S_{21,k}$. For open-loop readout, the signal flux time trace $\varphi_{\mathrm{out},k}$ can be calculated from the transmission time trace $S_{21,k}$ using the transfer coefficient $K_\Phi(\varphi_{\mathrm{bias}})$:

$$\varphi_{\mathrm{out},k} = \frac{S_{21,k}}{K_\Phi(\varphi_{\mathrm{bias}})}. \tag{6.64}$$

Here, the transfer coefficient $K_\Phi(\varphi_{\mathrm{bias}})$ is determined during the simulation by numerically calculating the transmission-to-flux characteristic $S_{21}(\varphi_l)$ for 1024 linearly spaced data points of $\varphi_l \in [0,2\pi)$, and then subsequently calculating the numerical derivative at the specified bias flux value φ_{bias}. The signal flux time trace has the same number of data points as the transmission time trace $S_{21,k}$.

To analyse the readout noise, we use the same methods commonly applied to experimental data. We have opted to use a modification of the noise PSD estimation method originally proposed by P. D. Welch [Wel67], which is based on calculating a number of Q individual periodograms $P^q(f)$, each covering a subset of data points of the output signal time trace $\varphi_{\mathrm{out},k}$. The length of these subsets L must be smaller than the total number of data points in the output signal time trace $\varphi_{\mathrm{out},k}$, and subsequent subsets overlap with $L - D$ data points. All Q datasets combined cover the entirety of $\varphi_{\mathrm{out},k}$.

Each periodogram is then given by

$$P^q(f) = \frac{2}{f_\mathrm{s} \sum_{n=0}^{L-1} w_n^2} \left| \sum_{n=0}^{L-1} w_n \phi_{\mathrm{out},qD+n} \mathrm{e}^{-2\pi \mathrm{i} f n / f s} \right|^2 , \tag{6.65}$$

with the weights w_n of a window function. We use a Blackman-Harris window in our simulation. The estimator $S_\Phi(f)$ of the noise spectral density of the output signal time trace $\varphi_{\mathrm{out},k}$ is then given by the average of all periodograms:

$$S_\Phi(f) = \frac{1}{Q} \sum_{q=0}^{Q-1} P^q(f). \tag{6.66}$$

If the length L of the subsets is chosen large, the estimator $S_\Phi(f)$ contains information even down to low frequencies f. However, the number Q of individual sets is rather small, and only few individual periodograms can be averaged, leading to a low fidelity of the estimator. A choice of short window lengths L results in many subsets and thus a high fidelity of the estimator, but the estimator can not resolve low frequencies. We hence repeat this process for multiple different window lengths L_i. The combination of different subset lengths allows both a high estimator fidelity at large frequencies f as well as information about low frequencies, albeit at a lower fidelity.

7. Applications of numerical μMUX simulations: Predicting noise, estimating linearity and modelling alternative readout schemes

In this chapter we will present some insights into the optimisation and operation of microwave SQUID multiplexers gathered from our numerical simulations. We will look at the influence of the probe tone frequency f_{exc}, the prone tone power P_{exc} and the screening parameter β_{L} on the total readout noise, in an effort to find ideal parameter values. We will also provide some comparisons of simulated data to both experimental data and theoretical predictions, highlighting that our software framework works as intended. To conclude, we will give some further examples for applications of our simulation software, e.g. to model system linearity or more complex readout schemes. Firstly however, we will quickly motivate and define the default set of simulation parameters.

7.1 Default simulation parameters

Due to the complexity of the underlying physics of microwave SQUID multiplexing, the full configuration space comprises more than 30 individual parameters. While some of these parameters describe the constituent components of the multiplexer (e.g. inductances or capacitances), others regard the operation of the device (e.g. probe tone frequency f_{exc} and power P_{exc}, or the ramp reset rate f_{ramp}), or affect the simulation procedure itself (e.g. the number of data points of the simulated time traces). Our software framework is deliberately implemented to cover a wide range of parameters (with some caveats we will discuss later), but given the vast scale of the configuration space we had to agree on a set of defaults. The time and computational effort required to study the effect of all parameters at once would exceed the scope of this thesis and might be the topic of future work. In any further discussion, all parameters not explicitly noted take the default value listed here.

The basis for our default parameter set is defined by the μMUXs and readout electronics developed for the ECHo experiment [Gas17, Ric21, Ahr22], and is graphically presented in figure 7.1. This experiment targets the continuous readout of several thousand MMCs using multiplexers with 400 μMUX channels per transmission line. The total frequency range, limited by the HEMT amplifier, is 4 GHz to 8 GHz. To resolve the 1 µs rise time of the MMCs, a resonator bandwidth of $\Delta f_{\mathrm{BW}} = 1\,\mathrm{MHz}$ will be used. A software-defined radio (SDR) [San19, Kar20] system will handle both the generation of the frequency comb containing all probe tones, and the monitoring of the transmitted tones to acquire the transmission data. The sampling rate, with which the SDR can record this transmission data, is $f_{\mathrm{s}} = 15.625\,\mathrm{MHz}$ [Kar20] for each of the 400 channels. Each resonator comprises a meander-shaped inductance with $L_{\mathrm{R}} = 2\,\mathrm{nH}$, a load inductor

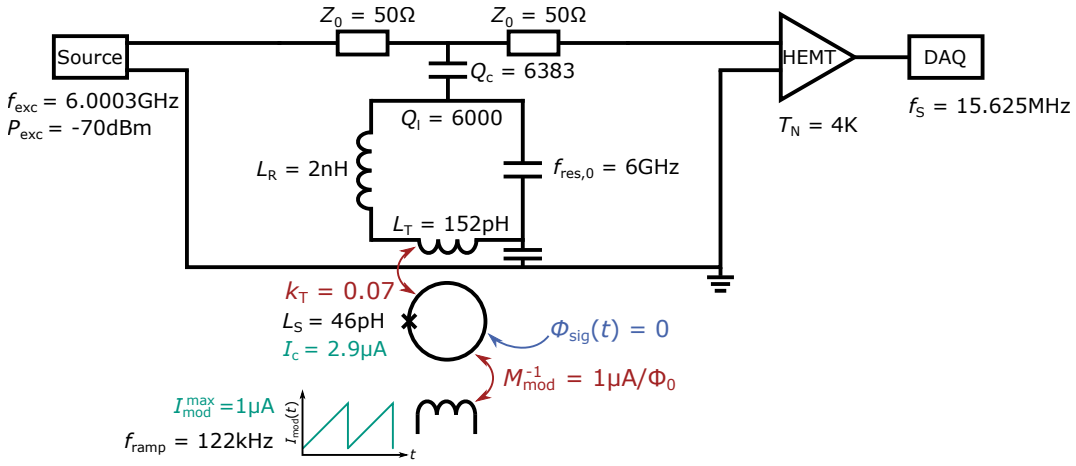


Fig. 7.1: Schematic circuit diagram of a single μMUX channel. The default values of device and readout parameters are depicted. The odd value of the coupling quality factor Q_c was chosen to yield a loaded quality factor $Q_l = 6000$ assuming an internal quality factor of $Q_i = 1 \times 10^5$. For clarity, we have omitted parameters which default to zero, such as unused noise sources.

with inductance $L_T = 152\,\mathrm{pH}$ and an interdigital capacitor whose capacitance C is set to yield a unique unloaded resonance frequency $f_{res,0}$. We will typically assume a resonance frequency of $f_{res,0} = 6\,\mathrm{GHz}$, at the centre of the available frequency interval.

We typically measure an internal quality factor $Q_i = 1 \times 10^5$ for real resonators. We adjust the effective coupling capacitance $C_{C,eff}$ (including both, the coupling inductance C_C and the parasitic inductance C_{para}) to yield the desired bandwidth of $\Delta f_{BW} = 1\,\mathrm{MHz}$. The default SQUID loop inductance is $L_S \simeq 46\,\mathrm{pH}$ with a critical current I_c of the Josephson tunnel junction to yield a screening parameter $\beta_L = 0.4$. The mutual inductance M_T is chosen to yield $\Delta f_{res}^{max} = \Delta f_{BW}$ and tuned by changing the value of the coupling factor k_T. It is worth noting that the Bessel function of the first kind, which appears in equation 6.8 can lead to jumps in the SQUID response if the radio frequency flux amplitude becomes too large. To mitigate this effect, the value of the coupling factor k_T has been restricted such that for any simulation the resonance frequency shift does not exceed 5 times the resonator bandwidth $\Delta f_{res}^{max} \leq 5\Delta f_{BW} = 5\,\mathrm{MHz}$. For different values of the internal quality factor Q_i, this threshold may have to be adjusted.

Projected is a readout bandwidth of 1 MHz per channel, using FRM linearisation. The default flux modulation ramp has an amplitude I_{mod}^{max} such that a maximum flux $1\,\Phi_0$ is induced. A ramp reset rate of $f_{ramp} = f_s/128 \approx 122.1\,\mathrm{kHz}$ provides sufficiently many data points per ramp segment for reliable and efficient demodulation. Infinitely steep ramp resets are assumed. The default excitation frequency is $f_{exc} = f_{res,0} + 0.3\,\mathrm{MHz}$, slightly above the largest resonance frequency f_{res} reached during modulation. We typically consider only amplifier white noise with an effective input noise temperature of $T_N = 4\,\mathrm{K}$ as resulting from state-of-the-art HEMT amplifiers connected to the multiplexer via superconducting coaxial cables and a cryogenic isolator.

The probe tone power is $P_{\mathrm{exc}} = -70\,\mathrm{dBm}$. Therefor, neither probe tone power nor screening currents are negligible, and we hence use the most general multiplexer model ($\beta_{\mathrm{L}} > 0, \varphi_{\mathrm{rf}} > 0$) for all simulations discussed in the following.

7.2 Software verification

Testing for proper functionality and finding bugs is an essential part of any software development. Of course, all components of our software framework were thoroughly tested individually. Given the scale and complexity of numerical microwave SQUID multiplexer simulations however, it is important to additionally verify the accuracy and reliability of the results as a whole. This poses an interesting challenge. There are two tests we have devised: A comparison between experimental data and simulated results is the most natural way to test our software framework. After all, accurately modelling a real device is the original motivation behind its development. Additionally, we can test for behaviour that is expected to emerge from simulations despite not being explicitly included. Such results are a powerful indication that the individual components of the software work together in the intended manner. As the in-depth bug searches of individual functions are likely to bore even the most dedicated reader, we will only present the latter two tests here.

7.2.1 Dependence of the flux noise on the probe tone power

One important result for μMUX operation is the ideal choice of probe tone power P_{exc}. Intuitively, we can understand that an increase in probe tone power improves the SNR at the HEMT amplifier input, which is the dominant source of noise. In reality, however, we need to take nonlinearities in the rf-SQUID into account, which will reduce the resonance frequency shift and thus the depth of the transmission modulation if the probe tone power becomes too large. As a result, an optimal value for the power of the probe tone can be found which minimises the readout flux noise.

In figure 7.2, experimental data of the white (i.e. high frequency) readout flux noise $\sqrt{S_{\Phi,\mathrm{white}}}$ versus the applied probe tone power P_{exc} is depicted (red dots). This specific channel has an unloaded resonance frequency of $f_{\mathrm{res},0} = 4.86\,\mathrm{GHz}$, resonator bandwidth $\Delta f_{\mathrm{BW}} = 3.1\,\mathrm{MHz}$, maximum resonance frequency shift $\Delta f_{\mathrm{res}}^{\mathrm{max}} = 0.95\,\mathrm{MHz}$, internal quality factor $Q_{\mathrm{i}} = 6400$ and screening parameter $\beta_{\mathrm{L}} = 0.4$. The measurement was performed with open-loop readout at a fixed magnetic bias flux $\Phi_{\mathrm{bias}} \approx 0.25\,\Phi_0$. For low probe tone powers $P_{\mathrm{exc}} < -70\,\mathrm{dBm}$, the effective readout noise decreases linearly with probe tone power. Here, the effect of power on the transmission response is negligible, and the increasing SNR dominates the power dependence. For large probe tone powers $P_{\mathrm{exc}} > -60\,\mathrm{dBm}$, the oscillating dependence with sharp peaks results from the nonlinearties introduced by the rf-SQUID at high rf excitation. This nonlinearity is expressed by the Bessel function of the first kind as it appears in the expressions 6.7 and 6.8 for the effective inductance $L_{\mathrm{T,eff}}$. In between both ranges, a characteristic

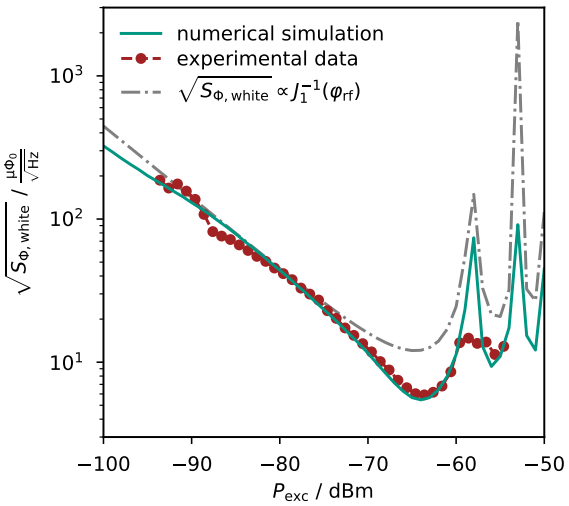


Fig. 7.2: Measured dependence of the white magnetic flux noise level $\sqrt{S_{\Phi,\mathrm{white}}}$ on the probe tone power P_{exc}. The data were acquired for an example channel of our most recent microwave SQUID multiplexer with lumped-element microresonators. Details about the device and readout parameters are given in the main text. The measurement was done in open-loop mode, i.e. without flux ramp modulation. In addition to measured data, the expected dependence using the analytical expression $\sqrt{S_{\Phi,\mathrm{white}}(\varphi_{\mathrm{rf}})} \propto J_1^{-1}(\varphi_{\mathrm{rf}})$ as well as results obtained with our simulation framework are shown.

minimum forms. Naturally, for optimised μMUX operation, we want to minimise the readout noise and thus operate in this minimum.

Using the expression given by our most recent multiplexer model [Weg22], we would expect the measured white noise level to follow the simple analytical model $\sqrt{S_{\Phi,\mathrm{white}}(\varphi_{\mathrm{rf}})} \propto J_1^{-1}(\varphi_{\mathrm{rf}})$ (grey dotted line), with $J_1^{-1}(\varphi_{\mathrm{rf}})$ being the Bessel function of the first kind. The overall shape describes the experimental data reasonably well, but the analytical fit predicts a strictly linear behaviour for low probe tone powers while the experiment has a slightly convex shape. Since the SQUID response for non-zero screening currents is no longer purely sinusoidal, the optimal value magnetic bias flux $\Phi_{\mathrm{bias}}^{\mathrm{opt}}$ depends on the probe tone power P_{exc}. If a constant value Φ_{bias} of the bias flux is used, as done in the measurement depicted here, this leads to an additional factor influencing the total readout flux noise. This leads to the minimum not being described well by the analytical model, neither in shape nor absolute value. A simple analytical model does not include this contribution, resulting in the visible deviation.

Using our numerical software framework, we can take the channel parameters determined during characterisation and simulate the depicted curve numerically (green line). The only free parameter was the effective system noise temperature T_{N}, which has not been determined experimentally. The agreement between our simulated data and the experiment is excellent, and much better than the analytical model. We can see that our numerical method correctly accounts for the power-dependent shift of the ideal bias point $\Phi_{\mathrm{bias}}^{\mathrm{opt}}$: The convex shape at low probe tone powers is described accurately, and so are both the shape and absolute position of the minimum.

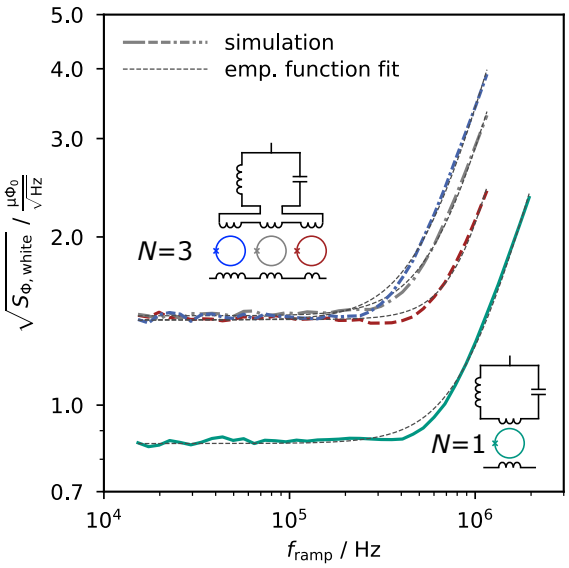


Fig. 7.3: Simulated flux noise level $\sqrt{S_{\Phi,\mathrm{white}}}$ versus flux ramp reset rate f_{ramp} for HμMUXs with $N = 1$ and $N = 3$. The inset shows the respective HμMUX configuration where the colours correspond to each other. For further analysis, an empirical function was fitted to each curve (thin grey dashed lines, see main text).

7.2.2 Bandwidth- and noise penalty of hybrid microwave SQUID multiplexing

In section 6.4 we have introduced the hybrid SQUID multiplexing method recently developed at IMS. It allows to increase the multiplexing factor in low-bandwidth, high channel count applications such as bolometric detector arrays, where μMUX becomes challenging due to fabrication constraints. As described in section 6.4.2, HμMUXing comes with two notable penalties, namely a reduction in efficiency regarding the use of signal capacity on the transmission line as well as an increase in the amplifier contribution to readout noise.

Neither of these two penalties is implemented explicitly within our software framework, i.e. the mathematical expressions 6.43 and 6.46 are not part of the source code. Nonetheless, if our simulation framework models real devices accurately, this behaviour should appear in simulations. Special care was taken from its initial inception to allow simulating HμMUX channels as well, which was easy due to the identical fundamentals in their operation shared with μMUX.

To analyse this in some detail we have performed several simulation runs to determine the dependence of the white noise level of the overall flux noise spectral density $\sqrt{S_{\Phi,\mathrm{white}}}$ on the flux ramp repetition rate f_{ramp} for six different HμMUX devices. These differ only by the number $N = 1,...,6$ of SQUIDs coupled to the resonator as well as their resonator bandwidth Δf_{BW}.

Bandwidth and probe tone power scale linearly with the SQUID number, i.e $\Delta f_{\mathrm{BW},N} \propto N$ and $P_{\mathrm{exc},N} \propto N$ respectively. For $N = 1$, i.e. a conventional microwave SQUID multiplexer, the default values $\Delta f_{\mathrm{BW},1} = 1\,\mathrm{MHz}$ and $P_{\mathrm{exc},1} = -70\,\mathrm{dBm}$ were assumed. Figure 7.3 shows as an example the simulation results for $N = 1$ and $N = 3$. It clearly shows that at low flux ramp repetition rates $f_{\mathrm{ramp}} \ll 1\,\mathrm{MHz}$ the white flux noise

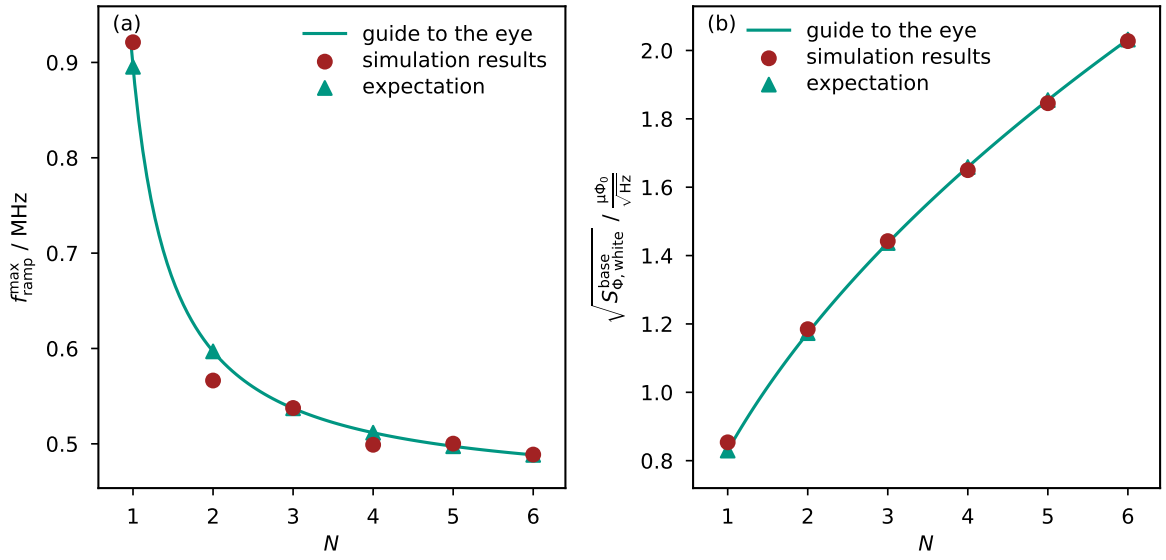


Fig. 7.4: (a) Limit frequency $f_{\mathrm{ramp}}^{\mathrm{max}}$ of a HμMUX device versus the SQUID number N as extracted from our simulations and as predicted from basic information theory. The SQUID with the lowest limit frequency $f_{\mathrm{ramp}}^{\mathrm{lim}}$ limits the channel bandwidth and has been depicted. A guide to the eye for non-integer N is provided as well. (b) Average white noise level $\sqrt{S_{\Phi,\mathrm{white}}^{\mathrm{base}}}$ in the low frequency limit for each simulated device, as well as predicted from information theory.

level $\sqrt{S_{\Phi,\mathrm{white}}}$ has a constant base value $\sqrt{S_{\Phi,\mathrm{white}}^{\mathrm{base}}}$. However, as the ramp reset rate increases, the flux noise level starts increasing above some limit frequency $f_{\mathrm{ramp}}^{\mathrm{lim}}$ as the resonator can no longer follow the SQUID modulation due to its finite response time. The limit frequency $f_{\mathrm{ramp}}^{\mathrm{lim}}$ takes different values for each SQUID because of the different mutual coupling between SQUID loop and modulation coil, resulting in a variation of modulation frequencies. The maximum flux ramp repetition rate suitable for operating the device is ultimately limited by the SQUID with the lowest limit frequency. For determining this frequency $f_{\mathrm{ramp}}^{\mathrm{lim}}$ and the white noise base value $\sqrt{S_{\Phi,\mathrm{white}}^{\mathrm{base}}}$, we fitted each curve by the empirical function

$$\sqrt{S_{\Phi,\mathrm{white}}(f)} = \sqrt{S_{\Phi,\mathrm{white}}^{\mathrm{base}}}\sqrt{1+\left(\frac{f}{f_{\mathrm{ramp}}^{\mathrm{lim}}}\right)^{b}}, \tag{7.1}$$

(see figure 7.3).

While not depicted in figure 7.3, we have determined both the base noise level $\sqrt{S_{\Phi,\mathrm{white}}^{\mathrm{base}}}$ and the limit frequency $f_{\mathrm{ramp}}^{\mathrm{lim}}$ for each SQUID or each of the simulated HμMUX devices. In figure 7.4(a), the maximum applicable ramp reset rate $f_{\mathrm{ramp}}^{\mathrm{max}} = \min_i f_{\mathrm{ramp},i}^{\mathrm{lim}}$ versus the total number N of SQUIDs per HμMUX is shown. The frequency $f_{\mathrm{ramp}}^{\mathrm{max}}$, equal to the

lowest limit frequency $f^{\mathrm{lim}}_{\mathrm{ramp},i}$ of all SQUIDs of the specific HμMUX channel, sets the maximum bandwidth with which the signal flux per readout channel can be acquired. As the number of SQUIDs per resonator and resonator bandwidth are proportional in this example, the density of readout channels in frequency space stays unchanged. With this fact we can use equation 6.43 to predict the expected relation between SQUID number N and measurement bandwidth, i.e. $f^{\mathrm{max}}_{\mathrm{ramp}}$. In figure 7.4(a) we can see that the simulation results agree very well with this theoretical prediction.

The increase in base white noise level $\sqrt{S^{\mathrm{base}}_{\Phi,\mathrm{white}}}$ with SQUID number N is graphically depicted in figure 7.4(b). Similarly, we can use equation 6.46 to predict the behaviour and compare to the results of our simulation run. From the excellent agreement between the theoretical expectations and our simulations we can conclude that our software framework correctly describes both these relations satisfactorily. Even though neither of the HμMUX penalties are hard-coded into our simulation framework, it describes the physics behind HμMUX and μMUX correctly, from which this behaviour arises.

As our software has successfully passed these two more complicated tests, in addition to the various bug searches during its implementation, we can now proceed to use the framework to further our understanding of μMUX.

7.3 Towards a full device optimisation of microwave SQUID multiplexers

In this section, we will attempt to find device- and readout parameters which minimise the white readout flux noise $\sqrt{S_{\Phi,\mathrm{white}}}$ caused by the amplifier chain, which is presently the dominant noise source for a typical μMUX. We might optimise with regard to other figures of merit, such as linearity or signal bandwidth, but this will be the topic of future work. Naturally, we want to find the global minimum of the entire parameter space with regards to readout noise. The computational effort, scaling exponentially with the size of the configuration space, makes this unfeasible for now. Instead, we will restrict our efforts to varying only a few parameters at a time, keeping the computational effort manageable. We will see that we can nonetheless gain some valuable insights into the optimisation of the μMUX performance.

7.3.1 Optimal screening parameter β_{L} and probe tone frequency f_{exc}

The screening parameter β_{L}, set during the design phase of a μMUX, has a crucial influence on its behaviour by affecting the shape and amplitude of the inductance modulation experienced by the resonator [Weg22]. It is thus difficult to immediately conclude an optimal choice. By way of its influence on the inductance modulation, β_{L} also affects the modulation of the resonance frequency. It would thus be unwise to only vary the screening parameter β_{L} without simultaneously varying the probe tone frequency f_{exc}.

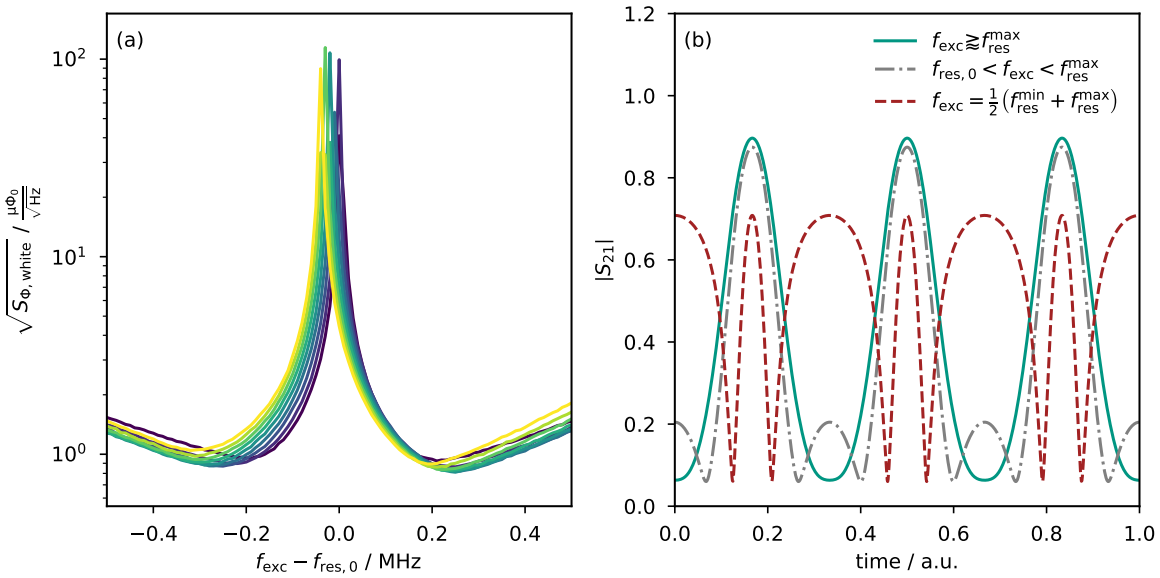


Fig. 7.5: (a) White readout flux noise $\sqrt{S_{\Phi,\mathrm{white}}}$ as a function of the probe tone frequency f_{exc} for different values of the SQUID screening parameter β_{L}. The latter was altered by varying the critical current I_{c}. (b) Illustration of the transmission time trace $|S_{21}|$ for three different values of the probe tone frequency f_{exc}. If the probe tone frequency is within the modulation range of the resonance frequency, the transmission response becomes strongly non-sinusoidal, and higher modes become much more significant.

In figure 7.5(a), we depict simulation runs of the white noise $\sqrt{S_{\Phi,\mathrm{white}}}$ for FRM readout versus the probe tone frequency f_{exc} for various values of the screening parameter β_{L}. To tune β_{L}, we kept the SQUID inductance constant, and varied only the critical current I_{c}. The overall shape of each curve is easily understood. During operation, the resonance frequency is modulated around its unloaded value $f_{\mathrm{res},0}$ between the extrema $f_{\mathrm{res}}^{\mathrm{max}}$ and $f_{\mathrm{res}}^{\mathrm{min}}$. The modulation amplitude $\Delta f_{\mathrm{res}}^{\mathrm{max}} = f_{\mathrm{res}}^{\mathrm{max}} - f_{\mathrm{res}}^{\mathrm{min}} \approx \Delta f_{\mathrm{BW}}$ is usually set equal to the resonator bandwidth. If the probe tone is much smaller or larger than the unloaded resonance frequency, i.e. $f_{\mathrm{res}}^{\mathrm{min}} - f_{\mathrm{exc}} \gg \Delta f_{\mathrm{BW}}$ or $f_{\mathrm{exc}} - f_{\mathrm{res}}^{\mathrm{max}} \gg \Delta f_{\mathrm{BW}}$, then the transmission S_{21} is not modulated with a large amplitude, resulting in a poor SNR and thus a large amplifier flux noise contribution. This is represented by the increasing noise towards the edges in figure 7.5(a). At the opposite extreme, choosing a probe tone within the range of modulation $f_{\mathrm{res}}^{\mathrm{min}} < f_{\mathrm{exc}} < f_{\mathrm{res}}^{\mathrm{max}}$ causes two minima in the transmission response per full period of the resonance frequency modulation, as depicted schematically in figure 7.5(b). The transmission response becomes strongly non-sinusoidal, with a significant signal power in higher modes not evaluated during the demodulation to retrieve the flux signal. As described in section 6.3, this results in an increased readout noise, which reaches its maximum if the probe tone is roughly at the centre of the modulation interval $f_{\mathrm{exc}} \approx (f_{\mathrm{res}}^{\mathrm{max}} - f_{\mathrm{res}}^{\mathrm{min}})/2 + f_{\mathrm{res}}^{\mathrm{min}}$ (red dashed line in figure 7.5(b)). This causes the central peaks of each curve seen in figure 7.5(a)

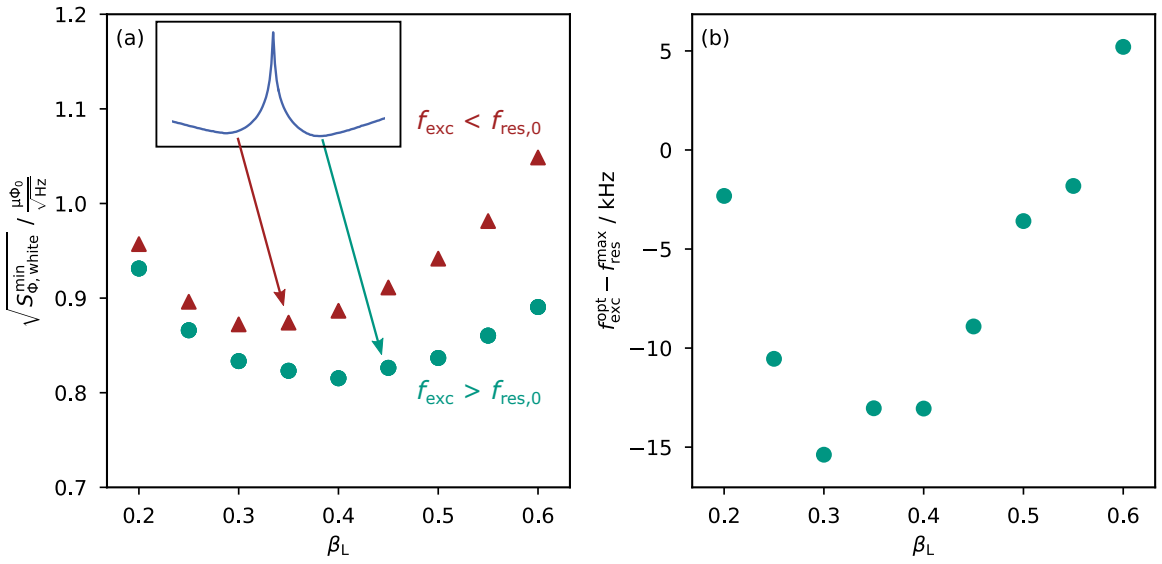


Fig. 7.6: (a) Minimum white noise level $\sqrt{S^{\mathrm{min}}_{\Phi,\mathrm{white}}}$ in both local minima of figure 7.5(a) for each value of β_L. (b) Probe tone frequency $f^{\mathrm{opt}}_{\mathrm{exc}}$ minimising the readout noise versus the screening parameter β_L. For clarity, the difference $f^{\mathrm{opt}}_{\mathrm{exc}} - f^{\mathrm{max}}_{\mathrm{res}}$ between the probe tone and maximum resonance frequency is shown. Relative to the MHz bandwidth, the difference between the probe tone and maximum resonance frequency is fairly small.

and explains the shift of the peak position with the screening parameter β_L, as stronger screening shifts the modulation interval towards lower frequencies [Weg22]. At intermediate ranges of the probe tone frequency f_exc, both to the left and right of the unloaded resonance frequency f_res, two local minima form. To find the ideal value of the screening parameter, we have plotted the white noise $\sqrt{S^{\mathrm{min}}_{\Phi,\mathrm{white}}}$ in each local minimum versus β_L in figure 7.6(a). We can immediately conclude that the global minimum for each curve is at probe tone frequencies $f_\mathrm{exc} > f_{\mathrm{res},0}$. We also see that the choice $\beta_\mathrm{L} \approx 0.4$ minimises the white readout flux noise. However, the minimum is fairly wide, so the entire range of $0.3 < \beta_\mathrm{L} < 0.5$ yields a noise value only marginally above the minimum.

The final piece of information to draw from this dataset is the probe tone frequency $f^{\mathrm{opt}}_{\mathrm{exc}}$ which minimises the readout noise. We have already seen that it is beneficial to read out at frequencies above the unloaded resonance frequency. In figure 7.6(b), the difference between the probe tone frequency $f^{\mathrm{opt}}_{\mathrm{exc}}$ and the largest resonance frequency $f^{\mathrm{max}}_{\mathrm{res}}$ reached during resonance frequency modulation is depicted, versus the screening parameter β_L. We can see that, for the entire range of screening parameters, the ideal frequency is basically identical to $f^{\mathrm{max}}_{\mathrm{res}}$. With about 15 kHz, the largest difference between them is considerably smaller than the resonator bandwidth in the MHz range. We can conclude that the ideal probe tone frequency should therefore be chosen to roughly equal the upper limit $f^{\mathrm{max}}_{\mathrm{res}}$ of the resonance frequency, as we have already alluded to in figure 6.4(b).

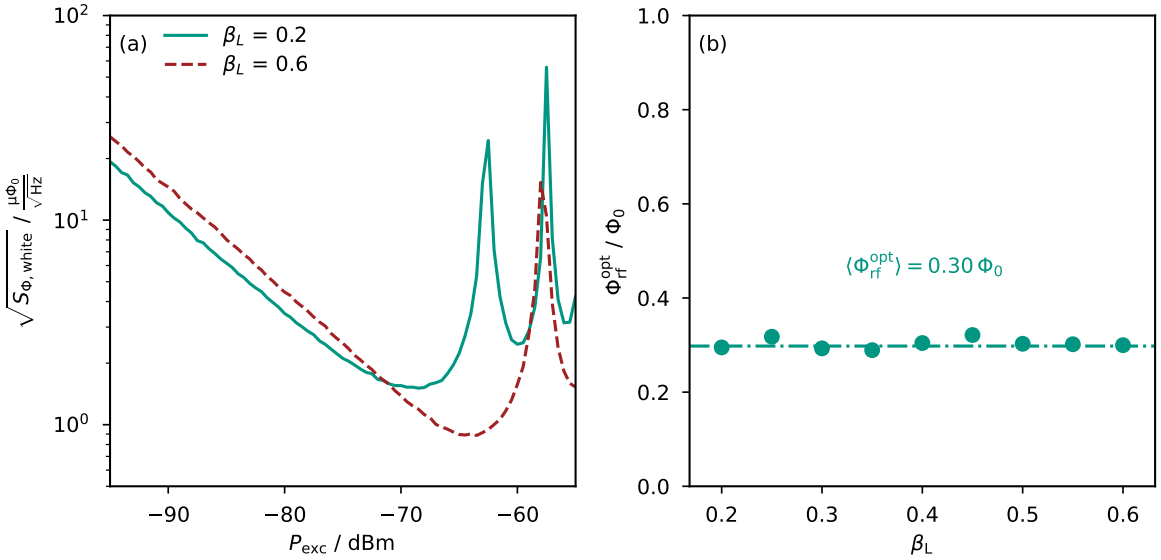


Fig. 7.7: (a) White readout flux noise $\sqrt{S_{\Phi,\mathrm{white}}}$ as a function of the probe tone power P_{exc} for two different values of the screening parameter β_{L}. (b) Optimum rf magnetic flux amplitude $\Phi_{\mathrm{rf}}^{\mathrm{opt}}$ yielding the lowest noise floor versus the SQUID screening parameter β_{L}.

7.3.2 Ideal probe tone power P_{exc}

Another important parameter is the power P_{exc} of the applied microwave probe tone. We have already described the overall expected behaviour of the white noise level $\sqrt{S_{\Phi,\mathrm{white}}}$ on probe tone power in section 7.2.1, where we have seen that an ideal probe tone power exists which minimises the readout flux noise. Here, we performed a set of simulation runs to determine the dependence of the white noise level $\sqrt{S_{\Phi,\mathrm{white}}}$ on the probe tone power P_{exc}, again for various values of the screening parameter β_{L}.

Two of the resulting curves, specifically the extreme values $\beta_{\mathrm{L}} = 0.2$ and $\beta_{\mathrm{L}} = 0.6$, are depicted in figure 7.7(a). The curves for other values of the screening parameter β_{L} look similar and have been omitted for clarity. The overall shape of the curves is equivalent to those discussed in section 7.2.1, with a linearly decreasing region at low probe tone powers, a generally increasing region with characteristic spikes for large probe tone powers, and a minimum forming in between. A notable difference to the curves described section 7.2.1 is that here, the linear region is much flatter and not convex. This results from the use of FRM rather than open-loop readout, and from the default set of simulation parameters regarding the resonance frequency shift $\Delta f_{\mathrm{res}}^{\mathrm{max}}$, bandwidth Δf_{BW} and probe tone frequency f_{exc}. We can see from the two depicted curves that with increasing screening, the minimum shifts towards higher probe tone powers P_{exc} and reaches a lower minimum value. Naturally, the position of the minimum is of major interest to us: We need to estimate the ideal probe tone power when designing a μMUX system, and take it into account when selecting the low-temperature amplifiers. The

total input power at the first amplifier stage, usually a HEMT amplifier operated at a temperature of $T = 4\,\mathrm{K}$, is defined by the probe tone power P_{exc} and total number of probe tones. During FRM, we can assume that, on average, half the power of each probe tone is transmitted. Especially at large input powers, the nonlinearity of an amplifier can lead to intermodulation products [Hen18]. If multiple frequencies are present at the input, these intermodulation products result in additional tones being present at the amplifier output. In μMUX, we use potentially hundreds of unique probe tones, resulting in a very large number of intermodulation tones. If one such intermodulation tone is very close to an excitation tone, it can cause a systematic error in the measurement of the transmitted amplitude of that excitation tone. This effectively causes an additional source of noise. To keep the amplitude of these intermodulation tones below a value degrading the overall noise performance, we must ensure that the total input power remains sufficiently below the saturation power of the amplifier [Hen18], and select either the probe tone power or amplifier accordingly. We can look at the optimal probe tone powers, i.e. those that minimise the readout noise, in more detail, and determine the resulting radio frequency flux amplitude Φ_{rf} which the resonator induces into the SQUID loop at these power levels. These values are graphically depicted in figure 7.7(b), versus the screening parameter β_{L}. Curiously, despite the varying screening parameter, the ideal value $\Phi_{\mathrm{rf}}^{\mathrm{opt}} \approx 0.3\Phi_0$ is practically constant. We will see later that a similar behaviour arises when varying other parameters within certain ranges, indicating that this result is good rule of thumb. This observation is in good agreement with results reported in [Mat17]. We can thus conclude that generally, the probe tone power P_{exc} should be chosen such that the radio frequency flux amplitude takes the value $\Phi_{\mathrm{rf}}^{\mathrm{opt}} \approx 0.3\Phi_0$. For our default set of parameters, this is typically the case for $P_{\mathrm{exc}} \approx -60\,\mathrm{dBm}$ to $-70\,\mathrm{dBm}$.

7.3.3 Optimal ratio between maximum frequency shift and resonator bandwidth

Typically, the ratio $\eta = \Delta f_{\mathrm{res}}^{\mathrm{max}}/\Delta f_{\mathrm{BW}}$ between the maximum frequency shift and the resonator bandwidth is deliberately chosen close to unity, i.e. $\eta \approx 1$, to guarantee optimal readout conditions [Kem17, Mat17]. This is based on the simple relation that for $\eta \ll 1$, i.e. $\Delta f_{\mathrm{BW}} \ll \Delta f_{\mathrm{res}}^{\mathrm{max}}$, during a large portion of the frequency modulation, the transmission is saturated. The resulting transmission response is thus highly non-sinusoidal, reducing the SNR after demodulation and resulting in an increased readout noise. Likewise, for $\eta \gg 1$, or $\Delta f_{\mathrm{BW}} \gg \Delta f_{\mathrm{res}}^{\mathrm{max}}$, the frequency modulation only covers a small fraction of the bandwidth and the resulting transmission response has a reduced amplitude, again increasing the readout noise. A choice of $\eta \approx 1$ offers a good balance with a mostly sinusoidal transmission response covering almost the entire available amplitude range. It is also well-understood that, as the probe tone power increases, nonlinearities in the rf-SQUID cause a reduction of the frequency modulation amplitude $\Delta f_{\mathrm{res}}^{\mathrm{max}}$ [Weg22]. When specifying the ratio η, we need to take this into account. We will thus define $\eta_0 = \lim_{P_{\mathrm{exc}}\to 0} \Delta f_{\mathrm{res}}^{\mathrm{max}}(P_{\mathrm{exc}})/\Delta f_{\mathrm{BW}}$ as the frequency-shift-to-bandwidth

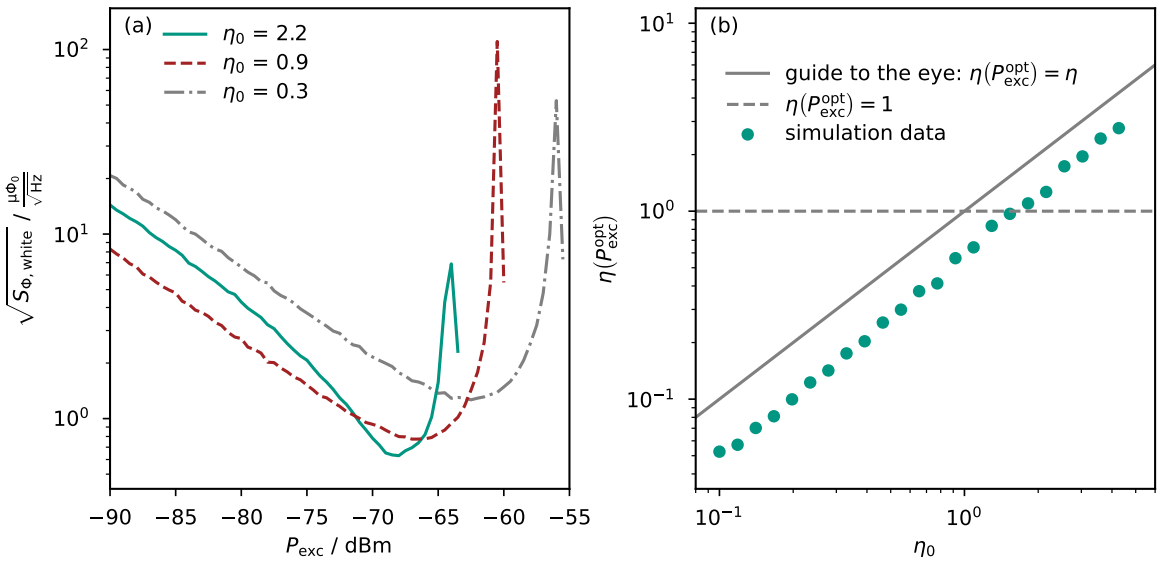


Fig. 7.8: (a) White noise level $\sqrt{S_{\Phi,\mathrm{white}}}$ of the magnetic flux as a function of the microwave probe tone power P_{exc} for three values of η_0, set by changing the coupling mutual inductance M_{T}. (b) Effective ratio $\eta\,(P_{\mathrm{exc}}^{\mathrm{opt}})$ at the probe tone power minimising the readout noise, versus η_0. A guide for the eye for a perfect one-to-one relation is given, and the important value $\eta = 1$ is highlighted.

ratio for vanishing probe tone power. At larger power levels, the frequency modulation amplitude $\Delta f_{\mathrm{res}}^{\mathrm{max}}$ and consequently the ratio $\eta = \Delta f_{\mathrm{res}}^{\mathrm{max}}(P_{\mathrm{exc}})/\Delta f_{\mathrm{BW}}$ are reduced. Considering this influence of probe tone power on the ratio η, it is not obvious which value for η_0 should ideally be implemented during the design of a device.

We have performed a simulation run, again determining the white noise level $\sqrt{S_{\Phi,\mathrm{white}}}$ as a function of the microwave probe tone power P_{exc}, this time for various values of the ratio $\eta_0 \in [0.1,5]$. Three such curves are exemplarily depicted in figure 7.8(a), from which we can deduce that not only position and depth of the minimum change, but so does its shape. This can be understood from the decreasing value of η with increasing probe tone power P_{exc}. For $\eta_0 > 1$, the ratio starts at a larger value than ideal, artificially increasing the readout noise. As the power increases, η is reduced and approaches the ideal value $\eta \approx 1$. The otherwise linear low-power region of the curve thus displays a convex shape, as is apparent from the data with $\eta_0 = 2.2$ (green curve) in figure 7.8(a). For optimised readout, we naturally want to make sure that optimal probe tone power and ideal η coincide, and choose η_0 accordingly. In figure 7.8(b), the effective value $\eta\,(P_{\mathrm{exc}}^{\mathrm{opt}})$ at the optimal probe tone power is depicted versus the low-power limit η_0. The reduction effect of the probe tone power can be seen from the deviation between the data (green circles) and a perfect one-to-one correlation (grey line): At the ideal probe tone power, the effective value is consistently below the low-power limit. As a consequence, $\eta\,(P_{\mathrm{exc}}^{\mathrm{opt}}) \approx 1$ is reached for a choice of $\eta \approx 2$.

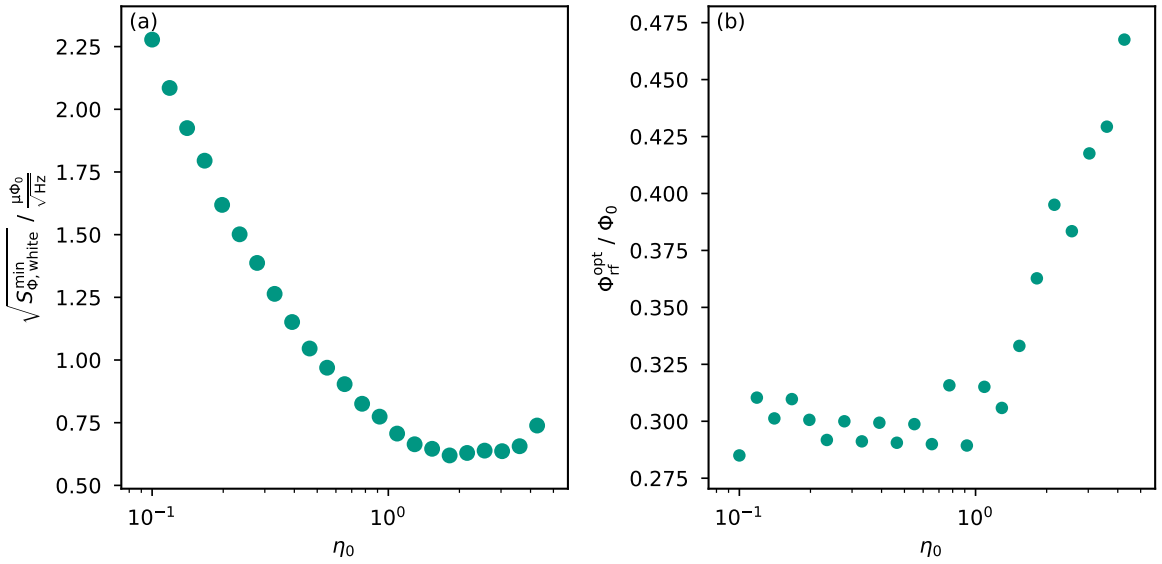


Fig. 7.9: (a) Minimum noise value $\sqrt{S^{\min}_{\Phi,\mathrm{white}}}$ versus the ratio parameter $\eta_0 = \lim_{P_{\mathrm{exc}}\to 0} \eta_{\mathrm{eff}}(P_{\mathrm{exc}})$. (b) Optimum rf magnetic flux amplitude $\Phi^{\mathrm{opt}}_{\mathrm{rf}}$ yielding the lowest noise floor versus η_0.

The minimum white noise $\sqrt{S^{\min}_{\Phi,\mathrm{white}}}$ is graphically depicted versus the ratio parameter η_0 in figure 7.9(a). Contrary to previous assumptions, it turns out that a choice of $\eta_0 > 1$ ultimately yields lower noise than the typical value $\eta_0 \approx 1$. The additional benefit that the optimal probe tone power is reduced relaxes requirements on the input saturation power of the first amplifier stage. One final aspect we can conclude from this dataset is the optimum rf magnetic flux amplitude $\Phi^{\mathrm{opt}}_{\mathrm{rf}}$ yielding the lowest noise floor, as described in the previous section. This is shown as a function of η_0 in figure 7.9(b). An interesting behaviour can be seen there: For values of $\eta_0 \leq 1$, the optimal radio frequency flux takes the value $\Phi^{\mathrm{opt}}_{\mathrm{rf}} = 0.3\Phi_0$ expected from our results in section 7.3.2. For larger values of the ratio parameter $\eta_0 > 1$ however, the optimal rf flux increases, reaching $\Phi^{\mathrm{opt}}_{\mathrm{rf}} \approx 0.4\Phi_0$ at $\eta_0 = 3$. The conclusion of $\Phi^{\mathrm{opt}}_{\mathrm{rf}} = 0.3\Phi_0$ should thus serve more as a rule of thumb rather than a fundamental law.

Here, we have used a simple approach of evaluating the readout noise for a number of values of a few individual parameters at a time. For a full μMUX optimisation with regard to all parameters simultaneously, this approach would require an enormous amount of computations (and thus time). A more efficient approach would be to select a random starting point in the configuration space, vary each parameter slightly, and follow the local gradient of the noise to the nearest local minimum. Doing this repeatedly for a number of different starting points should ultimately yield a global minimum. Such a large-scale optimisation will nonetheless require serious effort, and may be the subject of future work at IMS.

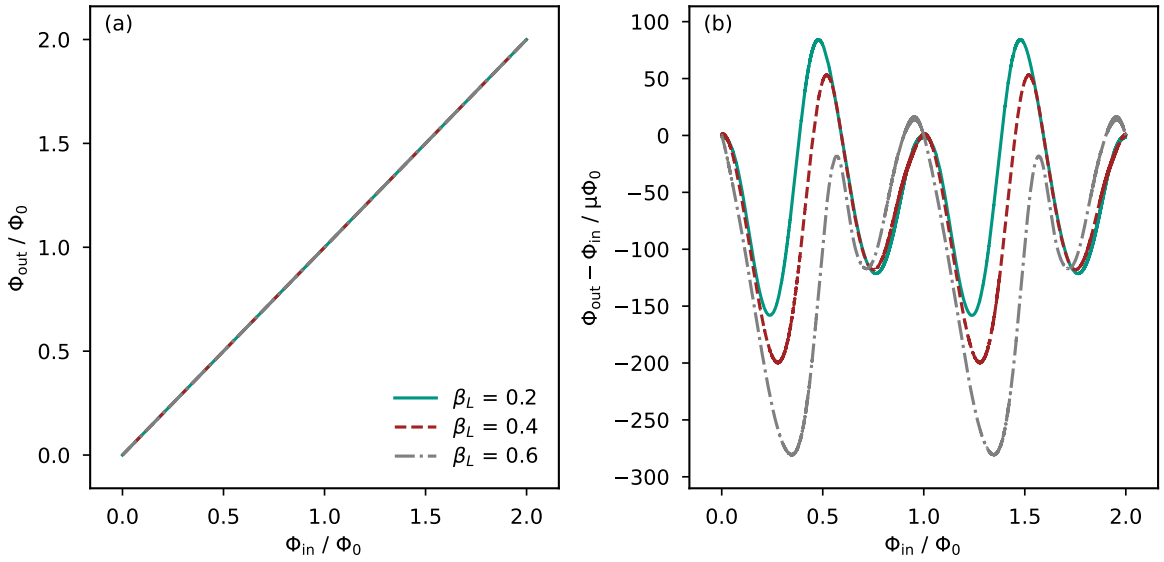


Fig. 7.10: (a) Output signal flux Φ_{out} as a function of the input signal flux Φ_{in} for different values of the screening parameter β_{L}. The individual curves are difficult to distinguish since they all overlap. (b) Deviation from perfect linearity, i.e. the difference $\Phi_{\text{out}} - \Phi_{\text{in}}$ as a function of the input signal flux Φ_{in}.

7.4 Potential other applications of the simulation framework

Finding optimised parameters for the design and operation of a μMUX is not the only useful application of our numerical software framework. Some other applications will be highlighted here, but the list is by no means exhaustive. The modularity of our software framework easily allows the construction of simulations to study any feature of μMUXs, or devices derived from them.

7.4.1 Linearity of FRM readout

One major concern for μMUXing is the linearity of the output signal. Using FRM, we expect a perfectly linear relation between the input signal flux Φ_{in} and the output signal Φ_{out} which we determine after demodulation. In reality, the non-linear junction dynamics, the finite resonator response time, and the finite bandwidth of the flux ramp signal cause deviations from perfect linearity which are difficult, if not impossible, to predict analytically.

With our software framework, we can perform numerical simulations to assess linearity rather easily. In figure 7.10(a), we show the flux Φ_{out} determined after demodulation versus the input signal Φ_{in}. Figure 7.10(b) displays the deviation from perfect linearity, i.e. $\Phi_{\text{out}} - \Phi_{\text{in}}$ versus the input signal. The finite flux ramp bandwidth may influence linearity, so we assume a flux ramp with an amplitude of at most $2.5\,\Phi_0$ in the SQUID loop, and use a second-order Butterworth low-pass filter with a cutoff frequency of

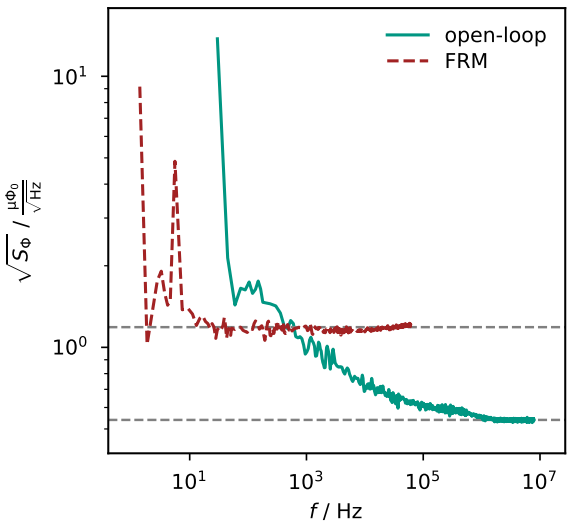


Fig. 7.11: Square root of the flux noise spectral density $\sqrt{S_\Phi(f)}$ for both open-loop and FRM readout, of an example μMUX device. Grey lines mark the white noise level at high frequencies.

$f_{\text{cutoff}} = 10\,\text{MHz}$ to emulate a finite flux ramp reset time. Data points amounting to 16 % at the start and 4 % at the end of each ramp segment were neglected to avoid transients of the ramp resets to affect demodulation. Moreover, we have not included any source of noise in order to focus on systematic nonlinearity, and performed simulations for three values of the screening parameter β_L. As expected, the relation is mostly linear with deviations of less than $300\,\mu\Phi_0$ peak-peak. As we have seen in section 6.1, μMUX have a perfectly periodic behaviour with respect to the total flux and a period of one flux quantum. Naturally we see the same periodicity here. Curiously, the choice of the screening parameter seems to affect the specific shape of the nonlinear deviation, but has little effect on its peak-peak magnitude at least with our default set of parameters.

7.4.2 Noise shaping

In section 6.3 introducing FRM readout, we have already discussed that FRM comes with penalties, with respect to apparent amplifier flux noise as well as measurement bandwidth. Nevertheless, FRM has a positive noise shaping effect where low-frequency noise at frequencies much lower than the ramp repetition rate f_ramp is effectively reduced. Describing this noise shaping analytically, considering the mathematical complexity of a μMUX, is a challenging task, but we may again use our software framework to study this effect conveniently.

Figure 7.11 shows the square root of the noise spectral density $\sqrt{S_\Phi(f)}$ of an example microwave SQUID multiplexer assuming open-loop and FRM readout. Both, a white amplifier noise with a noise temperature of $T_\text{N} = 4\,\text{K}$ and a $1/\sqrt{f}-$like TLS noise with a noise level of $\sqrt{S_\text{TLS}}/f_{\text{res},0} = 2.5 \times 10^{-9}\,1/\sqrt{\text{Hz}}$ at a frequency of 1 Hz were assumed for the simulations. These values serve as example values for microresonators [Gao07] to showcase the use of our software for this purpose. In reality of course, the TLS noise contribution depends on both probe tone power and resonator geometry, and would

need to be carefully chosen for each parameter set in order to get quantitative results. For open-loop readout, the bias flux Φ_{bias} was chosen such that the flux-to-transmission transfer coefficient $K_\phi(\Phi_{\mathrm{bias}})$ is maximised. For FRM readout, a modulation ramp inducing at most one flux quantum into the SQUID loop with a ramp repetition rate of $f_{\mathrm{ramp}} = f_{\mathrm{s}}/128 \approx 122\,\mathrm{kHz}$ was used. From the ramp repetition rate, we can immediately expect a reduction in measurement bandwidth by a factor $f_{\mathrm{s}}/f_{\mathrm{ramp}} = 128$, which is also clearly visible in figure 7.11. The level of white noise, clearly distinguishable at high frequencies, is larger for FRM readout by a factor of $c_{\mathrm{deg}} = 2.18$, which is expected from the noise degradation effects described in section 6.3. Notably, for open-loop readout, an increase in noise spectral density at frequencies below 100 kHz is visible due to the included, $1/\sqrt{f}-$like TLS noise. When comparing to the FRM noise spectrum, the noise shaping effect of FRM is apparent: Here, the noise spectrum is flat all the way down to about 10 Hz. As a consequence, FRM actually leads to a lower noise density at frequencies below ca. 1 kHz compared to open-loop readout, despite the noise degradation. Similar analysis can help to further investigate the effects that readout schemes like FRM have on the noise of μMUX and may ultimately lead to an improved understanding of the intricate behaviour of such devices.

7.4.3 Probe tone modulation

So far, we have focused entirely on fixed-frequency readout, where the probe tone frequency $f_{\mathrm{exc}} = \text{const.}$ is constant in time. Another method used in some μMUX applications is tone tracking (TT) [Yu23], where sophisticated electronics are used to monitor the time-dependent resonance frequency $f_{\mathrm{res}}(t)$ and adjust (in real time) the probe tone accordingly, i.e. $f_{\mathrm{exc}}(t) = f_{\mathrm{res}}(t)$. This has one major advantage: The power transmission S_{21} is minimal on resonance. The power level of the transmitted signal at the first amplifier stage is therefore significantly reduced compared to the probe tone at the resonator channel, strongly relaxing the requirements regarding the input saturation power of the first amplifier. This allows for a higher probe tone power, or more carrier signals of the same power, yielding improvements to readout noise or multiplexing factor respectively. The most significant downside is the lower bandwidth, current state-of-the-art TT systems operate at per-channel readout bandwidths of several 10 kHz [Yu23] compared to static probe tone methods operating near or at 1 MHz [Kar20] (see also our considerations for $f_{\mathrm{ramp}}^{\mathrm{max}}$ at $N = 1$ presented in section 7.2.2). This penalty to bandwidth mostly arises because the TT control electronics take a finite time to correct f_{exc}.

To combine some of the benefits of both methods, one can devise a simple idea. To prevent pile-up of events, the time between events at the detector is usually much longer than the detector signal decay time. For a majority of the time, the detector thus remains at the baseline, i.e. zero signal. Provided we know the behaviour of a readout channel during FRM modulation at zero signal, we can precompute the time-dependent resonance frequency $f_{\mathrm{res}}(t)|_{\Phi_{\mathrm{sig}}=0}$ which the channel will follow between events. If we programme the readout electronics such that the probe tone follows a pre-determined,

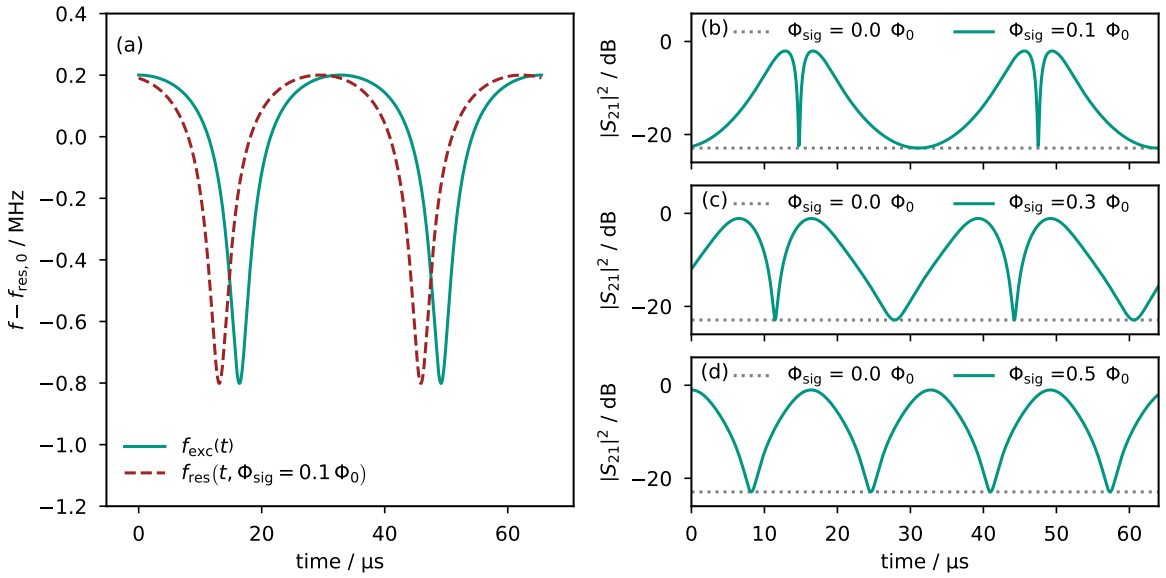


Fig. 7.12: (a) Time evolution of the resonance frequency $f_{\mathrm{res}}(t,\Phi_{\mathrm{sig}} = 0.1\Phi_0)$ and the probe tone $f_{\mathrm{exc}}(t)$ for PTM during FRM. Here, we assumed "perfect" PTM, i.e. $f_{\mathrm{exc}}(t) \approx f_{\mathrm{res}}(t)|_{\Phi_{\mathrm{sig}}=0}$. With no external signal $\Phi_{\mathrm{sig}} = 0$, both curves would be perfectly congruent. (b)-(d) Absolute transmission time traces $|S_{21}|^2$ for perfect PTM and different signal amplitudes $\Phi_{\mathrm{sig}} = 0.1\,\Phi_0$, $0.3\,\Phi_0$ and $0.5\,\Phi_0$. In each curve, the flat line with minimal transition for $\Phi_{\mathrm{sig}} = 0$ is also depicted.

time-dependent pattern $f_{\mathrm{exc}}(t) \approx f_{\mathrm{res}}(t)|_{\Phi_{\mathrm{sig}}=0}$, we can ensure that the transmission $|S_{21}|^2$ is minimal whenever there is no detector event, i.e. for a majority of the time. Since the probe tone $f_{\mathrm{exc}}(t)$ is pre-determined at all times, no real-time computations are required which may limit the bandwidth of the room-temperature electronics. The downside to this is that, depending on the choice of $f_{\mathrm{exc}}(t)$, the resulting transmission response $|S_{21}|^2$ during a detector signal looks very different from usual fixed probe tone operation. We can use our software framework to accurately model the resulting linearity and effects of noise of such a probe tone modulation (PTM) readout scheme without the need to design or implement any new electronics.

To illustrate the idea, we depict the behaviour of the resonance frequency $f_{\mathrm{res}}(t,\Phi_{\mathrm{sig}} = 0.1\Phi_0)$ during FRM and the probe tone $f_{\mathrm{exc}}(t)$ for PTM readout versus time in figure 7.12(a). For $\Phi_{\mathrm{sig}} = 0$, both displayed curves overlap. In this case, the probe tone always coincides with the resonance dip and the transmitted power is minimal at all times. Any external flux signal $\Phi_{\mathrm{sig}} \neq 0$ causes a phase shift between the resonance frequency modulation $f_{\mathrm{res}}(t,\Phi_{\mathrm{sig}})$ and the probe tone $f_{\mathrm{exc}}(t)$, and a periodic transmission response S_{21} results. In figures 7.12(b)-(d), we plot the transmission response $|S_{21}|^2$ versus time for three different values of the signal flux amplitudes Φ_{sig}. In each plot, the baseline for $\Phi_{\mathrm{sig}} = 0$ is also depicted for comparison. The resulting transmission response for PTM clearly differs from static probe tone methods: It is no longer (generally) sinusoidal, and while we can still associate a phase shift with

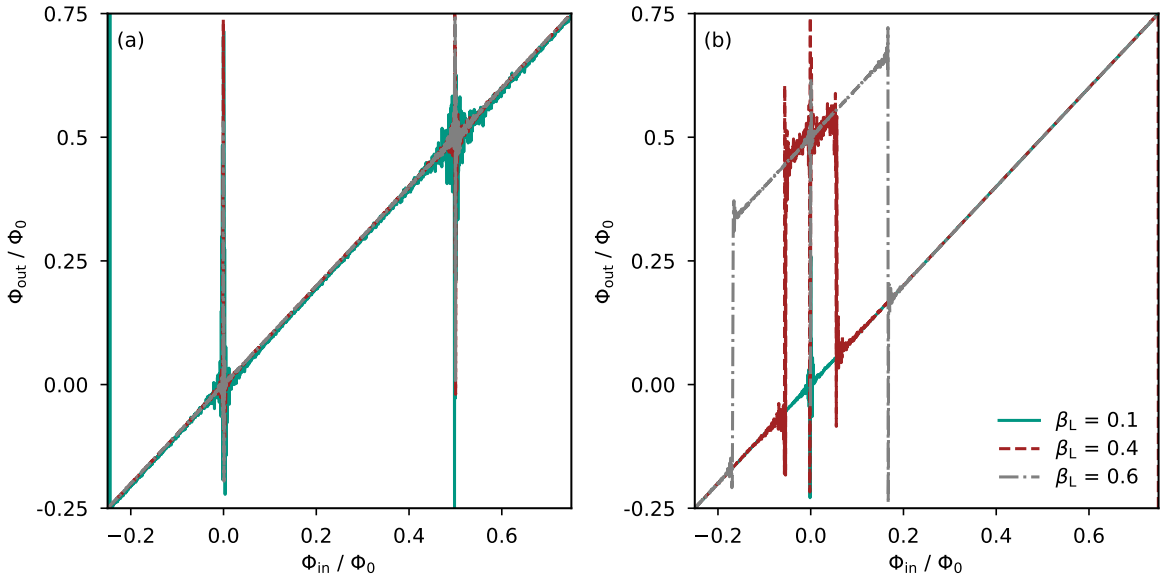


Fig. 7.13: Relation between the input signal Φ_{in} and the signal Φ_{out} retrieved via demodulation as applied to typical FRM readout. In (a), we demodulated the transmission response with the modulation frequency f_{mod}. For (b), the demodulation frequency was twice as large, i.e. $2f_{\text{mod}}$. Clearly, this simple approach to demodulating PTM data is insufficient, as very significant deviations from the desired linear relationship are present.

the signal, the signal shape also changes noticeably as the signal increases. One may be inclined to use the same demodulation method we have previously discussed to determine the phase of the transmission response during PTM, and use it to derive the signal flux. Given the non-sinusoidal shape of the transmission response, however, other methods to retrieve the signal might be more suited.

The results from using regular FRM demodulation are depicted in figures 7.13(a) and (b). Here, the relation between input signal Φ_{in} and output signal Φ_{out} retrieved from demodulation of the transmission response phase is shown. Naturally, we would desire a perfectly linear relation. In (a), the frequency used for demodulation equals the modulation frequency f_{mod} of the resonance frequency. In (b), the exact same simulated PTM transmission time trace was demodulated using twice the modulation frequency, i.e. $2f_{\text{mod}}$. Here, we deliberately included noise, as in reality any demodulation method has to perform in the presence of noise. Clearly, neither demodulation frequency yields ideal linearity across the tested range.

In figures 7.12(b)-(d), we actually see two peaks in the transmission response per modulation period of the resonance frequency (i.e. while the flux state in the rf-SQUID changes by a single flux quantum Φ_0). For low signals, both peaks "lean" towards each other. As the signal increases the peaks get more and more symmetrical, until at $\Phi_{\text{sig}} = 0.5\Phi_0$ they do not lean at all. In this case, the modulation frequency

of the transmission is exactly twice that of the resonance frequency modulation. At any non-zero signal in between, we have some signal contributions with the base modulation frequency f_{mod} of the resonance frequency (the base mode), as well as some signal contribution with twice that frequency (the second mode). As is visible from figures 7.12(b)-(d), at low signal amplitudes Φ_{sig} the base mode is strongly present, and the second mode becomes more dominant as the value of $\Phi_{\mathrm{sig}} = 0.5\Phi_0$ is approached. At this value, the base mode actually vanishes entirely.

To explain the behaviour we see in figures 7.13(a) and (b), we may first recall that for PTM, by design, the transmission response is entirely flat for zero input signal. Thus, at $\Phi_{\mathrm{in}} = 0$, the transmission time trace is solely noise, and regardless of the method used the determined phase is practically entirely random. This results in the large non-linearity around $\Phi_{\mathrm{in}} = 0$ in both figures 7.13(a) and (b). Likewise, the base mode has zero amplitude at the edge case of $\Phi_{\mathrm{in}} = 0.5\Phi_0$, so we see the same feature again there in figure 7.13(a), where we determine the phase of the base mode during demodulation. The second mode is present for any finite input signal, so nothing special occurs near $\Phi_{\mathrm{in}} = 0.5\Phi_0$. However, for larger values of the screening parameter β_{L} the mirror-like symmetry of the "leaning" peaks in the transmission response apparently leads to competing contributions with different phases in the second mode. This results in a sudden, highly nonlinear jump in the retrieved signal Φ_{out} of half a flux quantum.

Clearly, using simple demodulation of the transmission response phase for PTM does not yield suitably accurate information on the flux signal of the channel. To make use of the potential advantages of PTM, a different method to retrieve the signal from the transmission time trace must be used. One could imagine methods based on (or including) the amplitudes (rather than phases) of the base and/or second mode. We do not further elaborate on PTM as a readout concept here. It will be the subject of future work. Our intention was only to highlight the idea, and primarily to show that our simulation software framework can be applied to model such novel readout schemes without the need to design or manufacture any purpose-built electronics. New or application-specific readout schemes may help to improve noise performance or multiplexing factor in future versions of sophisticated μMUX systems.

8. Conclusion and Outlook

Cryogenic microcalorimeters, such as transition-edge sensors (TESs) [Irw05, Ull15] or magnetic microcalorimeters (MMCs) [Fle05, Kem18], are energy-dispersive single-particle detectors uniting remarkable energy resolution with near-unity quantum efficiency. This makes them highly attractive for applications in fields like astronomy, particle physics or dark matter search, where the energy of particles has to be measured with utmost precision. The energy deposited into the detector upon absorption in a suitable absorber results in a temperature rise, which is measured using a highly sensitive temperature sensor, that may be based on the resistance of a superconductor operated in its normal-to-superconductor transition (TES) or the magnetisation of a paramagnetic material situated in a weak magnetic field (MMC). Using an appropriate readout circuit, the thermometer signal is transformed into a change of magnetic flux threading the loop of a superconducting quantum interference device (SQUID) [Fag06] for high-precision readout. With TESs and MMCs, an energy resolution ΔE_{FWHM} of 0.72 eV for 1.5 keV photons [Lee15] and of 1.25 eV for 5.9 keV photons [Kra23] has been reported. In terms of relative resolution $\Delta E_{\mathrm{FWHM}}/E$, MMCs thus hold the world record at the time of writing. While these numbers prove the outstanding performance of contemporary cryogenic microcalorimeter systems, energy resolutions in the range of 100 meV have not yet been reached. Thus, they are not yet suitable for applications requiring such extreme sensitivity, e.g. the investigation of vibrations or d-d-excitations in soft X-ray spectroscopy [But96], or resonant inelastic X-ray scattering [Ame11].

For MMCs, the loss of signal due to the superconducting flux transformer between the paramagnetic sensor and readout SQUID degrades the SNR [Bur08, Bau22]. Additionally, MMCs must be operated at very low temperature, typically below 20 mK, setting rigid requirements on cryostat performance as well as the entire detector setup. In use, TES depict excess noise [Sei04, Lin04, Ull04, Jet09], the sources of which are still being researched [Luu03, Bag09, Wes21]. This excess noise currently prevents their energy resolution from reaching the thermodynamic limit. In addition, TESs are usually operated in electro-thermal feedback [Irw95, Irw05], and thus dissipate power.

In this thesis, we have presented the the λ-SQUID, a novel microcalorimeter type. The λ-SQUID is based on a regular dc-SQUID. The largest fraction of the device is made from a superconducting material with a critical temperature T_{c} much larger than the operating temperature T_0, i.e. $T_{\mathrm{c}} \gg T_0$. The λ-coil, forming a section with inductance L_λ of the λ-SQUID loop, consists of a different superconductor with a much lower critical temperature, i.e. $T_{\mathrm{c}}^{\lambda} \ll T_{\mathrm{c}}$. The λ-coil is inductively coupled to an input coil with inductance L_{in} via the mutual inductance M_{in}. The device is operated at a temperature $T_0 \lessapprox T_{\mathrm{c}}^{\lambda}$, such that the magnetic penetration depth λ of the λ-coil strongly depends on temperature. Thus, a small change in temperature causes a large change of the magnetic penetration depth λ, resulting in a redistribution of current within the

cross-section of the λ-coil. This changes the effective geometric mean distance between the λ-coil and the input coil, and consequently affects their mutual inductance M_{in}. If we now apply a dc current I_{in} to the input coil, a change in temperature, causing a shift ΔM_{in} of the mutual inductance, therefore changes the magnetic flux threading the λ-SQUID loop. We can measure this change in flux by operating the λ-SQUID just like a regular dc-SQUID.

Based on the expertise on dc-SQUIDs at IMS, we have successfully designed, fabricated and characterised first prototype λ-SQUIDs as a proof of concept. We have used niobium ($T_{\mathrm{c}}^{\mathrm{Nb}} \geq 8.9\,\mathrm{K}$) for the largest fraction of these devices, including the Josephson junction electrodes and auxiliary inductors. We have used aluminium ($T_{\mathrm{c}}^{\mathrm{Al}} \gtrapprox 1.2\,\mathrm{K}$) as the sensor material for most of our prototype devices, because its critical temperature is sufficiently below that of niobium, and because a deposition process for aluminium already existed at IMS. We have measured and discussed experimental data on the temperature-dependent mutual inductance $M_{\mathrm{in}}(T)$ of several devices, depicting a change of the mutual inductance M_{in} of about 0.5 % across the measured temperature range. From measurements with both increasing and falling temperature, we could determine that deviations between different cycles are below 100 ppm, i.e. we did not observe any hysteresis. The mutual inductance curve of a λ-SQUID thus appears to be stable over several days and many temperature cycles.

We have developed a software package based on reports by Chang *et al.* [Cha81] and Sheen *et al.* [She91] to analyse the effects by which the magnetic penetration depth λ affects the mutual inductance between the λ-coil and input coil in stripline geometries. We found excellent agreement between our simulations and experimental data gathered on prototype λ-SQUID devices. Using the measured mutual inductance curves of our prototypes with aluminium λ-coils, as well as simple SQUID theory, we have predicted the noise performance of a fully functional λ-SQUID-based microcalorimeter with $T_{\mathrm{c}}^{\lambda} \leq 100\,\mathrm{mK}$. As an example, we have assumed a microcalorimeter equipped with X-ray absorbers made from bismuth with a size of 250 µm × 250 µm and thickness of 8.6 µm. The λ-coil has the same heat capacity as the absorber and a critical temperature $T_{\mathrm{c}}^{\lambda} = 50\,\mathrm{mK}$. With an input current of $I_{\mathrm{in}} = 3\,\mathrm{mA}$, the estimated energy resolution is $\Delta E_{\mathrm{FWHM}} \approx 400\,\mathrm{meV}$ if the device is operated at $T_0 = 0.9 T_{\mathrm{c}}^{\lambda}$, and the absorption of soft X-ray photons would not drive this detector out of the superconducting state.

To close out our work on λ-SQUIDs presented in this thesis, we used simple theory and our software package to investigate the optimisation of λ-SQUIDs and what the next generation of λ-SQUIDs should look like. While our initial prototype devices featured an unoptimised design derived from our dc-SQUIDs, we can use our understanding of λ-SQUIDs to arrive at design parameters that maximise sensitivity. We could show that, to minimise the SQUID-like energy noise contribution, it is beneficial to match the specific heat of the λ-coil to that of the absorber, i.e. $C_{\mathrm{sens}} = C_{\mathrm{abs}}$. This finding is in good agreement with results for cryogenic microcalorimeters [McC05]. Interestingly, we could show that the total inductance L_λ of the λ-coil has no direct influence on the SQUID-like noise contribution, and can hence be freely chosen keeping other restrictions in mind, e.g. geometry or the SQUID screening parameter β_{L}. Secondly, using our

software package, we have computed mutual inductance curves for a variety of stripline geometries and could draw conclusions regarding the optimal width and thickness of the λ-coil. A fully functional λ-SQUID should be based on a simple stripline geometry of a single, narrow ($b_{\mathrm{sen}} \approx 2\,\mu\mathrm{m}$), thick ($a_{\mathrm{sen}} \gtrapprox 1\,\mu\mathrm{m}$) λ-coil placed on top of a suitably narrow ($b_{\mathrm{in}} \approx 4\,\mu\mathrm{m}$) input coil.

The second main part of this thesis is related to the development of a software framework for numerical simulations of the operation and performance of microwave SQUID multiplexers. The readout of large arrays of detectors comprising hundreds or thousands of individual pixels using individual dc-SQUIDs in two-stage setups for readout becomes is unfeasible due to the linearly increasing system cost, complexity, and heatload on the cryostat. Thus, SQUID-based multiplexing techniques must be used instead. Such methods include time division [Che99, Irw02, Dor16] or code division [Nie10, Irw12, Mor16] techniques, as well as frequency division techniques with MHz [dH14, Ric21] or MHz [Irw04, Mat08, Hir13, Kem17] carrier frequencies. Out of these, microwave SQUID multiplexing uses a large number of superconducting microwave resonators as frequency-encoding elements to modulate the signals of individual rf-SQUIDs onto the amplitude and phase of microwave carrier signals. The large signal capacity of state-of-the-art cryogenic amplifiers allows μMUX to outperform other multiplexing schemes in terms of multiplexing factor and readout channel bandwidth. Additionally, the readout channel noise of a μMUX is (to first order) independent of channel count, making it the most promising multiplexing technique for applications with very large detector arrays.

Our software framework is based on the state-of-the-art μMUX model including the nonlinear dynamics of rf-SQUIDs. To also allow for simulations of μMUX channels operated at or near their bandwidth limit, we have derived a dynamical model for lumped-element resonators, taking their finite response time into account. In real applications, such a fast operation mode is required to maximise the measurement bandwidth. We have included the three most dominant noise sources in our software, i.e. amplifier noise, TLS noise and noise of the rf-SQUID, as well as both, FRM and open-loop readout. A variety of parameters can be analysed, including the flux noise spectrum or linearity. This allows us to model μMUX performance for a variety of applications, taking most of the challenges into account that actual experiments have to face.

We have also introduced a hybrid SQUID multiplexing scheme (HμMUX) combining μMUX with MHz FRM multiplexing. The main benefit of this scheme is that the multiplexing factor can be increased without increasing the resonator count. This is a huge benefit for low bandwidth, high channel count applications, such as large bolometer arrays, where fabrication tolerances presently impose an upper limit on the resonator count. As a proof of concept, we have presented measurement data on a single HμMUX resonator channel containing three independent readout channels. We have shown that the operation of a HμMUX channel requires no additional room-temperature electronics compared to regular a μMUX, and have successfully demonstrated that we can fully reconstruct test signals. Using signal theory, we could furthermore determine the bandwidth- and noise performance of HμMUX compared to regular μMUX. We have

been able to reproduce these penalties to noise and bandwidth using our numerical simulations, from which we concluded that even such behaviour arising from the complex underlying physics are modelled correctly. We have also compared simulated data from our software framework to experimental results, and found excellent agreement.

Finding design parameters for μMUX which minimise the readout flux noise is important to maximise the performance of future experiments. Ideally, we would find the global minimum of the full configuration space with regards to noise, but given the large number of parameters this was beyond the scope of this work. Instead, we varied a few parameters at a time, looking for local minima in an attempt to identify ideal parameter ranges or conditions that should be met to minimise noise. We have varied the probe tone frequency f_{exc} and the screening parameter β_{L} simultaneously. From the results we concluded that the ideal value for the screening parameter is $\beta_{\mathrm{L}} \approx 0.4$, but the minimum is so broad that the readout flux noise barely increases over the range $0.3 < \beta_{\mathrm{L}} < 0.5$. The probe tone should ideally be chosen to equal the maximum resonance frequency reached during modulation, i.e. $f_{\mathrm{exc}} = f_{\mathrm{res}}^{\mathrm{max}}$. Additionally, we varied the probe tone power P_{exc}. We have seen that an ideal probe tone power exists which minimises the readout flux noise, and that this ideal power increases with the screening parameter β_{L}. We have noted that at the ideal probe tone power, the microwave resonator induces a radio frequency flux contribution of $\Phi_{\mathrm{rf}} \approx 0.3\Phi_0$ into the SQUID loop. The probe tone power should therefore be adjusted to meet this condition. Lastly, we have studied the influence of the ratio η between maximum frequency shift $\Delta f_{\mathrm{res}}^{\mathrm{max}}$ and resonator bandwidth Δf_{BW} on the readout flux noise. We have seen that, contrary to the typical choice, we should design μMUX channels with $\eta > 1$.

To conclude, we have described additional applications our software can be used for. These include modelling the linearity of a μMUX channel that remains after FRM demodulation, or investigating the noise shaping effects of FRM readout. The modular design of our software allows for a wide variety of uses, beyond the optimisation aspect we have focused on here. Lastly we have presented the use of our software framework to modelling novel readout schemes. We introduced the method of probe tone modulation (PTM), where the probe tone frequency is not static, but rather follows a pre-determined pattern in time that mimics the resonance frequency modulation of the channel during FRM with no external signal. While the complex shape of the transmission tome traces for PTM in the presence of external signals makes their demodulation challenging, we can easily model this behaviour using our software without having to design, modify or acquire any new readout electronics.

In this thesis, we have presented a novel SQUID-based microcalorimeter type with a potential energy resolution of $\mathcal{O}(400\,\mathrm{meV})$. Additionally, we have introduced the HμMUX multiplexing scheme and numerical methods to optimise the performance of microwave SQUID multiplexers. This work thus contributes to the development of ultra-large arrays comprising thousands of detectors, each with sub-eV energy resolution, which would be hugely beneficial for experiments in X-ray spectroscopy, astronomy, and particle physics, among others.

Acknowledgements

Over the last (almost) four years so many people have supported me, either directly or indirectly, that I am likely to forget at least someone in any attempt to make a complete list. But, whether you made it all the way to the end of my thesis or skipped straight to the acknowledgements to see if you made the cut, I will nonetheless provide you with the names of some of the people without whom this would not have been possible.

Firstly, I would greatly like to thank all of my colleagues at IMS. Without the professional, scientific and (not least of all) emotional support of Michael, Martin, Lena, Fabienne, Mathias and all other IMS staff, my time as a PhD student would most likely have come to a much more swift and much less accomplished end. You have bravely endured my complaints, woes and sorrows resulting from each fruitless experiment, each rapidly approaching deadline and any of thousands of lines of buggy code. The hundreds of discussions of various problems I have encountered have helped me to solve many of them. You were the best team I could have wished for.

Secondly, I want to thank my supervisors, Prof. Dr. Weber and Prof. Dr. Kempf. You gave me the opportunity to do my own research, and gave me the freedom to for both, my own mistakes and my own achievements. I always had all the support I needed, and the liberty to choose my own way forward.

I would also like to thank my family, especially my brother and my parents, for their unwavering support. Whenever I needed something you were always there for me.

And a bit of an apology to Jennifer: You have been there for me throughout my entire time as a PhD student, with all the ups and downs. More than once I chose conferences over holidays with you, or spent weekends at the institute rather than in your company, and yet your support never waned. I will make it up to you, I promise.

I am very grateful to Dr. Steffen Blomeier. You were the best physics teacher I could have hoped for. You kindled my passion for physics that ultimately got me here. In a way, this thesis is your fault.

Finally, I would like to thoroughly apologise to Samuel Butler (4 December 1835 – 18 June 1902) for my likely inconsequential yet finite contribution to the inevitable demise of humankind.

Bibliography

[Ade14] P. A. R. Ade, R. W. Aikin, M. Amiri, D. Barkats, S. J. Benton, C. A. Bischoff, J. J. Bock, J. A. Brevik, I. Buder, E. Bullock, G. Davis, P. K. Day, C. D. Dowell, L. Duband, J. P. Filippini, S. Fliescher, S. R. Golwala, M. Halpern, M. Hasselfield, S. R. Hildebrandt, G. C. Hilton, K. D. Irwin, K. S. Karkare, J. P. Kaufman, B. G. Keating, S. A. Kernasovskiy, J. M. Kovac, C. L. Kuo, E. M. Leitch, N. Llombart, M. Lueker, C. B. Netterfield, H. T. Nguyen, R. O'Brient, R. W. Ogburn, A. Orlando, C. Pryke, C. D. Reintsema, S. Richter, R. Schwarz, C. D. Sheehy, Z. K. Staniszewski, K. T. Story, R. V. Sudiwala, G. P. Teply, J. E. Tolan, A. D. Turner, A. G. Vieregg, P. Wilson, C. L. Wong, K. W. Yoon, (Bicep2 Collaboration), Bicep2. ii. experiment and three-year data set, *The Astrophysical Journal*, **792**(1), 62, 2014.

[Aeb17] H. A. Aebischer B. Aebischer, The gmd method for inductance calculation applied to conductors with skin effect, *Advanced Electromagnetics*, **6**(2), 77–92, 2017.

[Ahr22] Felix Klaus Ahrens, *Cryogenic read-out system and resonator optimisation for the microwave SQUID multiplexer within the ECHo experiment*, Dissertation, University of Heidelberg, 2022.

[Ame11] Luuk J. P. Ament, Michel van Veenendaal, Thomas P. Devereaux, John P. Hill, Jeroen van den Brink, Resonant inelastic x-ray scattering studies of elementary excitations, *Rev. Mod. Phys.*, **83**, 705–767, 2011.

[Bag09] Daniela Bagliani, Daniela F. Bogorin, Edvige Celasco, Marcello Celasco, Roberto Eggenhoffner, Lorenza Ferrari, Massimiliano Galeazzi, Flavio Gatti, Renzo Vaccarone, Riccardo Valle, A study of the excess noise of ir transition edge sensors in the frame of statistical models, *IEEE Transactions on Applied Superconductivity*, **19**(3), 445–450, 2009.

[Ban00] Simon Bandler, Eric Silver, Herbert Schnopper, Stephen Murray, Marco Barbera, Norm Madden, Don Landis, Jeff Beeman, Eugene Haller, Greg Tucker, Ntd-ge-based microcalorimeter performance, *Nuclear Instruments and Methods in Physics Research Section A: Accelerators, Spectrometers, Detectors and Associated Equipment*, **444**(1), 273–277, 2000.

[Ban12] S. R. Bandler, K. D. Irwin, D. Kelly, P. N. Nagler, J. P. Porst, H. Rotzinger, J. E. Sadleir, G. M. Seidel, S. J. Smith, T. R. Stevenson, Magnetically coupled microcalorimeters, *Journal of Low Temperature Physics*, **167**(3-4), 254–268, 2012.

[Ban19] Simon R. Bandler, James A. Chervenak, Aaron M. Datesman, Archana M. Devasia, Michael J. DiPirro, Kazuhiro Sakai, Stephen J. Smith, Thomas R. Stevenson, Wonsik Yoon, Douglas A. Bennett, Benjamin Mates, Daniel S. Swetz, Joel N. Ullom, Kent D. Irwin, Megan E. Eckart, Enectali Figueroa-Feliciano, Dan McCammon, Kevin K. Ryu, Jeffrey R. Olson, Ben Zeiger, Lynx x-ray microcalorimeter, *Journal of Astronomical Telescopes, Instruments, and Systems*, **5**(2), 021017, 2019.

[Bar18] Didier Barret, Thien Lam Trong, Jan-Willem den Herder, Luigi Piro, Massimo Cappi, Juhani Houvelin, Richard Kelley, J. Miguel Mas-Hesse, Kazuhisa Mitsuda, Stéphane Paltani, Gregor Rauw, Agata Rozanska, Joern Wilms, Simon Bandler, Marco Barbera, Xavier Barcons, Enrico Bozzo, Maria Teresa Ceballos, Ivan Charles, Elisa Costantini, Anne Decourchelle, Roland den Hartog, Lionel Duband, Jean-Marc Duval, Fabrizio Fiore, Flavio Gatti, Andrea Goldwurm, Brian Jackson, Peter Jonker, Caroline Kilbourne, Claudio Macculi, Mariano Mendez, Silvano Molendi, Piotr Orleanski, François Pajot, Etienne Pointecouteau, Frederick Porter, Gabriel W. Pratt, Damien Prêle, Laurent Ravera, Kosuke Sato, Joop Schaye, Keisuke Shinozaki, Tanguy Thibert, Luca Valenziano, Véronique Valette, Jacco Vink, Natalie Webb, Michael Wise, Noriko Yamasaki, Françoise Douchin, Jean-Michel Mesnager, Bernard Pontet, Alice Pradines, Graziella Branduardi-Raymont, Esra Bulbul, Mauro Dadina, Stefano Ettori, Alexis Finoguenov, Yasushi Fukazawa, Agnieszka Janiuk, Jelle Kaastra, Pasquale Mazzotta, Jon Miller, Giovanni Miniutti, Yael Naze, Fabrizio Nicastro, Salavtore Scioritino, Aurora Simonescu, Jose Miguel Torrejon, Benoit Frezouls, Hervé Geoffray, Philippe Peille, Corinne Aicardi, Jérôme André, Christophe Daniel, Antoine Clénet, Christophe Etcheverry, Emilie Gloaguen, Gilles Hervet, Antoine Jolly, Aurélien Ledot, Irwin Paillet, Roseline Schmisser, Bruno Vella, Jean-Charles Damery, Kevin Boyce, Mike Dipirro, Simone Lotti, Denis Schwander, Stephen Smith, Bert-Joost Van Leeuwen, Henk van Weers, Nicolas Clerc, Beatriz Cobo, Thomas Dauser, Christian Kirsch, Edoardo Cucchetti, Megan Eckart, Philippe Ferrando, Lorenzo Natalucci, The ATHENA X-ray Integral Field Unit (X-IFU), in Jan-Willem A. den Herder, Shouleh Nikzad, Kazuhiro Nakazawa (Ed.), *Space Telescopes and Instrumentation 2018: Ultraviolet to Gamma Ray*, volume 10699, 106991G, International Society for Optics and Photonics, SPIE, 2018.

[Bau22] Fabienne Bauer, *Rauscharme Stromsensor-dc-SQUIDs mit Impedanzanpassung für metallische magnetische Kalorimeter*, Dissertation, University of Heidelberg, 2022.

[Beh71] F. Behroozi M.P. Garfunkel, Penetration depth in superconducting aluminum as a function of magnetic field and temperature, *Physica*, **55**, 649–655, 1971.

[Bou05] R Boucher, T May, Th Wagner, V Zakosarenko, S Anders, H G Mayer, Structural and electrical properties of aupd/mo bi-layer films for transition edge sensors, *Superconductor Science and Technology*, **19**(1), 138, 2005.

[Bra10] Daniel Brandt George W. Fraser, Analytical expressions for transition edge sensor excess noise models, *Nuclear Instruments and Methods in Physics Research Section A: Accelerators, Spectrometers, Detectors and Associated Equipment*, **620**(2), 294–298, 2010.

[Bro08] A.-D. Brown, S. R. Bandler, R. Brekosky, J. A. Chervenak, E. Figueroa-Feliciano, F. Finkbeiner, N. Iyomoto, R. L. Kelley, C. A. Kilbourne, F. S. Porter, S. Smith, T. Saab, J. Sadleir, Absorber materials for transition-edge sensor x-ray microcalorimeters, *Journal of Low Temperature Physics*, **151**(1), 413–417, 2008.

[Bru82] J. J. P. Bruines, V. J. de Waal, J. E. Mooij, Comment on: "dc squid: Noise and optimization" by tesche and clarke, *Journal of Low Temperature Physics*, **46**(3), 383–386, 1982.

[Bur08] Andreas Burck, *Entwicklung großflächiger mikrostrukturierter magnetischer Kalorimeter mit Au:Er- und Ag:Er-Sensoren für den energieaufgelösten Nachweis von Röntgenquanten und hochenergetischen Teilchen*, Dissertation, University of Heidelberg, 2008.

[But96] S. M. Butorin, J.-H. Guo, M. Magnuson, P. Kuiper, J. Nordgren, Low-energy d-d excitations in mno studied by resonant x-ray fluorescence spectroscopy, *Phys. Rev. B*, **54**, 4405–4408, 1996.

[Can07] Robin Cantor, J. Ad Hall, Phil Blumenfeld, Stephen T. P. Boyd, Miniature thin-film superconducting quantum interference device susceptometer, *IEEE Transactions on Applied Superconductivity*, **17**(2), 738–741, 2007.

[Cha81] W. Chang, Numerical calculation of the inductances of a multi-superconductor transmission line system, *IEEE Transactions on Magnetics*, **17**(1), 764–766, 1981.

[Che99] J. A. Chervenak, K. D. Irwin, E. N. Grossman, John M. Martinis, C. D. Reintsema, M. E. Huber, Superconducting multiplexer for arrays of transition edge sensors, *Applied Physics Letters*, **74**(26), 4043–4045, 1999.

[Che04] Boris Chesca, Reinhold Kleiner, Dieter Koelle, *SQUID Theory*, chapter 2, 29–92, John Wiley & Sons, Ltd, 2004.

[Dau48] J. G. Daunt, A. R. Miller, A. B. Pippard, D. Shoenberg, Temperature dependence of penetration depth of a magnetic field in superconductors, *Phys. Rev.*, **74**, 842–842, 1948.

[dH14] R. H. den Hartog, M. P. Bruijn, A. Clenet, L. Gottardi, R. Hijmering, B. D. Jackson, J. van der Kuur, B. J. van Leeuwen, A. J. van der Linden, D. van Loon, A. Nieuwenhuizen, M. Ridder, P. van Winden, Progress on the FDM Development at SRON: Toward 160 Pixels, *Journal of Low Temperature Physics*, **176**, 439–445, 2014.

[Dor16] W. B. Doriese, K. M. Morgan, D. A. Bennett, E. V. Denison, C. P. Fitzgerald, J. W. Fowler, J. D. Gard, J. P. Hays-Wehle, G. C. Hilton, K. D. Irwin, Y. I. Joe, J. A. B. Mates, G. C. O'Neil, C. D. Reintsema, N. O. Robbins, D. R. Schmidt, D. S. Swetz, H. Tatsuno, L. R. Vale, J. N. Ullom, Developments in Time-Division Multiplexing of X-ray Transition-Edge Sensors, *Journal of Low Temperature Physics*, **184**, 389–395, 2016.

[Dor17] W. B. Doriese, P. Abbamonte, B. K. Alpert, D. A. Bennett, E. V. Denison, Y. Fang, D. A. Fischer, C. P. Fitzgerald, J. W. Fowler, J. D. Gard, J. P. Hays-Wehle, G. C. Hilton, C. Jaye, J. L. McChesney, L. Miaja-Avila, K. M. Morgan, Y. I. Joe, G. C. O'Neil, C. D. Reintsema, F. Rodolakis, D. R. Schmidt, H. Tatsuno, J. Uhlig, L. R. Vale, J. N. Ullom, D. S. Swetz, A practical superconducting-microcalorimeter X-ray spectrometer for beamline and laboratory science, *Review of Scientific Instruments*, **88**(5), 053108, 2017.

[Doy08] S. Doyle, P. Mauskopf, J. Naylon, A. Porch, C. Duncombe, Lumped element kinetic inductance detectors, *Journal of Low Temperature Physics*, **151**(1), 530–536, 2008.

[Dru96] Dietmar Drung, *Advanced Squid Read-Out Electronics*, 63–116, Springer Netherlands, Dordrecht, 1996.

[Dru04] Dietmar Drung Michael Mück, *SQUID Electronics*, chapter 4, 127–170, John Wiley & Sons, Ltd, 2004.

[Dru06] Dietmar Drung, Colmar Hinnrichs, Henry-Jobes Barthelmess, Low-noise ultra-high-speed dc squid readout electronics, *Superconductor Science and Technology*, **19**(5), S235, 2006.

[Dur23] Malcolm Durkin, Scott Backhaus, Simon R. Bandler, James A. Chervenak, Ed V. Denison, William B. Doriese, Johnathon D. Gard, Gene C. Hilton, Richard A. Lew, Tammy J. Lucas, Carl D. Reintsema, Daniel R. Schmidt, Stephen J. Smith, Joel N. Ullom, Leila R. Vale, Michael R. Vissers, Nicholas A. Wakeham, Symmetric time-division-multiplexed squid readout with two-layer switches for future tes observatories, *IEEE Transactions on Applied Superconductivity*, **33**(5), 1–5, 2023.

[Enp86] K. Enpuku, K. Yoshida, S. Kohjiro, Noise characteristics of a dc SQUID with a resistively shunted inductance. II. Optimum damping, *Journal of Applied Physics*, **60**(12), 4218–4223, 1986.

[Fag06] R. L. Fagaly, Superconducting quantum interference device instruments and applications, *Review of Scientific Instruments*, **77**(10), 101101, 2006.

[Fav16] M. Faverzani, B. Alpert, D. Backer, D. Bennet, M. Biasotti, C. Brofferio, V. Ceriale, G. Ceruti, D. Corsini, P. K. Day, M. De Gerone, R. Dressler,

E. Ferri, J. Fowler, E. Fumagalli, J. Gard, F. Gatti, A. Giachero, J. Hays-Wehle, S. Heinitz, G. Hilton, U. Köster, M. Lusignoli, M. Maino, J. Mates, S. Nisi, R. Nizzolo, A. Nucciotti, A. Orlando, L. Parodi, G. Pessina, G. Pizzigoni, A. Puiu, S. Ragazzi, C. Reintsema, M. Ribeiro-Gomez, D. Schmidt, D. Schuman, F. Siccardi, M. Sisti, D. Swetz, F. Terranova, J. Ullom, L. Vale, The holmes experiment, *Journal of Low Temperature Physics*, **184**(3), 922–929, 2016.

[Fer09] Lorenza Ferrari, S. Ambrosetti, D. Bagliani, F. Gatti, R. Vaccarone, R. Valle, Characterization of the superconducting transition of thin ir films for tes, *IEEE Transactions on Applied Superconductivity*, **19**(3), 477–480, 2009.

[Fio88] A. T. Fiory, A. F. Hebard, P. M. Mankiewich, R. E. Howard, Penetration depths of high Tc films measured by two-coil mutual inductances, *Applied Physics Letters*, **52**(25), 2165–2167, 1988.

[Fle05] A. Fleischmann, C. Enss, G.M. Seidel, *Metallic Magnetic Calorimeters*, 151–216, Springer Berlin Heidelberg, Berlin, Heidelberg, 2005.

[Fle09] A. Fleischmann, L. Gastaldo, S. Kempf, A. Kirsch, A. Pabinger, C. Pies, J.-P Porst, P. Ranitzsch, S. Schäfer, F. v. Seggern, T. Wolf, C. Enss, G. M. Seidel, Metallic magnetic calorimeters, *AIP Conference Proceedings*, **1185**(1), 571–578, 2009.

[Fri06] Stephan Friedrich, Cryogenic X-ray detectors for synchrotron science, *Journal of Synchrotron Radiation*, **13**(2), 159–171, 2006.

[Fri16] Stephan Friedrich, Stephen Boyd, Robin Cantor, Fabrication of gamma detectors based on magnetic ag:er microcalorimeters, 2016.

[Fà19] Lourdes Fàbrega, Agustin Camón, Pavel Strichovanec, Carlos Pobes, Exploring the proximity effect in mo/au bilayers, *IEEE Transactions on Applied Superconductivity*, **29**(5), 1–5, 2019.

[Gao07] Jiansong Gao, Jonas Zmuidzinas, Benjamin A. Mazin, Henry G. LeDuc, Peter K. Day, Noise properties of superconducting coplanar waveguide microwave resonators, *Applied Physics Letters*, **90**(10), 102507, 2007.

[Gao08] J. Gao, J. Zmuidzinas, A. Vayonakis, P. Day, B. Mazin, H. Leduc, Equivalence of the effects on the complex conductivity of superconductor due to temperature change and external pair breaking, *Journal of Low Temperature Physics*, **151**(1), 557–563, 2008.

[Gas17] L. Gastaldo, K. Blaum, K. Chrysalidis, T. Day Goodacre, A. Domula, M. Door, H. Dorrer, Ch E. Düllmann, K. Eberhardt, S. Eliseev, C. Enss, A. Faessler, P. Filianin, A. Fleischmann, D. Fonnesu, L. Gamer, R. Haas, C. Hassel, D. Hengstler, J. Jochum, K. Johnston, U. Kebschull, S. Kempf,

T. Kieck, U. Köster, S. Lahiri, M. Maiti, F. Mantegazzini, B. Marsh, P. Neroutsos, Yu N. Novikov, P. C.O. Ranitzsch, S. Rothe, A. Rischka, A. Saenz, O. Sander, F. Schneider, S. Scholl, R. X. Schüssler, Ch Schweiger, F. Simkovic, T. Stora, Z. Szücs, A. Türler, M. Veinhard, M. Weber, M. Wegner, K. Wendt, K. Zuber, The electron capture in 163Ho experiment – ECHo, *European Physical Journal: Special Topics*, **226**(8), 1623–1694, 2017.

[Gol11] D. J. Goldie, A. V. Velichko, D. M. Glowacka, S. Withington, Ultra-low-noise MoCu transition edge sensors for space applications, *Journal of Applied Physics*, **109**(8), 084507, 2011.

[Gub05] A. I. Gubin, K. S. Il'in, S. A. Vitusevich, M. Siegel, N. Klein, Dependence of magnetic penetration depth on the thickness of superconducting nb thin films, *Phys. Rev. B*, **72**, 064503, 2005.

[He16] X. He, A. Gozar, R. Sundling, I. Božović, High-precision measurement of magnetic penetration depth in superconducting films, *Review of Scientific Instruments*, **87**(11), 113903, 2016.

[Hen18] Shawn W. Henderson, Zeeshan Ahmed, Jason Austermann, Daniel Becker, Douglas A. Bennett, David Brown, Saptarshi Chaudhuri, Hsiao-Mei Sherry Cho, John M. D'Ewart, Bradley Dober, Shannon M. Duff, John E. Dusatko, Sofia Fatigoni, Josef C. Frisch, Jonathon D. Gard, Mark Halpern, Gene C. Hilton, Johannes Hubmayr, Kent D. Irwin, Ethan D. Karpel, Sarah S. Kernasovskiy, Stephen E. Kuenstner, Chao-Lin Kuo, Dale Li, John A. B. Mates, Carl D. Reintsema, Stephen R. Smith, Joel Ullom, Leila R. Vale, Daniel D. Van Winkle, Michael Vissers, Cyndia Yu, Highly-multiplexed microwave SQUID readout using the SLAC Microresonator Radio Frequency (SMuRF) electronics for future CMB and sub-millimeter surveys, in Jonas Zmuidzinas Jian-Rong Gao (Ed.), *Millimeter, Submillimeter, and Far-Infrared Detectors and Instrumentation for Astronomy IX*, volume 10708, 1070819, International Society for Optics and Photonics, SPIE, 2018.

[Hir13] F. Hirayama, S. Kohjiro, D. Fukuda, H. Yamamori, S. Nagasawa, M. Hidaka, Microwave squid multiplexer for tes readout, *IEEE Transactions on Applied Superconductivity*, **23**(3), 2500405–2500405, 2013.

[Hor08] Robert D. Horansky, Joel N. Ullom, James A. Beall, Gene C. Hilton, Kent D. Irwin, Donald E. Dry, Elizabeth P. Hastings, Stephen P. Lamont, Clifford R. Rudy, Michael W. Rabin, Superconducting calorimetric alpha particle sensors for nuclear nonproliferation applications, *Applied Physics Letters*, **93**(12), 123504, 2008.

[Hub13] J. Hubmayr, J. Beall, D. Becker, H.-M. Cho, B. Dober, M. Devlin, A. M. Fox, J. Gao, G. C. Hilton, K. D. Irwin, D. Li, M. D. Niemack, D. P. Pappas, L. Vale, M. Vissers, Dual-polarization sensitive mkids for far infrared astrophysics,

IEEE Transactions on Applied Superconductivity, **23**(3), 2400304–2400304, 2013.

[Hun18] J. Hunacek, J. Bock, C. M. Bradford, V. Butler, T.-C. Chang, Y.-T. Cheng, A. Cooray, A. Crites, C. Frez, S. Hailey-Dunsheath, B. Hoscheit, D. W. Kim, C.-T. Li, D. Marrone, L. Moncelsi, E. Shirokoff, B. Steinbach, G. Sun, I. Trumper, A. Turner, B. Uzgil, A. Weber, M. Zemcov, Hafnium films and magnetic shielding for time, a mm-wavelength spectrometer array, *Journal of Low Temperature Physics*, **193**(5), 893–900, 2018.

[Irw95] K. D. Irwin, An application of electrothermal feedback for high resolution cryogenic particle detection, *Applied Physics Letters*, **66**(15), 1998–2000, 1995.

[Irw02] K. D. Irwin, L. R. Vale, N. E. Bergren, S. Deiker, E. N. Grossman, G. C. Hilton, S. W. Nam, C. D. Reintsema, D. A. Rudman, M. E. Huber, Time-division SQUID multiplexers, *AIP Conference Proceedings*, **605**(1), 301–304, 2002.

[Irw04] K. D. Irwin K. W. Lehnert, Microwave squid multiplexer, *Applied Physics Letters*, **85**(11), 2107–2109, 2004.

[Irw05] G.C. Irwin, K.D.and Hilton, *Transition-Edge Sensors*, 63–150, Springer Berlin Heidelberg, Berlin, Heidelberg, 2005.

[Irw10] K D Irwin, M D Niemack, J Beyer, H M Cho, W B Doriese, G C Hilton, C D Reintsema, D R Schmidt, J N Ullom, L R Vale, Code-division multiplexing of superconducting transition-edge sensor arrays, *Superconductor Science and Technology*, **23**(3), 034004, 2010.

[Irw12] K. D. Irwin, H. M. Cho, W. B. Doriese, J. W. Fowler, G. C. Hilton, M. D. Niemack, C. D. Reintsema, D. R. Schmidt, J. N. Ullom, L. R. Vale, Advanced code-division multiplexers for superconducting detector arrays, *Journal of Low Temperature Physics*, **167**(5), 588–594, 2012.

[Irw18] K. D. Irwin, S. Chaudhuri, H. M. Cho, C. Dawson, S. Kuenstner, D. Li, C. J. Titus, B. A. Young, A spread-spectrum squid multiplexer, *Journal of Low Temperature Physics*, **193**(3-4), 476–484, 2018.

[Jet09] Nikhil Jethava, Joel N. Ullom, Kent D. Irwin, W. B. Doriese, J. A. Beall, G. C. Hilton, L. R. Vale, Barry Zink, Dependence of Excess Noise on the Partial Derivatives of Resistance in Superconducting Transition Edge Sensors, *AIP Conference Proceedings*, **1185**(1), 31–33, 2009.

[Kan17] C S Kang, J A Jeon, H S Jo, G B Kim, H L Kim, I Kim, S R Kim, Y H Kim, D H Kwon, C Lee, H J Lee, M K Lee, S H Lee, S Y Oh, J H So, Y S Yoon, Mmc-based low-temperature detector system of the amore-pilot experiment, *Superconductor Science and Technology*, **30**(8), 084011, 2017.

[Kar20] N. Karcher, D. Richter, F. Ahrens, R. Gartmann, M. Wegner, O. Krömer, Sina Kempf, C. Enss, Margit Weber, O. Sander, Sdr-based readout electronics for the echo experiment, *Journal of Low Temperature Physics*, **200**, 2020.

[Kem17] S. Kempf, M. Wegner, L. Deeg, A. Fleischmann, L. Gastaldo, F. Herrmann, D. Richter, C. Enss, Design, fabrication and characterization of a 64 pixel metallic magnetic calorimeter array with integrated, on-chip microwave squid multiplexer, *Superconductor Science and Technology*, **30**(6), 065002, 2017.

[Kem18] S. Kempf, A. Fleischmann, L. Gastaldo, C. Enss, Physics and Applications of Metallic Magnetic Calorimeters, *Journal of Low Temperature Physics*, 1–15, 2018.

[Ket84] M. B. Ketchen, T. Kopley, H. Ling, Miniature SQUID susceptometer, *Applied Physics Letters*, **44**(10), 1008–1010, 1984.

[Kim18] G. B. Kim, C. C. Flynn, S. Kempf, L. Gastaldo, A. Fleischmann, C. Enss, S. Friedrich, Development of mmc gamma detectors for precise characterization of uranium isotopes, *Journal of Low Temperature Physics*, **193**(5), 1236–1242, 2018.

[Kra23] M. Krantz, F. Toschi, B Maier, G. Heine, C. Enss, S. Kempf, Magnetic microcalorimeter with paramagnetic temperature sensor and integrated dc-squid readout for high-resolution x-ray emission spectroscopy, *in preparation*, 2023.

[Lee15] S. J. Lee, J. S. Adams, S. R. Bandler, J. A. Chervenak, M. E. Eckart, F. M. Finkbeiner, R. L. Kelley, C. A. Kilbourne, F. S. Porter, J. E. Sadleir, S. J. Smith, E. J. Wassell, Fine pitch transition-edge sensor X-ray microcalorimeters with sub-eV energy resolution at 1.5 keV, *Applied Physics Letters*, **107**(22), 223503, 2015.

[Lee19] Sang-Jun Lee, Charles J. Titus, Roberto Alonso Mori, Michael L. Baker, Douglas A. Bennett, Hsiao-Mei Cho, William B. Doriese, Joseph W. Fowler, Kelly J. Gaffney, Alessandro Gallo, Johnathon D. Gard, Gene C. Hilton, Hoyoung Jang, Young Il Joe, Christopher J. Kenney, Jason Knight, Thomas Kroll, Jun-Sik Lee, Dale Li, Donghui Lu, Ronald Marks, Michael P. Minitti, Kelsey M. Morgan, Hirohito Ogasawara, Galen C. O'Neil, Carl D. Reintsema, Daniel R. Schmidt, Dimosthenis Sokaras, Joel N. Ullom, Tsu-Chien Weng, Christopher Williams, Betty A. Young, Daniel S. Swetz, Kent D. Irwin, Dennis Nordlund, Soft X-ray spectroscopy with transition-edge sensors at Stanford Synchrotron Radiation Lightsource beamline 10-1, *Review of Scientific Instruments*, **90**(11), 113101, 2019.

[Lin04] Mark A. Lindeman, Simon Bandler, Regis P. Brekosky, James A. Chervenak, Enectali Figueroa-Feliciano, Fred M. Finkbeiner, Tarek Saab, Caroline K.

Stahle, Characterization and reduction of noise in mo/au transition edge sensors, *Nuclear Instruments and Methods in Physics Research Section A: Accelerators, Spectrometers, Detectors and Associated Equipment*, **520**(1), 348–350, 2004, Proceedings of the 10th International Workshop on Low Temperature Detectors.

[Lit05] A.E. Lita, D. Rosenberg, S. Nam, A.J. Miller, D. Balzar, L.M. Kaatz, R.E. Schwall, Tuning of tungsten thin film superconducting transition temperature for fabrication of photon number resolving detectors, *IEEE Transactions on Applied Superconductivity*, **15**(2), 3528–3531, 2005.

[Loi18] M. Loidl, J. Beyer, L. Bockhorn, C. Enss, D. Györi, S. Kempf, K. Kossert, R. Mariam, O. Nähle, M. Paulsen, M. Rodrigues, M. Schmidt, Metrobeta: Beta spectrometry with metallic magnetic calorimeters in the framework of the european program of ionizing radiation metrology, *Journal of Low Temperature Physics*, **193**(5), 1251–1256, 2018.

[Lon35] F. London, H. London, Frederick Alexander Lindemann, The electromagnetic equations of the supraconductor, *Proceedings of the Royal Society of London. Series A - Mathematical and Physical Sciences*, **149**(866), 71–88, 1935.

[Luu03] A. Luukanen, K. M. Kinnunen, A. K. Nuottajärvi, H. F. C. Hoevers, W. M. Bergmann Tiest, J. P. Pekola, Fluctuation-limited noise in a superconducting transition-edge sensor, *Phys. Rev. Lett.*, **90**, 238306, 2003.

[Mar00] John M. Martinis, G. C. Hilton, Kent D. Irwin, David A. Wollman, Calculation of tc in a normal-superconductor bilayer using the microscopic-based usadel theory, *Nuclear Instruments & Methods in Physics Research Section A-accelerators Spectrometers Detectors and Associated Equipment*, **444**, 23–27, 2000.

[Mat08] J. A. B. Mates, G. C. Hilton, K. D. Irwin, L. R. Vale, K. W. Lehnert, Demonstration of a multiplexer of dissipationless superconducting quantum interference devices, *Applied Physics Letters*, **92**(2), 023514, 2008.

[Mat11] John Arthur Ben Mates, *The Microwave SQUID Multiplexer*, Dissertation, University of Colorado, 2011.

[Mat12] J. A.B. Mates, K. D. Irwin, L. R. Vale, G. C. Hilton, J. Gao, K. W. Lehnert, Flux-ramp modulation for SQUID multiplexing, *Journal of Low Temperature Physics*, **167**(5-6), 707–712, 2012.

[Mat17] J. A. B. Mates, D. T. Becker, D. A. Bennett, B. J. Dober, J. D. Gard, J. P. Hays-Wehle, J. W. Fowler, G. C. Hilton, C. D. Reintsema, D. R. Schmidt, D. S. Swetz, L. R. Vale, J. N. Ullom, Simultaneous readout of 128 x-ray and gamma-ray transition-edge microcalorimeters using microwave squid multiplexing, *Applied Physics Letters*, **111**(6), 062601, 2017.

[Max72] James Clerk Maxwell, On the geometrical mean distance of two figures on a plane, *Trans. Roy. Soc. Edinb.*, (XXVI), 729–733, 1872.

[Maz09] Benjamin A. Mazin, Microwave Kinetic Inductance Detectors: The First Decade, *AIP Conference Proceedings*, **1185**(1), 135–142, 2009.

[McC68] D. E. McCumber, Effect of ac Impedance on dc Voltage-Current Characteristics of Superconductor Weak-Link Junctions, *Journal of Applied Physics*, **39**(7), 3113–3118, 1968.

[McC93] D. McCammon, W. Cui, M. Juda, J. Morgenthaler, J. Zhang, R.L. Kelley, S.S. Holt, G.M. Madejski, S.H. Moseley, A.E. Szymkowiak, Thermal calorimeters for high resolution x-ray spectroscopy, *Nuclear Instruments and Methods in Physics Research Section A: Accelerators, Spectrometers, Detectors and Associated Equipment*, **326**(1), 157–165, 1993.

[McC05] D. McCammon, *Thermal Equilibrium Calorimeters – An Introduction*, 1–34, Springer Berlin Heidelberg, Berlin, Heidelberg, 2005.

[McD87] D. G. McDonald, Novel superconducting thermometer for bolometric applications, *Applied Physics Letters*, **50**(12), 775–777, 1987.

[Mes69] R. Meservey P. M. Tedrow, Measurements of the Kinetic Inductance of Superconducting Linear Structures, *Journal of Applied Physics*, **40**(5), 2028–2034, 1969.

[Mor16] K. M. Morgan, B. K. Alpert, D. A. Bennett, E. V. Denison, W. B. Doriese, J. W. Fowler, J. D. Gard, G. C. Hilton, K. D. Irwin, Y. I. Joe, G. C. O'Neil, C. D. Reintsema, D. R. Schmidt, J. N. Ullom, D. S. Swetz, Code-division-multiplexed readout of large arrays of tes microcalorimeters, *Applied Physics Letters*, **109**(11), 112604, 2016.

[Mül24] Michael Müller, Matias Rodrigues, Jörn Beyer, Martin Loidl, Sebastian Kempf, Magnetic microcalorimeters for primary activity standardization within the empir project prima-ltd, *Journal of Low Temperature Physics*, 1–9, 2024.

[Nag12] P. C. Nagler, J. S. Adams, M. A. Balvin, S. R. Bandler, K. L. Denis, W. T. Hsieh, D. P. Kelly, J. P. Porst, J. E. Sadleir, G. M. Seidel, S. J. Smith, T. R. Stevenson, Performance of magnetic penetration thermometers for x-ray astronomy, *Journal of Low Temperature Physics*, **167**(3-4), 455–460, 2012.

[Nie10] M. D. Niemack, J. Beyer, H. M. Cho, W. B. Doriese, G. C. Hilton, K. D. Irwin, C. D. Reintsema, D. R. Schmidt, J. N. Ullom, L. R. Vale, Code-division SQUID multiplexing, *Applied Physics Letters*, **96**(16), 163509, 2010.

[Nov15] O. Novotný, S. Allgeier, C. Enss, A. Fleischmann, L. Gamer, D. Hengstler, S. Kempf, C. Krantz, A. Pabinger, C. Pies, D. W. Savin, D. Schwalm, A. Wolf, Cryogenic micro-calorimeters for mass spectrometric identification of neutral molecules and molecular fragments, *Journal of Applied Physics*, **118**(10), 104503, 2015.

[Prê16] D. Prêle, F. Voisin, M. Piat, T. Decourcelle, C. Perbost, C. Chapron, D. Rambaud, S. Maestre, W. Marty, L. Montier, A 128 multiplexing factor time-domain squid multiplexer, *Journal of Low Temperature Physics*, **184**(1), 363–368, 2016.

[Rei08] C. D. Reintsema, J. Beall, W. Doriese, W. Duncan, L. Ferreira, G. C. Hilton, K. D. Irwin, D. Schmidt, J. Ullom, L. Vale, Y. Xu, A tdma hybrid squid multiplexer, *Journal of Low Temperature Physics*, **151**(3-4), 927–933, 2008.

[Rei09] C. D. Reintsema, J. S. Adams, R. Baker, S. R. Bandler, W. R. Doriese, E. Figueroa-Feliciano, G. C. Hilton, K. D. Irwin, R. L. Kelly, C. A. Kilbourne, J. W. Krinsky, F. S. Porter, P. Wikus, Electronics for a Next-Generation SQUID-Based Time-Domain Multiplexing System, *AIP Conference Proceedings*, **1185**(1), 237–240, 2009.

[Rei19] Carl D. Reintsema, Doug A. Bennett, Edward V. Denison, Malcolm Durkin, Willaim B. Doriese, Joseph W. Fowler, Johnathon D. Gard, Arpi Grigorian, Gene C. Hilton, Johannes Hubmayr, Galen C. O'Neil, John A. B. Mates, Kelsey M. Morgan, Dan R. Schmidt, Robert W. Stevens, Daniel S. Swetz, Leila R. Vale, Joel N. Ullom, Kent D. Irwin, Saptarshi Chaudhuri, Charles J. Titus, Carl S. Dawson, High-throughput, dc-parametric evaluation of flux-activated-switch-based tdm and cdm squid multiplexers, *IEEE Transactions on Applied Superconductivity*, **29**(5), 1–6, 2019.

[RG13] M. Ribeiro Gomes, F. Gatti, A. Nucciotti, P. Manfrinetti, M. Galeazzi, E. Alves, D. Bagliani, N. Barradas, S. Basak, M. Biasotti, E. Ferri, A. Kling, G. Pizzigoni, K. Prasai, J. Rocha, Status of the mare experiment, *IEEE Transactions on Applied Superconductivity*, **23**(3), 2101204–2101204, 2013.

[Ric21] Daniel Richter, Ludwig Hoibl, Thomas Wolber, Nick Karcher, Andreas Fleischmann, Christian Enss, Marc Weber, Oliver Sander, Sebastian Kempf, Flux ramp modulation based mhz frequency-division dc-squid multiplexer, *Applied Physics Letters*, **118**(12), 122601, 2021.

[Ros08] E.B. Rosa United States. National Bureau of Standards, *The Self and Mutual Inductances of Linear Conductors*, Number Nr. 80 in Bulletin of the Bureau of Standards, U.S. Department of Commerce and Labor, Bureau of Standards, 1908.

[Rot18] J. Rothe, G. Angloher, P. Bauer, A. Bento, C. Bucci, L. Canonica, A. D'Addabbo, X. Defay, A. Erb, F. v. Feilitzsch, N. Ferreiro Iachellini,

P. Gorla, A. Gütlein, D. Hauff, J. Jochum, M. Kiefer, H. Kluck, H. Kraus, J.-C. Lanfranchi, A. Langenkämper, J. Loebell, M. Mancuso, E. Mondragon, A. Münster, C. Pagliarone, F. Petricca, W. Potzel, F. Pröbst, R. Puig, F. Reindl, K. Schäffner, J. Schieck, V. Schipperges, S. Schönert, W. Seidel, M. Stahlberg, L. Stodolsky, C. Strandhagen, R. Strauss, A. Tanzke, H. H. Trinh Thi, C. Türkoğlu, A. Ulrich, I. Usherov, S. Wawoczny, M. Willers, M. Wüstrich, Tes-based light detectors for the cresst direct dark matter search, *Journal of Low Temperature Physics*, **193**(5), 1160–1166, 2018.

[San19] O. Sander, N. Karcher, O. Kromer, S. Kempf, M. Wegner, C. Enss, M. Weber, Software-Defined Radio Readout System for the ECHo Experiment, *IEEE Transactions on Nuclear Science*, **PP**, 1–1, 2019.

[Sch22] Constantin Schuster, Mathias Wegner, Christian Enss, Sebastian Kempf, Flux ramp modulation based hybrid microwave squid multiplexer, *Applied Physics Letters*, **120**(16), 162601, 2022.

[Sch23] C. Schuster, M. Wegner, S. Kempf, Simulation framework for microwave SQUID multiplexer optimization, *Journal of Applied Physics*, **133**(4), 044503, 2023.

[Sei04] G.M Seidel I.S Beloborodov, Intrinsic excess noise in a transition edge sensor, *Nuclear Instruments and Methods in Physics Research Section A: Accelerators, Spectrometers, Detectors and Associated Equipment*, **520**(1), 325–328, 2004, Proceedings of the 10th International Workshop on Low Temperature Detectors.

[She91] D.M. Sheen, S.M. Ali, D.E. Oates, R.S. Withers, J.A. Kong, Current distribution, resistance, and inductance for superconducting strip transmission lines, *IEEE Transactions on Applied Superconductivity*, **1**(2), 108–115, 1991.

[Sim84] R. W. Simon P. M. Chaikin, Penetration depth in proximity-effect superconductors, *Phys. Rev. B*, **30**, 3750–3756, 1984.

[Sin23] V. Singh, M. Beretta, E.V. Hansen, K.J. Vetter, G. Benato, L. Marini, C. Capelli, B.K. Fujikawa, B. Schmidt, C.L. Chang, Yu.G. Kolomensky, B. Welliver, W.K. Kwok, J. Pearson, U. Welp, M. Lisovenko, G. Wang, V. Yefremenko, J. Zhang, V. Novosad, Large-area photon calorimeter with ir-pt bilayer transition-edge sensor for the cupid experiment, *Phys. Rev. Appl.*, **20**, 064017, 2023.

[Smi12] S. J. Smith, J. S. Adams, C. N. Bailey, S. R. Bandler, J. A. Chervenak, M. E. Eckart, F. M. Finkbeiner, R. L. Kelley, C. A. Kilbourne, F. S. Porter, J. E. Sadleir, Small Pitch Transition-Edge Sensors with Broadband High Spectral Resolution for Solar Physics, *Journal of Low Temperature Physics*, **167**(3), 168–175, 2012.

[Ste68] W. C. Stewart, CURRENT-VOLTAGE CHARACTERISTICS OF JOSEPHSON JUNCTIONS, *Applied Physics Letters*, **12**(8), 277–280, 1968.

[Ste13] T. R. Stevenson, M. A. Balvin, S. R. Bandler, S. E. Busch, K. L. Denis, W.-T. Hsieh, D. P. Kelly, W. Merrell, P. C. Nagler, J.-P. Porst, J. E. Sadleir, G. M. Seidel, S. J. Smith, Superconducting effects in optimization of magnetic penetration thermometers for x-ray microcalorimeters, *IEEE Transactions on Applied Superconductivity*, **23**(3), 2300605–2300605, 2013.

[Tes77] Claudia D. Tesche John Clarke, dc SQUID: Noise and optimization, *Journal of Low Temperature Physics*, **29**, 301–331, 1977.

[Tol22] Sergey K. Tolpygo, Evan B. Golden, Terence J. Weir, Vladimir Bolkhovsky, Mutual and self-inductance in planarized multilayered superconductor integrated circuits: Microstrips, striplines, bends, meanders, ground plane perforations, *IEEE Transactions on Applied Superconductivity*, **32**(5), 1–31, 2022.

[Uhl15] J. Uhlig, W. B. Doriese, J. W. Fowler, D. S. Swetz, C. Jaye, D. A. Fischer, C. D. Reintsema, D. A. Bennett, L. R. Vale, U. Mandal, G. C. O'Neil, L. Miaja-Avila, Y. I. Joe, A. El Nahhas, W. Fullagar, F. Parnefjord Gustafsson, V. Sundström, D. Kurunthu, G. C. Hilton, D. R. Schmidt, J. N. Ullom, High-resolution X-ray emission spectroscopy with transition-edge sensors: present performance and future potential, *Journal of Synchrotron Radiation*, **22**(3), 766–775, 2015.

[Ull04] J.N. Ullom, W.B. Doriese, G.C. Hilton, J.A. Beall, S. Deiker, K.D. Irwin, C.D. Reintsema, L.R. Vale, Y. Xu, Suppression of excess noise in transition-edge sensors using magnetic field and geometry, *Nuclear Instruments and Methods in Physics Research Section A: Accelerators, Spectrometers, Detectors and Associated Equipment*, **520**(1), 333–335, 2004, Proceedings of the 10th International Workshop on Low Temperature Detectors.

[Ull15] Joel N. Ullom Douglas A. Bennett, Review of superconducting transition-edge sensors for x-ray and gamma-ray spectroscopy, *Superconductor Science and Technology*, **28**(8), 084003, 2015.

[Ung24] Daniel Unger, Andreas Abeln, Thomas Elias Cocolios, Ofir Eizenberg, Christian Enss, Andreas Fleischmann, Loredana Gastaldo, César Godinho, Michael Heines, Daniel Hengstler, Paul Indelicato, Ashish Jadhav, Daniel Kreuzberger, Klaus Kirch, Andreas Knecht, Jorge Machado, Ben Ohayon, Nancy Paul, Randolf Pohl, Katharina von Schoeler, Stergiani Marina Vogiatzi, Frederik Wauters, Mmc array to study x-ray transitions in muonic atoms, *Journal of Low Temperature Physics*, 2024.

[vK23] Belina von Krosigk, Klaus Eitel, Christian Enss, Torben Ferber, Loredana Gastaldo, Felix Kahlhoefer, Sebastian Kempf, Markus Klute, Sebastian Lindemann, Marc Schumann, Francesco Toschi, Kathrin Valerius, DELight: A

Direct search Experiment for Light dark matter with superfluid helium, *SciPost Phys. Proc.*, 016, 2023.

[Wea16] Robert Weaver, Geometric Mean Distance - Its Derivation and Application in Inductance Calculations, 2016.

[Wee79] W. T. Weeks, L. L.-H. Wu, M. F. McAllister, A. Singh, Resistive and inductive skin effect in rectangular conductors, *IBM Journal of Research and Development*, **23**(6), 652–660, 1979.

[Weg22] M Wegner, C Enss, S Kempf, Analytical model of the readout power and SQUID hysteresis parameter dependence of the resonator characteristics of microwave SQUID multiplexers, *Superconductor Science and Technology*, **35**(7), 075011, 2022.

[Wel67] Peter D. Welch, The use of fast fourier transform for the estimation of power spectra: A method based on time averaging over short, modified periodograms, *IEEE Transactions on Audio and Electroacoustics*, **15**, 70–73, 1967.

[Wel93] R.P. Welty J.M. Martinis, Two-stage integrated squid amplifier with series array output, *IEEE Transactions on Applied Superconductivity*, **3**(1), 2605–2608, 1993.

[Wes21] Abigail Wessels, Kelsey Morgan, Johnathon D. Gard, Gene C. Hilton, John A. B. Mates, Carl D. Reintsema, Daniel R. Schmidt, Daniel S. Swetz, Joel N. Ullom, Leila R. Vale, Douglas A. Bennett, A model for excess Johnson noise in superconducting transition-edge sensors, *Applied Physics Letters*, **118**(20), 202601, 2021.

[Yag23] Yuta Yagi, Tasuku Hayashi, Keita Tanaka, Rikuta Miyagawa, Ryo Ota, Noriko Y. Yamasaki, Kazuhisa Mitsuda, Nao Yoshida, Mikiko Saito, Takayuki Homma, Fabrication of a 64-pixel tes microcalorimeter array with iron absorbers uniquely designed for 14.4-kev solar axion search, *IEEE Transactions on Applied Superconductivity*, **33**(5), 1–5, 2023.

[Yoo01] Jongsoo Yoon, John Clarke, J. M. Gildemeister, Adrian T. Lee, M. J. Myers, P. L. Richards, J. T. Skidmore, Single superconducting quantum interference device multiplexer for arrays of low-temperature sensors, *Applied Physics Letters*, **78**(3), 371–373, 2001.

[Yu20] C. Yu, A. Ames, S. Chaudhuri, C. Dawson, K. D. Irwin, S. E. Kuenstner, D. Li, C. J. Titus, An impedance-modulated code-division microwave squid multiplexer, *Engineering Research Express*, **2**(1), 2020.

[Yu23] Cyndia Yu, Zeeshan Ahmed, Josef C. Frisch, Shawn W. Henderson, Max Silva-Feaver, Kam Arnold, David Brown, Jake Connors, Ari J. Cukierman, J. Mitch

D'Ewart, Bradley J. Dober, John E. Dusatko, Gunther Haller, Ryan Herbst, Gene C. Hilton, Johannes Hubmayr, Kent D. Irwin, Chao-Lin Kuo, John A. B. Mates, Larry Ruckman, Joel Ullom, Leila Vale, Daniel D. Van Winkle, Jesus Vasquez, Edward Young, SLAC microresonator RF (SMuRF) electronics: A tone-tracking readout system for superconducting microwave resonator arrays, *Review of Scientific Instruments*, **94**(1), 014712, 2023.

[Zah24] Mostafa Lokman Zahir, Matias Rodrigues, Martin Loidl, Arshjot Kaur, Energy non-linearity study of a high-resolution metallic magnetic calorimeter, *Radiation Physics and Chemistry*, **220**, 111730, 2024.